



Namensnennung-Keine kommerzielle Nutzung-Keine Bearbeitung 2.5 Schweiz

Sie dürfen:



das Werk vervielfältigen, verbreiten und öffentlich zugänglich machen

Zu den folgenden Bedingungen:



Namensnennung. Sie müssen den Namen des Autors/Rechteinhabers in der von ihm festgelegten Weise nennen (wodurch aber nicht der Eindruck entstehen darf, Sie oder die Nutzung des Werkes durch Sie würden entlohnt).



Keine kommerzielle Nutzung. Dieses Werk darf nicht für kommerzielle Zwecke verwendet werden.



Keine Bearbeitung. Dieses Werk darf nicht bearbeitet oder in anderer Weise verändert werden.

- Im Falle einer Verbreitung müssen Sie anderen die Lizenzbedingungen, unter welche dieses Werk fällt, mitteilen. Am Einfachsten ist es, einen Link auf diese Seite einzubinden.
- Jede der vorgenannten Bedingungen kann aufgehoben werden, sofern Sie die Einwilligung des Rechteinhabers dazu erhalten.
- Diese Lizenz lässt die Urheberpersönlichkeitsrechte unberührt.

Die gesetzlichen Schranken des Urheberrechts bleiben hiervon unberührt.

Die Commons Deed ist eine Zusammenfassung des Lizenzvertrags in allgemeinverständlicher Sprache: <http://creativecommons.org/licenses/by-nc-nd/2.5/ch/legalcode.de>

Haftungsausschluss:

Die Commons Deed ist kein Lizenzvertrag. Sie ist lediglich ein Referenztext, der den zugrundeliegenden Lizenzvertrag übersichtlich und in allgemeinverständlicher Sprache wiedergibt. Die Deed selbst entfaltet keine juristische Wirkung und erscheint im eigentlichen Lizenzvertrag nicht. Creative Commons ist keine Rechtsanwalts-gesellschaft und leistet keine Rechtsberatung. Die Weitergabe und Verlinkung des Commons Deeds führt zu keinem Mandatsverhältnis.



*Linear and Nonlinear Spectroscopic
Techniques applied to Study of Transient
Molecular Species*

Inauguraldissertation

zur
Erlangung der Würde eines Doktors der Philosophie
vorgelegt der
Philosophisch-Naturwissenschaftliche Fakultät
der Universität Basel

von

Ranjini Raghunandan

aus

Kochi, Indien

Basel, 2011

Genehmigt von der Philosophisch-Naturwissenschaftliche Fakultät

auf Antrag von

Prof. Dr. John P. Maier und Prof. Dr. Stefan Willitsch

Basel, den 21.06.2011

Prof. Dr. Martin Spiess

Acknowledgement

This dissertation would not have been possible without the guidance and support of several individuals, who contributed their valuable time and assistance for the completion of my doctoral studies.

First and foremost, I extend my sincere gratitude to Prof. John Paul Maier who gave me the opportunity to work in his wonderful group and whose supervision and support, from the preliminary to concluding level, enabled me to get a better understanding of the subject.

I specially thank Prof. Stefan Willitsch for being the co-referee of my thesis. I also thank him for suggestions and encouragement during the group seminars.

Many thanks to Prof. Thomas Pfohl who kindly agreed to chair my Ph.D. defence.

It was a great pleasure working with Dr. Fabio J. Mazzotti and I am grateful for his encouragement and help throughout my doctoral studies. Without him, life would have been much difficult. Thank you Faby! I also take this opportunity to thank Dr. Corey Rice for his suggestions and support, especially during the correction of this thesis. My sincere gratitude is extended to Dr. Marek Tulej for his guidance on the four-wave mixing experiments.

I would like to thank Prof. Thomas F. Giesen for his time and patience with the numerous mails and discussions we had regarding the laser vaporization unit. I also enjoyed our conversations at all those conferences where we sat opposite each other on the vegetarian table.

My sincere thanks go to Prof. Jon T. Hougen and Prof. Dennis J. Clouthier for their valuable advice on the Renner-Teller problem. I also thank Prof. Geoffrey Duxbury for giving us all a better insight to the R-T effect during his three week stay in Basel. He is someone who can engage you in any subject, be it chemistry, physics, geography or movies. I got a better understanding of astrophysics and diffuse interstellar bands during the discussions with Prof. Gordon Walker and I am deeply obliged to him for it.

I owe my appreciation to Dr. Richa Chauhan for her guidance and friendship when I was a newcomer here. I also wish the newest member of the CRD-FWM lab and my friend for years, Aaseef, all the best for his doctorate studies.

I would also like to thank Dr. Anatoly Johnson for helping with the lasers every time there was a problem. He has been a great help throughout. The experiments would have been difficult had it not been for the technical expertise of Mr. Grischa Martin and Mr. Dieter Wild from the mechanical workshop. I am highly grateful to Mr. Georg Holderfeld for his help with the electronics and Mr. Jacques Lecoultre for synthesizing diacetylene on demand.

Further, I would also like to extend my sincere appreciation to Ms. Daniela Tischauser, Ms. Esther Stalder and Ms. Maya Greuter for their help with regard to the administrative matters. The Swiss National Science Foundation and the University of Basel are thanked for their financial support.

A big thank you to Dr. Rainer Dietsche and Satrajit for the good times we had after work. Long live Best Pizza and Shree Krishna Take Away!!! I also wish to express my sincere thanks to Dr. Ramya Nagarajan who has always been a constant source of inspiration and encouragement.

In addition, my heartiest thanks go to all other group members, past and present, and my dear Indian friends in Basel, who were always there during good and bad times. I especially thank Somedutta, Divya-Vijay, Vimal, Pankaj and Sudhir. Vimal also needs special mention for helping me with the formalities of thesis submission. I also thank Adil for being a wonderful friend and a perfect host at Ghent.

Words are not enough to express my gratitude to Varun who has stood by me through thick and thin for the last seven years.

Last but not the least, I acknowledge my parents and sister for their love and support in all walks of life and without whom none of this would have happened.

Ranjini Raghunandan

Table of Contents

1. Introduction - From Sunlight to Lasers	1
1.1. Spectroscopy – An Early History	1
1.2. Molecular Spectra.....	2
1.3. Laser Spectroscopy.....	6
1.4. Structure of the Thesis	10
Bibliography	13
2. Cavity Ring-down Spectroscopy	15
2.1. Introduction.....	15
2.2. Basic Considerations.....	18
2.3. Mode Formation and CRDS.....	21
2.4. Factors affecting CRDS	25
2.5. Cavity Ring-down variants.....	26
Bibliography	29
3. Four Wave Mixing Spectroscopy	31
3.1. Introduction.....	31
3.2. Theoretical Background	34
3.3. Experimental Geometries	38
3.4. The Laser Induced Grating Approach.....	40
3.5. Optical Saturation Effects and Line Profiles	42
3.6. Phase Matching Considerations in TC-LIGS.....	44
Bibliography	47
4. Experimental Set-up	49
4.1. Supersonic Jet Expansion.....	49
4.2. Molecular Sources.....	53
4.2.1. Electric Discharge	53
4.2.2. Laser Ablation.....	55
4.3. Source Chamber and Vacuum System.....	57
4.4. Light Sources.....	57

4.5. Signal Detection	60
4.6. Experimental Arrangement	61
4.6.1. Cavity Ring-down Spectroscopy	61
4.6.2. Four-wave Mixing Spectroscopy	63
Bibliography	67
5. Electronic Spectra of Gas Phase Hydrocarbons by Cavity Ring-down Technique .	69
5.1. Introduction.....	69
5.2. Experimental.....	70
5.3. C_6H^+	70
5.3.1. Results and Discussion	71
5.4. HC_4H^+	77
5.4.1. Results and discussion.....	78
5.5. $C_6H_3^+$	80
5.5.1. Results and discussion.....	80
Bibliography	82
6. Broad absorption features of <i>l</i>-C_3H_2 - Relevance to the DIB Problem.....	84
6.1. Introduction.....	84
6.2. Diffuse Interstellar Bands.....	85
6.2.1. DIB Properties	88
6.3. <i>l</i> - C_3H_2	89
6.3.1. Experimental.....	91
6.3.2. Results.....	91
6.3.2.1. Simulation of Band Profile.....	95
6.3.2.1.1. Bands above 6000 Å.....	95
6.3.2.1.2. The 5450 Å Band.....	97
6.3.2.2. Astronomical Observations.....	98
6.3.2.2.1. Broad Bands.....	98
6.3.2.2.2. Narrow Triplets above 6000 Å.....	100
6.3.3. Discussion.....	102
Bibliography	104

7. Selective Determination of Radicals and Ions by Four wave Mixing Technique.	107
7.1. Introduction.....	107
7.2. Experimental.....	108
7.3. Species Selectivity in the Temporal Domain.....	109
7.4. Species selectivity by Two-Color Resonant FWM.....	110
7.5. Detection of ions by FWM.....	112
7.6. Sensitivity of DFWM.....	115
Bibliography.....	117
8. Non-Adiabatic Interactions - Renner Teller and Fermi Resonance Effects	118
8.1. Introduction.....	118
8.2. The Molecular Hamiltonian and the Born-Oppenheimer Approximation.....	118
8.3. Perturbations between Two Levels.....	122
8.4. Types of Perturbations.....	122
8.4.1. Spin-Orbit Coupling.....	123
8.4.2. Vibrational Coupling - Fermi Resonance.....	123
8.4.3. Renner-Teller Coupling.....	125
8.5. HC ₄ H ⁺	127
8.5.1. Experimental.....	128
8.5.2. Renner Teller and Fermi Resonance Analysis.....	128
8.6. C ₄ H.....	132
8.6.1. Experimental.....	133
8.6.2. Results.....	135
8.6.2.1. Single Color.....	135
8.6.2.2. Double Resonance.....	136
8.6.2.3. A ² Π _u State Spin-Orbit Splitting.....	138
8.6.3. Renner Teller Analysis: Effective Hamiltonian.....	139
Bibliography.....	144
9. Concluding Remarks	146
Bibliography.....	150

Appendices	151
A. Dispersion Effects in CRDS.....	151
B. Electronic Spectra of Linear C_{2n+1} Chains.....	153
B.1. C_5	154
B.1.1. Comparison to previous CRD-laser ablation setups	154
B.1.2. Comparison with high voltage discharge spectra	156
B.1.3. Detection of vibronic transitions in $A^1\Pi_u$ electronic state	157
B.2. Detection feasibility for Linear C_{2n+1} Chains	158
Bibliography	160
C. Rotational Assignment for the 3_0^1 and $7_0^2 A^2\Pi_u - X^2\Pi_g$ transitions of HC_4H^+	161
D. Precursor Tests: $l-C_3H_2$	163
E. Unidentified Broad Bands Recorded by CRDS.....	165
F. Perturbed Energy Levels - C_4H	170
G. Resolved Ground State Vibrational Levels of HC_2S Studied by Two-Color Resonant Four-wave Mixing	174
Curriculum Vitae	179

Chapter 1

Introduction

From Sunlight to Lasers

1.1. Spectroscopy – An Early History

The rainbow effect, which was observed as unwanted color fringes in the early telescopes of the 17th century, remained an unexplained curiosity of the time. For years man marveled at the multicolored arc of visible light without recognizing its significance. In 1666 Newton showed that white light from the sun, when allowed to pass through a small hole in a window shutter and onto a glass prism, could be dispersed into a regular series of colors [1]. Newton introduced the word "spectrum" to describe this phenomenon, which he projected onto a screen. Newton's analysis of light marked the beginning of the science of spectroscopy.

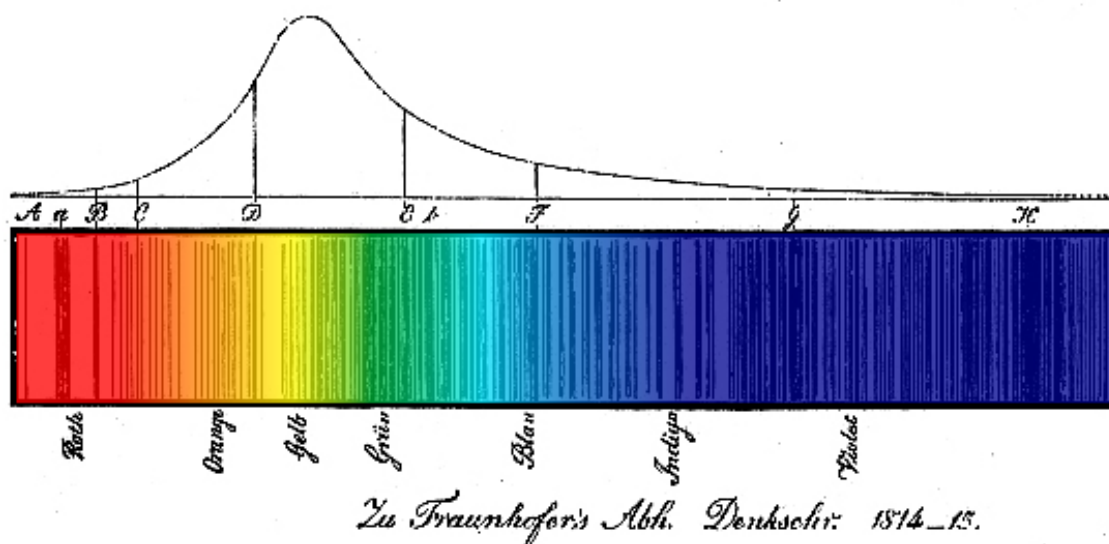


Figure 1.1: The solar spectrum with Fraunhofer lines.

The achievements of Joseph von Fraunhofer provided the quantitative basis for experimental spectroscopy. In 1814 Fraunhofer extended Newton's discovery by observing that a dispersed solar spectrum was crossed by a large number of fine dark lines parallel to the slit, known as Fraunhofer lines [2]. Using a convex lens between the

slit and the prism, he obtained a better defined series of images. William Wollaston had earlier observed a few of these lines in 1802 [3], but failed to attach any significance to them. These were the first spectral lines ever observed, and Fraunhofer assigned the stronger ones the letters A to H, A being in the red and H in the violet region (Figure 1.1). He also studied spectra of the stars and planets, using a telescope objective to collect the light. This laid the foundation for the science of astrophysics.

In 1822 Sir John Herschel studied the visible spectra of colored flames and noted: “The colors thus contributed by different objects to flame afford in many cases a ready and neat way of detecting extremely minute quantities of them” [4]. Armed with the theory of absorption and emission, and the fact that each atom and molecule produced a unique and characteristic spectrum, Kirchhoff and Bunsen established spectroscopy as a scientific tool for probing atomic and molecular structure [5], and founded the field of spectrochemical analysis for analyzing the composition of materials.

With the development of the electric arc lamp over the earlier Bunsen burner, the atomic spectra of all elements could be studied. In 1885 Balmer observed the spectrum of hydrogen with emission wavelengths at 6563, 4861, 4341, 4102 and 3970 Å. This showed that atoms emitted light at discrete frequencies. A new era in spectral interpretation was initiated by Niels Bohr in 1913 [6] by linking line spectra to the quantum theory proposed by Planck and Einstein.

The electronic structure of matter could now be investigated using visible emission spectroscopy as a tool as it helped one study the transitions of outer electrons in atoms and molecules. Later on, August Beer by proposing the Beer’s law [7] established that like in emission, absorption spectra could be used to identify elements or study electronic transitions. The science of optical absorption spectroscopy was thus born.

1.2. Molecular Spectra

Spectroscopy is the study of the interaction of light with matter. When an isolated atom or molecule absorbs or emits a photon of energy $h\nu$ it produces a transition from a state with energy E_1 to another state with energy E_2 . Energy conservation requires that

$$h\nu = E_2 - E_1 . \quad (1.1)$$

The states involved can be discrete, bound states with sharply defined energies. In a spectrum such a transition shows up as a sharp line at the wavelength $\lambda = c/\nu$. The unstable, repulsive states, which lead to a dissociation of the molecule are characterized by a frequency continuum and transitions into or from such states produce a broad absorption or emission spectrum.

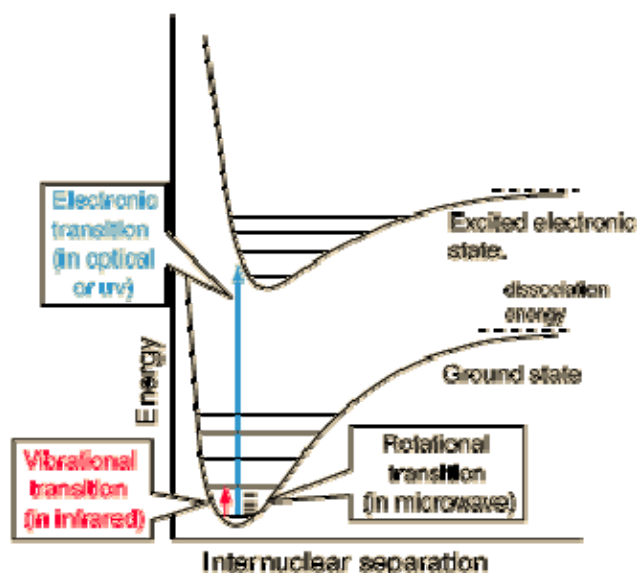


Figure 1.2: Schematic visualization of the energy levels of a molecule.

In general, molecular spectra are more complicated than atomic spectra because of the additional internal degrees of freedom and also the geometrical arrangement of the nuclei and their movements. First, molecules possess more electronic states than atoms. Second, the nuclei of a molecule can vibrate around their equilibrium positions. Finally, a molecule as a whole may rotate around axes through its center of mass. Therefore, for each electronic molecular state there exist a large number of vibrational and rotational energy levels (Figure 1.2).

Molecular spectra can then be characterized as:

- Transitions between different rotational levels for the same vibrational (and electronic) state which lead to pure rotational spectra with wavelengths in the microwave region ($\lambda \approx 1 \text{ mm to } 1 \text{ m}$).
- Transitions between rotational levels in different vibrational levels of the same electronic state which lead to vibration-rotation spectra in the infrared ($\lambda \approx 2\text{-}20 \mu\text{m}$).

- Transitions between two different electronic states having wavelengths from the UV to the near IR ($\lambda \approx 0.1-2 \mu\text{m}$).

Each electronic transition comprises many vibrational bands corresponding to transitions between the different vibrational levels of the two electronic states involved. Each of these bands could also be rotationally resolved (rovibronic transitions). To a very good approximation, the frequency of the absorbed or emitted photon is then given by

$$h\nu = (E_2^{el} + E_2^{vib} + E_2^{rot}) - (E_1^{el} + E_1^{vib} + E_1^{rot}). \quad (1.2)$$

The thesis concerns itself mainly with the electronic structure and properties of linear polyatomic molecules. With all atoms in a straight line two symmetry classes are distinguished, which comprise molecules with a center of symmetry ($D_{\infty h}$) and those with no center of symmetry ($C_{\infty v}$). The Σ terms are non-degenerate; all other terms in the character table are two-fold degenerate. The subscripts g and u refer to symmetrical and antisymmetrical behavior of the electronic eigenfunctions with respect to the center of symmetry. σ_v symbolizes planes through the figure axis. The signs $+$ and $-$ denote symmetrical and antisymmetrical behavior with regard to reflections in these planes, corresponding to Σ^+ and Σ^- terms. According to group theory, the symbols for the electronic terms and the transformation properties can be multiplied with each other. The process is called formation of the direct product, the result of which is again a term symbol, or when two degenerate terms are multiplied, several term symbols. Thus, $\Sigma_u^- \times \Delta_g$ gives Δ_u and $\Pi_g \times \Delta_u$ gives Π_u and Φ_u .

Electronic transition probabilities are determined by the matrix elements of the dipole moment $\int \psi_2^{el} M \psi_1^{el} d\tau_{el}$. Here ψ_2^{el} and ψ_1^{el} are electronic eigenfunctions in the upper and lower states, and M is the dipole moment of the system of nuclei and electrons for a definite electronic configuration. The integral differs from zero only if the direct product of the transformation properties of the separate factors contains a totally symmetric term. In other words, a combination between two states is allowed if their direct product contains a term which transforms like one of the translations T_x , T_y or T_z .

The vibrations of a polyatomic molecule can be classified according to their symmetries in a similar way as the electronic states. There are both non-degenerate and

degenerate vibrations; in non-degenerate vibrations the atoms of a molecule move along straight lines and all are in phase. These vibrations are symmetrical or anti-symmetrical with respect to various symmetry operations. If they preserve the symmetry during all symmetry operations, they are called totally symmetric. Degenerate vibrations occur when several independent motions exist with the same frequency. In the case of linear molecules, Σ and Π terms correspond to non-degenerate and degenerate vibrations respectively. The lowest vibrational state is always totally symmetric. If two different normal vibrations are excited, the symmetry of the resulting vibrational levels is obtained by the direct product of the terms belonging to the separate normal vibrations. The vibronic eigenfunction is given by the product of the electronic and the vibrational eigenfunctions. The transition probabilities are proportional to the square of the matrix elements $\int \psi_{el}^{(a)} \psi_{vib}^{(a)} M \psi_{el}^{(b)} \psi_{vib}^{(b)} d\tau_{el} d\tau_{nuc}$. It is proportional to $|\mathcal{M}|^2 \left| \int \psi_{vib}^{(a)} \psi_{vib}^{(b)} d\tau_{nuc} \right|^2$, the first factor $|\mathcal{M}|^2$ giving the electronic part of the transition probability, while the probability for changes in vibrational quantum numbers is given by the second factor. In other words, the transition probability will be different from zero only if the vibrational eigenfunction has the same symmetry in the initial and final states. Often, the electronic degeneracy, which is a consequence of the symmetry of the molecule, may be split when the nuclei occupy an asymmetric position. Figure 1.3 shows the splitting of a Π electronic state by a deformation vibration.

The rotational structure in polyatomic spectra yields not only an estimate of the moments of inertia but also information about the position of electronic transition moment within the molecule. The only important deviation from the rotational levels in infra-red spectra is that the moments of inertia may be different in the initial and final states. Rotational bands with pronounced heads and a shading towards the red or violet side result. For linear molecules the moment of inertia about the molecular axis is zero while the two other moments of inertia are equal. The rotational energy levels are $\left(\frac{h^2}{8\pi^2 I}\right) [J(J+1) - \theta^2]$, where I is the moment of inertia about an axis perpendicular to the figure axis, J is the total angular momentum and θ is the angular momentum about the molecular axis. In polyatomic molecules θ is obtained by adding the vibrational angular momentum to the electronic angular momentum Ω . The rotational selection rules are $\Delta J = 0, \pm 1$. In addition $\Delta J = 0$ is forbidden if $J = 0$ or if the band corresponds

to a $\theta = 0 \rightarrow \theta = 0$ transition. For $\Delta\theta = 0, \theta \neq 0$ the lines $\Delta J = 0$ are weak, particularly for high J values.

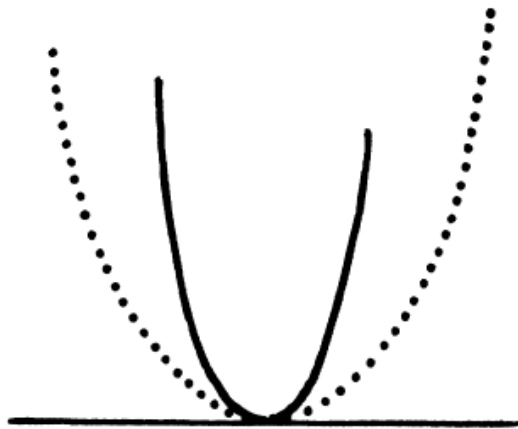


Figure 1.3: Splitting of a Π state by a deformation vibration.

Wavelength measurements of spectral lines allow the determination of energy levels of the atomic or molecular system. The line intensity is proportional to the transition probability, which measures how strongly the two levels of a molecular transition are coupled. The rotational spectra yield the geometrical structure of the molecule, the vibrational spectra give information on the forces between the vibrating atoms of a molecule, and the electronic spectra determine the electronic states, their stabilities, and the electron distributions. The natural linewidth of a spectral line can yield the lifetimes of excited states or dissociation energies. Qualitatively, the spectrum can also be matched with reference spectra of interest and the molecular species identified [8]. Thus, the complete analysis of a spectrum of sufficient spectral resolution provides a plethora of information for a particular molecule.

1.3. Laser Spectroscopy

The introduction of lasers to spectroscopy gave a highly stimulating impetus to the field of molecular physics. The much higher spectral intensity as compared to classical radiation sources, narrow linewidths, good beam collimation, and the availability of ultrashort pulses of light have enabled a vast number of new spectroscopic techniques that surpass experimental limitations of classical spectroscopy in terms of detection sensitivity and spectral and temporal resolution. Some of these techniques include

intracavity laser spectroscopy [9], photoacoustic spectroscopy (PAS) [10], laser induced fluorescence (LIF) [11] etc. For example, in LIF (Figure 1.4), when the laser wavelength λ_L is tuned to an absorbing molecular transition $E_k \leftarrow E_i$ the number of photons absorbed per second along the pathlength Δx is

$$n_a = N_i n_L \sigma_{ik} \Delta x , \quad (1.3)$$

where n_L is the number of incident laser photons per second, σ_{ik} the absorption cross section per molecule, and N_i the density of molecules in the absorbing state $|i\rangle$.

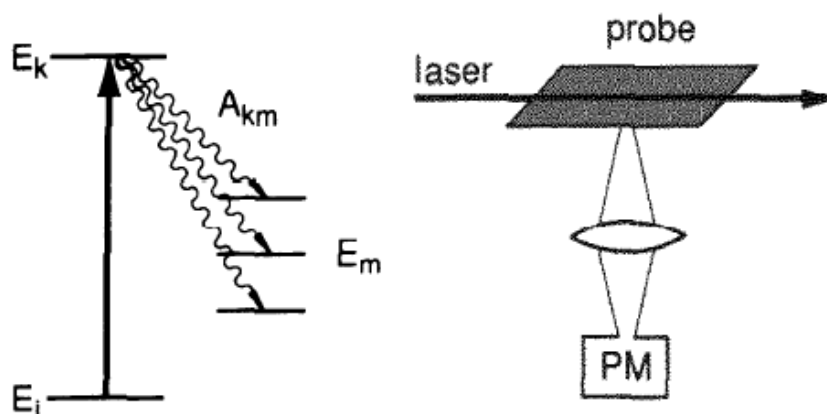


Figure 1.4: Basic Principle of LIF.

The number of fluorescence photons emitted per second from the excited level E_k is

$$n_{FL} = N_k A_k = n_a \eta_k , \quad (1.4)$$

where $A_k = \sum_m A_{km}$ stands for the total spontaneous transition probability to all levels with $E_m < E_k$ and η_k , the quantum efficiency of the excited state which can possibly also be deactivated by other radiationless processes.

The extremely high sensitivity of this technique has been demonstrated impressively by Fairbank et al. [12], who performed absolute density measurements of sodium vapor in a particle density of $N = 10^{11}$ cm⁻³. However, due to collisional quenching and increased scattering, the technique is less suited to applications at high pressure. The same applies to excited electronic states that have poor quantum yields for emission.

Throughout the present work, focus is brought on laser absorption spectroscopic techniques. In the case of laser absorption spectroscopy, the loss of electromagnetic energy after the radiation passes through a cell containing the sample is measured (Figure 1.5). According to the Beer-Lambert law, the transmitted intensity, $I_{\text{trans}}(\lambda)$, at the wavelength λ is related to the incident intensity $I_0(\lambda)$ by

$$I_{\text{trans}}(\lambda) = I_0(\lambda) e^{-\alpha(\lambda)l_{\text{eff}}}, \quad (1.5)$$

where $\alpha(\lambda)$ is the absorption coefficient, and l_{eff} is the effective pathlength of the sample. For a weak absorption, the absorption coefficient can be computed from

$$\alpha(\lambda) = \frac{I_0(\lambda) - I_{\text{trans}}(\lambda)}{I_0(\lambda)l_{\text{eff}}} = \frac{\Delta I(\lambda)}{I_0(\lambda)l_{\text{eff}}}. \quad (1.6)$$

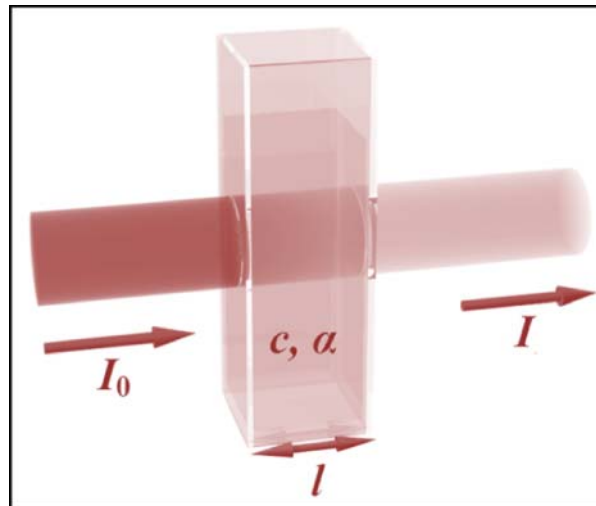


Figure 1.5: Conventional direct absorption measurement.

Clearly, the minimum detectable concentration of absorbers for a specific absorption transition is inversely proportional to the effective sample pathlength and directly proportional to the minimum intensity fluctuation of the system. However, the sensitivity of such a technique is limited by the accuracy of measurement $\Delta I(\lambda)$ and the stability of the light source. Therefore, other techniques which are based on increased absorption pathlength (Herriott/White cell) or frequency modulation have been developed, pushing detection limits to the parts-per-billion range. An example is cavity ring-down (CRD) spectroscopy [13], a direct linear laser absorption technique which is based on the measurements of decay times of optical resonators filled with the absorbing species. The subsequent chapters detail this technique along with four wave

mixing (FWM) [14] spectroscopy, which involves the non-linear interaction of three incident light waves to produce the fourth wave via the third order susceptibility $\chi^{(3)}$.

The relevance of laser spectroscopy for numerous applications in physics, chemistry, biology and medicine or to environmental studies and atmospheric monitoring [15] has rapidly gained enormous significance. Applications in analytical chemistry include ultrasensitive detection of small concentrations of pollutants and trace elements [16]. Because of its high sensitivity, laser spectroscopy can be successfully used to monitor short-lived intermediate products in chemical reactions [17] or temperature measurements in combustion environments [18]. Detailed information on the internal state distribution $N_i(v_i'' J_i'')$ of reactant products and collision induced energy transfer processes [19] can also be extracted. Other applications of laser spectroscopy include surface analysis and plasma characterization [20], study of DNA complexes [21], time-resolved spectroscopic measurements of biological processes [22], cancer diagnostics [23], breath analysis [24] and so forth.

$N=2$	$N=3$	$N=4$	$N=5$	$N=6$	$N=7$	$N=8$	$N=9$	$N=10$	$N=11$
H ₂	H ₃ ⁺	NH ₃	CH ₄	CH ₃ OH	CH ₃ NH ₂	HCOOCH ₃	(CH ₃) ₂ O	(CH ₃) ₂ CO	HC ₈ CN
CH	CH ₂	H ₃ O ⁺	SiH ₄	CH ₃ SH	CH ₃ CCH	CH ₃ C ₂ CN	C ₂ H ₅ OH	CH ₃ C ₄ CN	CH ₃ C ₆ H
CH ⁺	NH ₂	H ₂ CO	CH ₂ NH	C ₂ H ₄	CH ₃ CHO	H ₂ C ₆	C ₂ H ₅ CN	(CH ₂ OH) ₂	
NH	H ₂ O	H ₂ CS	H ₂ C ₃	CH ₃ CN	c-CH ₂ OCH ₂	C ₇ H	CH ₃ C ₄ H	C ₂ H ₅ CHO	
OH	H ₂ S	C ₃ H	c-C ₃ H ₂	CH ₃ NC	CH ₂ CHCN	HOCH ₂ CHO	C ₈ H		
HF	C ₂ H	HCCH	CH ₂ CN	HC ₂ CHO	HC ₄ CN	CH ₂ CCHCN	HC ₆ CN		
C ₂	HCN	HCNH ⁺	NH ₂ CN	NH ₂ CHO	C ₆ H		CH ₃ CONH ₂		$\frac{N=13}{HC_{10}CN}$
CN	HNC	H ₂ CN	CH ₂ CO	HC ₃ NH ⁺	C ₆ H ⁻		C ₈ H ⁻		
CO	HCO	c-C ₃ H	HCOOH	H ₂ C ₄			C ₃ H ₆		
CSi	HCO ⁺	HCCN	C ₄ H	HC ₄ N					
CP	HOC ⁺	HNCO	HC ₂ CN	C ₃ H					
NO	HN ₂ ⁺	HOCO ⁺	HC ₂ NC	C ₅ N					
NS	HNO	HNCS	C ₄ Si	C ₅ O					
SO	HCS ⁺	C ₂ CN	C ₅	C ₅ S		$\frac{N=2}{C_5}$	$\frac{N=3}{C_5}$		
HCl	C ₃	C ₂ O	H ₂ COH ⁺	c-H ₂ C ₃ O					
KCl	C ₂ O	C ₃ S	C ₄ H ⁻			PN O ₂	OCS		
AlCl	C ₂ S	c-SiC ₃				SiN CF ⁺	MgCN		
AlF	SiC ₂	C ₃ N ⁻				SiO PO	MgNC		
						SiS	NaCN		
						CO ⁺	SO ₂		
						SO ⁺	N ₂ O		
						CS	SiCN		
						SH	SiNC		
						FeO	HCP		
							AlNC		

Table 1.1: Interstellar molecules.

Molecular spectroscopy and astronomy have gone in sync over the years. Spectral features in various frequency regions of the electromagnetic radiation are used

to indicate the presence of atomic or molecular species in stellar or planetary atmospheres, including the Earth, or in the interstellar (ISM) or circumstellar medium (CSM). Table 1.1 shows some of the molecules which have been identified in the ISM [25]. The structure and spectroscopic properties of bare carbon species and ions have been studied over the past several years because of their astrophysical significance. C₂ and C₃, two of the best characterized among these, have been detected in diffuse and translucent molecular clouds [26, 27] via their electronic transitions. In addition, C₃ and C₅ have been detected in circumstellar shells of the carbon rich star, IRC+10216 by IR spectroscopy [28].

In the laboratory, the origin band of the ${}^3\Sigma_u^- \leftarrow X\,{}^3\Sigma_g^-$ transition of C₄ was recorded using the CRD technique [29]. Electronic spectra of C₅, C₆, C₈ and C₉ have been measured in the gas phase by Resonance Enhanced Multi-photon Ionization (REMPI) spectroscopy [30]. Besides pure carbon radicals, hydrogen terminated carbon chains, C_nH (n=2-8) have been detected in dark molecular clouds and envelopes of evolved stars [31]. The ground electronic states are well characterized for these species by microwave spectroscopy [32]. The electronic spectrum of the $B^2\Pi \leftarrow X^2\Sigma^+$ band system of C₃N which has been detected in the ISM [33], was measured using LIF [34]. The availability of transition frequencies and intensities with appropriate accuracies is required to identify and quantify the abundance of a certain species unambiguously.

1.4. Structure of the Thesis

The laboratory and astronomical investigations in the millimeter-wave region lead to the identification of many carbon chains in space, including ions and radicals. Measurements on these molecules are difficult because they are short-lived species generated in small number densities. Discharge and laser vaporization sources coupled to a supersonic jet expansion are, so far, the most effective techniques used to generate sufficiently large densities suitable for spectroscopic studies of these transients. The present work describes the combination of these molecular sources with high resolution CRD and FWM spectroscopic techniques applied to detection of radicals and ions of astrophysical significance.

Chapters 2 and 3 describe the theoretical background of CRD and FWM techniques, respectively. Both degenerate and two-color FWM are elaborated on.

Chapter 4 focuses on the details of the current experimental set-up. The chapter describes supersonic slit expansion and its advantages when coupled to discharge and vaporization sources. Details about the laser ablation source are given with experimental demonstration of its sensitivity and selectivity compared to older ablation sources and an electric discharge nozzle (Appendix B). Detection feasibility for higher carbon chains is also presented.

Chapter 5 discusses how CRDS has been employed to detect the ${}^3\Pi\leftarrow{}^3\Pi$ electronic transition of C_6H^+ for the first time in the gas phase. Partially resolved P lines and observation of band heads permitted a rotational contour fit. Spectroscopic constants in the ground and excited-state were determined. This chapter also gives the results for the study of $C_6H_3^+$ to resolve its rotational structure using CRDS. The rotational analysis of 3_0^1 and 7_0^2 vibronic bands of the $A^2\Pi_u\leftarrow X^2\Pi_g$ electronic transition of diacetylene cation is also described.

The discovery of visible diffuse absorption bands in stellar spectra dates back to 1922 when a report on the observation of two spectral features, centered at 5780Å and 5797Å in the binary spectra was published by Heger [35]. These stationary features were named Diffuse Interstellar Bands (DIBs), presumed to arise from gaseous molecules. Several hypotheses have been put forward for their origin, most prominent being carbon chains and polycyclic hydrocarbon cations [36]. However, apart from small carbon molecules like C_2 , C_3 , CH [26] etc., no reliable identification of any complex DIB carrier has been reported so far. **Chapter 6** presents an astronomical breakthrough giving laboratory and astronomical evidence for $l-C_3H_2$ in the diffuse interstellar clouds and its identification as a DIB carrier [8]. This also depicts the sensitivity of CRDS in detecting weak, broad absorption features.

Chapter 7 demonstrates how slit jet expansion coupled with FWM offers both selectivity and sensitivity in the spectroscopic detection of neutrals and ions generated in diluted plasmas. The first spectroscopic detections of a polyatomic cation HC_4H^+ and an anion C_2^- produced in an electrical discharge by FWM spectroscopy are presented. The potential of FWM in selective determination of radicals is demonstrated in the case of C_3/C_4H , C_3/HC_2S and furthermore, within the $\Omega=3/2$ and $1/2$ spin-orbit components of the origin band of the $A^2\Pi_u\leftarrow X^2\Pi_g$ electronic transition of HC_4H^+ .

The ${}^2\Pi$ electronic states of both HC_4H^+ and C_4H are affected by the non-adiabatic Renner-Teller (R-T) coupling effects. The high spin-orbit quenching upon vibrational excitation in the 3_0^1 and 7_0^2 vibronic bands of the $A^2\Pi_u \leftarrow X^2\Pi_g$ electronic transition of HC_4H^+ is explained by carrying out a vibronic analysis taking into consideration the R-T, spin-orbit and Fermi resonance interactions between the ν_3 and ν_7 modes. The analysis is described in detail in **chapter 8**. The detection of vibronic energy levels above the ${}^2\Sigma^+$ ground state of C_4H using double resonance FWM is also presented. The sensitivity and unique characteristics of the technique permit detection of new levels. The $A^2\Pi$ state lying 222 cm^{-1} above the $X^2\Sigma^+$ ground state is also observed, confirming the analysis from anion photoelectron spectroscopy but with improved accuracy. In this case, an analysis is carried out for the lowest bending modes ν_6 and ν_7 in the $A^2\Pi_u$ state of C_4H .

Lastly, **chapter 9** concludes and provides an outlook of the presented work, entailing modifications which can be made to the incorporated experimental set-up.

Bibliography

- [1] Newton, I. *Phil. Trans. Roy. Soc. London.* 5, 3075, **1672**.
- [2] Fraunhofer, J. *Ann. Phys.* 26, 264, **1817**.
- [3] Wollaston, W. H. *Phil. Trans. Roy. Soc.* 11, 365, **1802**.
- [4] Lewis, J. *Spectroscopy in Science and Industry; Blackie: Great Britain.* **1936**.
- [5] Kirchhoff, G.; Bunsen, R. *Ann. Physik. Chem.* 110, 161, **1860**.
- [6] Bohr, N. *Phil. Mag.* 26, 1, **1913**.
- [7] Beer, A. *Einleitung in die höhere Optik; Wieweg: Braunschweig.* **1853**.
- [8] Maier, J. P.; Walker, G. A. H.; Bohlender, D. A.; Mazzotti, F. J.; Raghunandan, R.; Fulara, J.; Garkusha, I.; Nagy, A. *Astrophys. J.* 726, 41, **2011**.
- [9] Baev, V. M.; Eschner, J.; Paeth, E.; Schuler, R.; Toschek, P. E. *Appl. Phys. B* 55, 463, **1992**.
- [10] Paldus, B. A.; Spence, T. G.; Zare, R. N.; Oomens, J.; Harren, F. J. M.; Parker, D. H.; Gmachl, C.; Capasso, F.; Sivco, D. L.; Baillargeon, J. N.; Hutchinson, A. L.; Cho, A. Y. *Opt. Lett.* 24, 178, **1999**.
- [11] Kinsey, J. L. *Ann. Rev. Phys. Chem.* 28, 349, **1977**.
- [12] Fairbank, W. M. Jr.; Hänsch, T. W.; Schawlow, A. L. *J. Opt. Soc. Am.* 65, 199, **1975**.
- [13] O'Keefe, A.; Deacon, D. A. G. *Rev. Sci. Instrum.* 59, 2544, **1988**.
- [14] Ewart, P.; O'Leary, S. V. *Opt. Lett.* 11, 279, **1986**.
- [15] Bufton, J. L.; Itabe, T.; Larrabee Strow, L.; Korb, C. L.; Gentry, B. M.; Weng, C. Y. *Appl. Opt.* 22, 2592, **1983**.
- [16] Jongma, R. T.; Boogaarts, M. G. H.; Holleman, I.; Meijer, G. *Rev. Sci. Instrum.* 66, 2821, **1995**.
- [17] Neumark, D. M. *Ann. Rev. Phys. Chem.* 43, 153, **1992**.
- [18] Yueh, F. Y.; Beiting, E. J. *Appl. Opt.* 27, 3233, **1988**.
- [19] Spaanjaars, J. J. L.; ter Meulen, J. J.; Meijer, G. *J. Chem. Phys.* 107, 2242, **1997**.
- [20] Sabsabi, M.; Cielo, P. *Appl. Spectrosc.* 49, 499, **1995**.
- [21] Jankowiak, R.; Lu, P. Q.; Small, G. J.; Geacintov, N. E. *Chem. Res. Toxicol.* 3, 39, **1990**.
- [22] Lewis, J. W.; Goldbeck, R. A.; Kliger, D. S.; Xie, X.; Dunn, R. C.; Simon, J. D. *J. Phys. Chem.* 96, 5243, **1992**.
- [23] Alfano, R. R.; Pradhan, A.; Tang, G. C.; Wahl, S. J. *J. Opt. Soc. Am. B.* 6, 1015, **1989**.

- [24] Manne, J.; Sukhorukov, O.; Jäger, W.; Tulip, J. *Appl. Opt.* 45, 9230, **2006**.
- [25] Jochnowitz, E. B.; Maier, J. P. *Mol. Phys.* 106, 2093, **2008**.
- [26] Snow, T. P.; McCall, B. J. *Annu. Rev. Astron. Astrophys.* 44, 367, **2006**.
- [27] Haffner, L. M.; Meyer, D. M. *Astrophys. J.* 453, 450, **1995**.
- [28] Bernath, P. F. Hinkle, K. H.; Keady, J. J. *Science* 244, 562, **1989**.
- [29] Linnartz, H.; Vaizert, O.; Motylewski, T.; Maier, J. P. *J. Chem. Phys.* 112, 9777, **2000**.
- [30] Boguslavskiy, A. E.; Maier, J. P. *J. Chem. Phys.*, 125, 094308, **2006**.
- [31] Guelin, M.; Cernicharo, J.; Travers, M. J.; McCarthy, M. C.; Gottlieb, C. A.; Thaddeus, P.; Ohishi, M.; Saito, S.; Yamamaoto, S. *Astron. Astrophys.* 317, L1, **1997**.
- [32] Gottlieb, C. A.; McCarthy, M. C.; Travers, M. J.; Grabow, J.-U.; Thaddeus, P. *J. Chem. Phys.* 109, 5433, **1998**.
- [33] Guelin, M.; Thaddeus, P. *Astrophys. J.* 212, L81, **1977**.
- [34] Hoshina, K.; Endo, Y. *J. Chem. Phys.* 127, 184304, **2007**.
- [35] Heger, M. L. *Lick Obsv. Bull.* 10, 141, **1922**.
- [36] Herbig, G. H. *Astrophys. J.* 542, 334, **2000**.

Chapter 2

Cavity Ring-down Spectroscopy

2.1. Introduction

The measurement of electronic spectra of supersonically cooled molecules and clusters using techniques like laser induced fluorescence (LIF) or resonant enhanced multi photon ionization (REMPI) is a widely incorporated approach for addressing many problems in chemistry. However, these methods often fail for systems affected by rapid internal conversion, predissociation, or other dynamical processes, in these cases they cannot be used for reliable intensity measurements. It would be convenient to measure the spectra in direct absorption, as the method determines absolute band intensities and accesses states that are invisible to LIF or REMPI [1]. However, direct absorption methods are generally orders of magnitude less sensitive than these “action” techniques and are, therefore, difficult to apply to transient species, such as clusters or radicals.

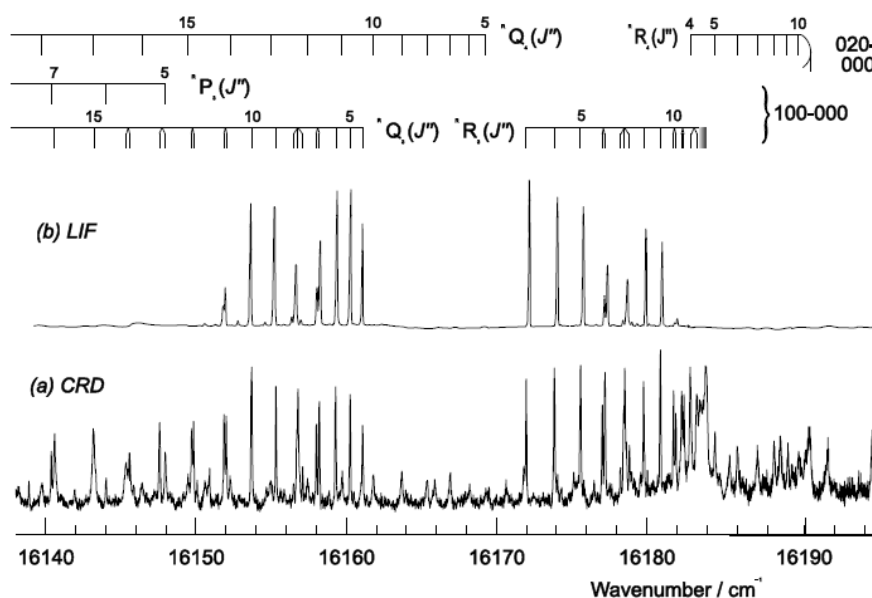


Figure 2.1: The (a) Cavity Ring Down and (b) Laser Induced Fluorescence spectra of HNO in the region of the $A^1A'' - X^1A'$ 100-000 4-3 and 020-000 5-4 sub-bands [2].

Cavity Ring-down Spectroscopy (CRDS) is a linear, direct absorption technique that scores over traditional absorption techniques in terms of ease of implementation

and high sensitivity, sufficient for transient detection of radical species in molecular beams. In particular, CRDS is largely immune to shot-to-shot variations in the laser intensity, and benefits from tremendously long effective pathlengths through a sample simply by the use of a cavity consisting of two high finesse mirrors ($R > 99.99\%$). The advantages of pulsed-CRDS are that one can reach any wavelength from the IR (4-5 μm with OPO lasers) to the UV (≈ 200 nm by harmonic generation with pulsed dye lasers) and the simple experimental set-up. Besides, the high resolution of the tunable lasers used for CRDS makes it a versatile tool for studies of molecular spectroscopy and dynamics. A good example of the advantage of CRDS over LIF has been demonstrated in the case of HNO [2]. Much of the structure seen in the CRD spectrum is absent in the LIF spectrum because of predissociation of the excited state (Figure 2.1).

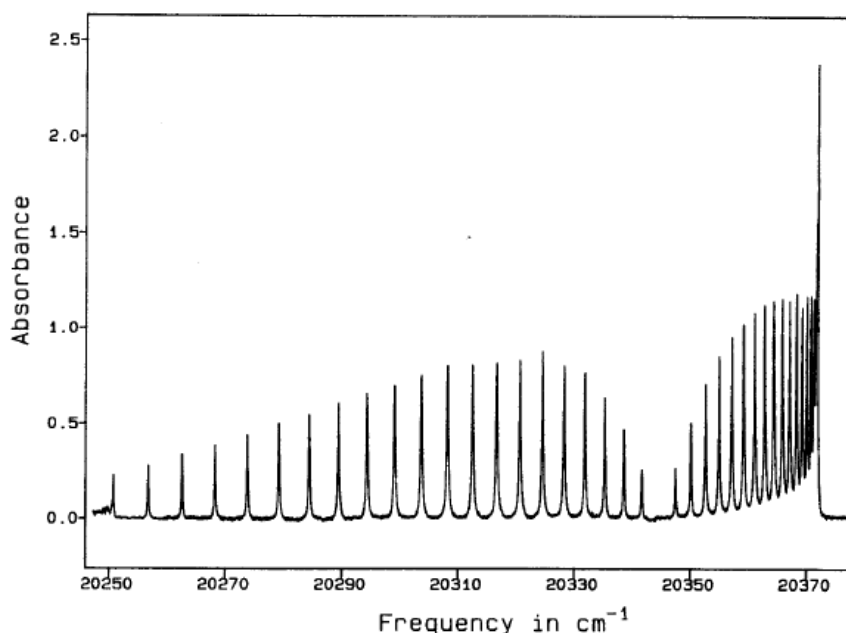


Figure 2.2: Cavity Ring Down absorption spectrum of the $106 \leftarrow 000$ transition of HCN at 100 Torr. By recording this spectrum at different pressures, it was shown that there is a large collisional line mixing effect in the proximity of the R heads. Figure reproduced from [9].

The first demonstration of the use of CRDS with pulsed lasers for sensitive absorption measurements was made by O'Keefe and Deacon [3] dating back to 1988. They detected the overtone transitions of O_2 in air, with a fractional absorbance per pass of *ca.* 1 ppm, whilst follow up work demonstrated 1 ppb detection for NO_2 [4]. Since then, trace gas detection by CRD absorption spectroscopy has been demonstrated for radicals like OH [5], CH_3 [6] in flames and discharges, and for trace amounts of

atomic mercury vapor and ammonia [7] in ambient air. CRDS was also applied for investigation of jet-cooled metal clusters in a molecular beam [8].

Applications of the technique were extended to detailed spectroscopic studies of line intensities, transition wavelengths, and coupling effects in vibrational and rotational spectra of gas phase species by Lehmann and Romanini. They used CRDS for measurement of absolute oscillator strengths of forbidden transitions of HCN [9, 10] in static gas cells and extended the range of observed overtones in the molecule to six, seven and eight stretching quanta for various isotopomers (Figure 2.2). Kinematic studies of aromatic radical reactions rate have been performed by Lin and coworkers [11]. Reactions of NH_2 with NO were studied by photolysing NH_3 in the presence of NO and monitoring the loss of absorption by NH_2 at 537.6 nm [12].

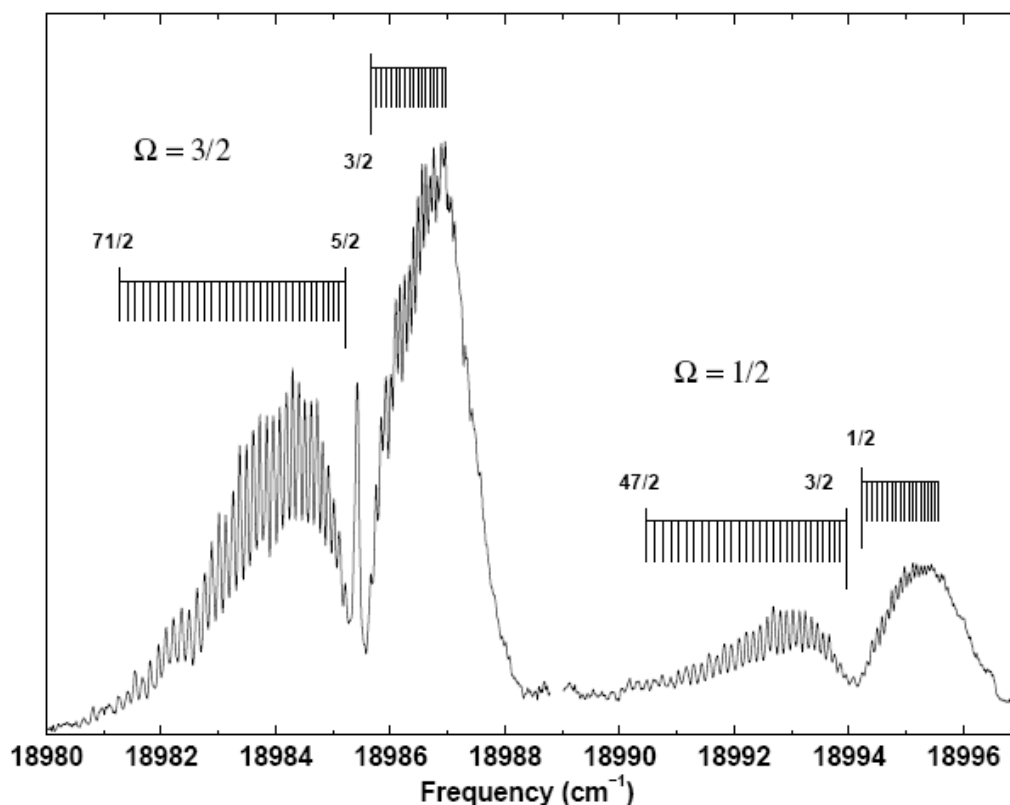


Figure 2.3: The rotationally resolved origin band of the $A^2\Pi \leftarrow X^2\Pi$ transition of C_6H [13].

The exceptional sensitivity of CRDS makes it suitable for applications to electronic spectroscopy of gas phase molecules in hostile environments. A combination of CRDS with cathode discharges has enabled detection of the species C_{2n}H ($n=3, 4, 5$) [13, 14]. Figure 2.3 shows the rotationally resolved electronic spectrum of the origin

band of the $A^2\Pi \leftarrow X^2\Pi$ transition in C_6H [13] recorded by CRDS in a slit nozzle plasma discharge. The even/odd numbered polyacetylene cations have $^2\Pi$ ground states arising from π^3/π^1 configuration. In even numbered chains, electronic spectra show signatures of vibronic coupling between the low-lying $^2\Pi$ and $^2\Sigma^+$ states. The $^2\Pi$ state progressively redshifts as the chain length increases. These species are particularly important due to their astrophysical significance [15]. The $A^2\Pi \leftarrow X^2\Pi$ electronic systems of HC_nH^+ ($n=4, 6, 8$) have been rotationally resolved using pulsed-CRDS [16, 17, 18]. CRDS has also been applied to study of rapid predissociation of small radicals and reactive molecules [19].

2.2. Basic Considerations

Light from a pulsed laser is stored typically in the order of microseconds in a high-finesse optical cavity formed by two dielectric plano-concave mirrors ($R = 0.9999$) during which it makes thousands of round trips. In the absence of any absorbing species in the volume between the mirrors, the primary losses of the cavity are from the transmittance of the mirrors and diffraction losses. An injected laser pulse is reflected back and forth within the cavity with intensity decreasing exponentially in time with a rate determined by the reflectivity of the mirrors and the length of the cavity (Figure 2.4). The reflectivity of the mirrors can be determined by measuring the time constant for the intensity decay of light stored inside the cavity. This is termed as the ring-down time τ , which equals the time taken for the light pulse to reach to e^{-1} the intensity of the initial pulse. With an absorbing species introduced into the cavity, the losses of the cavity increase as a result of which the exponential decay occurs over a shorter time frame than that observed without the species.

In the case of an empty cavity with two mirrors of the same reflectivity R , the intensity within the cavity decreases exponentially (Figure 2.4) as

$$I(t) = I_0 \exp \left[- \left(\frac{\text{number of reflections}}{\text{round trip}} \right) \left(\frac{\text{loss}}{\text{reflection}} \right) (\text{number of round trips}) \right] , \quad (2.1)$$

where I_0 is the intensity of the initial pulse and $I(t)$ is the intensity after time t . If the mirrors are separated by a length L , the number of round trips in time t will be $tc/2L$, c being the speed of light. Taking the loss per reflection as $1-R$, the above equation can be expressed as

$$I(t) = I_0 \exp \left[-(1-R) \left(\frac{tc}{L} \right) \right]. \quad (2.2)$$

By the definition of the ring down time then, τ_0 is given by the relation

$$\tau_0 = \frac{t_r}{2(1-R)}, \quad (2.3)$$

where t_r is the transit time for a round trip, typically in the order of 0.7-7 ns.

For a round trip in the cavity now containing species that absorb at the frequency ω of the injected laser pulse, the loss due to absorption is given by

$$\text{Absorption loss} = \left(\frac{\text{loss}}{\text{round trip}} \right) (\text{number of round trips}) = (2\alpha L) \frac{tc}{2L}, \quad (2.4)$$

where $\alpha = \sigma N$ is the absorption coefficient (cm^{-1}). The total loss in the cavity now becomes $[(1-R) + (\alpha L)] \frac{tc}{L}$, from which it follows that

$$I(t) = I_0 \exp \left\{ -[(1-R) + \alpha L] \frac{tc}{L} \right\}, \quad (2.5)$$

giving the ring-down time τ as

$$\tau = \frac{t_r}{2[(1-R) + \alpha L]}. \quad (2.6)$$

On combining (2.3) and (2.6), one gets

$$\alpha = \frac{1}{c} \left(\frac{1}{\tau} - \frac{1}{\tau_0} \right). \quad (2.7)$$

This equation shows that the absorption coefficient for a given frequency can be obtained just by knowing the two ring-down times of the cavity.

To extract spectra from exponential decays recorded at each laser wavelength ensuring the lowest possible detector and shot noise, an AD converter (12/16 bit resolution) or a digital oscilloscope is used to digitize the detector decay signal, after which one can do a weighted least squares fit to the resulting signal. The analog signal entering the AD converter is low pass filtered to produce minimum distortion of the early part of the ring down signal. The data is iteratively fit to a functional form $Ae^{-kt} + B$. When the DC level of the detector is not sufficiently stable, the fit includes an adjustable baseline. Alternately, two gated integrators with the same window size and different delays t_a and $t_a + \Delta t$ from the beginning of the ring down signal can be used. By taking the logarithm of the ratio of these two integral values, one obtains $\Delta t/\tau$ directly.

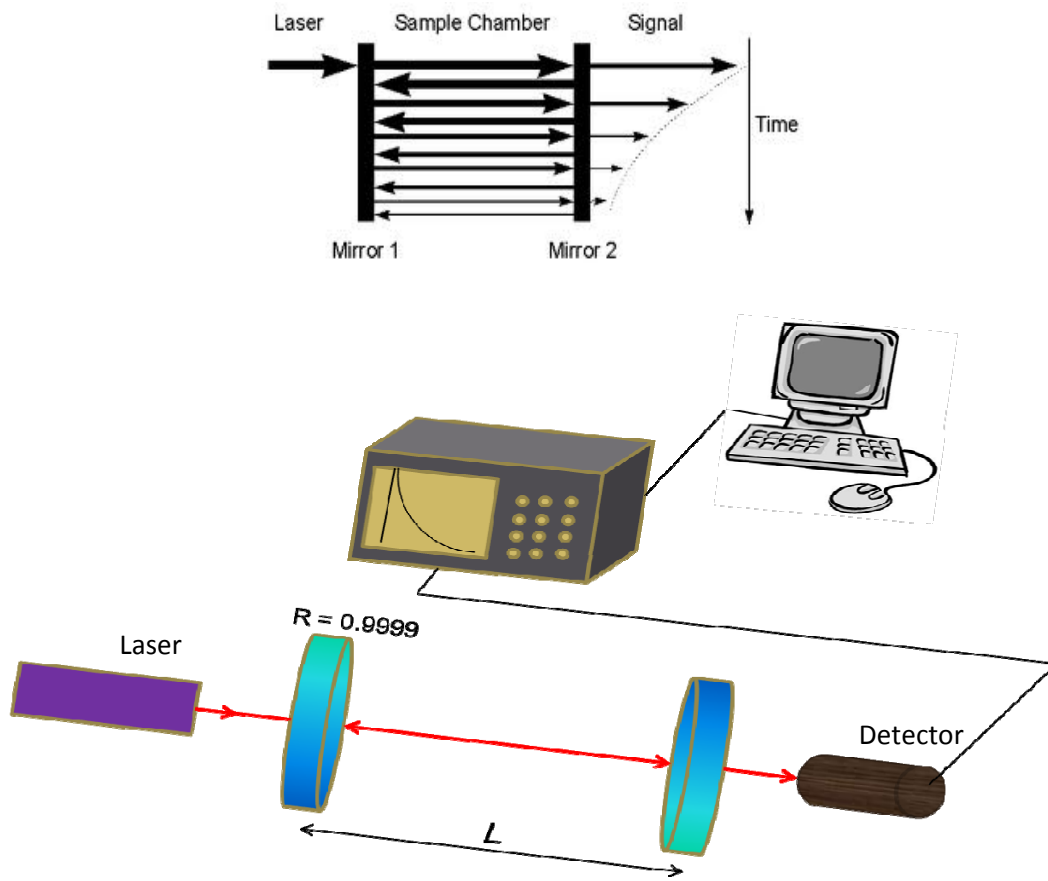


Figure 2.4: Basic principle and setup of cavity ring down experiment. The sample is contained in the ring down cavity formed by mirrors of reflectivity R separated by distance L .

In a cavity with two mirrors of reflectivity R , the number of round trips N within the time taken for the intensity to fall to e^{-1} of its initial value is given by $N = -1/[2\ln(R)]$. For example, a mirror reflectivity of 0.99999 results in 50000 round trips, giving a pathlength of 100 km in a 1 m cavity. The stability condition is always satisfied in terms of the radii of curvature of the mirrors, R and the length of the cavity, L . This is given as

$$0 < \left(1 - \frac{L}{R}\right)^2 < 1. \quad (2.8)$$

The fact that the technique is immune to shot-to-shot laser fluctuations and long pathlengths are achieved inside the cavity increases the sensitivity of CRDS manifold over other absorption spectroscopy. Sensitivity in CRDS measurements is expressed in terms of the minimum detectable fractional absorption per pass through the cavity, which is given as

$$\delta I = \frac{I_0 - I}{I_0} \approx \alpha L = \sigma N L . \quad (2.9)$$

This is characteristic for very small absorbance in a single pass so that $\alpha L \ll 1$.

Taking the change in the ring down time upon tuning to an absorption feature as $\Delta\tau = \tau_0 - \tau$, and combining (2.3) and (2.7), the minimum detectable absorbance per pass can be written as

$$\delta I_{\min} \approx (1 - R) \frac{\Delta\tau_{\min}}{\tau} . \quad (2.10)$$

As an illustration, suppose a 1 m cavity is bounded by mirrors of reflectivity $R = 0.99999$, so that τ_0 equals 30 μs . If the minimum detectable change in the ring down time is 6.7 ns, then the minimum fractional absorption per pass is $\delta I_{\min} = 2 \times 10^{-8}$ or 20ppb, giving a minimum absorption coefficient of $\alpha_{\min} = 2 \times 10^{-10} \text{ cm}^{-1}$.

2.3. Mode Formation and CRDS

In a Fabry-Perot cavity, the longitudinal modes determine the frequencies of radiation that satisfy the wavelength requirements. In general, the allowed oscillation frequencies for these modes are given by

$$\nu_p = \frac{c}{2L} \left(p - \frac{\alpha}{2\pi} \right) , \quad (2.11)$$

where ν_p is the frequency of the radiation, p is the longitudinal mode index and α is the corrective term to account for the non-planar wavefront. This gives the spacing between two adjacent longitudinal modes as

$$\Delta\nu = \frac{c}{2L} = \frac{1}{\tau_r} . \quad (2.12)$$

In addition to longitudinal or axial modes, various types of transverse electromagnetic modes, which determine the cross-sectional profile of the beam, can develop in cavities. The lowest order transverse mode, TEM₀₀, has a Gaussian cross-sectional profile, while higher order modes are broken up into an array of sub-beams. For a given transverse mode, there are an infinite number of longitudinal modes associated with it, separated by $\Delta\nu$. The phase delay for a round trip through the cavity differs slightly for different transverse modes. The frequency spacing between two successive transverse modes is usually much smaller than the spacing between two successive longitudinal modes, and depends on the characteristics of the cavity.

For a 52 cm cavity which has been used in the present experiments, the longitudinal mode spacing for the TEM₀₀ transverse mode is 288 MHz (0.009 cm⁻¹), as shown in Figure 2.5. Excitation of a single, Lorentzian cavity mode results in exponential decay of light intensity in the cavity. If the laser pulse does not match the TEM₀₀ mode of the cavity or is not injected perfectly axially into the cavity, transverse modes are established with frequencies lying between those of the longitudinal cavity modes.

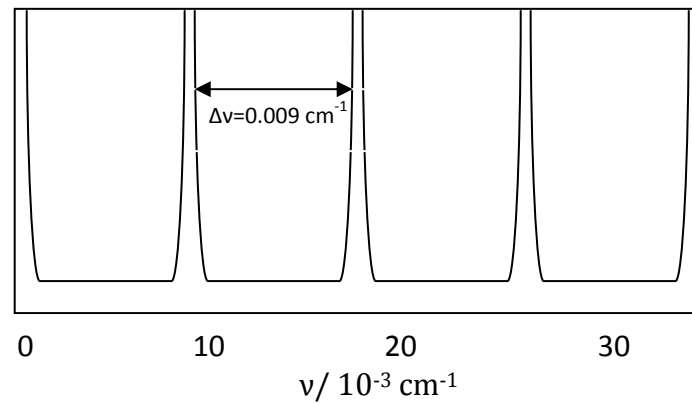


Figure 2.5: Longitudinal mode structure of a 52 cm long cavity.

A non-exponential decay of intensity is observed if the Beer-Lambert behavior for a single pass of light through the cavity is violated. The Beer-Lambert behavior requires that the widths of the absorption spectral lines be greater than the laser linewidth within the cavity. This is common to all kinds of absorption spectroscopy, however, in CRDS, if the loss from absorption by species in the cavity is much less than the total cavity loss, an approximately exponential decay results and an effective absorption coefficient can be measured even if the laser linewidth exceeds the absorption linewidth. A modulation in the exponential decay also results from beating of different frequency components in case of multiple longitudinal mode excitations. However, this beat pattern is usually washed out after multiple averaging of the decay waveform. Also, with pronounced interference effects between the longitudinal and transverse modes in the cavity, a non-exponential decay is observed and spectral intensities and absorption coefficients obtained by single exponential analysis becomes inaccurate.

The effects of mode formation on CRDS [20], or the conditions for which (2.6) holds are established in terms of the relationship between the pulse duration t_p , the round-trip transit time t_r , and the relaxation time of the absorbing species T_2 . For both

cases discussed below, the linewidth of the absorbing species must be greater than the longitudinal mode spacing to avoid missing spectral features [21].

Case 1: $T_2 \ll t_p$

In this case, the absorbing species interacts with a quasi-continuous light wave. The amplitude of the pulse envelope is invariant during the relaxation time T_2 . Under the condition that $t_p < t_r$, longitudinal mode formation cannot occur. However, if the pulse duration is greater than than the round-trip transit time, cavity modes develop due to interference between pulse fragments propagating in the same direction as a result of which absorption occurs when the transition coincides with one or more of these modes.

Case 2: $T_2 \gg t_p$

For $T_2 \gg t_p$, the species inside the cavity absorb a series of light pulses during their lifetime. The molecules in the cavity do not absorb light except at the longitudinal mode frequencies. Thus absorption is enhanced for the resonant transitions while it is suppressed for the non-resonant ones.

When a large number of transverse modes are excited in the cavity, the longitudinal mode frequencies overlap, and a quasi-continuum of longitudinal modes results [5]. This guarantees the presence of cavity modes under the linewidth of any spectral transition. In this way, it is possible to couple even a narrowband laser into the cavity.

The above conditions can be demonstrated using a cavity transmission function assuming a single transverse cavity mode. The intensity of the signal $S(t + nt_r)$ emerging from the cavity can be expressed as

$$S(t + nt_r) = I_0(\omega)T(\omega)e^{-n\mathcal{L}}, \quad (2.13)$$

where $I_0(\omega)$ is the intensity of the single-mode pulse of frequency ω before it enters the cavity, $T(\omega)$ is the cavity transmission at ω , and the exponential factor describes the decay with the round-trip loss coefficient for the cavity with sample as $\mathcal{L} = 2[(1 - R) + \alpha L]$. The function $T(\omega)$ depends on the relation between the pulse length t_p and the cavity round trip length t_r . Figure 2.6 shows three separate cases for a

transverse mode in a cavity with the pulse length shorter and longer than the cavity round trip length, and also for pulse length longer than the ring down time τ .

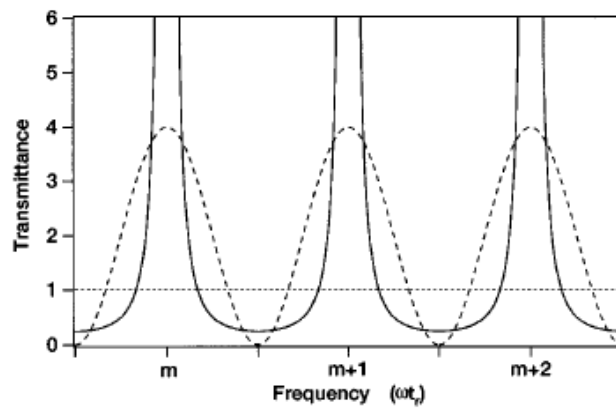


Figure 2.6: Transmittance of an optical cavity as a function of pulse frequency for different pulse lengths [20]. The dotted line represents the case $l_p < l_r$, the dashed $l_p = 2l_r$, and the solid line $l_p \gg \tau$.

For a pulse shorter than l_r , the cavity transmission is not frequency selective and depends only on the mirror transmittivity T . In this case the transmission function is given as

$$T(\omega) = T^2 \quad (2.14)$$

For a pulse length equal to twice l_r , the cavity transmission function increases at frequencies resonant with the cavity mode frequencies and decreases for off-resonant frequencies. The transmission function will be a cosine squared function given as

$$T(\omega) = 4T^2 \cos^2(\omega t_r / 2) \quad (2.15)$$

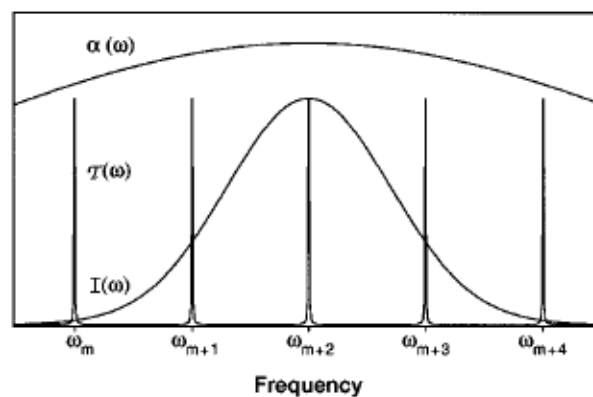


Figure 2.7: Experimental condition for single exponential decay of ring down transient. The absorption line is broad compared to the cavity longitudinal mode spacing, and the pulse length is much longer than the cavity round-trip length. The line-center frequency of the pulse is tuned to the center of the absorption line and excites a single cavity mode.

For pulses longer than τ , the on-resonance transmittance approaches 100% in the absence of absorption losses while the off-resonance transmittance is proportional to $T^2/4$. An example of an experimental situation where the necessary conditions for the exponential decay model are satisfied is shown in Figure 2.7.

The mode structure of a cavity, its consequences for CRDS, and the influence of laser bandwidth have been discussed in detail in articles by Zalicki and Zare [20], Lehmann and Romanini [21], Hodges et al. [22, 23], Scherer et al [24] and the development of the technique and its applications in various book compilations like Busch and Busch [25] and Berden and Engeln [26].

2.4. Factors affecting CRDS

In CRDS, the best sensitivity is obtained when a single longitudinal mode of the cavity is excited. This is difficult to achieve with pulsed lasers since they have a relatively large bandwidth. In the UV-VIS spectral region, the longitudinal mode spacing of the cavities is much narrower than even most Doppler broadened lines, however, as one moves to the IR and Doppler widths narrow, substantial distortion occurs in the sampling of the lineshape. The pulsed technique also suffers from inefficient mode matching of the laser beam to the TEM₀₀ cavity mode. An experimental procedure to optimize mode matching was realized by Lee et al. [27] by monitoring the non-degenerate transverse mode beating brought about by splitting the eigenmode frequencies from the induced asymmetry of the cavity.

A sample with wavelength dependent loss also has dispersion which leads to shifts in the resonance frequency of the cavity modes [25]. A detailed treatment of its effect on CRDS is given in Appendix A. The dielectric mirrors themselves introduce some cavity dispersion, which changes the cavity mode spacing. These shifts must be considered if one wants to effectively couple a laser source with a spectral frequency comb with a CRDS cavity. Also, the broad bandwidth Amplified Spontaneous Emission (ASE) associated with pulsed lasers contributes to the ring down decay transient. Without corrections like narrow band interference filters to suppress the ASE, the accuracies of the absolute spectral intensities will suffer.

Another important effect is that any feedback of light leaving the cavity that is back reflected into the cavity mode will interfere with light inside the cavity. A ring optical cavity has an advantage in this regard as any back reflection is couple into the oppositely propagating mode. Also, the high-reflectivity mirrors used in CRDS are too delicate, they may get dirty, and in general the cavity quality may be spoiled. These mirrors are commercially available over short wavelength ranges too and have residual birefringence of a few μrad per reflection.

2.5. Cavity Ring-down variants

There are various elaborations to the standard pulsed CRD experiment (Figure 2.8). Single longitudinal mode excitations are easily achieved using continuous wave lasers which have bandwidth typically below 10 MHz. CRDS performed with CW lasers is entitled CW-CRDS. However, this technique is not a CW technique at all. Compared to pulsed CRDS, CW-CRDS offers better sensitivity and spectral resolution [26]. Also the method allows the use of compact, robust and inexpensive diode lasers. In cavity enhanced absorption spectroscopy (CEAS), one measures the time averaged transmission of the cavity without modulating the light intensity. The measured time-integrated intensity is proportional to the ring down time of the cavity, and thus, inversely proportional to the absorption coefficient. A comparison of the Phase Shift CRDS (PS-CRDS) technique relative to the CRD technique using tunable pulsed light sources has been demonstrated by absorption measurements on the $X^1\Sigma_g^+(v' = 2) \leftarrow X^3\Sigma_g^-(v' = 0)$ band of $^{18}\text{O}_2$ [28].

CRDS has also been coupled with broadband radiation sources, an example of which is the Fourier Transform CRDS approach (FT-CRDS) [29]. In this method, the broadband output of the cavity is passed through an interferometer capable of making time-resolved measurements on the time scale of a ring down transient. A phase-shift version of the technique has also been developed [30]. Another approach to broadband ring down measurements is to disperse the broadband light through a spectrograph as it leaves the cavity and image the resulting pattern using a gated CCD camera [31]. More recent development in this area has been the use of supercontinuum generated by photonic crystal fibers when pumped by a high repetition rate Nd:YAG laser [26].

Combination of CRDS with magnetic polarization spectroscopy (PD-CRDS) makes use of polarization dependent absorption leading to magnetic dichroism which can be measured experimentally [25]. Vaccaro and coworkers developed a technique known as cavity ring down polarimetry (CRDP) which overcomes the limitations posed by PD-CRDS [32] in terms of optical rotation due to molecular chirality.

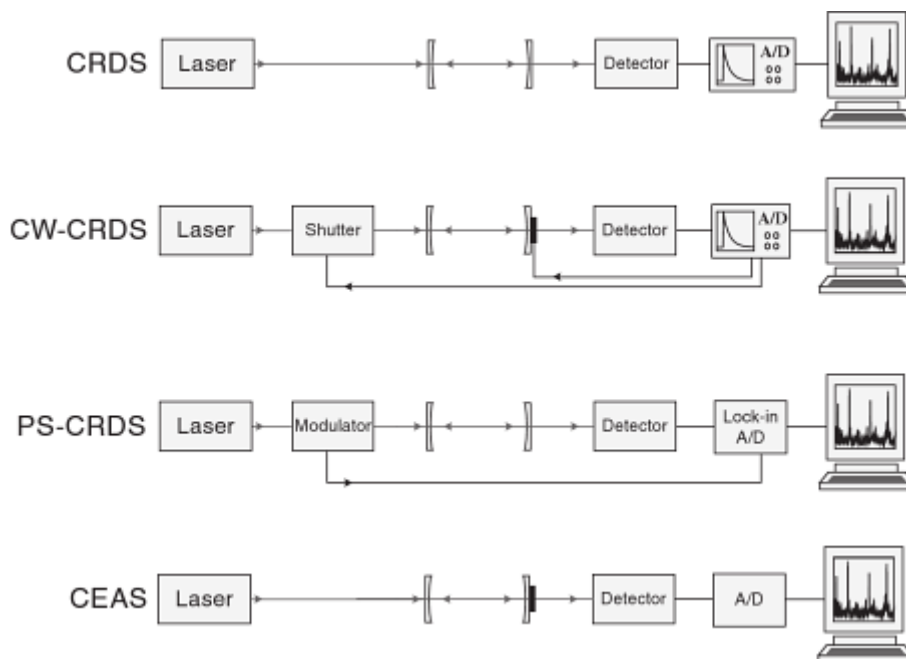


Figure 2.8: Sketches of some commonly used cavity ring-down spectroscopy schemes.

Another approach to CEAS is to combine the high sensitivity of low loss cavities to additional loss with frequency modulation spectroscopy. This is realized using Noise Immune Cavity enhanced Optical Heterodyne Molecular spectroscopy (NICE-OHMS). Here, one locks a narrow frequency laser to one of the cavity resonances and frequency modulates the laser beam at exactly the splitting frequency of the cavity FSR [25].

A ring down cavity based on total internal reflection [33] has the advantage that it is effective over a broad range of wavelengths and is suited for making measurements on both gas phase and condensed phase samples. Such a cavity consists of an optical cube with a single convex face, which refocuses the internally circulating light to form a stable resonator. Fiber-optic CRDS based on linear fiber cavities act the same way as standard CRDS except that instead of placing the sample inside the cavity, the species of interest absorbs the evanescent wave present near the surface of the fiber core. One of the most recent and promising developments is fiber loop ring down spectroscopy [34],

based on circulation of light within a closed loop of optical fiber. Light from a pulsed dye laser is coupled into the loop through side illumination of a bent section of fiber, and further around the loop, a small amount of light is coupled out through another bend to a photomultiplier (Figure 2.9).

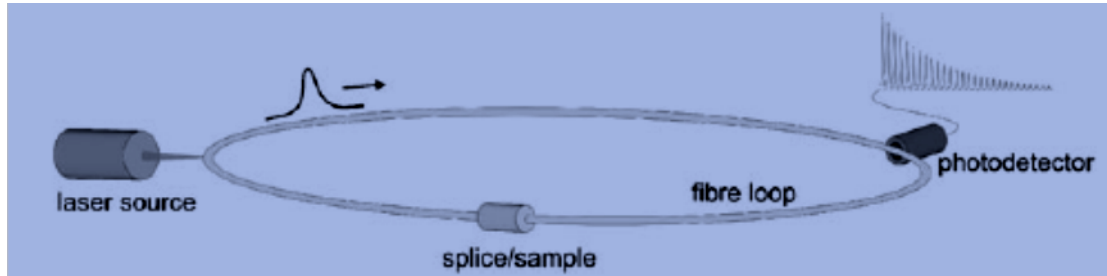


Figure 2.9: Fiber loop ring down spectroscopy.

CRDS is a linear, direct absorption technique providing the absorption coefficient on an absolute scale. There is no intrinsic limitation to the spectral region in which CRDS can be applied [35, 36] as long as high reflectivity mirrors, fast detectors and tunable lasers are available. A sensitivity of 10^{-6} cm^{-1} can be easily obtained using a simple experimental set-up while sensitivities as high as 10^{-14} cm^{-1} have been reported using techniques like NICE-OHMS [37].

Bibliography

- [1] Spaanjaars, J. J. L.; ter Meulen, J. J.; Meijer, G. *J. Chem. Phys.* 107, 2242, **1997**.
- [2] Pearson, J.; Orr-Ewing, A. J.; Ashfold, M. N. R.; Dixon, R. N. *J. Chem. Phys.* 106, 5850, **1997**.
- [3] O'Keefe, A.; Deacon, D. A. G. *Rev. Sci. Instrum.* 59, 2544, **1988**.
- [4] O'Keefe, A.; Lee, O. *Am. Lab.* 21, 19, **1989**.
- [5] Meijer, G.; Boogaarts, M. G. H.; Jongma, R. T.; Parker, D. H.; Wodtke, A. M. *Chem. Phys. Lett.* 217, 112, **1994**.
- [6] Zalicki, P.; Ma, Y.; Zare, R. N.; Wahl, E. H.; Dadamio, J. R.; Owano, T. G.; Kruger, C. H. *Chem. Phys. Lett.* 234, 269, **1995**.
- [7] Jongma, R. T.; Boogaarts, M. G. H.; Holleman, I.; Meijer, G. *Rev. Sci. Instrum.* 66, 2821, **1995**.
- [8] O'Keefe, A.; Scherer, J. J.; Cooksy, A. L.; Sheeks, R.; Heath, J.; Saykally R. J. *Chem. Phys. Lett.* 172, 214, **1990**.
- [9] Romanini, D.; Lehmann, K. K. *J. Chem. Phys.* 99, 6287, **1993**.
- [10] Romanini, D.; Lehmann, K. K. *J. Chem. Phys.* 102, 633, **1995**.
- [11] Yu, T.; Lin, M. C. *J. Am. Chem. Soc.* 115, 4371, **1993**.
- [12] Diau, E. W.; Yu, T.; Wagner, M. A. G.; Lin, M. C. *J. Phys. Chem.* 98, 4034, **1994**.
- [13] Linnartz, H.; Motylewski, T.; Vaizert, O.; Maier, J. P.; Apponi, A. J.; McCarthy, M. C.; Gottlieb, C. A.; Thaddeus, P. *J. Mol. Spectrosc.* 197, 1, **1999**.
- [14] Linnartz, H.; Motylewski, T.; Maier, J. P. *J. Chem. Phys.* 109, 3819, **1998**.
- [15] Guelin, M.; Cernicharo, J.; Travers, M. J.; McCarthy, M. C.; Gottlieb, C. A.; Thaddeus, P.; Ohishi, M.; Saito, S.; Yamamoto, S. *Astron. Astrophys.* 317, L1, **1997**.
- [16] Raghunandan, R.; Mazzotti, F. J.; Chauhan, R.; Tulej, M.; Maier, J. P. *J. Phys. Chem. A.* 113, 13402, **2009**.
- [17] Pfluger, D.; Sinclair, W. E.; Linnartz, H.; Maier, J. P. *Chem. Phys. Lett.* 313, 171, **1999**.
- [18] Pfluger, D.; Motylewski, T.; Linnartz, H.; Sinclair, W. E.; Maier, J. P. *Chem. Phys. Lett.* 329, 29, **2000**.
- [19] Wheeler, M. D.; Orr-Ewing, A. J.; Ashfold, M. N. R. *J. Chem. Phys.* 107, 7591, **1997**.
- [20] Zalicki, P.; Zare, R. N. *J. Chem. Phys.* 102, 2708, **1995**.
- [21] Lehmann, K. K.; Romanini, D. *J. Chem. Phys.* 105, 10263, **1996**.

- [22] Hodges, J. T.; Looney, J. P.; van Zee, R. D. *Appl. Opt.* 35, 4112, **1996**.
- [23] Hodges, J. T.; Looney, J. P.; van Zee, R. D. *J. Chem. Phys.* 105, 10278, **1996**.
- [24] Scherer, J. J.; Paul, J. B.; O'Keefe, A.; Saykally, R. J. *Chem. Rev.* 97, 25, **1997**.
- [25] Busch, K. W.; Busch, M. A. *Cavity-Ringdown Spectroscopy An Ultratrace-Absorption Measurement Technique: ACS Symposium Series 720: American Chemical Society: Washington DC: 1999*.
- [26] Berden, G.; Engeln, R. *Cavity-Ringdown Spectroscopy Techniques and Applications: Blackwell Publishing Ltd.: United Kingdom: 2009*.
- [27] Lee, D. H.; Yoon, Y.; Kim, B.; Lee, J. Y.; Yoo, Y. S.; Hahn, J. W. *Appl. Phys. B.* 74, 435, **2002**.
- [28] Engeln, R.; von Helden, G.; Berden, G.; Meijer, G. *Chem. Phys. Lett.* 262, 105, **1996**.
- [29] Engeln, R.; Meijer, G. *Rev. Sci. Instrum.* 67, 2708, **1996**.
- [30] Hamers, E.; Schram, D.; Engeln, R. *Chem. Phys. Lett.* 365, 237, **2002**.
- [31] Czyżewski, A.; Chudzyński, S.; Ernst, K.; Karasiz'nski, G.; Kilianek, L.; Pietruczuk, A.; Skubiszak, W.; Stacewicz, T.; Stelmaszczyk, K.; Koch, B.; Rairoux, P. *Opt. Commun.* 191, 271, **2001**.
- [32] Vallance, C. *New J. Chem.* 29, 867, **2005**.
- [33] Pipino, A. C. R. *Appl. Opt.* 39, 1449, **2000**.
- [34] Jakubinek, M.; Tong, Z.; Manzhos, S.; Looock, H.-P. *Can. J. Chem.* 82, 873, **2004**.
- [35] Sneepe, M.; Hannemann, S.; van Duijn, E. J.; Ubachs, W. *Opt. Lett.* 29, 1378, **2004**.
- [36] Gopalsami, N.; Raptis, A. C.; Meier, J. *Rev. Sci. Instrum.* 73, 259, **2002**.
- [37] Ye, J.; Ma, L. S.; Hall, J. L. *J. Opt. Soc. Am. B.* 15, 6, **1998**.

Chapter 3

Four-Wave Mixing Spectroscopy

3.1. Introduction

As the name suggests, four-wave mixing (FWM) refers to the interaction of four waves via the third order nonlinear polarization. It involves detecting a signal beam that is diffracted off an optically induced grating, hence is classified under laser induced grating (LIG) spectroscopy. The basics of the FWM theory can be explained by the transient LIG analogy. Two coherent beams (pumps) of the same frequency, overlapping in space and time, create a population grating in the medium when tuned to a molecular transition, causing macroscopic variations of the index of refraction. A third beam (probe) is then diffracted by the induced grating when it comes into resonance with the pump transition and creates a fourth beam (signal) that is detected. The geometrical arrangement of the incident beams requires that the phase-matching condition be satisfied. When the pump and probe beams have the same wavelength, the technique is called degenerate four-wave mixing (DFWM); otherwise, two-color four-wave mixing (TCFWM). The latter is a double-resonance method and can be used to disentangle overlapping or congested spectra.

DFWM was traditionally employed for investigation of optical phase conjugation processes [1] and ultrafast relaxation phenomena [2], but later was successfully applied to spectroscopy because of the signal enhancement occurring at atomic and molecular resonant energies. The FWM interaction involves a high degree of resonance enhancement permitting background free detection of molecular transitions with high sensitivity. At high pressures where collision effects are important, FWM techniques offer advantages over other spectroscopic methods, making it suitable for applications in probing atmospheric pressure flames and plasmas.

In the study by Ewart et al. [3], the phase-conjugate signal obtained from Na atoms in a heat pipe was found to increase with buffer-gas pressure. This observation, which suggested high sensitivity for trace species in atmospheric pressure flames,

triggered the use of DFWM as a means of monitoring radicals like OH [4] in combustion environments. Using a frequency-doubled pulsed dye laser the DFWM spectrum of the strongest R₁ and R₂ lines of the OH $A^2\Sigma^+ \leftarrow X^2\Pi (0,0)$ band was recorded. This was followed by subsequent research in FWM spectroscopy. DFWM has been carried out on a variety of stable diatomics like NO [5], CO [6], H₂ [7] and O₂ [6], and transients like NH [8], C₂ [9], CH [9] etc.

The use of DFWM spectroscopy as a temperature probe was first demonstrated by Dreier and Rakestraw [8] who also probed the OH $A^2\Sigma^+ \leftarrow X^2\Pi (0,0)$ transition. They found that the integrated DFWM signals were dependent on the square of the rotational line-strengths. Based on their observations, it was concluded that in the DFWM experiment the stimulated pumping rate determines the lifetime of the electronically excited OH rather than collisional quenching. This observation implied that collisional quenching had little effect on the relative signal levels, and excited interest in the use of DFWM as combustion diagnostic.

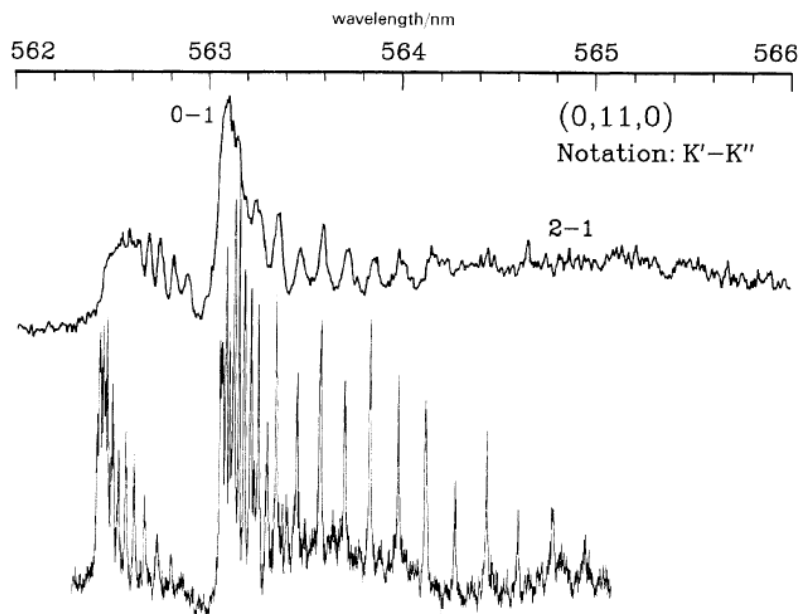


Figure 3:1: Comparison of the HCO spectrum recorded by DFWM and PHOFEX studies [10]. Note the enhanced resolution in the Degenerate Four Wave Mixing spectrum.

Resonant DFWM measurements built on VIS/UV excitation of electronic transitions have also been conducted on polyatomic molecules like HCO [10], NO₂ [11], NH₃ [12] etc., non-fluorescing species [13] and weakly bound complexes [14]. In the case of HCO, the DFWM spectrum (Figure 3.1) showed rotational structure at the P and

R bandheads, which had not been seen before in corresponding LIF [15] and photofragment excitation (PHOFEX) [16] spectra. NO₂ was used to demonstrate the coherent imaging application of DFWM in flames [17].

The two-color variants provide a useful method for detecting optical transitions from rovibronically excited molecules, even for intermediate predissociative states. TCFWM was first demonstrated on the 32-0 P(51) and 34-0 P(102) rovibrational transitions in the $B^3\Pi_{0u}^+ \leftarrow X^1\Sigma_g^+$ absorption band of I₂ [18]. The technique can be implemented both in the stimulated emission pumping (SEP, resonant upper energy state) or upward pumping (UP, common lower energy state) schemes, enabling one to obtain information on both the electronic states where the pump frequency is parked (Figure 3.2). For example, in an UP transition the signal arises because the optical pumping also creates a ‘depletion’ grating in the rovibrational levels of the ground state, which diffracts the probe beam whenever its frequency is resonant with a transition out of one of these levels.

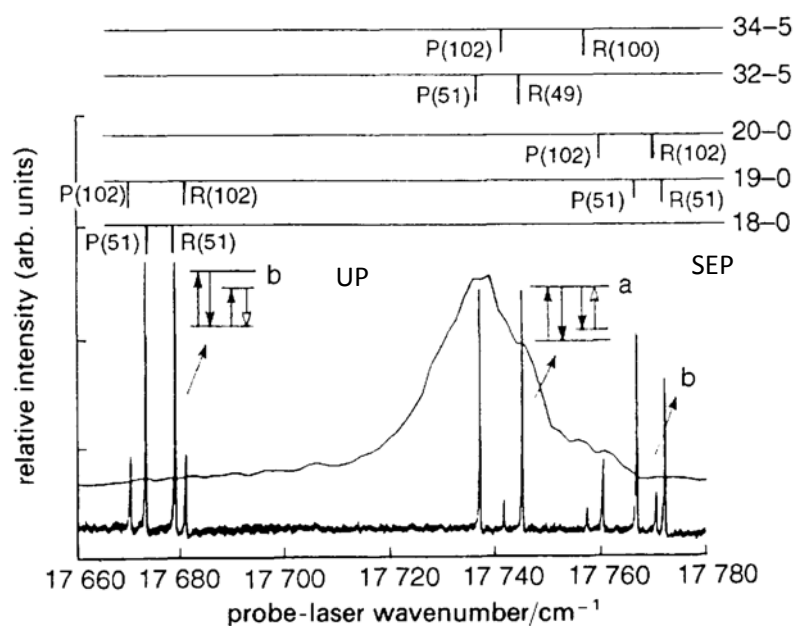


Figure 3.2: Two Color Four Wave Mixing spectrum of I₂. Both (a) SEP and (b) UP variants are shown. Overlaid is the dispersion emission spectrum observed following laser excitation of the pump [18].

The photodissociation studies on NO₂ by Butenhoff and Rohlring [19] using TCFWM demonstrated the application of the technique to non-fluorescing species. Although the excited-state grating vanishes on a very short timescale as a result of

photodissociation, the signal originates from the long-lived ground-state depletion grating. In a subsequent work [20], the temporal behavior of the signal as a function of the time delay between the pump and probe laser pulse was examined.

LIG spectroscopy has been used to measure weak overtone and combination bands of methane within the pressure range of 0.2 to 4 bar at an ambient temperature [21]. The study showed that the LIG technique can measure rotationally resolved spectra for transitions with cross sections as low as 10^{-26} cm²/molecule. DFWM analyses have identified different polarization schemes that lead to signal generation only in the presence of rotational anisotropy, thereby enabling selective determination of molecular orientation and alignment [22].

For applications like interrogation of molecules in hostile or luminous environments, FWM has the distinct advantage of generating a response in the form of a coherent and well-collimated beam of light. Apart from providing a viable mechanism for the rejection of background interference, this remote sensing capability enables spectroscopic measurements to be performed requiring minimal access to the target region. In contrast, the majority of linear techniques result in signals that radiate in an isotropic fashion, thereby decreasing the efficiency with which they can be collected and discriminated. The exceptional temporal and spatial selectivity accompanying the FWM interaction enables investigation of transient species and their distribution in a non-uniform medium.

3.2. Theoretical Background

In the following discussion, the FWM case when all three incident waves have the same frequency is taken to consideration. The DFWM interaction exploits the inherent nonlinearity of a target medium to couple and redirect the flow of energy among three intersecting optical fields of degenerate frequency ω , giving rise to a fourth signal field constrained to be of the same frequency ω (Figure 3.3). Each electromagnetic wave possesses its own unique polarization and propagation characteristics.

For an individual electromagnetic wave, the electric field, $\mathbf{E}_i(\mathbf{r}, t)$ can be specified in terms of its central frequency ω_i and vector amplitude \mathbf{E}_{ω_i} as

$$\mathbf{E}_i(\mathbf{r}, t) = \frac{1}{2} (\mathbf{E}_{\omega_i} e^{-i\omega_i t} + \mathbf{E}_{\omega_i}^* e^{+i\omega_i t}), \quad (3.1)$$

where the relation $E_{\omega_i} = \mathcal{E}_i \epsilon_i e^{ik_i \cdot r}$ defines the corresponding scalar amplitude \mathcal{E}_i , transverse polarization unit vector ϵ_i and propagation wave vector k_i . The intensity of the electromagnetic wave I_i can be expressed as

$$I_i = \frac{1}{2} \epsilon_0 c |\mathcal{E}_i|^2, \quad (3.2)$$

where ϵ_0 and c are the permittivity of free space and speed of light in vacuum.

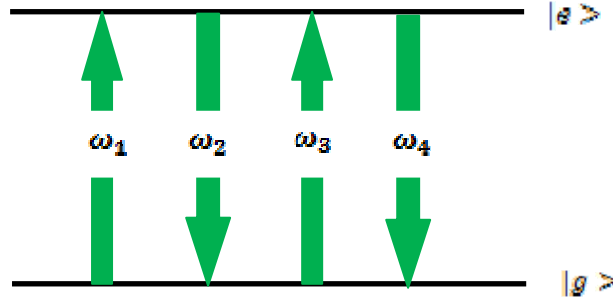


Figure 3.3: Energy level diagram for Degenerate Four Wave Mixing interaction between the ground and excited energy levels of the target, $\omega_1 = \omega_2 = \omega_3 = \omega_4 = \omega$.

A signal field generated in this manner satisfies energy and momentum conservation criteria with the various optical fields so that $\omega_4 = \omega_1 - \omega_2 + \omega_3$ and $k_4 = k_1 - k_2 + k_3$.

Although the incident beams are degenerate in the laboratory fixed frame of reference, molecules in a gas-phase ensemble will experience first order Doppler shifts [23] that are proportional to their velocity vector, \mathbf{v} , thereby resulting in an effective frequency of $\omega_i = \omega - k_i \cdot \mathbf{v}$ for each wave.

The induced electric polarization vector consisting of both linear and nonlinear components can be expanded in a Taylor series as

$$\mathbf{P}(\mathbf{r}, t) = \mathbf{P}^{(1)}(\mathbf{r}, t) + \mathbf{P}^{(2)}(\mathbf{r}, t) + \mathbf{P}^{(3)}(\mathbf{r}, t) + \mathbf{P}^{(4)}(\mathbf{r}, t) + \dots \quad (3.3)$$

Assuming that the molecular sample can be treated as an isolated ensemble of independent and distinguishable particles that interact with electromagnetic radiation under the dipole approximation, the time domain expression for the third order polarization vector, which is responsible for the wave mixing interaction $\mathbf{P}_4^{(3)}(\mathbf{r}, t)$, can be expressed as the quantum mechanical expectation value of the dipole operator, $\boldsymbol{\mu}$ as

$$\mathbf{P}_4^{(3)}(\mathbf{r}, t) = N \text{Tr}[\rho^{(3)}(\mathbf{r}, t) \boldsymbol{\mu}], \quad (3.4)$$

where N represents the total number density of target species, $\rho^{(3)}(t)$ denotes the third order term arising from a time-dependent perturbative expansion of the density operator, and the trace operation, symbolized by $Tr[.]$, is performed over the unperturbed eigenstates of the ensemble. In particular, the diagonal and off-diagonal elements of $\rho^{(3)}(t)$ in an energy eigenbasis describe molecular populations and coherences, respectively, that are created and/or modified through three successive matter-field interactions.

This optically induced polarization $P_j^{(3)}(t)$ oscillates at the characteristic frequency ω_4 and can be expressed as

$$P_j^{(3)}(t) = \frac{1}{2} \left[P_{\omega_4}^{(3)} e^{-i\omega_4 t} + P_{-\omega_4}^{(3)} e^{+i\omega_4 t} \right], \quad P_{-\omega_4}^{(3)} = \left(P_{\omega_4}^{(3)} \right)^* . \quad (3.5)$$

The overall strength of the DFWM response is embodied in the amplitude vector $P_{\omega_4}^{(3)}$ which can be expressed in terms of the incident electromagnetic fields and the third order susceptibility tensor:

$$P_{\omega_4}^{(3)} = \frac{3}{4} \epsilon_0 [\chi^{(3)}(-\omega_4; \omega_1, -\omega_2, \omega_3) \vdots \epsilon_1 \epsilon_2^* \epsilon_3] \mathcal{E}_1 \mathcal{E}_2^* \mathcal{E}_3 e^{i(k_1 - k_2 + k_3) \cdot r} . \quad (3.6)$$

Here, the operator \vdots represents tensor contraction. Individual Cartesian components of the induced polarization are denoted by

$$\left(P_{\omega_4}^{(3)} \right)_j = \epsilon_j^* \cdot P_{\omega_4}^{(3)}, \quad j = x, y, z . \quad (3.7)$$

The amplitude vector for the DFWM signal polarization can be reformulated as a sum of three distinct terms:

$$P_{\omega_4}^{(3)} = \mathcal{A}(\mathcal{E}_{\omega_2} \cdot \mathcal{E}_{\omega_2}^*) \mathcal{E}_{\omega_1} + \mathcal{B}(\mathcal{E}_{\omega_1} \cdot \mathcal{E}_{\omega_2}^*) \mathcal{E}_{\omega_2} + \mathcal{C}(\mathcal{E}_{\omega_1} \cdot \mathcal{E}_{\omega_3}) \mathcal{E}_{\omega_3}^* , \quad (3.8)$$

where the coefficients $\mathcal{A}, \mathcal{B}, \mathcal{C}$ depend on the linearly independent components of the susceptibility tensor.

In the weak response limit, where the pump and probe beams propagate through an optically thin sample of length l without experiencing significant attenuation or amplification, the expression for the intensity of the signal wave I_4 reduces to:

$$I_4 = \frac{\omega_4^2 l^2}{8c \epsilon_0} |\epsilon_4^* \cdot P_{\omega_4}^{(3)}|^2 = \left(\frac{3\omega_4 l}{4c^2 \epsilon_0} \right)^2 |\epsilon_4^* \cdot \chi^{(3)}(-\omega_4; \omega_1, -\omega_2, \omega_3) \vdots \epsilon_1 \epsilon_2^* \epsilon_3|^2 I_1 I_2 I_3 . \quad (3.9)$$

The above expression shows that the unsaturated DFWM signal strength scales as square of the interaction length, l , and as the product of intensities for all three incident beams I_1 , I_2 and I_3 . Because the degenerate pump and probe waves are derived from a common source of tunable light, the weak field magnitude of I_4 exhibits a cubic dependence upon applied laser power with small variations in the incident intensity translating to large fluctuations of observed signal magnitude. The quadratic dependence on l suggests that a significant enhancement in detection sensitivity can be realized through use of experimental configurations that maximize effective sample pathlength.

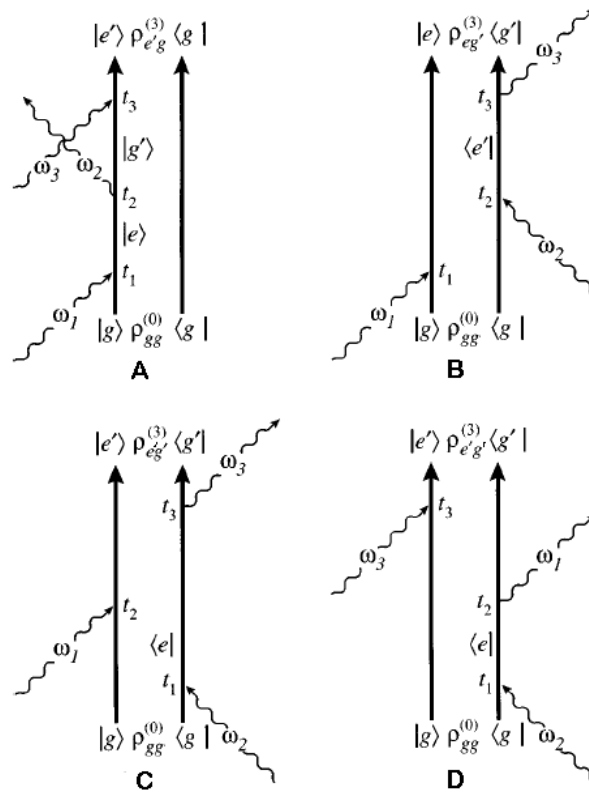


Figure 3.4: Double sided Feynmann diagrams for degenerate four wave mixing spectroscopy.

Equation (3.4) indicates that calculation of the DFWM signal polarization $\mathbf{P}_4^{(3)}(\mathbf{t})$ and associated susceptibility tensor $\chi^{(3)}(-\omega_4; \omega_1, -\omega_2, \omega_3)$ requires knowledge of the third order density operator $\rho^{(3)}(\mathbf{t})$. The explicit form of $\rho^{(3)}(\mathbf{t})$ follows from solution of the quantum-mechanical Liouville equation that determines temporal behavior of the target medium under the influence of both applied electromagnetic fields and intrinsic relaxation pathways [24]. The requisite perturbation analysis is summarized

schematically by the double-sided Feynman diagrams [24] (Figure 3.4) which give a pictorial representation for the optically induced transformation of $\rho^{(0)}$ into $\rho^{(2)}(t)$.

Each of the depicted panels represents a specific sequence of matter-field interactions that contribute to the overall four-wave mixing response. The density operator is denoted by two vertical arrows corresponding to the bra-ket of a matrix representation. Time is defined to increase from bottom to top and interactions with electromagnetic waves are designated by wavy arrows indicating absorption or emission. The molecular quantum states involved in an optically induced transition are indicated above and below each interaction arrow with the n th matter-field coupling taking place at time t_n where $-\infty \leq t_1 \leq t_2 \leq t_3 \leq t$. The matrix representations for the $\rho^{(n)}(t)$ terms corresponding to Fig 3.4(A) leads to the following temporal progression:

$$\rho_{gg}^{(0)} \xrightarrow{\hbar\omega_1, t_1} \rho_{eg}^{(1)}(t_1 \leq t \leq t_2) \xrightarrow{\hbar\omega_2, t_2} \rho_{g'g}^{(2)}(t_2 \leq t \leq t_3) \xrightarrow{\hbar\omega_3, t_3} \rho_{e'g}^{(3)}(t \geq t_3) \quad (3.10)$$

3.3. Experimental Geometries

The DFWM methodology can be implemented successfully through use of numerous beam crossing geometries. Three broad categories of experimental configurations can be identified, the most common of which is the phase-conjugate scheme shown in Figure 3.5. In this arrangement, two of the incident optical waves, designated by electric vectors \mathbf{E}_1 and \mathbf{E}_3 , propagate through the target medium in a coaxial and counter-propagating manner ($\mathbf{k}_3 = -\mathbf{k}_1$). The remaining input wave, \mathbf{E}_2 , intersects these beams under a small crossing angle θ . The region of mutual overlap of the waves defines the four-wave mixing interaction volume. Momentum conservation ($\mathbf{k}_4 = \mathbf{k}_1 - \mathbf{k}_2 + \mathbf{k}_3 = -\mathbf{k}_2$), demands that the signal field, \mathbf{E}_4 , emerge in a direction that exactly retraces the path of \mathbf{E}_2 , thus making the signal an exact spatial and temporal replica of the probe. While the signal photons can be isolated most directly by inserting a beamsplitter into the optical train of \mathbf{E}_2 , a variety of polarization-sensitive detection techniques can be exploited for their extraction and discrimination from spurious background light [23]. The planar phase-conjugate geometry has the distinct advantage of experimental simplicity over other geometries.

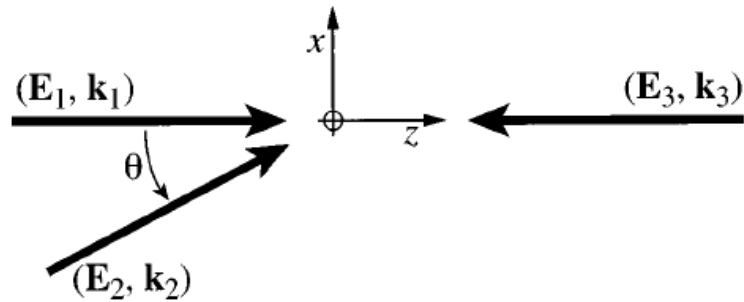


Figure 3.5: The phase-conjugate four wave mixing geometry.

The other categories of DFWM phase matching can be classified broadly as “box” geometries. Built upon the crossed-beam configuration of CARS known as BOXCARS, both of these schemes require the incident electromagnetic waves to propagate through the target medium along three distinct diagonals of a rectangular parallelepiped. The signal field is then generated along the spatially distinct and “dark” axis of detection defined by the fourth diagonal. Although more complicated to execute than the phase-conjugate technique, such box arrangements do not require collection optics in the path of the input wave, thereby eliminating a major source of incoherently scattered background light. The implementations of these geometries entail the crossing of two impinging beams, denoted as \mathbf{E}_1 and \mathbf{E}_2 , at a small angle such that $\mathbf{k}_1 \approx \mathbf{k}_2$. The forward-box and backward-box schemes differ in the direction of the remaining input field, \mathbf{E}_3 , with the former having it nearly co-propagating with respect to \mathbf{E}_1 and \mathbf{E}_2 ($\mathbf{k}_3 \approx \mathbf{k}_1$) while the latter has it nearly counter-propagating ($\mathbf{k}_3 \approx -\mathbf{k}_1$). Figure 3.6 below depicts forward-box geometry of DFWM.

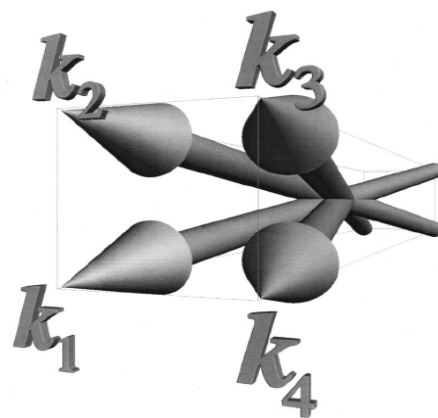


Figure 3.6: Forward box configuration for four wave mixing spectroscopy.

3.4. The Laser Induced Grating Approach

The transient grating perspective provides a qualitative understanding for the various processes contributing to a resonant FWM response and is a succinct interpretation for the method. In this approach, the classical interference between two overlapping light beams in the presence of strong matter-field interactions produces a spatial modulation in the magnitude and/or polarization of the net electric field in the overlap region of the beams. This gives rise to a spatially periodic modulation of the complex refractive index which acts as a transient diffraction grating [25]. The remaining incident beam subsequently Bragg scatters from this grating, thereby producing the observed signal photons.

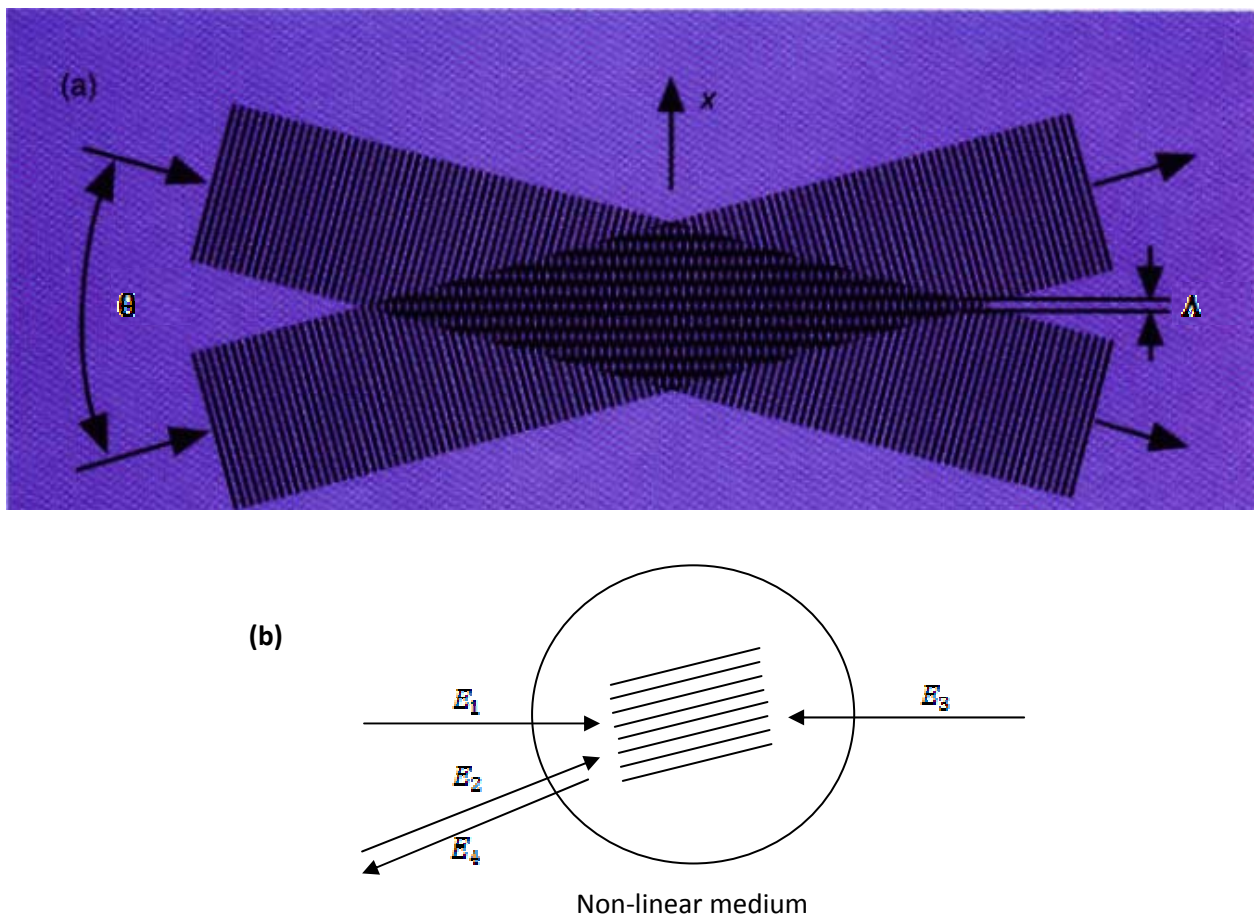


Figure 3.7: (a) Interference created by two frequency degenerate beams at wavelength λ_{exc} crossing at an angle of θ producing fringes separated by distance Λ . (b) Laser induced phase conjugate grating with the backward propagating pump field E_3 Bragg scattered and producing E_4 upon absorption.

In the gas phase the dominant grating formation processes are electrostriction and heat exchange with a thermal bath in the course of collisional relaxation of the absorbed laser energy. Optical gratings generated by electrostriction and collisional relaxation of the absorbed laser radiation are referred to as electrostrictive and thermal gratings, respectively. The laser radiation is absorbed by the molecules through electronic (and/or vibrational) transitions of the medium. A spatially periodic modulation of the population, reflecting the intensity distribution of the interference structure, is formed in the ground and the excited state, respectively. Such a spatially periodic modulation of the population of the energy levels involved causes the respective modulation of the refractive index and of the absorption coefficient, called a population LIG. Fast thermalization of internal energy due to collisions may provide a spatial modulation of the refractive index resulting from density variations and thus lead to the formation of thermal LIGs. Adiabatic compression of the gas by the inhomogeneous pump electromagnetic field strength, simultaneous with resonant excitation, generates electrostrictive LIGs.

The interference fringe pattern is characterized by a grating vector \mathbf{q} expressed as a function of the wave vectors of the excitation beams

$$\mathbf{q} = \pm(\mathbf{k}_1 - \mathbf{k}_2) . \quad (3.11)$$

The length of the grating vector, $q = |\mathbf{q}|$, is related to the fringe spacing Λ of the interference pattern according to

$$q = \frac{2\pi}{\Lambda} , \quad (3.12)$$

$$\text{where } \Lambda = \frac{\lambda_{\text{exc}}}{2 \sin(\frac{\theta}{2})} . \quad (3.13)$$

Here, λ_{exc} denotes the wavelength of the excitation laser, and θ the intersection angle of the two excitation beams (Figure 3.7(a)). The material excitation couples to the refractive index n and to the absorption coefficient α which then exhibits a grating-like modulation with amplitudes $\Delta n(\lambda_{\text{pr}})$ and $\Delta \alpha(\lambda_{\text{pr}})$, respectively. Both amplitudes are functions of the probing wavelength λ_{pr} of the third laser beam which is diffracted off the induced grating. Probe and excitation beams are typically of different frequency. In the phase-conjugate geometry, interference of the probe field, \mathbf{E}_2 , and the forward propagating pump field, \mathbf{E}_1 , forms a large period grating exactly phase-matched to

Bragg scatter the backward propagating pump field, E_3 , into the signal beam, E_4 (Figure 3.7(b)). That part of the probe beam diffracted by the grating is called the signal beam. The diffraction efficiency of an LIG can be expressed as

$$\eta = \frac{I_4}{I_2} = \left(\frac{\pi \Delta n d}{\lambda_{pr}} \right)^2 + \left(\frac{\Delta \alpha d}{4} \right)^2, \quad (3.14)$$

where I_2 and I_4 are the intensities of the probe beam and the diffracted beam, respectively, and d is the thickness of the grating.

3.5. Optical Saturation Effects and Line Profiles

Originally formulated by Abrams and Lind [1, 26, 27], the saturable absorber model focuses upon a system of motionless two-level atoms, with the common spectroscopic transition between their non-degenerate ground, $|g\rangle$ and excited, $|e\rangle$ states having resonant frequency ω_{eg} and dipole moment matrix element μ_{eg} (Figure 3.3).

The unperturbed energies and population decay rates for eigenstates are given by E_α and $\Gamma_{\alpha\alpha}$ where the subscript α can assume values of “g” or “e”. The longitudinal relaxation time $T_{1\alpha}$ or effective lifetime τ_α for state $|\alpha\rangle$ is equal to the inverse of $\Gamma_{\alpha\alpha}$ and the rest angular frequency for the $|\beta\rangle \leftrightarrow |\alpha\rangle$ resonance is defined by $\omega_{\beta\alpha} = (E_\beta - E_\alpha)/\hbar$. Optical coherences created between various molecular eigenstates by resonant matter-field interactions are characterized by the off-diagonal components of matrices corresponding to higher order terms in the density operator expansion, $\rho_{\alpha\beta}^{(n)}$; $n > 0$. The temporal dissipation of these coherences is related to the depopulation rates as

$$\Gamma_{\beta\alpha} = \frac{1}{2}(\Gamma_{\beta\beta} + \Gamma_{\alpha\alpha}) + \Gamma_{\beta\alpha}^\dagger = \frac{1}{T_{2\beta\alpha}}, \quad (3.15)$$

where $T_{2\beta\alpha}$ is the transverse relaxation time for the transition between the states. The quantity $\Gamma_{\beta\alpha}^\dagger$ represents the pure dipole dephasing rates which stems from processes like elastic collisions that destroy molecular coherence without disrupting corresponding molecular populations [28].

Assume the rates for dissipation of population and coherence are denoted by Γ_0 and Γ_{eg} respectively. The longitudinal relaxation parameter is given by the inverse of

the average lifetimes for the ground and excited states: $\Gamma_0^{-1} = (\Gamma_{gg}^{-1} + \Gamma_{ee}^{-1})/2$. The incident and generated electromagnetic waves are monochromatic and of the same frequency ω . For small overall absorption or gain, with $I_1 = I_3 = I$, the magnitude of the signal wave I_4 emerging from a DFWM interaction length l [29] is given as

$$I_4 = RI_2 = \frac{(\alpha_0 l)^2}{1 + \delta^2} \frac{(2I/I_{sat})^2}{1 + 4I/I_{sat}} I_2, \quad (3.16)$$

where R is the phase conjugate reflectivity experienced by I_2 . The signal strength increases quadratically with the field absorption coefficient at line center, α_0 ,

$$\alpha_0 = \frac{\omega_{eg} |\mu_{eg}|^2}{2\hbar c \epsilon_0 \Gamma_{eg}} \Delta N_0. \quad (3.17)$$

Here $\Delta N_0 = N_g - N_e$ denotes the initial population difference between the ground and excited states. The normalized detuning parameter, δ includes the frequency response of the four-wave mixing interaction and is expressed as

$$\delta = \frac{\Delta\omega}{\Gamma_{eg}} = \frac{\omega - \omega_{eg}}{\Gamma_{eg}}. \quad (3.18)$$

The expression (3.16) shows that the signal strength scales as the square of the field absorbance at line center, meaning quadratic dependence on sample number density and interaction pathlength. The optical saturation intensity is given as

$$I_{sat} = I_{sat}^c (1 + \delta^2), \quad (3.19)$$

where I_{sat}^c gives the field strength for which the Rabi frequency equals the rates of relaxation/dephasing processes,

$$I_{sat}^c = \frac{\hbar^2 c \omega_{eg} \Gamma_{eg} \Gamma_e}{2 |\mu_{eg}|^2}. \quad (3.20)$$

The resonant FWM response correlates strongly with the ratio of incident pump and line-center saturation intensities, I/I_{sat}^c . The asymptotic forms for the FWM response at line center, I_4^c can be obtained from Eq. (3.16) by substituting $\delta = 0$ and performing a series expansion of the intensity-dependent denominator.

$$I \ll I_{sat}^c \quad I_4^c = (\alpha_0 l)^2 \left(\frac{2I}{I_{sat}^c} \right)^2 I_2 \propto (\Delta N_0 l)^2 \frac{|\mu_{eg}|^4}{\Gamma_{eg}^2 \Gamma_e^2} I^2 I_2 \quad (3.21)$$

$$I \gg I_{sat}^c \quad I_4^c = \left(\frac{\alpha_0 l}{4} \right)^2 \left(\frac{I_{sat}^c}{I} \right) I_2 \propto (\Delta N_0 l)^2 \frac{|\mu_{eg}|^2 \Gamma_e I_2}{\Gamma_{eg} I} \quad (3.22)$$

Since for DFWM, $I = I_2$, the saturable absorber response for $I \ll I_{sat}^2$ varies as the cube of the incident intensity. The high power limit for I_{sat}^2 shows a behavior independent of both I and I_2 . Thus, while working in the saturated regime, the amplitude fluctuations of the laser beams are not transferred to the DFWM signal.

The saturable absorber model also provides information on the FWM spectral profile [29]. The power-broadening rate parameter is given as

$$\Gamma_{PB} = \Gamma_{eg} \sqrt{1 + 4I/I_{sat}^2} \quad (3.23)$$

so that the intensity of the signal can be expressed as

$$I_4 = R I_2 = (2\alpha_0 l)^2 \left(\frac{I}{I_{sat}}\right)^3 \left[\frac{\Gamma_{eg}^2}{(\Delta\omega)^2 + \Gamma_{PB}^2}\right]^3 I_2. \quad (3.24)$$

This gives a Lorentzian cubed spectral profile. However, the saturable absorber lineshape broadens in proportion to the common intensity of the pump waves with the effective Half Width at Half Maximum as,

$$\Delta\omega_{\text{HWHM}} = \Gamma_{eg} \sqrt{(2^{1/3} - 1)(1 + 4I/I_{sat}^2)}. \quad (3.25)$$

For weak incident pump field ($I \ll I_{sat}^2$), $\Delta\omega_{\text{HWHM}} \approx \Gamma_{eg} \sqrt{(2^{1/3} - 1)}$. In contrast, the lineshape for $I \gg I_{sat}^2$ is given by $\Delta\omega_{\text{HWHM}} = \Gamma_{eg} \sqrt{(I/I_{sat}^2)}$ meaning a frequency independent response in the high intensity regime. Detailed investigations of saturation processes and comparisons to the Abrams and Lind theory in molecular DFWM spectra have been carried out in the past years [29, 30, 31].

3.6. Phase Matching Considerations in TC-LIGS

Unlike DFWM which is phase matched for all frequencies, the detrimental effects of phase mismatch must be considered for two-color laser induced grating spectroscopy (TC-LIGS). The signal and probe beams have identical frequency (Figure 3.8), with the energy constraint $\omega_4 = \omega_1 - \omega_1 + \omega_2 = \omega_2$, and phase matching constraint given by the vector sum: $k_1 + k_2 = k_3 + k_4$ where the wave vector magnitudes are $k_i = 2\pi/\lambda_i$. The two grating beams are denoted by k_1 and k_3 ($k_1 = k_3$), and $k_4 = k_2$. Typically, the grating and probe-beam angles are fixed and either λ_1 (λ_{exc}) or λ_2 (λ_{pr}) is scanned.

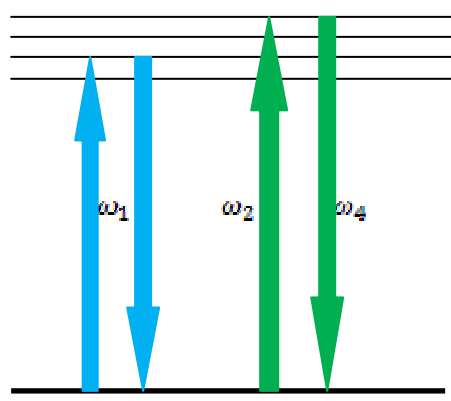


Figure 3.8: Energy level diagram showing the UP-laser induced grating spectroscopy scheme.

Figure 3.9 shows a wave vector diagram for TCLIGS in the forward geometry for a case in which the probe frequency is less than the phase matched value. The two grating beams cross at a half-angle θ_1 , to form a grating with wave vector, k_g ; the magnitude of this vector is $k_g = 2k_1 \sin \theta_1$, and the grating fringe spacing is $\Lambda = 2\pi/k_g = \lambda_1/(2 \sin \theta_1)$. The probe beam at ω_2 crosses the interaction region at a half angle θ_2 and the signal beam at $\omega_4 = \omega_2$ is generated at an angle θ_4 . The phase mismatch Δk is determined by the vector sum: $k_g + k_2 + (k_4 + \Delta k) = 0$. For a given probe frequency, exact phase matching ($\Delta k = 0$) occurs at the angle given by $\sin \theta_2 = \left(\frac{k_1}{k_2}\right) \sin \theta_1 = \left(\frac{\lambda_2}{\lambda_1}\right) \sin \theta_1$. In the phase matched case the signal beam diffracts at the probe-beam input angle ($\theta_4 = \theta_2$) i.e., the probe beam is Bragg scattered off the induced grating. The signal beam is generated in a direction that minimizes the phase mismatch, i.e., Δk and k_4 are collinear as depicted.

The signal beam angle is given by

$$\tan \theta_4 = \left(\frac{2 \sin \theta_1}{\lambda_2 \cos \theta_2}\right) \lambda_2 - \tan \theta_2 . \quad (3.26)$$

Inclusion of the fringe spacing Λ gives

$$\sin \theta_4 = \left(\frac{\cos \theta_2}{\cos \theta_1}\right) \left[\left(\frac{\lambda_2}{\Lambda}\right) - \sin \theta_2\right] . \quad (3.27)$$

In the small angle limit, this becomes

$$\theta_4 = \left(\frac{\lambda_2}{\Lambda}\right) - \theta_2 . \quad (3.28)$$

For a wave vector mismatch of Δk , the TCLIGS response varies proportional to $\sin^2(\Delta k l / 2) / (\Delta k l / 2)^2$, which is given as the FWHM of the central lobe of the phase mismatch function, l being the interaction length. Figure 3.9 gives

$$(k_4 + \Delta k)^2 = k_2^2 + k_g^2 - 2k_2 k_g \cos \phi = k_2^2 + k_g^2 - 2k_2 k_g \cos \theta_2. \quad (3.29)$$

The above equation is solved for Δk to determine the frequency bandwidth for tuning the probe frequency given as

$$\Delta \bar{\nu}_2 \approx \left(\frac{0.443}{n_2 l} \right) \left(\frac{\lambda_2}{\lambda_1} \right)^2 \left(\frac{1}{\sin^2 \theta_1} \right). \quad (3.30)$$

In contrast, the bandwidth for tuning the grating frequency is given as

$$\Delta \bar{\nu}_1 \approx \left(\frac{0.443}{n_1 l} \right) \left(\frac{\lambda_1}{\lambda_2} \right) \left(\frac{1}{\sin^2 \theta_1} \right). \quad (3.31)$$

Here, n_1 and n_2 are the real refractive indices of the medium at λ_1 and λ_2 , respectively. The effects of phase matching on the signal-beam angle and frequency tuning bandwidths in two-color LIGS were studied through measurements in methanol dye solution [19].

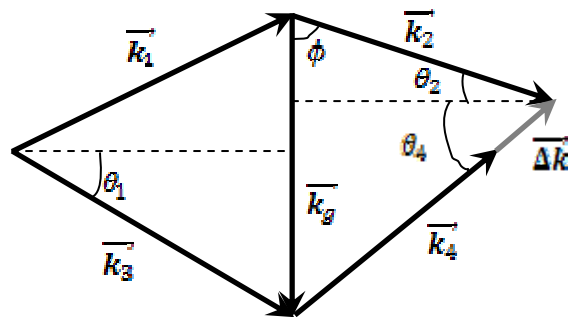


Figure 3.9: The wave vector scheme for two color laser induced grating spectroscopy in the forward-box geometry where the probe frequency lies below the phase matched value. k_1 and k_3 denote the wave vectors of grating beams, k_2 and k_4 denote those of probe and signal waves respectively, and k_g is the wave vector of the grating. Δk defines the phase mismatch.

The double resonance feature of TCLIGS has the distinct advantage for unraveling spectra that are otherwise extremely congested, thus giving unambiguous spectral assignments. This aspect is detailed in Chapter 7.

Bibliography

- [1] Fisher, R. A. *Optical Phase Conjugation: Academic Press: San Diego: 1983.*
- [2] Eichler, H. J.; Günter, P.; Pohl, D. W. *Laser Induced Dynamic Gratings: Springer-Verlag: Berlin: 1986.*
- [3] Ewart, P.; O'Leary, S. V. *J. Phys. B.* 15, 3669, **1982.**
- [4] Ewart, P.; O'Leary, S. V. *Opt. Lett.* 11, 279, **1986.**
- [5] Konz, E.; Fabelinsky, V.; Marowsky, G.; Rubahn, H. G. *Chem. Phys. Lett.* 247, 522, **1995.**
- [6] Versluis, M.; Meijer, G.; Chandler, D. W. *Appl. Opt.* 33, 3289, **1994.**
- [7] Gray, J. A.; Trebino, R. *Chem. Phys. Lett.* 216, 519, **1993.**
- [8] Dreier, T.; Rakestraw, D. J. *Appl. Phys. B.* 50, 479, **1990.**
- [9] Green, D. S.; Owano, T. G.; Williams, S.; Goodwin, D. G.; Zare, R. N.; Kruger, C. H. *Science* 259, 1726, **1993.**
- [10] Hall, G.; Suits, A. G.; Whitaker, B. J. *Chem. Phys. Lett.* 203, 277, **1993.**
- [11] Mann, B. A.; White, R. F.; Morrison, R. J. *S. Appl. Opt.* 35, 475, **1996.**
- [12] Ashfold, M. N. R.; Chandler, D. W.; Hayden, C. C.; McKay, R. I.; Heck, A. J. R. *Chem. Phys.* 201, 237, **1995.**
- [13] Dunlop, J. R.; Rohlfing, E. A. *J. Chem. Phys.* 100, 856, **1993.**
- [14] DeRose, P.; Dai, H. L.; Cheng, P. Y. *Chem. Phys. Lett.* 220, 207, **1994.**
- [15] Stone, B. M.; Noble, M.; Lee, E. K. C. *Chem. Phys. Lett.* 118, 83, **1985.**
- [16] Kable, S. H.; Loison, J-C.; Neyer, D. W.; Houston, P. L.; Burak, I.; Dixon, R. N. *J. Phys. Chem.* 95, 8013, **1991.**
- [17] Mann, B. A.; O'Leary, S. V.; Astill, A. G.; Greenhalgh, D. A. *Appl. Phys. B.* 54, 271, **1992.**
- [18] Buntine, M. A.; Chandler, D. W.; Hayden, C. C. *J. Chem. Phys.* 97, 707, **1992.**
- [19] Butenhoff, T. J.; Rohlfing, E. A. *J. Chem. Phys.* 98, 5460, **1993.**
- [20] Butenhoff, T. J.; Rohlfing, E. A. *J. Chem. Phys.* 98, 5469, **1993.**
- [21] Kozlov, D. N.; Radi, P. P. *J. Raman Spec.* 39, 730, **2008.**
- [22] Wasserman, T. A. W.; Vaccaro, P. H.; Johnson, B. R. *J. Chem. Phys.* 108, 7713, **1998.**
- [23] Field, R. W.; Hirota, E.; Maier, J. P.; Tsuchiya, S. *Nonlinear Spectroscopy for Molecular Structure Determination: Blackwell Science: 1998.*

- [24] Mukamel, S. *Principles of Nonlinear Optical Spectroscopy: Oxford University Press: New York: 1995.*
- [25] Stampanoni-Panariello, A.; Kozlov, D. N.; Radi, P. P.; Hemmerling, B. *Appl. Phys. B.* 81, 101, **2005.**
- [26] Abrams, R. L.; Lind, R. C. *Opt. Lett.* 2, 94, **1978.**
- [27] Abrams, R. L.; Lind, R. C. *Opt. Lett.* 3, 205, **1978.**
- [28] Berman, P. R. *Phys. Rev. A.* 5, 927, **1972.**
- [29] Brown, M. S.; Rahn, L. A.; Drier, T. *Opt. Lett.* 17, 76, **1992.**
- [30] Rahn, L. A.; Brown, M. S. *Opt. Lett.* 19, 1249, **1994.**
- [31] Brown, M. S.; Rahn, L. A.; Lucht, R. P. *Appl. Opt.* 34, 3274, **1995.**

Chapter 4

Experimental Set-up

4.1. Supersonic Jet Expansion

The emission or absorption spectra of molecules are usually affected by factors like Doppler broadening and high population of excited rovibronic levels in the ground electronic state at high temperatures. This usually results in congested spectra which are difficult to interpret. An alternative is to measure spectra of isolated molecules cooled to a very low temperature, and this is achieved by use of a supersonic free jet expansion. Also, free jet expansions are useful in producing transient radicals which cannot be effectively produced by other methods.

In a supersonic expansion the molecule of interest is expanded adiabatically through a small orifice or nozzle of diameter D from a high pressure source (P_0, T_0) to a low pressure (P) region. This results in conversion of internal energy of the gas into kinetic energy leading to sharpening of the Maxwell-Boltzmann distribution of molecular velocities and hence translational cooling to a temperature T . In the post-nozzle region of the expansion the cold translational bath acts as a refrigerant for the other degrees of freedom [1]. The decrease in temperature reduces the Doppler broadening significantly. Due to partial cooling of rotational and vibrational degrees of freedom, only the lowest rovibronic levels in the ground electronic state of a molecule are populated. Most of the hot band transitions do not occur, simplifying the otherwise congested molecular spectra and providing an easier analysis. The low densities attained in a jet also allow transient molecules to survive enough for spectroscopic investigations. The translational cooling in the supersonic jet is effective when the diameter of the nozzle is relatively larger than the mean free path of the molecules. Many examples of spectral structure simplifying upon cooling of rotations of molecules can be found in Levy [1] and Engelking [2].

Figure 4.1 shows the basic features of a supersonic jet expansion. An acceleration of the gas out of the reservoir takes place due to the pressure difference $P_0 - P$ created as the gas reaches the decreased nozzle area toward the exit. When the pressure ratio P_0/P exceeds the critical value $\frac{0.5\gamma(\gamma+1)}{\gamma-1}$, where γ is the ratio of heat capacities $\frac{c_p}{c_v}$ of the expanded gas, the gas flow exits the nozzle with sonic speed, with the Mach number $M = 1$ [3]. The flow becomes supersonic as the flow area increases, hence $M > 1$ beyond the nozzle exit. The temperature and density of a gas decrease with increasing distance from the nozzle.

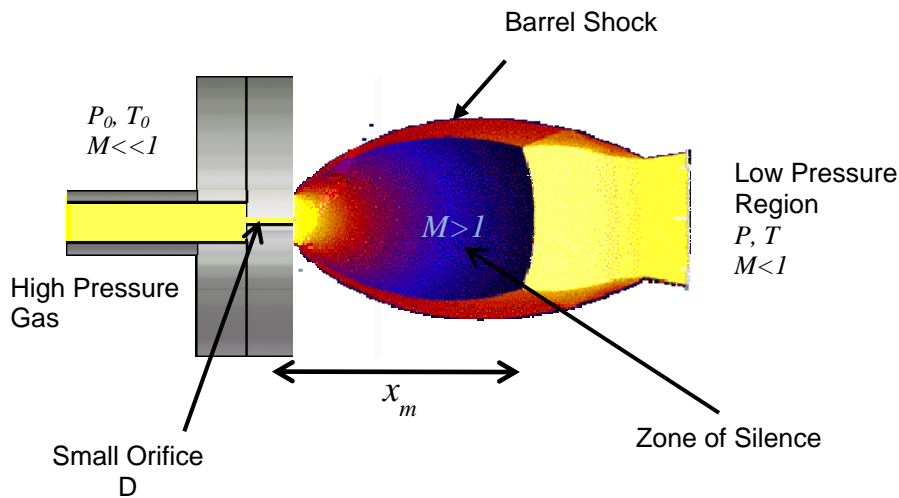


Figure 4.1: Schematic of supersonic expansion.

For a continuous gas at distances greater than a few nozzle diameters from the orifice, it has been shown [4] that the Mach number is given by

$$M = A \left(\frac{x}{D} \right)^{\gamma-1}, \quad (4.1)$$

where x is the downstream distance and A is a constant that depends on γ and is 3.26 for a monatomic gas. Under isentropic conditions, the properties of an adiabatically expanding gas are given by

$$\frac{T}{T_0} = \left(\frac{P}{P_0} \right)^{\frac{\gamma-1}{\gamma}} = \left(\frac{\rho}{\rho_0} \right)^{\frac{\gamma-1}{\gamma}} = \left[1 + \frac{(\gamma-1)M^2}{2} \right]^{-1}. \quad (4.2)$$

In Figure 4.2 the Mach number and the temperature, pressure, and density ratios for a monatomic gas ($\gamma = 5/3$) are plotted as a function of distance downstream of the nozzle. At some point downstream density becomes sufficiently low so that there are no collisions and the Mach number and temperature are frozen from this point on

downstream. Anderson & Fenn [5] have predicted that for a monatomic gas the terminal Mach number, M_T is a function only of the product $P_0 D$ and is given by

$$M_T = 133(P_0 D)^{0.4}, \quad (4.3)$$

where P_0 is in atmospheres and D is in cm. For gases other than helium this equation was found to adequately describe the Mach number freezing. In the case of helium, quantum effects cause the collisional cross section to increase with decreasing relative energy, and this leads to very much larger terminal Mach numbers than those predicted by Eq. 4.3 [6].

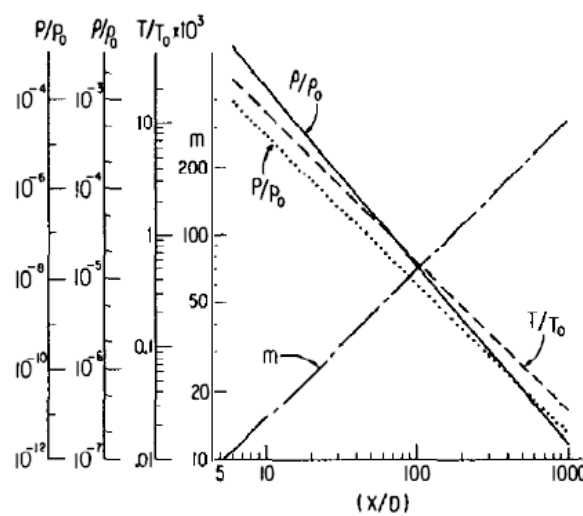


Figure 4.2: Pressure, density, temperature and Mach number for a supersonic expansion of a monoatomic gas as a function of downstream distance [1].

This simplistic view gets complicated by the presence of barrel shock waves which are produced when the cold molecules of the flow collide with warm molecules present inside the vacuum chamber. The shock waves, formed by molecular regions of large density, pressure, temperature and velocity gradients, change the direction of the supersonic flow and reduce the Mach number to subsonic values. This causes the pressure to increase in the region, until the Mach disk appears normal to the flow at a distance from the nozzle given by

$$x_m = 0.67D \left(\frac{P_0}{P} \right)^{0.5}. \quad (4.3)$$

The core of the expansion is isentropic and unperturbed by external influences, hence called the zone of silence. Spectroscopic measurements are carried out within the

isentropic region typically starting around 5-10 nozzle diameters downstream from the orifice and extending to the Mach disk. In an expansion of 1000 Torr into a chamber of 0.1 Torr out of a nozzle of 0.1 mm diameter, the Mach disk appears 6.7 mm downstream. Supersonic expansions have been dealt in detail since the early works by Kantowitz and Grey [7], Kistiakowsky and Slichter [8] etc.

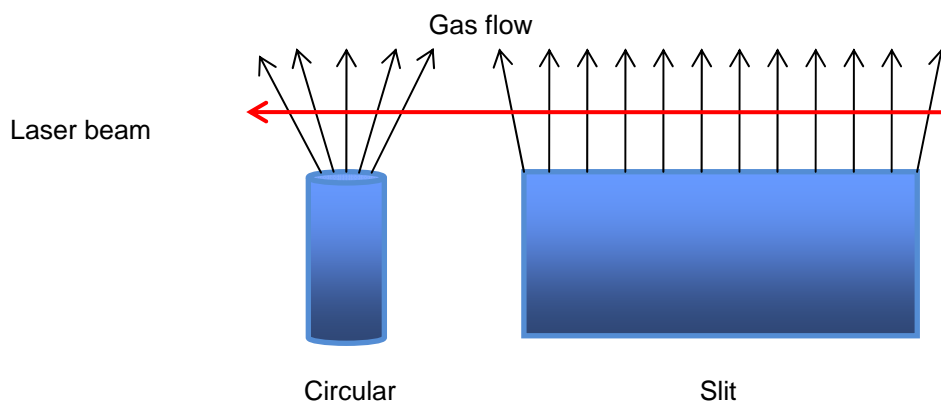


Figure 4.3: Comparison of slit and circular nozzles.

The density of molecules in a supersonic expansion can be expressed in terms of the diameter of the nozzle, D and distance from the source, x as

$$\frac{n}{n_0} = KD^i x^{-i}. \quad (4.4)$$

In the above equation, $i=1$ for a slit nozzle and $i=2$ for a circular nozzle, and the value of the constant K depends on the gas used. For example, in a slit nozzle, K is 0.2 for a monoatomic gas and 0.136 for a diatomic gas [9]. Thus, slit nozzles are convenient in spectroscopic applications because the species density decreases linearly with the distance from the slit instead of quadratically, as occurs with pinhole jets.

The first attempt to combine supersonic expansion with plasma techniques was reported in 1983 [10, 11] and employed a single pinhole discharge via a continuous gas flow through a small circular nozzle. The source was used successfully for several emission and laser-induced fluorescence studies on rotationally cold radicals [2], but for direct absorption spectroscopic techniques, the effective pathlength turned out to be too small. This necessitated the introduction of larger systems [12], which resulted in the use of slit nozzles [13, 14]. Planar jets also offer significantly longer pathlengths for absorption studies (Figure 4.3) and the 2-D expansion has no Doppler component in the direction of the laser beam providing Doppler free environments [15].

The practical limit to performance of a supersonic expansion is the requirement of adequate pumping capacity to handle the gas discharge through the nozzle [1]. This is overcome by use of pulsed nozzles. In this case the gas flows for only a small fraction of the time, and if the expansion chamber is sufficiently large, the pumping needed has to only be large enough to evacuate the chamber before the next pulse, and therefore pumping speed affects only the repetition rate, not the properties of the expansion. Moreover, by using pulsed jets, one achieves lower sample consumption and higher sensitivity using lasers synchronized with the nozzle. The use of pulsed nozzles with supersonic expansions have been demonstrated in studies of the hyperfine-resolved structure of the methyl radical in a nearly Doppler-free jet [16] and infrared high-resolution measurements on HD_2O^+ [17].

4.2. Molecular Sources

Charged and neutral carbon radicals are of importance in various reactive environments, including planet atmospheres, combustion, and interstellar media. The means of their identification in situ as well as the information on the physical and chemical conditions present in the reactive medium has resulted in considerable interest in the laboratory detection of such species by spectroscopic techniques. This motivated such studies on several carbon-bearing radicals [18, 19]. The laboratory and astronomical investigations in the millimeter-wave region lead to the identification of many carbon chains in space, including ions and radicals [20]. Measurements on these molecules are difficult because they are short lived species generated in small number densities. Discharge and laser vaporization sources coupled to a supersonic jet expansion are, so far, the most effective techniques used to generate sufficiently large densities suitable for spectroscopic studies of these transients.

4.2.1. Electric Discharge

The high voltage electric discharge source employed for this work combines the long pathlength of the slit with high particle densities accessible in a pulsed supersonic expansion. The multichannel slit nozzle determines the expansion conditions, the efficiency of the radical and ion production and the final temperatures. Examples of such sources can also be found in the works of Davis et al. [21] and Anderson et al. [22].

As shown in Figure 4.4, the orifice of the slit is comprised of an insulator, a metal plate, a second insulator, and two jaws that form the actual slit (typically 10/30/100 x 1 mm² wide, 60° exit angle). The position of the knife/edge plates is variable. Precision spacers are mounted between the plates to check the uniformity of the slit before the measurement. A pulsed valve (3 mm orifice) is mounted on top of the slit nozzle body and controls the gas flow into the system. Both metal plate and insulators have slit openings of the same dimension as the slit orifice. In this way a two-dimensional multilayer channel is formed by the plates. The components are mounted to the body by electrically isolated screws.

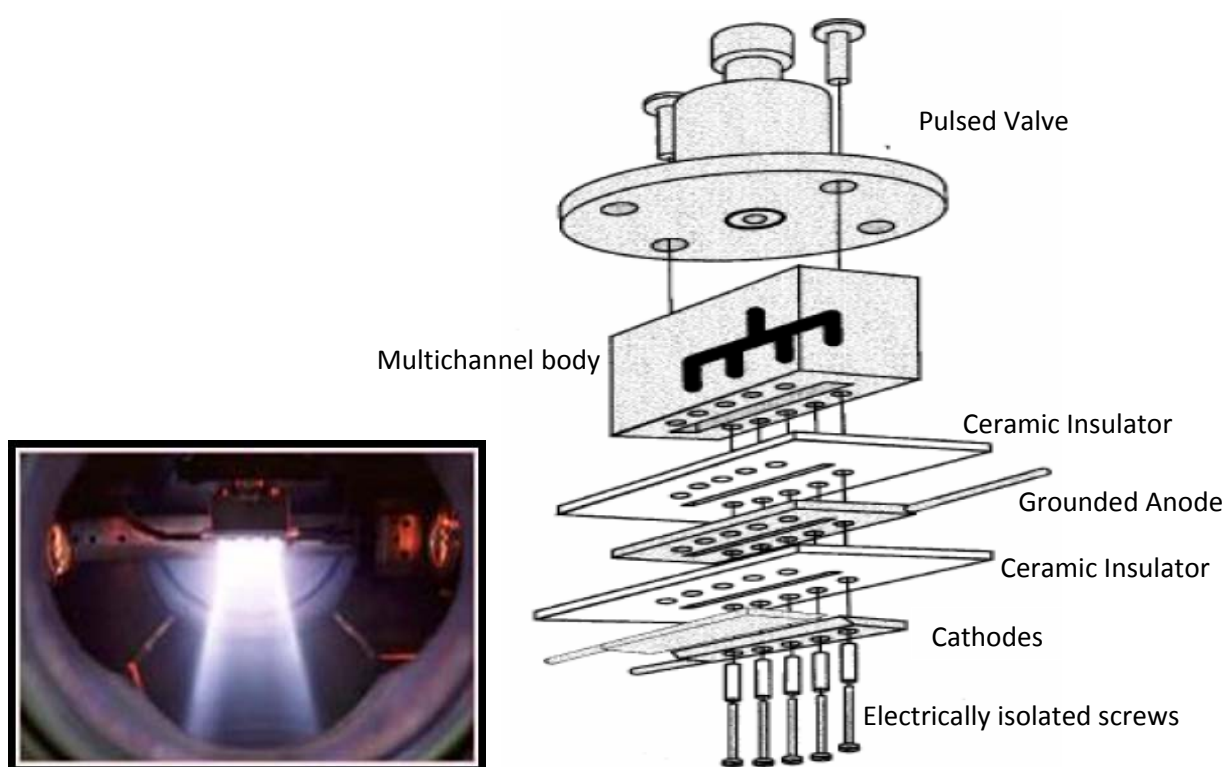


Figure 4.4: Schematic of the pulsed slit nozzle discharge.

The precursor ($C_2H_2/C_3H_4/C_4H_2/C_2D_2$) diluted in a buffer gas (0.3-1% in Ar/He or a mixture of both prepared in a gas mixing system, depending on the species of interest) is expanded through the body at typical backing pressures of 10 bar. Allene gas mixtures tend to cause graphite bridges on the stainless steel plates of the cathode, thus making the discharge unstable and sparking. This requires one to clean the discharge more often than with other precursors. The pressure in the vacuum setup is computer controlled and kept constant between 0.05-0.1 mbar during jet operation by adjusting

the pulse length of the valve ($\sim 350 \mu\text{s}$). This procedure significantly reduces fluctuations in the radical production. A 10 Hz, pulsed (0.3-300 μs) negative voltage of -400 to -1200 V (Velonex power supply) is applied to the both jaws via 4 k Ω ballast resistors (max. current 300 mA). The conditions of production vary for different molecules. The exact conditions for the radicals and ions studied in this work are mentioned in the corresponding chapters. The discharge is confined upstream of the supersonic expansion. This results in a much more efficient cooling as the localized discharge before the expansion does not interfere with the subsequent cooling in the expansion. The source is mounted on an XY translation system, and the distance between the slit and the probe can be varied from 0-11 mm to ensure the overlap of the plasma and the laser beam.

4.2.2. Laser Ablation

Following the suggestion by Douglas [23] that bare carbon chains comprising a handful or two of carbon atoms are good candidates as carriers of these absorptions—the diffuse interstellar bands (DIBs)—it took around 20 years to obtain a number of gas-phase electronic spectra in the laboratory [19]. Later, based on laboratory gas phase studies by Maier et al. [24, 25] it became evident that the abundance and oscillator strength of carbon chains up to 10 atoms are too small to account for the stronger DIBs. It was concluded that in order to be a DIB carrier, besides having electronic transitions in the visible, the oscillator strengths of the transitions have to be in the range 1-10. This applies for carbon chains with odd number of atoms, starting from C₁₅, C₁₇...

Nevertheless, neutral pure carbon chains are of astrophysical interest because electronic transitions of C₂ and C₃ have been observed in diffuse and translucent interstellar clouds [26]. In the infrared region, C₃ and C₅ have been detected in circumstellar shells of carbon-rich stars [27]. Thus, the goal has been to produce these pure carbon chains in enough abundance to be observable. This has been made possible by combining laser ablation with pulsed slit jet supersonic expansion. In contrast to discharge sources, laser ablation sources are implemented to maximize the yield of pure carbon chain radicals, especially long chains. But the combination of laser ablation with CRDS is not straightforward as instabilities occur due to the presence of soot particles in

the expansion [28]. However, the technique proves useful if one were to detect electronic spectra of metal containing clusters [29].

The ablation unit [30] works by the principle of laser vaporization of graphite. Figure 4.5 shows the basic diagram of the ablation unit. A target rod of 8 mm diameter and 50 mm length is rotated and translated to continuously expose a fresh surface to the ablation laser (30 mJ, 7 ns pulse, 10 Hz, 355 nm output neodymium-doped yttrium aluminium garnet; Nd:Y₃Al₅O₁₂ (Nd:YAG)) focused using cylindrical lens of 50 cm focal length onto the slit source of length 12 mm). The pulsed valve is connected to the ablation unit and controls the flow of gas over the target as the laser shots are fired. The vaporized graphite is flushed out adiabatically by pulses of He/ Ar buffer gas at background pressures of typically 10 bar and cross the interaction region on the basis of their masses. Thus, by varying the delay between the ablation and the probe laser, the species can be selected out. Within a few μ sec the temperature of the carbon vapor drops down from several thousand K plasma temperature to a few K rotational temperature of the condensed clusters. A roots blower unit keeps the chamber pressure below 10^{-1} mbar. The entire unit is mounted on an XY translation stage to optimize the alignment between the ablation and probe beams. The probe laser beam intersects the pulsed cluster jet of the laser ablation source around 4 mm downstream from the nozzle.

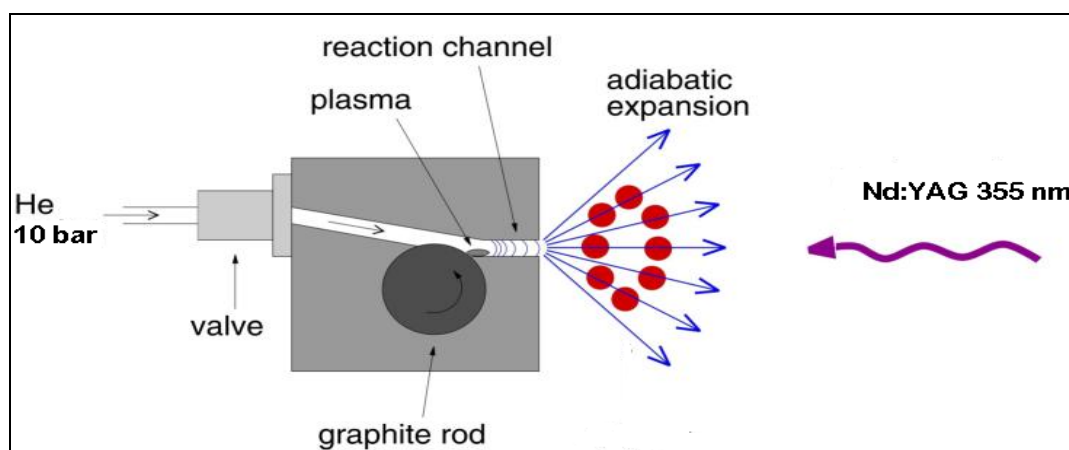


Figure 4.5: Schematic of laser ablation.

The current design enables better flow of buffer gas compared to the previous design [31] because of the elevated position of the pulsed valve, which leads to more efficient adiabatic expansion and cooling. The sensitivity of the present setup has been

tested to measure the electronic spectra of the origin and vibronic bands of the ${}^1\Pi_u \leftarrow X^1\Sigma_g^+$ transition of C_5 in the gas phase (Appendix B).

4.3. Source Chamber and Vacuum System

The source chamber consists of a large stainless steel cross piece (30 cm diameter, 20 dm³ capacity). The vacuum system comprises of an Edwards model water cooled mechanical booster roots pump (EH2600) backed by a rotary pump (Edwards E2M175), with a total pumping capacity of 500 m³/h. The pressure attained inside the chamber without the plasma is 10⁻³ mbar, which increases to 10⁻² mbar during experimental conditions. It is monitored using a Pirani type pressure gauge (Thermovac TM20) and fed through a feedback system to the computer for control of the pulsed valve. The stability of the discharge/ablation can be monitored visually through the pyrex windows installed on opposite/adjacent sides the cross piece. The slit discharge source is set on the top of the chamber while the ablation unit is attached to the front side. In case of ablation, the Nd:YAG laser is incident via the back side of the chamber. Better stability of the plasma expansion was achieved by evacuation from the bottom of the cross piece than with the previous configuration in which the chamber was evacuated from the back side.

4.4. Light Sources

Pulsed tunable dye lasers pumped by frequency doubled/ tripled solid state Nd:YAG lasers are used for both CRD and FWM experiments. A laser pumped pulsed dye laser provides tunable ultra narrow frequency pulsed output over wavelengths ranging from 190 nm to 4.5 μ m (the extended frequencies being produced by sum-difference frequency mixing of the basic frequency range, 380-900 nm) using either a dispersive element (prism) within the cavity or a variable-frequency high variable-frequency high reflector (diffraction grating) as one of the mirrors of the cavity. The diffraction grating has higher dispersion than a prism and therefore offers more precise wavelength. The combination of a diffraction grating in the Littrow mounting configuration with an intracavity beam-expanding telescope and a tilted Fabry-Perot intra-cavity etalon provides additional frequency selectivity.

The dye laser is side-pumped by a pulsed pump laser to produce a narrow-stripe gain medium in the gain cell. The pulsed output from the high-gain laser medium is expanded with the beam-expanding telescope to produce a wide collimated beam arriving at the high-dispersion diffraction grating that serves as a reflecting mirror for the laser cavity. The fine tuning is achieved by rotating the diffraction grating. Figure 4.6 shows a basic dye laser configuration where the pump beam is split off into several separate beams. One beam is used to pump a narrow-frequency-output tunable oscillator containing the beam expander, grating, and etalon. The other beams are used to either side pump or end pump a series of dye amplifiers. The use of two prisms/gratings provides more dispersion than a single prism/grating. The basic electronic energy levels of a typical laser dye and the processes involved are depicted in Figure 4.7.

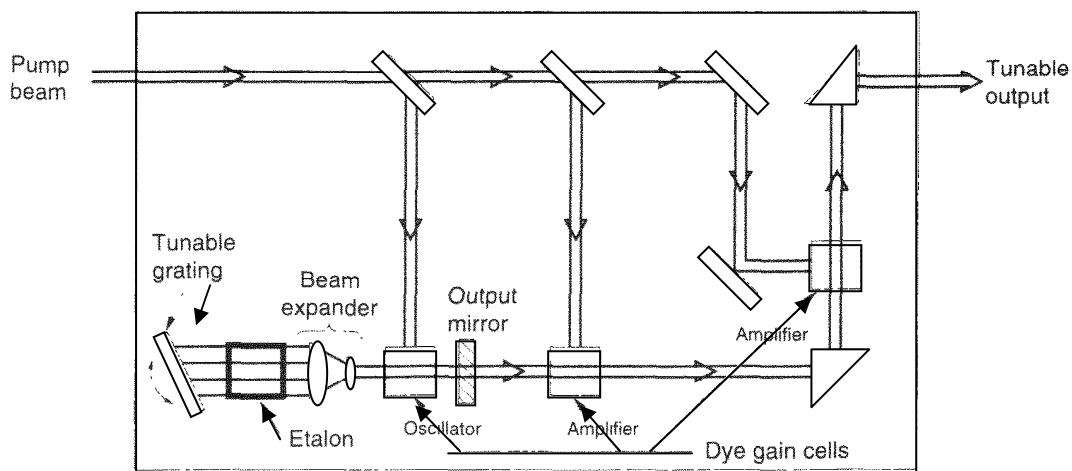


Figure 4.6: Schematic of a pulsed dye laser [32].

The tunable laser systems include a 7 ns, 20 Hz double grating pulsed dye laser (Sirah *Cobra-Stretch*TM) and a single grating SCANmateTM 2E laser from Lambda Physik (with an intracavity etalon) which offer tuning ranges from 370-900 nm and 340-900 nm respectively. In most cases, methanol is used as the dye (Coumarine, Rhodamine etc.) solvent whereas in the UV (Exalite), p-Dioxan is used. Typically, the amplifiers of the Sirah and the SCANmate require a solvent dilution of 8 and 3 times that in the oscillator cell, respectively. The dye lasers are pumped by the 355/532 nm output of water cooled Q switched Nd:YAG lasers (Innolas, SpitlightTM 600) with about 120 mJ energy. Care should be taken to align the pump beams properly so as not to burn the

quartz dye cuvette. The resulting power depends strongly on the used dye, its range and the alignment of the pump and the dye laser. Typical values lie between 1-5 mJ in the visible and 10 mJ in the UV. The linewidth of the Sirah is 0.06 cm^{-1} while that of the SCANmate 2E is 0.15 cm^{-1} . With the etalon, the linewidth can be reduced to 0.04 cm^{-1} .

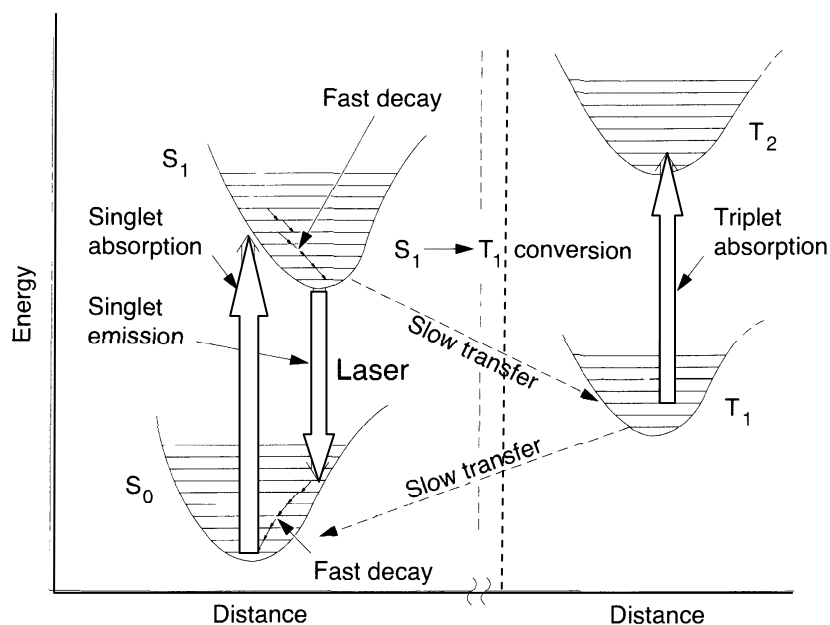


Figure 4.7: Electronic energy level diagram of a typical laser dye [32].

The Sirah control is programmed with Lab View and the communication with the laser is established through a USB to RS232 adapter. The grating configuration and wavelength can be set using this program provided it is within the accessible wavelength range. The residual wavelength discrepancies between the laser and the experiment can also be compensated using the control program. Changing the dye usually requires a slight realignment of the laser. The SCANmate is tuned by the diffraction grating, and communicated with the PC via a multimode optics fiber interface. The commands are sent by the *scanmate.exe* DOS program. The wavelength scans are controlled by the *lcmeter* program which also calculates positions of the grating and the etalon. Etalon scans require manual finding of the etalon's normal position where the alignment is optimized by looking at the laser light on a sheet of white paper. The flash lamps and Q switch of the solid state Nd:YAG lasers are usually externally triggered using a pulse/delay generator (BNC Model 575) for better control of timings between the various components of the experimental system. The Nd:YAG

output can be controlled varying the delay between the flashlamp and the Q switch. The typical delays for the Spotlight Nd:YAG laser system are 215 -280 μs .

4.5. Signal Detection

The light detectors used in the experiments include photodiodes (PD) and photomultiplier tubes (PMT). A photovoltaic detector generates a photo induced voltage upon illumination. In the non illuminated diode, the diffusion of electrons from the n region to the p region generates a space charge, which results in the diffusion voltage V_D and a corresponding electric field across the p - n junction. When the detector is illuminated, electron-hole pairs are created by photon absorption within the p - n junction. The electrons and holes are driven by the diffusion voltage into the n and p regions respectively. This leads to a decrease of the diffusion voltage, which appears as the photo-voltage $V_{ph} = \Delta V_D$ (Figure 4.8). A broad band UV-VIS-NIR silicon photodiode (ST336-44BQ Hamamatsu) is used as the light detector. The sensitivity of the diode is in the range 190-1100 nm and the active area was 3.6 mm^2 . The output of the diode is amplified using a low noise LM6365 amplifier of 10 MHz bandwidth.

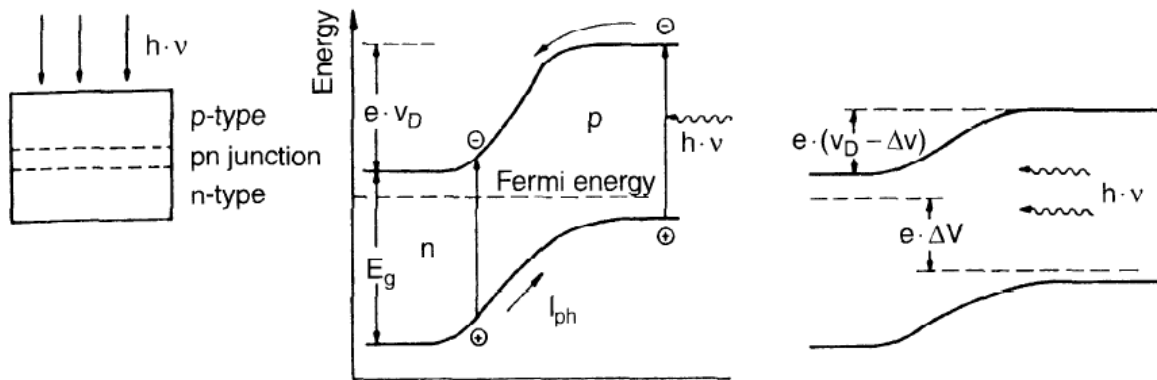


Figure 4.8: Schematic diagram of a photovoltaic diode showing generation of electron-hole pairs upon photon absorption [32].

On the other hand, photomultipliers are a better choice for detection of low light levels, as in FWM. They internally amplify the photocurrent using secondary electron emission from internal dynodes to multiply the number of photoelectrons. The photoelectrons emitted by the cathode are accelerated by the applied voltage and are focused on the metal surface of the first dynode where each impinging electron releases q secondary electrons, which then produce tertiary electrons and so on (Figure 4.9).

Each photoelectron in a photomultiplier with N dynodes produces a charge avalanche at the anode of $Q = q^N e$ and a corresponding voltage pulse of $V = Q/C$ where C is the capacitance of the anode. The present setup uses a 12 stage Hamamatsu H3177-50 with an effective area of 46 mm^2 . The PMT has a spectral response between 190-650 nm. A $10 \mu\text{m}$ pinhole is used to spatially filter the output beam.

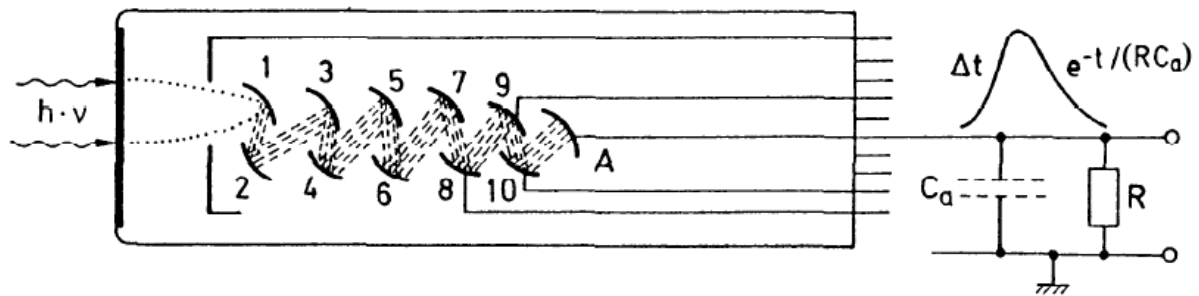


Figure 4.9: Photomultiplier with output voltage pulse induced by an electron avalanche [32].

The output from the detectors is recorded directly on the computer or sent to a fast oscilloscope (LeCroy Waverunner 44Xi, 400 MHz, 5GS/s) for the accumulation and digitization of the data.

4.6. Experimental Arrangement

4.6.1. Cavity Ring-down Spectroscopy

As mentioned before, the CRDS setup essentially has a high finesse optical cavity, formed by two plano-concave dielectrically coated mirrors (Layertec/LGR/Research Electro-optics, $R > 99.99\%$, radius of curvature 1m, diameter 7.5 mm) facing each other separated by a length of 52 cm. To protect the mirrors from dust and other plasma impurities, helium curtains of 0.02 mbar pressure are flown through each mirror holder. These mirrors are cleaned using drops of optical grade iso-propanol or methanol. Typical ring-down time obtained in the visible region is around $25 \mu\text{s}$. Figure 4.10 shows the experimental arrangement of CRDS coupled with a discharge source. The tunable radiation is spatially filtered and focused into the cavity using a 1:1 telescope with a $50 \mu\text{m}$ pinhole.

To align the cavity, initially both mirrors are removed and the focused laser beam is centered at the middle of the mirror diaphragms and aligned parallel to the optical axis of the mirrors. The rear mirror is attached, and the reflection from this

mirror made to return along the same path as the incident beam. Next, the front mirror is aligned in a similar way.

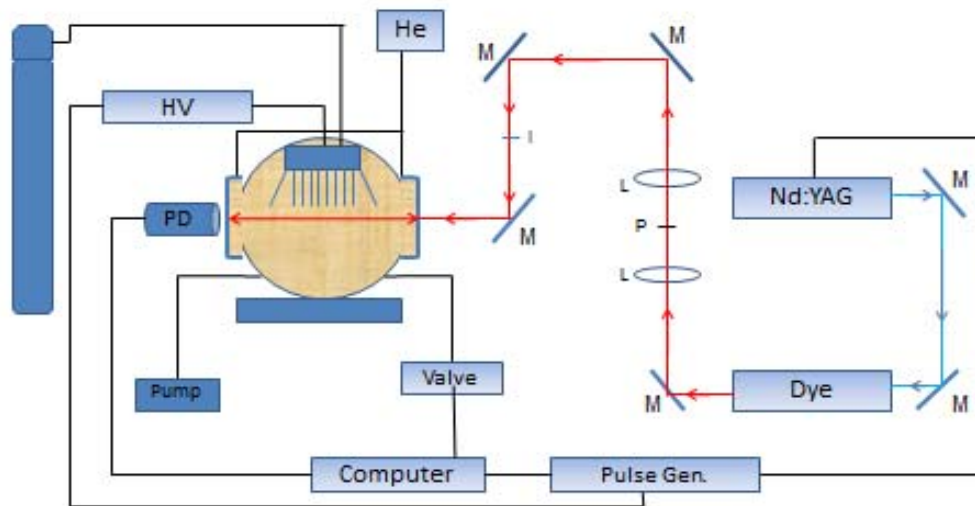


Figure 4.10: Experimental configuration-cavity ring-down coupled with electric discharge. M: Mirror, P: Pinhole, L: Lens, I: Iris.

Once this is done, one should be able to detect the ring down signal, which is detected using the amplified coupled broad band UV-VIS-NIR Si photodiode. The final alignment is done after the chamber is evacuated by adjusting the threaded screws on the mirror mounts. The data acquisition and analysis is computer controlled using Lab View, which is also used to operate the lasers. Typically 45 ring-down events are averaged at each wavelength before iteratively fitting to an exponential function of the form

$$f(t) = Ae^{-Bt} + C, \quad (4.5)$$

where A is the amplitude of the signal, B is the decay rate and C the offset. The discharge/ ablation is turned off every alternate pulse to record the ring-down times with the plasma on and off. The final ring-down data points are sent to the program *lcmeter* together with the corresponding wavenumber of the laser. The absolute wavelength calibration is achieved by a wavelength meter (High Finesse/Angstrom, WS7, 350-1120 nm, 150 Hz measurement speed) with an accuracy of 0.002 cm^{-1} . A

fraction of the laser beam is deflected by a beam splitter onto a collimator. The light is coupled to a single mode fiber which is connected to the wavelength meter. The data is transferred to the PC via a USB interface. The device can also be used to measure the line width of the laser beam. Narrow band filters are used to cut off the plasma emissions and decrease the amplified spontaneous emission level.

The computer uses the master trigger signal to trigger the digital pulse generator and the pulsed valve which opens for typically $350\ \mu\text{s}$. This is automatically adjusted depending on the pressure kept inside the vacuum chamber which is given by the feedback signal from the pressure gauge. The actual gas expansion through the slit however amounts to about $1200\ \mu\text{s}$. The delay generator provides the synchronization for the probe laser and discharge/ablation laser. The width of the discharge pulse is of the order of $100\ \mu\text{s}$ (the ablation pulse is 7ns long), and comes $600\text{-}1000\ \mu\text{s}$ after the electric pulse opening the valve. The discharge/ablation laser pulse is fired before the probe laser and continues at least to the end of the ring-down signal. The time sequence of operation for the discharge experiment is shown in Figure 4.11.

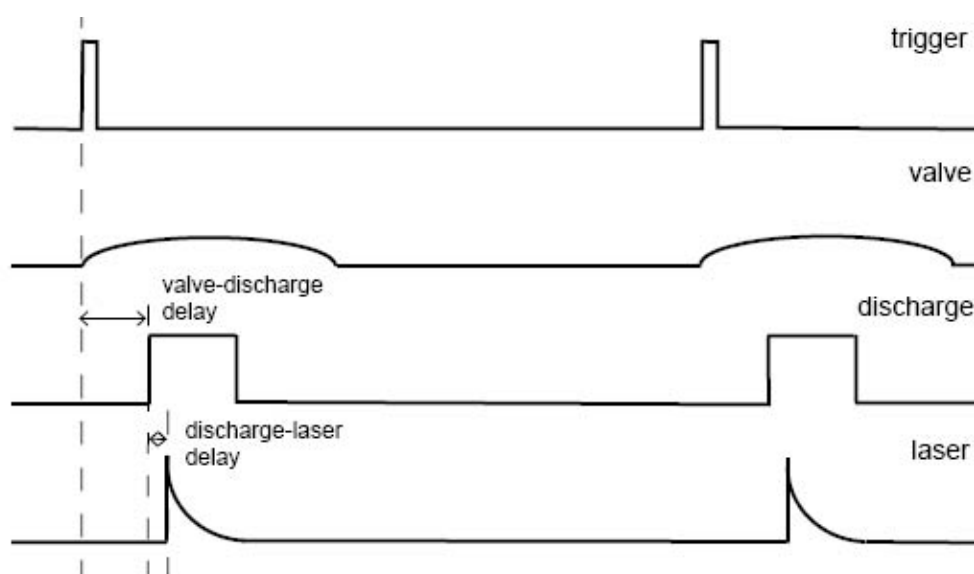


Figure 4.11: Timing sequence of operation for the discharge experiment.

4.6.2. Four-wave Mixing Spectroscopy

The DFWM configuration opted for was a forward BOXCARS scheme (Figure 4.12) for which virtually all signal photons are collected. The mirrors of the CRD setup are replaced by optical windows of 1" diameter. As can be noted from the figure, the

experimental configuration consists of the Sirah dye laser pumped by the third harmonic of the Nd:YAG laser. The beam is spatially filtered to obtain a homogenous profile using a 1:1 telescope with a 50 μm pinhole and collimated to a beam diameter of 1 mm at the interaction region. Neutral density filters are inserted in the path of the probe laser beam to decrease the pulse energy to around 100 μJ . The laser beam is divided into three components of equal intensity (with 70/30 and 50/50 beam splitters) that are reflected by broadband mirrors and are focused by a 1000 mm focal length lens into the vacuum chamber. A pump crossing angle of approximately 1.5° and a beam diameter of ~ 2 mm before the lens define an interaction region of ~ 30 mm, therefore making use of the whole slit expansion length. Because the signal beam created by the FWM process is coherent in nature, it is efficiently rejected against stray or scattered radiation by the use of spatial filters, irises, and a long path length of 4 m from the interaction region to the photomultiplier tube. This enables the recording of background-free spectra with a high signal-to-noise (S/N) offering both high sensitivity and precise line positioning. The data collection and digitization is carried out by the 400 MHz oscilloscope and transmitted to the PC via GPIB interface. The signal was averaged for 2 to 3 s, equivalent to 40-60 laser shots. The probing time of the DFWM technique is equal to the laser pulse duration (7 ns). All experiments with FWM presented in this work have been done employing the discharge source.

The probing duration of DFWM offers the possibility of using short but intense high-voltage pulses while maintaining appropriate generation conditions. The application of a pulse in the submicrosecond range, however, has a drastic effect on the temporal distribution of the radicals in the molecular beam which makes the technique far better than CRDS in terms of selectivity. Details about this aspect can be found in chapter 7. The timings between the gas pulse, discharge and the probe laser are optimized using the pulse/delay generator depending on the species studied, which also provides the trigger to the oscilloscope. Frequencies are calibrated using a wavelength meter.

In contrast to CRDS, the alignment procedure of DFWM is more tedious and time-consuming. Masks with holes at the four corners and center of a rectangle are positioned along the optical axis of the cavity using a He-Ne diode beam. The split incident beams are then aligned to pass through the three corners of both the masks.

Now, the lens of 1000 mm focal length is positioned in place of the first mask. The beams should pass through the window into the cavity at this stage. To ensure the spatial overlap of beams at the interaction region, a 50 μm pinhole is positioned at the middle of the chamber and the incident beams made to pass through it. Further alignment is then performed by positioning a thin quartz cell containing a dye (absorber) in the interaction region. Once the signal is optimized using the dye cuvette, the chamber is evacuated and the spectroscopic measurements carried out. Recently, motorized mirror mounts have been proposed for better alignment of the setup.

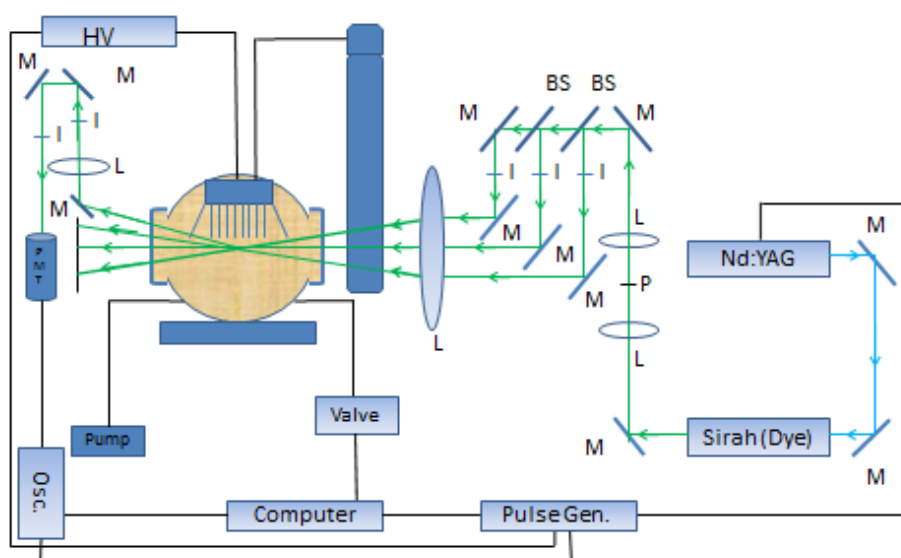


Figure 4.12: Schematic-degenerate four-wave mixing. M: Mirror, P: Pinhole, L: Lens, I: Iris, BS: Beam Splitter.

Figure 4.13 shows the schematic diagram for two-color resonant four-wave mixing (TCRFWM). Instead of the degenerate beams in the DFWM setup, the technique utilizes two pump beams of the same frequency, and a probe (DUMP) of different frequency. The probe is scanned in frequency in a SEP or UP fashion keeping the pump laser at a fixed wavelength. For the TCRFWM experiments, the pump beams are chosen so that the interference fringes are directed along the jet to avoid washing out of the gratings by the gas flow and, consequently, a decreased signal beam [33]. The pump and probe beams are produced by outputs of two dye lasers (Sirah, SCANmate 2E-Lambda Physik) and are collimated before being directed to the interaction region. Masks are

used to position the three beam crossing angles to satisfy the phase matching condition. The rest of the alignment procedure follows as in DFWM. The delay between the two lasers, the triggering of the valve and the discharge are controlled by the delay generator.

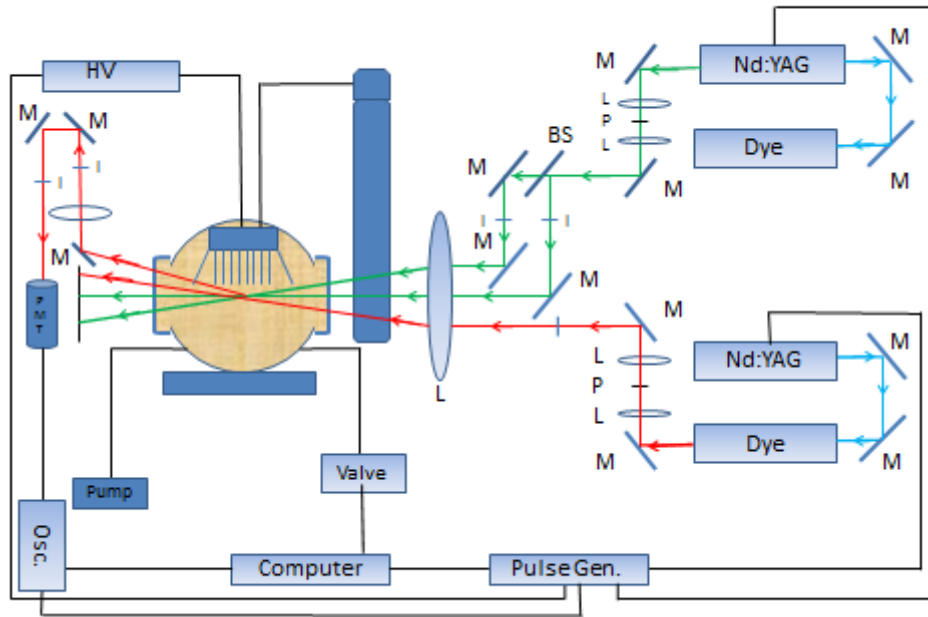


Figure 4.13: Schematic-two color resonant four-wave mixing. M: Mirror, P: Pinhole, L: Lens, I: Iris, BS: Beam Splitter.

Bibliography

- [1] Levy, D. H. *Ann. Rev. Phys. Chem.* 31, 197, **1980**.
- [2] Engelking, P. C. *Chem. Rev.* 91, 399, **1991**.
- [3] Hollas, J. M.; Phillips, D. *Jet Spectroscopy and Molecular Dynamics: Chapman & Hall: London: 1995*.
- [4] De Leeuw, J. H. *Rarefied Gas Dynamics, 4th Symp.: Academic Press: New York: 1966*.
- [5] Anderson, J. B.; Fenn, J. B. *Phys. Fluids* 8, 780, **1965**.
- [6] Becker, M.; Fiebig, M. *Rarefied Gas Dynamics, 9th Symp. DFVLR Press: Porz- Wahn: 1974*.
- [7] Kantrowitz, A.; Grey, J. *Rev. Sci. Instrum.* 22, 328, **1951**.
- [8] Kistiakowsky, G. B.; Slichter, W. P. *Rev. Sci. Instrum.* 22, 333, **1951**.
- [9] Hagena, O. F. *Surf. Sci.*, 106, 101, **1981**.
- [10] Droege, A. T.; Engelking, P. C. *Chem. Phys. Lett.* 96, 316, **1983**.
- [11] Engelking, P. C. *Rev. Sci. Instrum.* 57, 2274, **1986**.
- [12] Sulkes, M.; Jouvett, C.; Rice, S. A. *Chem. Phys. Lett.* 87, 515, **1982**.
- [13] Busarow, K. L.; Blake, G. A. ; Laughlin, K. B.; Cohen, R. C.; Lee, Y. T.; Saykally, R. J. *Chem. Phys. Lett.* 141, 289, **1987**.
- [14] Nesbitt, D. J. *Chem. Rev.* 88, 843, **1988**.
- [15] Veeken, K.; Reuss, J. *Appl. Phys. B.* 38, 117, **1985**.
- [16] Tanaka, K.; Sumiyoshi, Y.; Ohshima, Y.; Endo, Y.; Kawaguchi, K. *J. Chem. Phys.*, 107, 2728, **1997**.
- [17] Dong, F.; Uy, D.; Davis, S.; Child, M.; Nesbitt, D. J. *J. Chem. Phys.* 122, 224301, **2005**.
- [18] Van Orden, A.; Saykally, R. J. *Chem. Rev.* 98, 2313, **1998**.
- [19] Jochnowitz, E. B.; Maier, J. P. *Mol. Phys.* 106, 2093, **2008**.
- [20] Thaddeus, P.; McCarthy, M. C. *Spectrochim. Acta, Part A.* 57, 757, **2001**.
- [21] Davis, S.; Anderson, D. T.; Duxbury, G.; Nesbitt, D. J. *J. Chem. Phys.* 107, 5661, **1997**.
- [22] Anderson, D. T.; Davis, S.; Zwier, T. S.; Nesbitt, D. J. *Chem. Phys. Lett.* 258, 207, **1996**.
- [23] Douglas, A. E. *Nature* **269**, 130, **1997**.

- [24] Maier, J. P.; Walker, G. A. H.; Bohlender, D. A. *Astrophys. J.* 566, 332, **2002**.
- [25] Maier, J. P.; ; Walker, G. A. H.; Bohlender, D. A. *Astrophys. J.* 602, 286, **2004**.
- [26] Haffner, L. M.; Meyer, D. M. *Astrophys. J.* 453, 450, **1995**.
- [27] Bernath, P. F.; Hinkle, K. H.; Keady, J. J. *Science*, 244, 562, **1989**.
- [28] Motylewski, T.; Vaizert, O.; Giesen, T. F.; Linnartz, H.; Maier, J. P. *J. Chem. Phys.* 111, 6161, **1999**.
- [29] Apetrei, C.; Knight, A. E.; Chasovskih, E.; Jochnowitz, E. B.; Ding, H.; Maier, J. P. *J. Chem. Phys.* 131, 064305, **2009**.
- [30] Neubauer-Guenther, P.; Giesen, T. F.; Berndt, U.; Fuchs, Fuchs, G.; Winnewisser, G. *Spectrochim. Acta, Part A.* 59, 431, **2002**.
- [31] PhD thesis, Chauhan, R. *University of Basel*, **2010**.
- [32] Demtröder, W. *Laser Spectroscopy, Basic Concepts and Instrumentation: Springer-Verlag: Berlin: 1981*.
- [33] PhD thesis, Achkasova, E. *University of Basel*, **2007**.

Chapter 5

Electronic Spectra of Gas Phase Hydrocarbons by Cavity Ring-down Technique

5.1 Introduction

This chapter presents the gas phase electronic spectra of C_6H^+ [1], HC_4H^+ [2] and $C_6H_3^+$ [1]. In the case of C_6H^+ , this is the first detection in the gas phase.

In connection with the astronomical observation of absorption features through diffuse interstellar clouds [3], the measurement of the electronic spectra in the gas phase of carbon chains and their simple derivatives including H, N, and O has been a goal. After the proposal by Douglas that bare carbon chains comprising a handful or two of carbon atoms are good candidates as carriers of these diffuse interstellar bands (DIBs) [4], it took around 20 years to obtain a number of gas phase electronic spectra in the laboratory [5]. Thus it became possible for the first time to make a direct comparison with the astronomical data under comparable conditions: collision free environment and low, 10-30 K temperatures. This was achieved in the laboratory by producing the species in high voltage discharge supersonic expansions, coupled with sensitive laser methods such as cavity ring-down absorption, frequency modulation techniques and resonant multiphoton ionisation approaches [6].

Important milestones were the observations of the neutral carbon chains C_4 , C_5 , and of their hydrogen derivatives, C_nH , the latter being well known constituents of dark interstellar clouds, identified by mm wave astronomy. The species were selected because they have electronic transitions in the visible region of the spectrum, where the DIBs are observed.

In all these cases, the comparisons with the DIB data were negative, leading to upper limits of column densities of around 10^{12} cm^{-3} . Only in the case of C_3 could very weak interstellar absorptions be detected and the species unambiguously identified in the diffuse medium [7]. The analysis of this data led to the conclusion that Douglas'

hypothesis [4] is now excluded; the carbon chains comprising up to a dozen or so atoms or their hydrogen containing analogues C_nH cannot be the carriers of the stronger DIBs [8]. In turn the analysis pointed to future studies of potential carriers; apart from having electronic transitions in the optical regions, the oscillator strengths would have to be two orders of magnitude larger than for the afore-mentioned chains. Examples of such systems are the carbon chains with odd number of atoms, starting with C_{15} , C_{17} ...

Interest in polyacetylene cation species stems from the observation of hydrocarbons in combustion and interstellar environments [9-12]. In terms of astrophysical relevance, polyacetylene chains are often speculated as being possible carriers of the unidentified absorptions in diffuse interstellar clouds. In particular, diacetylene is one of the largest molecular species identified in planetary atmospheres [13] and is also considered as a precursor to larger hydrocarbons in interstellar environments [14]. Recently, diacetylene cation was suggested as a DIB carrier [15], but the claim was soon refuted [16].

5.2. Experimental

Details on the experimental set-up can be found in chapter 4 of this thesis. The spectra have been recorded by the pulsed cavity ring-down technique using a supersonic expansion of plasma from a slit nozzle discharge. The molecules were produced in a pulsed supersonic plasma which was generated by discharging a mixture of 1% HCCH (for C_6H^+ and $C_6H_3^+$) or 0.5% C_4H_2 (for HC_4H^+) diluted in argon or helium. The slit used was $30 \times 1 \text{ mm}^2$. The applied voltage was in the range of 600-900 V while the backing pressure was kept around 11 bar. The average pressure in the vacuum chamber was 0.07 mbar for C_6H^+ and HC_4H^+ , and 0.15 mbar for $C_6H_3^+$. Typical ring-down time was 20 μs . A dye laser with 0.06 cm^{-1} running at 20 Hz was used and the wavelength was calibrated with a wavemeter.

5.3. C_6H^+

The electronic band systems of the C_n^+ and C_nH^+ cations have hitherto not been obtained in the gas phase because of technical difficulties. A few measurements of the electronic transitions have been achieved in neon matrices, namely for C_n^+ $n=6-9$ [17], and C_nH^+ $n=6, 8$ [18]. Apart from the fact that these species have electronic band systems in the

visible region, both theory and the experiments in matrices indicate that the oscillator strengths are larger than for the neutral species. In this work, the measurement of the ${}^3\Pi - {}^3\Pi$ transition of C_6H^+ in the gas phase near 19486 cm^{-1} is reported. The identification follows by comparison with the matrix data, the partial resolution of the rotational structure and changes upon deuteration. Partially resolved lines in the P branch and observation of band heads permitted a rotational contour fit. Spectroscopic constants in the ground and excited-state were determined.

5.3.1. Results and Discussion

The energy region searched was based on the observation made in neon matrices, where the origin band of the $(1) {}^3\Sigma^- - X {}^3\Sigma^-$ transition of mass-selected C_6H^+ was identified at 19387 cm^{-1} [18]. The corresponding band was observed in the gas phase around 19486 cm^{-1} , as can be shown in Figure 5.1. The top trace shows the actual recording, accumulated in several scans. Apart from the band showing resolved rotational peaks in the P-branch at lower energies, the dominant features overlapping are C_2 lines ($a^3\Pi_g - a^3\Pi_u$). The middle trace shows the resulting spectrum when the C_2 lines are removed and the baseline is corrected. The C_2 peaks (synthetic spectrum shown in bottom trace) were subtracted after fitting by a Voigt line shape of variable width, amplitude and baseline, including both Lorentzian and Doppler line broadening mechanisms. The band is blue-shifted by 99 cm^{-1} from the neon matrix value, similar to the 142 cm^{-1} change observed for the C_6H ${}^2\Pi - {}^2\Pi$ electronic transition [19, 20]. Both systems have similar characteristics involving $2\pi^4 3\pi^3 \rightarrow 2\pi^3 3\pi^4$ for C_6H and $2\pi^4 13\sigma^2 3\pi^2 \rightarrow 2\pi^3 13\sigma^2 3\pi^3$ orbital configuration for C_6H^+ with the same π electron being excited.

To confirm that the detected band is due to C_6H^+ , the following measurements were carried out. The absorption spectrum recorded in the 6 K neon matrix displays three main transitions ($6_0^1, 5_0^1, 4_0^1$) to excited vibrational levels in the upper electronic state [18]. Of these, the most intense 4_0^1 is displaced by 1903 cm^{-1} to higher energy relative to the origin band, with a quarter of its intensity. Thus, a corresponding band was searched for in the gas phase and found at 21402 cm^{-1} , showing the same band profile as seen in Figure 5.1. The energy difference between the 0_0^0 and 4_0^1 bands in the

gas phase is 1916 cm^{-1} . Though the absolute neon-gas shifts are large, it is known that the vibrational frequencies generally lie within a few cm^{-1} [21]. The second set of measurements involved using deuterio-acetylene in the discharge. An absorption band of the same profile characteristics as the one seen in Figure 5.1 was detected at 19538 cm^{-1} , shifted 52 cm^{-1} to higher energy relative to C_6H^+ . This is comparable to the $51(2)\text{ cm}^{-1}$ displacement observed for the $\text{C}_6\text{H}/\text{C}_6\text{D}$ pair [18]. The corresponding blue shift in the neon matrix for the cation is 38 cm^{-1} (Table 5.1) upon deuteration. Figure 5.2 shows the experimentally obtained $4\frac{1}{6}$ vibronic and $0\frac{0}{0}$ deuterated band systems of C_6H^+ .

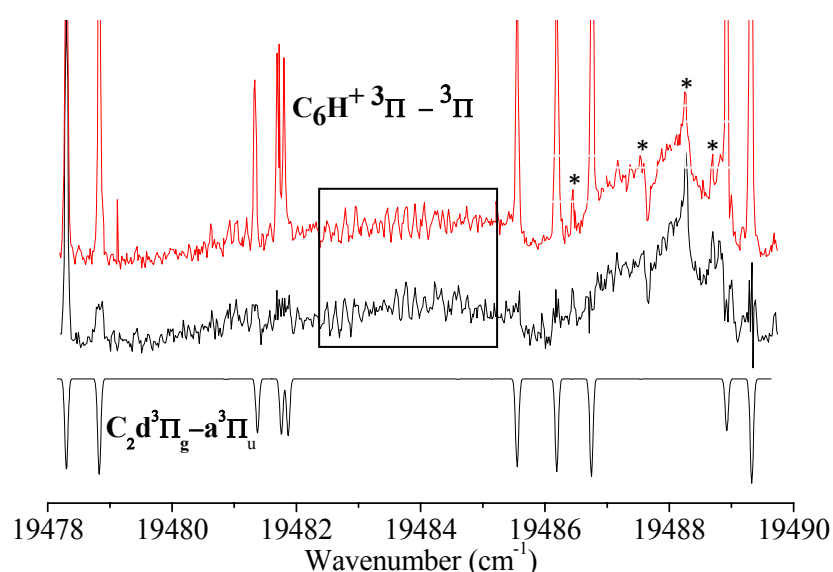


Figure 5.1: Absorption spectrum of C_6H^+ in the gas-phase recorded by a pulsed cavity ring-down method. The middle trace shows the C_2 lines subtracted. The box and asterisks indicate partially resolved P lines, and R-band heads and Q branch respectively.

As can be seen in Figure 5.1, the spectrum displays three band heads along with a distinct protrusion near 19486 cm^{-1} and a band head like feature at 19487 cm^{-1} . It should be noted that the presence of the three R-band heads (at the higher energy end) readily differentiates the spectrum from the absorptions belonging to a band within the ${}^2\Pi - {}^2\Pi$ system of C_6H which are seen throughout this wavelength region [20]. Furthermore, the assignment to a band within the ${}^3\Sigma^- - X{}^3\Sigma^-$ transition of C_6 , with observed origin at 19558 cm^{-1} in a neon matrix [19] is excluded as the rotational spacing would be roughly twice as large as between the lines for C_6H^+ because of nuclear spin statistics.

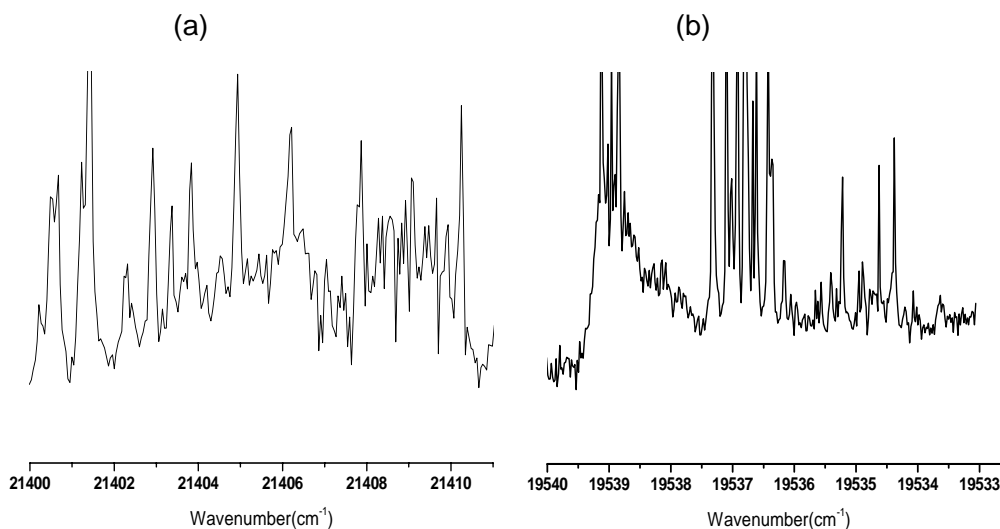


Figure 5.2: Absorption spectra of (a) 4_1^1 vibronic and (b) 0_0^0 deuterated bands of C_6H^+ .

Radical	Vibrational band	Ne Matrix	Gas Phase T_{00}	Shift
l- C_6H^+	0_0^0	19387(8) [18]	19486(1)	-99
	4_1^1	21290(8) [18]	21402(1)	-112
l- C_6D^+	0_0^0	19425(8) [18]	19538(1)	-113
l- C_6H	0_0^0 ${}^2\Pi - {}^2\Pi$	18854(5) [19]	18996(1) [20]	-142
	6_3^1 ${}^2\Pi - {}^2\Pi$	19512(5) [19]	19649(1) [20]	-137
l- HC_6H^+	0_0^0 ${}^4\Pi_u - {}^4\Pi_g$	16535(5) [22]	16654(1) [23]	-119

Table 5.1: Frequencies (cm^{-1}) measured in a neon matrix and in the gas-phase for the ${}^3\Pi - X {}^2\Pi$ electronic transition of C_6H^+ and C_6D^+ . Previously published data for linear C_6H and HC_6H^+ electronic transitions are also given.

An electronic state diagram of C_6H^+ is depicted in Figure 5.3, showing the lowest energy observed transitions. In connection with the study of the electronic absorption of C_6H^+ in the neon matrix, it was suggested that the transition being observed was

${}^3\Sigma^- - X{}^3\Sigma^-$. The first argument for this was that C_6H^+ and C_6 are isoelectronic and the ${}^3\Sigma^- - X{}^3\Sigma^-$ transition of the latter was located in a neon matrix with origin band at 19558 cm^{-1} . However, CASSCF calculations, the results of which are given in reference [18], show that the ${}^3\Pi$ state arising from the $2\pi^413\sigma^13\pi^3$ configuration lies just 0.04 eV lower than the ${}^3\Sigma^-$ ($2\pi^413\sigma^23\pi^2$) and would thus be the ground state of C_6H^+ . Furthermore, the ${}^3\Pi - {}^3\Pi$ system at $T_v = 2.36\text{ eV}$ is strong (transition moment $TM = 3.2\text{ D}$). On the other hand higher level RCCSD(T)/cc calculations indicated a preference for ${}^3\Sigma^-$ as the ground state (with ${}^3\Pi$ lying 0.33 eV higher) and that the transition is ${}^3\Sigma^- - X{}^3\Sigma^-$ at $T_0 = 2.77\text{ eV}$ with $TM = 1.48\text{ D}$. The ${}^3\Pi - {}^3\Sigma^-$ transition is predicted at 2.24 eV but is very weak ($TM = 0.03\text{ D}$). Consequently the choice of ${}^3\Sigma^- - X{}^3\Sigma^-$ for the absorption system in the neon matrix was proposed [18].

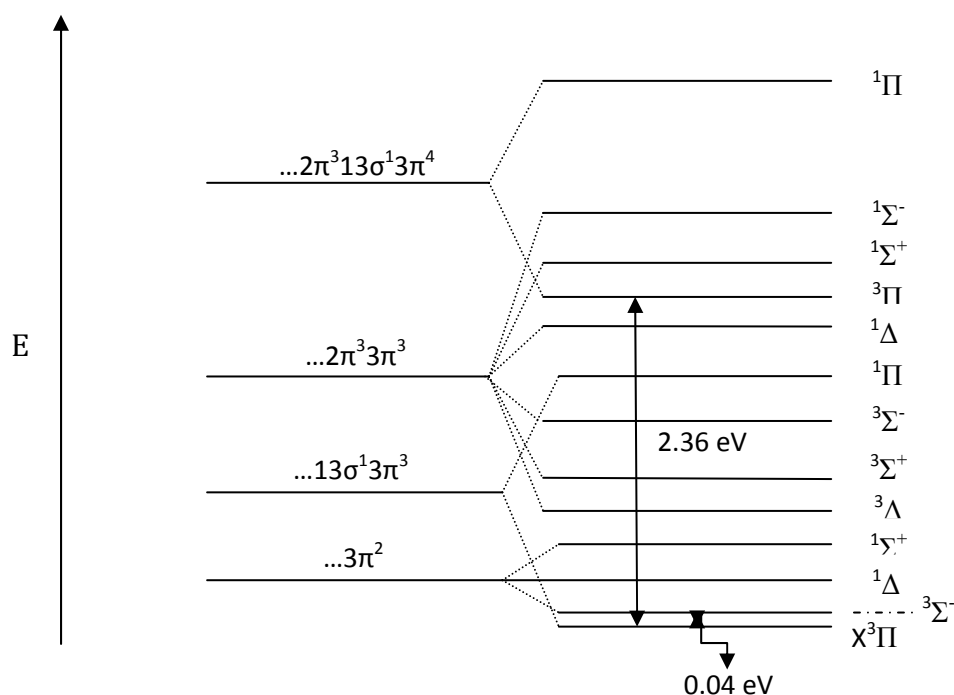


Figure 5.3: Electronic state diagram of C_6H^+ .

Thus, in the analysis of the rotational structure and contour of the gas-phase band seen in Figure 5.1, it was initially assumed that the band has ${}^3\Sigma^- - {}^3\Sigma^-$ symmetry. A simulation of the rotational features was undertaken using PGOPHER [24]. The optimized calculated ground state geometry, as given in [18], was used for the $X^3\Sigma^-$

ground state in the first instance and the constants in the excited ${}^3\Sigma^-$ state were the parameters, in addition to the rotational temperature. A second iteration was made by slightly varying the lower state B" constant as well. Ambiguity in the fit is caused by the lack of sufficient number of resolved rotational lines (mainly observed in the P-branch). For the final fit the ground state rotational constant value was also then used as parameter. However, the simulation failed to reproduce important features in the spectrum, as can be seen in Figure 5.4. Specifically, the peak at 19486.5 cm^{-1} labeled as Q-head above the experimental trace, is not seen, neither the prominent dip at 19487.6 cm^{-1} . Thus, it was then considered whether the transition could be of ${}^3\Pi - {}^3\Pi$ or ${}^3\Sigma^- - {}^3\Pi$ symmetry. The same procedure was followed in the simulations as above, using the calculated geometry for the lowest lying ${}^3\Pi$ state also given in [18]. A ${}^3\Pi - {}^3\Sigma^-$ transition would result in three well separated branches, by roughly 13 cm^{-1} due to the spin-orbit splitting of the ${}^3\Pi$ state [25]. In this case, the intensities of the three band heads would not depend on the internal temperature of the radical. According to theory [18] this transition is much weaker. Similarly, a ${}^3\Sigma^- - {}^3\Pi$ system should show three well-separated structures, provided that the internal temperature of the radical is around 80 K. This is not in agreement with the spectra recorded in the $19050\text{--}19600\text{ cm}^{-1}$ region: all transitions occurring nearby were identified as part of the $\text{C}_6\text{H } {}^2\Pi - {}^2\Pi$ electronic transition, excluding this case also. A ${}^3\Sigma^- - {}^3\Pi$ transition does not match the observed profile as well; no Q head is apparent.

${}^3\Pi - {}^3\Pi$ fits best (at 60–80 K) reproducing the shape, especially the dip at 19487.8 cm^{-1} caused by an R-head and the Q head at 19486.5 cm^{-1} , as shown in Figure 5.4. In the corresponding band of C_6D^+ (at 19538 cm^{-1}) the rotational lines were not resolved though the profile showed the same features as for C_6H^+ . The lines in the P branch have been fitted, yielding the spectroscopic constants given in Table 5.2. The positions of the band heads and the observed dip while keeping the ground state rotational constant at the *ab initio* value and varying the upper state B' as well as T_{00} gave enough constraint so as to reproduce the overall shape of the P branch (Figure 5.4). The value obtained for the lower electronic state from the calculated rotational fit

for ${}^3\Pi$ ($0.0486(2) \text{ cm}^{-1}$) is comparable to the value 0.0475 cm^{-1} obtained from *ab initio* calculations [18]. Thus it is concluded that the ${}^3\Pi - {}^5\Pi$ transition is being observed.

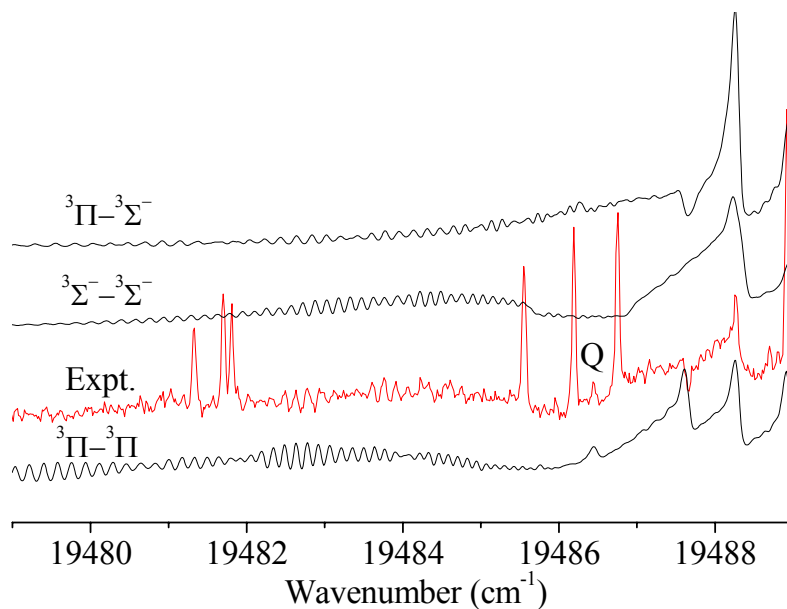


Figure 5.4: Simulation of the possible transition symmetries involved for C_6H^+ at 80 K and 0.06 cm^{-1} linewidth.

T_{00}	19485.776(11)
B''	0.0486(2)
B'	0.0477(2)
B''/B'	1.019
A''	-13 (fixed)
A'	-12.33(1)

Table 5.2: Spectroscopic constants obtained from the rotational contour fit.

In the neon matrix at 6 K, the absorption stems from the ground electronic state even if a near-lying excited electronic state is located just 0.04 eV above. It is not populated due to the complete relaxation at 6 K in the solid-state environment. The

same transition is being observed in the gas phase (based on the gas-matrix and isotopic shifts discussed above) and, thus, the symmetry appears to be ${}^3\Pi$. It is up to even higher level of theory to prove this. Furthermore, the *ab initio* calculations carried out [18] predict for the ${}^3\Pi - {}^3\Pi$ transition $T_{00} = 2.36$ eV compared with the observed 2.42 eV. On the other hand the ${}^3\Sigma^- - {}^3\Sigma^-$ system is calculated at 2.77 eV, a region to higher energy than scanned experimentally. If the ${}^3\Sigma^-$ state remains sufficiently populated in the supersonic expansion, in contrast to the 6 K neon matrix, it may be possible to find this transition. Also, cavity ring-down measurements at higher temperatures may be feasible and advantageous. In the P-branch, individual rotational lines are discernible, with ≈ 0.1 cm^{-1} widths. Broadening of the spectral lines indicates the excited-state lifetime to be ≈ 100 ps. Using the oscillator strength of the transition, the rotational temperature and the estimated Voigt line shape, the density of the C_6H^+ cations sampled is inferred to be around 2×10^8 cm^{-3} .

5.4. HC_4H^+

The vibrational frequencies in the ground $X^2\Pi_g$ state of the diacetylene cation have been inferred from the $A^2\Pi_u - X^2\Pi_g$ emission spectrum in 1956 [26] to be $\nu_3 = 860.5$ cm^{-1} , the C-C stretching frequency, and $2\nu_7 = 971.5$ cm^{-1} the first overtone of the degenerate π_g ν_7 vibration which borrows intensity from ν_3 due to Fermi resonance. The assignment of the two modes was later switched [27] based on the analysis of Rydberg series of neutral diacetylene and the intensity ratio in the electronic spectrum of HC_4H^+ . The vibrational frequencies in the $X^2\Pi$ state reported in stimulated emission pumping studies are $\nu_3 = 971.5$ cm^{-1} and $2\nu_7 = 861$ cm^{-1} [28, 29]. Lifetime measurements in the $A^2\Pi_u$ state of the cation [30] gave a value of 58(3) ns for the $\nu_3' = 1$ level compared to 71(3) ns for $\nu_3' = 0$. The rotational numbering for the origin band of the $A^2\Pi_u - X^2\Pi_g$ transition was later adjusted by one quantum [31] and the constants $T_{00} = 19722.594(3)$ cm^{-1} , $B' = 0.14009(4)$ cm^{-1} , $B'' = 0.14690(4)$ cm^{-1} , $A' = -31.1(8)$ cm^{-1} and $A'' = -33.3(8)$ cm^{-1} were given. The spectrum was also studied in a neon matrix [32]. The degenerate bending vibrations of HC_4H^+ result in a Renner-Teller (R-T) interaction, splitting the vibronic states into several components. Also, the frequencies of the $\nu_3 = 1$ and $\nu_7 = 2$ modes are close and Fermi resonance terms causes mixing of the

ν_7^+ vibrational states. The otherwise weak overtone of the ν_7 bend thus gains intensity from the ν_3 stretch.

The ground and the first excited electronic states of HC_4H^+ have the π electron configurations $(\pi_u)^4(\pi_g)^3$ and $(\pi_u)^3(\pi_g)^4$ respectively. The resulting electronic states ${}^2\Pi_g$ and ${}^2\Pi_u$ are inverted, with the $A^2\Pi_{u,3/2} - X^2\Pi_{g,3/2}$ transition lying $\sim 2 \text{ cm}^{-1}$ higher in energy relative to the $\Omega = 1/2$ component. In the present work, the observation of the rotationally resolved 3_0^1 and 7_0^2 bands in the 20550 cm^{-1} region by cavity ring down spectroscopy is reported. Spectroscopic constants and symmetries of energy levels are inferred.

5.4.1. Results and discussion

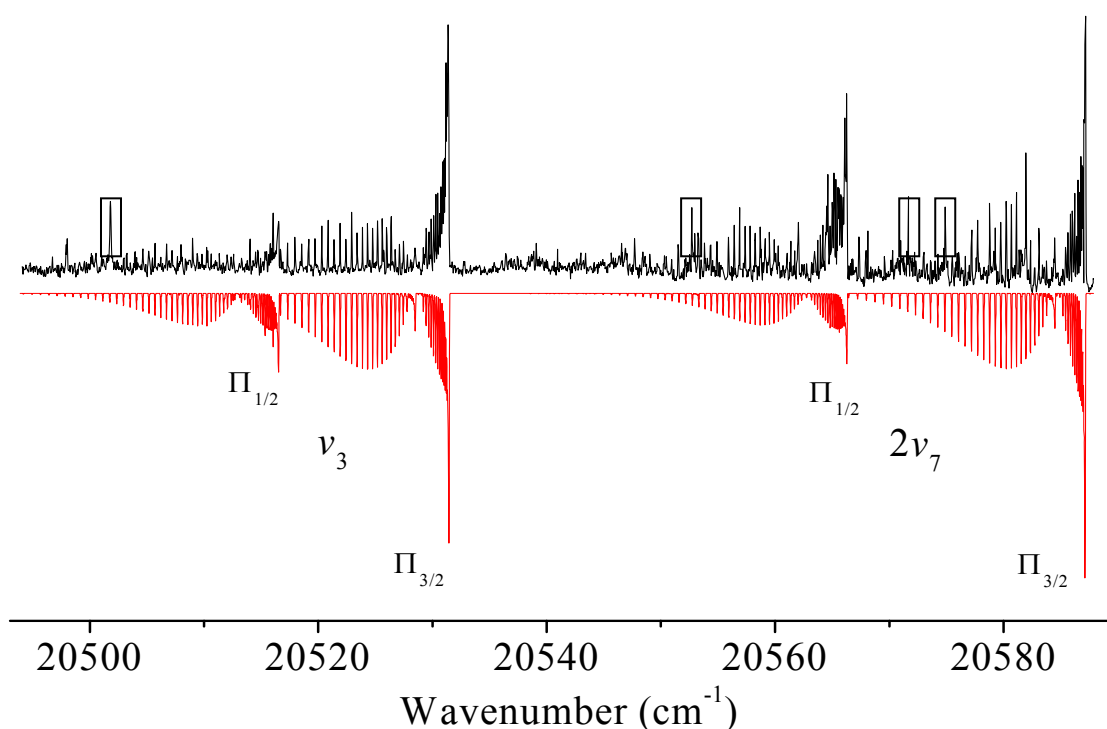


Figure 5.5: The $A^2\Pi_u-X^2\Pi_g$ 3_0^1 and 7_0^2 electronic transitions of HC_4H^+ measured in absorption using cavity ring down spectroscopy. The bottom trace shows the simulation at a temperature of 55 K and a 0.06 cm^{-1} linewidth. Intensity variations (indicated in boxes) in the experimental spectrum are caused by discharge fluctuations.

Figure 5.5 shows the rotationally resolved spectrum of the 3_0^1 and 7_0^2 vibronic bands of the $A^2\Pi_u-X^2\Pi_g$ transition obtained by a cavity ring down arrangement. The

rotational fits of the upper levels were carried out with the PGOPHER software [24], while the already known ground state spectroscopic constants [32] were kept fixed. This gives the s-o coupling constant $A' = -17.95(1) \text{ cm}^{-1}$ and the rotational constant $B' = 0.14047(1) \text{ cm}^{-1}$ for the upper state of the $3\frac{1}{2}_0$ transition. The analysis for the $7\frac{3}{2}_0$ transition yields $A' = -11.55(1) \text{ cm}^{-1}$ and $B' = 0.14018(3) \text{ cm}^{-1}$ (Table 5.3). A Gaussian linewidth of 0.06 cm^{-1} and a rotational temperature of $55 \pm 3 \text{ K}$ were used for the spectral simulations. The comparatively high latter value could be a result of the ions being probed at a short distance from the slit nozzle. The s-o temperature calculated from the ratio of the intensities of the $\Omega = 3/2$ and $\Omega = 1/2$ $A^2\Pi_u-X^2\Pi_g$ components for the $3\frac{1}{2}_0$ band is $50 \pm 5 \text{ K}$, similar to the rotational temperature. Intensity variations in the rotational profile are caused by the shot-to-shot instabilities during the discharge. The assigned lines for both the bands are listed in Appendix C.

The separation between the $\Omega = 3/2$ and $\Omega = 1/2$ components (ΔA) in the $3\frac{1}{2}_0$ and $7\frac{3}{2}_0$ bands of the $A^2\Pi_u-X^2\Pi_g$ transition is $\sim 15\text{-}20 \text{ cm}^{-1}$, much larger than that observed for the origin band at $T_{00} = 19722.5 \text{ cm}^{-1}$ ($\Delta A \sim 2.2 \text{ cm}^{-1}$). Also, the R_1 (15.5-19.5) and $R_1(14.5\text{-}18.5)$ bandheads ($\Omega = 3/2$) of the $3\frac{1}{2}_0$ and $7\frac{3}{2}_0$ bands at 20531.35 cm^{-1} and 20587.16 cm^{-1} are separated by $\sim 56 \text{ cm}^{-1}$. Quantitative treatment of the R-T, s-o and Fermi resonance interactions between the two modes is necessary to explain these observations. A vibronic analysis of the $A^2\Pi_u-X^2\Pi_g$ electronic transition is made by using a restricted Hamiltonian which takes into account the spin-orbit (s-o), the R-T and the Fermi interaction between the modes is described in detail in chapter 8.

	$7\frac{3}{2}_0$	$3\frac{1}{2}_0$
T_{00}	20573.659(4)	20520.828(4)
B'	0.14018(3)	0.14047(2)
A'	-11.55(1)	-17.95(1)
$D' (10^{-7})$	4.5(7)	0.11(4)

Table 5.3: Spectroscopic constants (cm^{-1}) obtained from the rotational line fit of the $7\frac{3}{2}_0$ and $3\frac{1}{2}_0$ bands in the $A^2\Pi_u-X^2\Pi_g$ transition of HC_4H^+ .

5.5. $C_6H_3^+$

The protonated triacetylene was chosen due to its chemical and astrophysical significance. Unsaturated hydrocarbons have been shown to be present in the interstellar medium (ISM) and model predictions also anticipate the presence of large polyacetylenic chains [33, 34]. As many chemical reactions in the ISM are of the ion-molecule type, protonated polyacetylenes stand out as important intermediates bridging the gap in the chemistry of carbon chains and cumulenes [35].

5.5.1. Results and discussion

An electronic band system of $C_6H_3^+$ was also observed in a 6 K neon matrix following mass selection [36]. This was subsequently detected at 26402 cm^{-1} in the gas phase in an ion trap [37]. A two-color photon scheme was used to observe the spectrum; a bound-bound transition out of the ground electronic state was excited with one laser while the second UV laser subsequently produced the fragment ion C_6H^+ , which was monitored. In the latter experiment, the rotational profile was seen but the individual lines could not be resolved. Their resolution would prove the structure of the species; either the “classical” $HC_6H_2^+$ with C_{2v} symmetry, or the nonclassical linear HC_6H form with a loosely bound H^+ undergoing large amplitude motion. According to *ab initio* calculations [37], the electronic transition observed could correspond to ${}^1A_1 - X{}^1A_1$ in C_{2v} symmetry. On the basis of the infrared frequencies observed in measurements on mass-selected $C_6H_3^+$ in neon-matrices [36], the classical $H_2C_6H^+$ structure was also implied.

It was not clear whether the reasons for the rotational structure not being resolved was due to the short lifetime of the excited electronic state because of intramolecular processes or power broadening in the two-color laser approach. It was decided to measure the band with cavity ring-down spectroscopy for which the measured signal is not dependent on the intensity of the probing laser beam, avoiding power broadening effects. This was achieved here with the cavity ring-down approach. However, the structure could still not be resolved; the measured rotational profile is shown in Figure 5.6. The Q head could not be discerned because of the low S/N. Thus, it is concluded that the excited electronic state is short-lived as a result of lifetime

broadening by intramolecular processes. The lines have a Lorentzian FWHM of 0.08 cm^{-1} (obtained from the contour fit) and the rotational structure is smeared out. This corresponds to the excited-state lifetime of 60 ps.

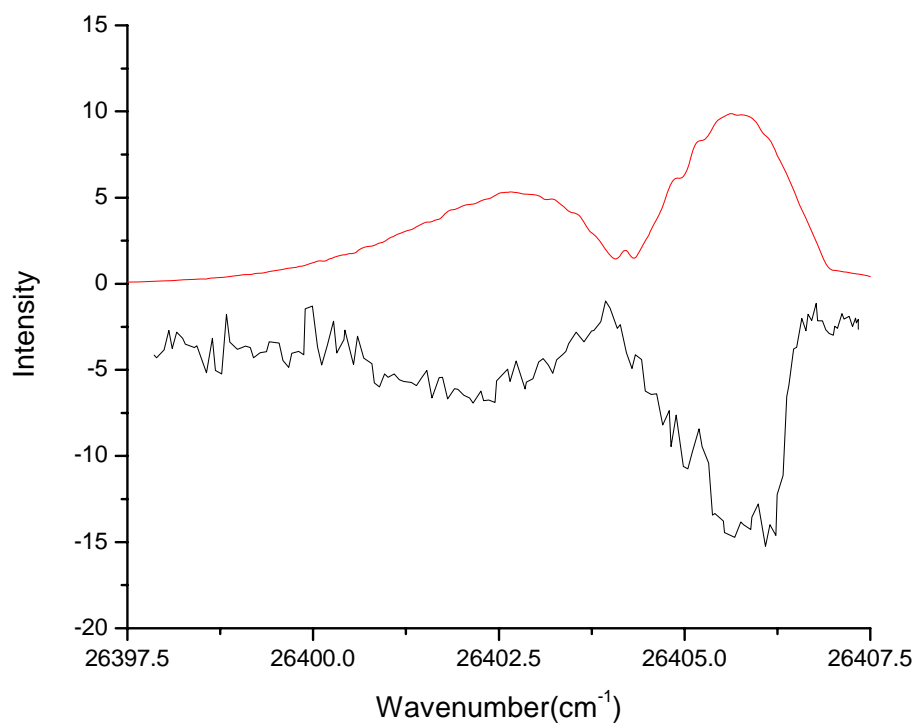


Figure 5.6: Electronic Spectrum of C_6H_3^+ recorded by cavity ring-down spectroscopy (black trace) and its simulation (red trace). The Q branch could not be discerned due to low S/N.

Bibliography

- [1] Raghunandan, R.; Mazzotti, F. J.; Maier, J. P. *J. Am. Soc. Mass Spectrom.* 21, 694, **2010**.
- [2] Raghunandan, R.; Mazzotti, F. J.; Esmail, A. M.; Maier, J. P. *J. Phys. Chem. A*, 115, 9365, **2011**.
- [3] Snow, T. P.; McCall, B. J. *Annu. Rev. Astron. Astrophys.* 44, 367, **2006**.
- [4] Douglas, A. E. *Nature* 269, 130, **1997**.
- [5] Jochnowitz, E. B.; Maier, J. P. *Mol. Phys.* 106, 2093, **2008**.
- [6] Jochnowitz, E. B.; Maier, J. P. *Annu. Rev. Phys. Chem.* 59, 519, **2008**.
- [7] Maier, J. P.; Lakin, N. M.; Walker, G. A. H.; Bohlender, D. A. *Astrophys. J.* 553, 267, **2001**.
- [8] Maier, J. P.; Walker, G. A. H.; Bohlender, D. A. *Astrophys. J.* 602, 286, **2004**.
- [9] Homann, K. H. *Angew. Chem.-Int. Ed.* 7, 414, 1968.
- [10] Tielens, A. G. G. M.; Snow, T. P. *The diffuse interstellar bands*; Kluwer Academic Publishers: Dordrecht, Netherlands, 1995.
- [11] McCarthy, M. C.; Travers, M. J.; Kovacs, A.; Gottlieb, C. A.; Thaddeus, P. *Astrophys. J. Suppl. Ser.* 113, 105, **1997**.
- [12] Shindo, F.; Benilan, Y.; Guillemin, J. C.; Chaquin, P.; Jolly, A.; Raulin, F. *Planet. Space Sci.* 51, 9, 2003.
- [13] Kunde, V. J.; Aiken, A. C.; Hanel, R. A.; Jennings, D. E.; Maguire, W. C.; Samuelson, R. *E. Nature* 292, 686, **1981**.
- [14] Zwier, T. S.; Allen, M. *Icarus* 123, 578, **1996**.
- [15] Krełowski, J.; Beletsky, Y.; Galazutdinov, G. A.; Kołos, R.; Gronowski, M.; LoCurto, G. *Astrophys. J.* 714, L64, **2010**.
- [16] Maier, J. P.; Chakrabarty, S.; Mazzotti, F. J.; Rice, C. A.; Dietsche, R.; Walker, G. A. H.; Bohlender, D. A. *Astrophys. J.* 729, L20, **2011**.
- [17] Fulara, J.; Shnitko, I.; Batalov, A.; Maier, J. P. *J. Chem. Phys.* 123, 044305/1, **2005**.
- [18] Shnitko, I.; Fulara, J.; Batalov, A.; Gillery, C.; Masso, H.; Rosmus, P.; Maier, J. P. *J. Phys. Chem.* 110, 2885, **2006**.
- [19] Forney, D.; Fulara, J.; Freivogel, P.; Jakobi, M.; Lessen, D.; Maier, J. P. *J. Chem. Phys.* 103, 48, **1995**.
- [20] Kotterer, M.; Maier, J. P. *Chem. Phys. Lett.* 266, 342, **1997**.

- [21] Jacox, M. E. *J. Phys. Chem Ref. Data* 17, 269, **1998**.
- [22] Freivogel, P.; Fulara, J.; Lessen, D.; Forney, D.; Maier, J. P. *Chem. Phys.* 189, 335, **1994**.
- [23] Pfluger, D.; Motylewski, T.; Linnartz, H.; Sinclair, W. E.; Maier, J. P. *Chem. Phys. Lett.* 329, 29, **2000**.
- [24] Western, C. M. *PGOPHER, A Program for Simulating Rotational Structure. University of Bristol*; <http://pgopher.chm.bris.ac.uk>.
- [25] Saykally, R. J.; Evenson, K. M. *Astrophys. J.* 238, L107, **1980**.
- [26] Callomon, J. H. *Can. J. Phys.* 34, 1046, **1956**.
- [27] Smith, W. L. *Proc. R. Soc. London, Ser. A* 300, 519, **1967**.
- [28] Celii, F. G.; Maier, J. P.; Ochsner, M. *J. Chem. Phys.* 85, 6230, **1986**.
- [29] Celii, F. G.; Maier, J. P. *J. Opt. Soc. Am. B* 7, 1944, **1990**.
- [30] Allan, M.; Kloster-Jensen, E.; Maier, J. P. *Chem. Phys.* 7, 11, **1976**.
- [31] Kuhn, R.; Maier, J. P.; Ochsner, M. *Mol. Phys.* 59, 441, **1986**.
- [32] Bondybey, V. E.; English, J. H. *J. Chem. Phys.* 71, 777, **1979**.
- [33] McCarthy, M. C.; Travers, M. J.; Kovacs, A.; Gottlieb, C. A.; Thaddeus, P. *Astrophys. J. Suppl. Ser.* 113, 105, **1997**.
- [34] Shindo, F.; Benilan, Y.; Guillemin, J. C.; Chaquin, P.; Jolly, A.; Raulin, F. *Planet. Space Sci.* 51, 9, 2003.
- [35] Turner, B. E.; Herbst, E.; Terzieva, R. *Astrophys. J., Suppl. Ser.* 126, 427, **2000**.
- [36] Batalov, A.; Fulara, J.; Shnitko, I.; Maier, J. P. *J. Phys. Chem.* 110, 10404, **2006**.
- [37] Dzhonson, A.; Jochnowitz, E. B.; Kim, E.; Maier, J. P. *J. Chem. Phys.* 126, 044305/1, **2007**.

Chapter 6

Broad absorption features of *l*-C₃H₂ – Relevance to the Diffuse Interstellar Band Problem

6.1. Introduction

The recombination era saw the first signs of molecules in the universe, which marked the transition from an ionized state to a predominantly neutral environment made up of H, He, D and Li. Radiative association reactions triggered the formation of simple molecules, such as H₂, LiH and HD as well as molecular ions like He_2^+ , HeH^+ and HD^+ [1]. As the universe began to cool and expand, stars were formed from giant clouds of hydrogen, thereby setting the stage for the formation of heavier and complex molecules containing C, O, N, S, P, halides and metals. Until now, approximately 150 molecules have been detected in the interstellar medium (ISM). The interstellar chemistry is largely carbon dominated; this is evident from the first molecule CH to the most recent detection of ethylformate (C₂H₅OCHO) and n-propylcyanide (C₃H₇CN) [2].

Apart from studying their electronic structure and properties, the other main goal of the spectroscopic research carried out in this work is to characterize carbon containing radicals and ions because of their astrophysical relevance. Of special focus are the Diffuse Interstellar bands (DIBs), absorptions in the optical region by molecules in diffuse clouds. Diffuse interstellar clouds have long been thought to be relatively devoid of molecules, because of their low densities and high radiation fields. However, in the past ten years or so, a surplus of polyatomic molecules have been observed in diffuse clouds, via their rotational, vibrational, and electronic transitions.

Since their discovery in 1922 [3], the identification of molecules responsible for these bands remains one of the challenges the astronomical community faces till date. Comparison of laboratory gas phase and astronomical spectra is the way to identify the carriers responsible for these bands. This chapter presents an overview of these DIBs and their properties before proceeding to the results on detection of gas phase *l*-C₃H₂

recorded by CRDS [4]. The measured vibronic bands show exact match to the profiles and wavelengths of the two broad DIBs at 5450 and 4881 Å, implying its role as a carrier of these DIBs.

6.2. Diffuse Interstellar Bands

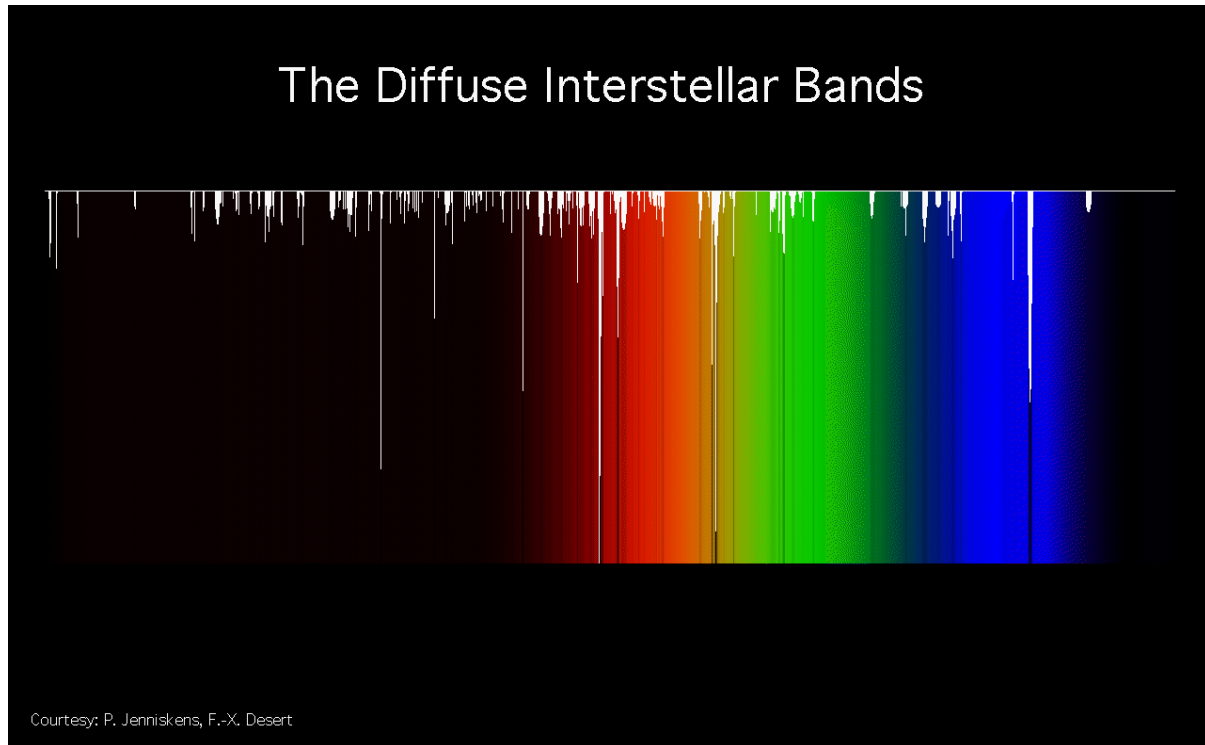


Figure 6.1: Diffuse interstellar bands [5].

The DIBs are a series of absorption lines that are observed in near-UV, visible and near-IR spectra (Figure 6.1) recorded towards stars that are partially obscured by interstellar dust. They are known to be interstellar, because they do not suffer the periodic Doppler shifts associated with stellar lines in binary star systems. These interstellar features appeared "diffuse," or fuzzy, on early photographic plates, hence the term diffuse interstellar bands. DIBs were first noted in the spectra of "red" B stars, but only recognized as arising from the interstellar medium in the 1930s [3, 6]. Initially, broad bands some tens of Å wide were identified, but with improved instrumentation many hundreds were subsequently found—mostly in the yellow/red with each being only a few Å wide.

There had already been various theories about these DIBs being formed by molecules in the ISM in the early days [7, 8], but in time the emphasis swung to solid-

state absorption as the origin of the DIBs [9, 10] as formation mechanisms for maintaining a sufficient population of gas phase molecules were not known. An appealing idea with regard to the solid state origin of DIBs was that the carriers might be dispersed as an impurity through the spherical dust particles and the electric field of the crystal lattice in which such an atom would be imbedded could shift and split the atom's energy levels. Non-conclusive experimental data [11] together with lack of tight correlation between the strength of DIBs and colour excess cast doubt that DIBs originate in the dust grains pointed otherwise. Furthermore, the absence of the detectable change in interstellar polarization across some of stronger DIBs shows that these features do not originate in the aligned grains responsible for polarization of light in the optical region [12].

Later, when the first radiowavelength detections of molecules occurred [13] and concurrently astronomers realized that rapid molecular formation through ion-neutral reactions was possible, molecules in the diffuse ISM received new respect. Arguments against a solid-state origin of the DIBs and for a molecular carrier were put forward [14, 15]. The most powerful of arguments favoring gas-phase carriers are the observed constancy of DIB wavelengths and profiles from sightline to sightline and the existence of fine structure in some DIBs [16]. The DIB carriers are presumed to be fairly large molecules and the breadth of the DIBs is likely due to unresolved rotational structure and/or intramolecular vibrational relaxation. It has been put forward that some DIB carriers could be ionized molecules [17]. With regard to their origin, it is believed that DIB carriers are composed of cosmically abundant elements like H, C, O, and N rather than trace elements. Many of the DIB carriers appear to exist primarily in the diffuse atomic clouds; where hydrogen is atomic and the radiation environment is harsh, though there have been a few observations in the diffuse molecular clouds [18].

Much of the speculation about which specific molecules form the DIBs is centered on two classes of molecules: PAHs and carbon chains. The essential points that make PAHs very promising molecules are their survivability against photodissociation in the interstellar radiation field, abundance of carbon in the interstellar medium sufficient enough to account for the DIB strength, and the strong electronic transitions of PAHs in the optical region. The speculation is furthered by the likely aromatic nature of the Unidentified Infrared Band (UIB) carriers which were identified in carbon-rich

planetary nebulae and some carbon star atmospheres [19] and their probable presence in diffuse clouds. The speculation about carbon chains is because many of the molecular species observed in cold dense molecular clouds are carbon chains. Constraints on possible carriers in the PAH and carbon chain families have been reported [20, 21]. After numerous laboratory studies and astronomical comparisons, in case of neutral carbon chains as DIB carriers, it was pointed out by Maier et al. [20] that besides having electronic transitions in the DIB region (4000-9000 Å), these molecules must have oscillator strengths of the transitions in the range 1-10. This would apply to closed shell systems which include the odd-numbered bare carbon chains in the C₁₅-C₃₁ size range having very strong transitions in this region.

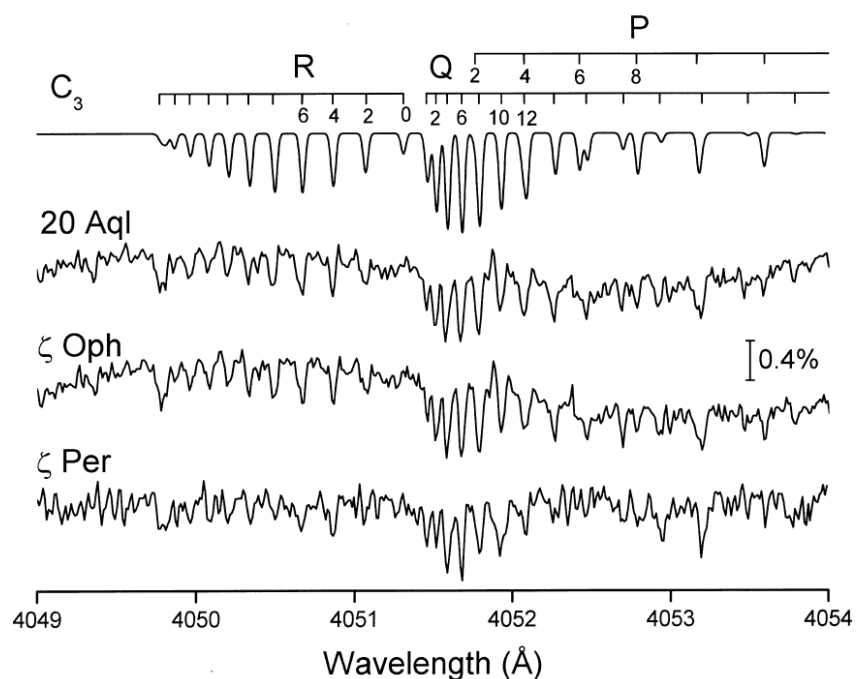


Figure 6.2: Rotational lines in the origin band of the C₃ $A^1\Pi_u \leftarrow X^1\Sigma_g^+$ transition toward ζ Oph, ζ Per, and 20 Aql [23].

The first three interstellar molecules ever detected, CH, CH⁺, and CN [22], were diatomics, but detection of additional diatomics has generally been a challenge, as most species fall well below H₂, CO, CH, CH⁺, and CN in abundance. However, a number of di- and triatomics are known to be present in the diffuse clouds: CO, C₂, OH, NH etc. as well as H₃⁺ and C₃ [22]. Figure 6.2 shows the rotational lines in the origin band of the C₃ $A^1\Pi_u \leftarrow X^1\Sigma_g^+$ transition toward ζ Oph, ζ Per, and 20 Aql [23]. In addition, millimeter-

wave observations indicate the presence of more complex carbon containing molecules, e.g., $c\text{-C}_3\text{H}_2$ [24] and C_4H [25]. Extensive research on DIBs can be found in works by Snow & McCall [22], Herbig [26], etc.

Advances in laboratory techniques over the last decade have enabled the measurement of a number of astrophysically relevant molecules in the gas phase. These include some bare carbon chains [21], those containing one hydrogen, nitrogen and their ions [27], and a few aromatic cations [28]. Individual coincidences of three very weak DIBs with the gas-phase absorptions of naphthalene cation [29] and that of the 5069 Å DIB with the origin band of the $A^2\Pi_u \leftarrow X^2\Pi_g$ electronic transition of diacetylene cation [30] were reported earlier, but both these claims have been disproved [31, 32].

6.2.1. DIB Properties

The main parameters describing DIBs include the central wavelength of the feature ($\lambda_{\text{in Å}}$), the central depth of the band A_c which is described by percent of the continuum level, the full width of the band at its half-maximum (FWHM, Å) and the equivalent width (W_{λ}) in Å or mÅ. The equivalent width describes width of a hypothetical line of the same area, of a rectangular profile, and normalized to unity. The ratio of equivalent width reflects the ratio of the oscillator strength when DIBs are due to one carrier.

The profiles of the majority of DIBs are relatively narrow (their FWHM is usually of the order of few Å), however wider bands also can be found in some spectra [33, 34]. The central depths of the majority of DIBs are of the order of 1-2 % of continuum, but there are few exceptions, e.g. the central depth of 5780 DIB in some spectra [35, 36] reaches 30%. The parameters describing DIBs are not stable and vary from one line of sight to another: the survey of DIBs [37] showed that the value of the equivalent width may change drastically. For the strong 5780 DIB it varies from 0.11 (target star - HD30614) to 0.72 (target star HD183143).

One of the strong arguments supporting the interstellar origin of the DIBs is the Doppler splitting observed in these bands due to the variable velocities associated with the interstellar clouds. The broad profiles of the bands are only slightly altered, and only in the case of very sharp DIBs can the Doppler splitting be observed.

Dust grains in the interstellar medium have a typical size that is comparable to the wavelength of blue light. The result is that the blue light coming from distant objects is strongly absorbed and scattered by the dust, essentially removing it from the light reaching earth and making the objects appear redder than they really are. This phenomenon is known as interstellar reddening. The extinction produced by interstellar matter refers to the combined effects of the scattering and absorption of electromagnetic radiation by the matter along sight lines through the interstellar space. The interstellar extinction curve depicts the absorption and scattering due to various interstellar dust components and spans from the near infrared to the far ultraviolet and affects the DIB strength. The correlation analysis of the dependence of the strength of DIB 4428 Å on reddening was carried out by Deeming and Walker in 1967 [38]. The degree of reddening is inversely proportional to the wavelength and is characterized as the color excess $E(B-V)$ by measuring the colour index $(B-V)$ of the object and comparing that to its true colour index $(B-V)_0$. The DIBs have been correlated by the measure of their color excess [39]. The bands are also classified on the basis of their profiles (broad and shallow/symmetric/asymmetric).

6.3. *l*-C₃H₂

Recently, a match between a broad DIB, at 5450 Å with FWHM ~ 10 Å, and the absorption of an unknown species produced in a plasma discharge of acetylene was reported [40]. The available experimental data pointed to a molecule containing only carbon and hydrogen. The following sections present evidence that the molecule responsible is propadienylidene, H₂CCC-linear three carbon atoms with two hydrogens off-axis on the terminal carbon, henceforth and usually designated as *l*-C₃H₂. The molecule has two other broad absorption bands at around 4890 and 5170 Å, close to known DIBs, as well as rotationally resolved bands at wavelengths above 6000 Å. Narrow DIBs of the expected strength are also found at the positions of two of the triplet systems predicted to be centered near 6159 and 6252 Å. The spectral region for the third system, weaker than the other two, is too confused by strong telluric oxygen features. All of this is evidence for an identification of a carrier molecule which gives rise to a series of DIBs.

The recognition that the broad band seen in the laboratory which coincided with the 5450 Å DIB was due to absorption by *l*-C₃H₂ became evident from a number of previous studies together with the present ones. In its electronic ground state X^1A_1 , *l*-C₃H₂ (C_{2v} symmetry) has been well characterized by millimeter-wave spectroscopy in the laboratory [41] and identified by this signature in dense interstellar clouds [42] and in the diffuse medium [43]. It is an isomer of the ubiquitous cyclic C₃H₂ [44]. The electronic absorption spectrum of *l*-C₃H₂ was first observed in a neon matrix at 6 K [45]. In the visible region, it shows two electronic systems; a weak dipole forbidden $A^1A_2 - X^1A_1$ transition which becomes partly allowed by vibronic effects with the near lying B^1B_1 electronic state. Then, it shows an intense $B^1B_1 - X^1A_1$ transition in the 4000-5500 Å range. The spectrum was re-recorded [4] in the matrix laboratory, Basel. The spectra were by and large identical, except that the recordings at Basel (Figure 6.3) showed better resolution of the bands and there were wavelength errors for some of the reported absorptions. Due to matrix-gas shifts, a direct comparison with DIB data is inconclusive.

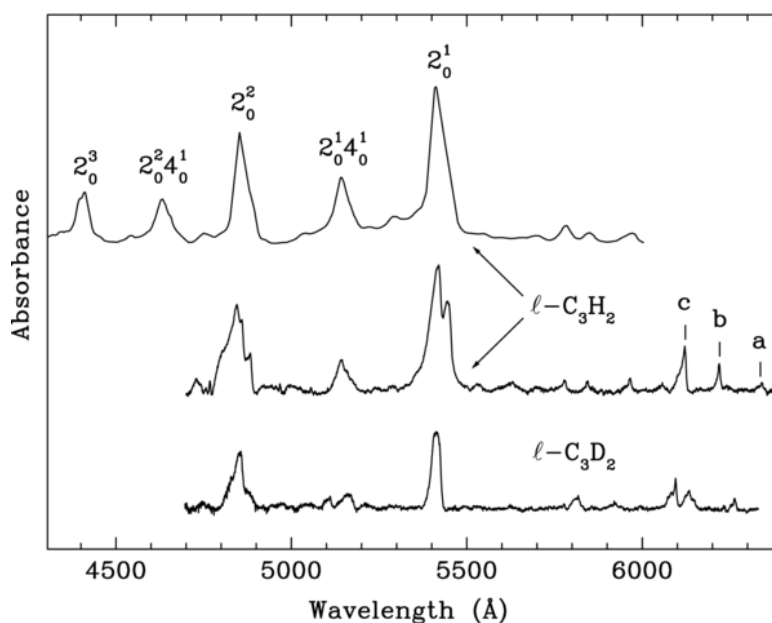


Figure 6.3: Absorption spectra of *l*-C₃H₂ measured in 6 K neon matrices. *Courtesy: Matrix Isolation Spectroscopy Laboratory, Basel.* The top trace was obtained by 1470 Å photolysis of allene embedded in the matrix. The middle and bottom traces were observed using mass-selected deposition. Labels a, b, c refer to the rotationally resolved gas-phase measurements [46, 47].

Thus, a goal a number of years ago was to observe the $B^1B_1 - X^1A_1$ system of *l*-C₃H₂ in the gas phase. Three techniques were employed: absorption measurements in a

supersonic jet expansion through which a discharge runs and detection with cavity ring-down (CRD) either with pulsed or continuous lasers, as well as resonance-enhanced multi-photon ionization. The experiments were unsuccessful [46], from which it was concluded that the B^1B_1 excited electronic state has a lifetime less than a picosecond, causing individual line broadening of over 10 cm^{-1} . However, at the same time, three rotationally resolved bands lying in the $6000\text{-}6600\text{ \AA}$ region were observed [46, 47]. In the latter two articles, the rotational analysis proved that these belong to $l\text{-C}_3\text{H}_2$, corresponding to transitions from the $v = 0$ level of the ground X^1A_1 state to vibronic levels in the A^1A_2 state, lying near the origin of the B^1B_1 electronic state. The bands in the dipole forbidden $A^1A_2 - X^1A_1$ transition gain intensity by vibronic mixing with the B^1B_1 levels. The rotational analysis is unambiguous. These bands, lying around 6159 , 6252 , and 6319 \AA , in the gas phase show a complex structure characteristic of an asymmetric top.

6.3.1. Experimental

In the gas phase, $l\text{-C}_3\text{H}_2$ was produced in a supersonic free-jet expansion discharge. As precursor, $0.5\text{-}1\%$ allene in argon, or acetylene and diacetylene in helium, was used. The discharge was operated at 10 Hz , while the laser was fired at 20 Hz . It was found that the strongest signals were observed with allene, but at the same time the vibrational and rotational temperatures attained were a bit higher than with diacetylene. Furthermore, allene produced other species causing broad absorptions in the range of interest (e.g., $l\text{-C}_3\text{H}$). Dideutero-acetylene in helium was used in the discharge expansion for the measurements on $l\text{-C}_3\text{D}_2$.

6.3.2. Results

It was focused on whether the 5450 \AA absorption band coinciding with the DIB at this wavelength [40] could be the $B^1B_1 - X^1A_1$ transition of $l\text{-C}_3\text{H}_2$, i.e., corresponding to the most intense band in the 6 K mass selected neon matrix spectrum at 5417 \AA (Figure 6.3).

The assignment of the bands to vibrational excitation in the upper electronic state of $l\text{-C}_3\text{H}_2$ is established [45]. All the transitions originate from the $v = 0$ level of the X^1A_1 ground state because the temperature of the neon matrix is 6 K . The strongest

5417 Å band corresponds to the excitation of the totally symmetric ν_2 (C=C stretch) mode in the B^1B_1 state (2^1_0 transition). Other strong bands in the spectrum of C_3H_2 are due to its overtone (2^2_0 at 4856 Å) and combination with the ν_4 mode ($2^1_0 4^1_0$ at 5143 Å) as indicated in Figure 6.3. The origin band of the $B^1B_1 - X^1A_1$ transition is weaker and is influenced by vibronic interaction of B^1B_1 with the nearby lying A^1A_2 state. It is located somewhere within the group of weak bands above 6000 Å (between a and c in Figure 6.3). This has been considered theoretically [45] and also discussed in the analysis of the rotationally resolved spectra in the gas phase in this region [46].

Neon Matrix [4]				Gas Phase		Transition	Band
$\lambda(l-C_3H_2)$	<i>I</i>	$\lambda(l-C_3D_2)$	<i>I</i>	$\lambda(l-C_3H_2)$	$\lambda(l-C_3D_2)$		
6284	0.2	6260	0.4	6318.9		$A^1A_2 \leftarrow X^1A_1$	a
6219	0.3	6130	1.4	6251.7		"	b
6122	0.9	6093	1.5	6159.2		"	c
5445/5417	10	5412	10	5450(3)	5458(3)	$B^1B_1 \leftarrow X^1A_1$	2^1_0
5143	3	5160	3.5	5165-5185 ^a		"	$2^1_0 4^1_0$
4856	9	4857	12	4887(3)		"	2^2_0
4633	4.4			4645-4665 ^a		"	$2^2_0 4^1_0$
4412	4.7			4425-4445 ^a		"	2^2_0

Table 6.1: Absorption Band Maxima (Å) of $l-C_3H_2$ and $l-C_3D_2$ measured in a 6 K Neon Matrix [4] and in the Gas Phase ($K = 1-0$).

^a Extrapolated values based on the neon matrix to gas phase shift of the 2^1_0 band.

CRD is a sensitive detection method; however, the lack of mass selection is a drawback. Therefore, the matrix spectra of the mass-selected C_3H_2 and C_3D_2 serve for the identification of the bands in the gas-phase CRD experiments. Though the wavelength shift going from neon matrix to gas phase can be 10-50 Å for electronic transitions, the separation of vibrational peaks rarely differs by more than a few Å within one state [48]. Thus, by knowing the wavelength of the 2^1_0 transition in the gas phase, the positions of other bands (e.g., 2^2_0 or $2^1_0 4^1_0$) can be predicted from the separation of the peaks in the neon spectrum (Figure 6.3). However, this procedure

cannot be applied for the 2_0^1 band of $l\text{-C}_3\text{H}_2$ itself because the separation from the origin to the 2_0^1 peak is not known.

The aim was therefore to detect the gas-phase band of $l\text{-C}_3\text{H}_2$ that corresponds to the 2_0^1 transition in the neon matrix at 5417 Å. The known rotationally resolved bands of $l\text{-C}_3\text{H}_2$ above 6000 Å were first detected using acetylene, diacetylene, or allene seeded in argon in the discharge. The strongest signal was observed with allene. The spectrum was then measured in the (5420 ± 50) Å range as indicated by the 2_0^1 absorption in neon. Broad absorptions were detected with all the precursors and under the same discharge conditions as for the rotationally resolved $\lambda > 6000$ Å bands of $l\text{-C}_3\text{H}_2$. The spectrum obtained with allene precursor is shown in Figure 6.4 (a). It consists of two broad absorptions, whose relative intensities vary with the precursor proving that they originate from two different molecules (Appendix D).

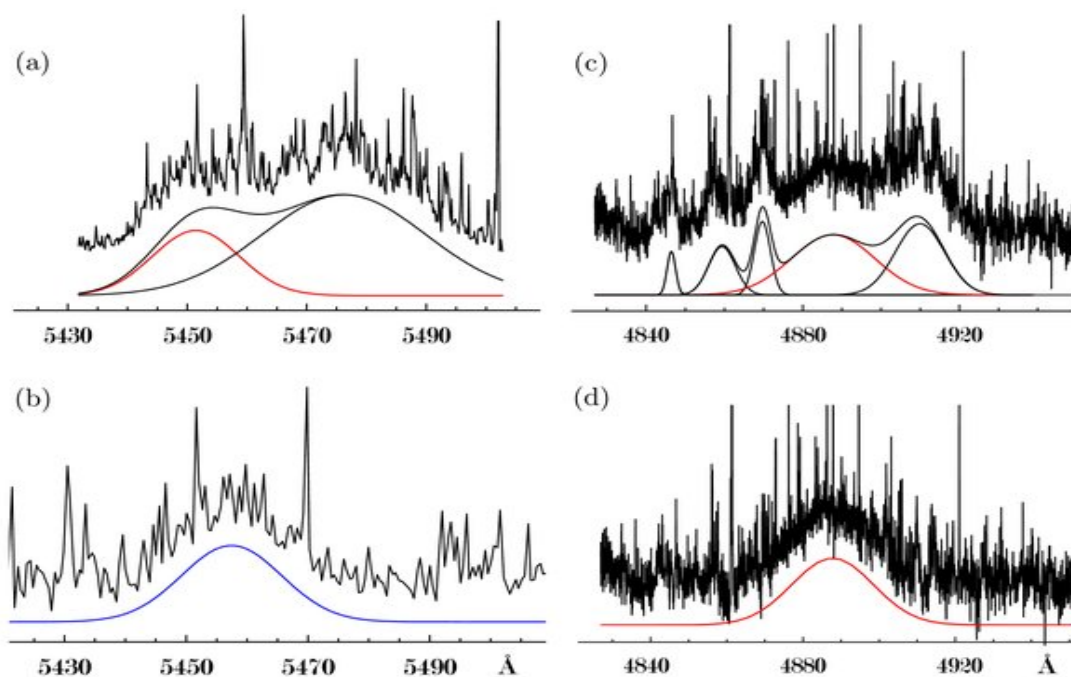


Figure 6.4: Gas-phase laboratory spectra recorded by cavity ring-down spectroscopy in a supersonic slit jet expansion discharge using allene (traces a, c, d) and DC_2D (trace b) as precursors. The continuous, solid lines are Gaussians fitted to the data, after partial removal of the C_2 lines and subtraction of the known $l\text{-C}_3\text{H}$ absorptions (trace c). Absorptions in red are due to $l\text{-C}_3\text{H}_2$.

The absorptions in Figure 6.4 (a) have been deconvoluted using the two Gaussians shown. The central wavelength of the first peak is ~ 5450 Å (FWHM $\sim 13\text{-}17$

Å), whereas the other is centered at 5473-5476 Å (FWHM ~32-42 Å). The prominent C₂ absorption lines have been partially removed from the spectrum by taking a wavelength window of 10 points, finding the minimum, and then repeating the procedure at the following position of the spectrum. By this means, the broad underlying absorption is retained and fitted by a Gaussian. Figure 6.4 (a) shows the superposition of the two Gaussians and the quality of the fit.

Gas-phase measurements on *l*-C₃D₂ were also carried out. In the spectral window of interest, only one broad band (central wavelength at 5458(3) Å and FWHM ~19-24 Å) has been detected using dideutero-acetylene as precursor (Figure 6.4 (b)). The FWHM does not differ much from that of the 5450 Å band. The position of this band is shifted by ~ 27 cm⁻¹ to the lower energy relative to the 5450 Å band, similar to the neon matrix change (17 cm⁻¹).

Comparison of the neon matrix spectra of *l*-C₃H₂ and *l*-C₃D₂ (Figure 6.3) with the CRD spectra (Figure 6.4) leads to the conclusion that the 5417 Å band in the neon matrix and that at 5450 Å in the gas phase originate from the same molecule, namely *l*-C₃H₂. From the position of the 2^1_0 band of *l*-C₃H₂ in the gas phase (5450 Å), the wavelengths of the 2^0_0 and $2^1_0 4^1_0$ transitions in the gas phase can be predicted using the separation of the peaks in the neon spectrum. For this the most intense peaks are taken (5417, 5143, and 4856 Å), because the lowest energy site is not resolved (though its presence is indicated by the asymmetry of the peak). The difference between the 2^0_0 and 2^1_0 band maxima is 2130 cm⁻¹ and this leads to a gas-phase prediction of 4883 Å for the 2^0_0 transition; the uncertainty is difficult to guess because of broadening mechanisms in the matrix. The $2^1_0 4^1_0$ band is located 984 cm⁻¹ above the transition in the neon matrix; in the gas phase it is then in the 5173 Å wavelength region.

In the region around 4883 Å predicted for the 2^0_0 band, broad absorptions are detected (Figure 6.4(c)) with narrower components imposed on them. The four bands at 4913, 4870, 4856, and 4844 Å belong to *l*-C₃H because they have been identified in earlier mass-selected studies in the gas phase [49]. After subtraction of the *l*-C₃H absorptions (the four Gaussians shown in Figure 6.4 (c)) from the laboratory recording, the residual broad band is obtained (Figure 6.4(d)). The Gaussian fit is centered at

4887(3) Å with FWHM of ~ 25 Å. Its position matches the 4883 Å wavelength predicted from the neon matrix spectrum of *l*-C₃H₂. The FWHM of this band is somewhat larger than that of the 2_0^1 band at 5450 Å, probably due to a shorter lifetime in the $v_2 = 2$ vibrational state of B^1B_1 . These arguments, together with the fact that the 5450 and 4887 Å bands were observed under the same experimental conditions as the rotationally resolved transitions of *l*-C₃H₂ above 6000 Å, provide the evidence that these absorptions originate from the *l*-C₃H₂ molecule.

The detection of the band around 5173 Å, corresponding to the $2_0^1 4_0^1$ transition of *l*-C₃H₂, was not successful. This is because this transition is a factor of three weaker than 2_0^1 and its intensity is below the detection limit of the CRD setup.

It was already established [40] that the 5450 Å gas-phase absorption coincides with a DIB at this wavelength. This band is now assigned to the $2_0^1 B^1B_1 - X^1A_1$ transition of *l*-C₃H₂. A DIB corresponding to the 2_0^1 band in the gas-phase observations is present.

Appendix E lists all the spectra which have been recorded from 4350-6250 Å as a part of this study. This also includes the vibronic transitions of *l*-C₃H₂ and *l*-C₃H. No other feature which matched all criteria as the 5450 and 4887 Å could be detected. The measurements also show many unidentified broad features throughout the region. The rotationally resolved C₃H₂ *b*-vibronic band of the dipole forbidden $A^1A_2 - X^1A_1$ electronic transition is shown in the appendix.

6.3.2.1. Simulation of Band Profile

6.3.2.1.1. Bands above 6000 Å

Three systems in the 6150-6330 Å region have been the subjects of two earlier high-resolution, gas-phase studies [46, 47]. The rotational analysis is unambiguous and proves that the absorptions belong to *l*-C₃H₂.

l-C₃H₂ has a near prolate top structure with C_{2v} symmetry. The rotational constants in the X^1A_1 ground state are $A = 9.6451$, $B = 0.3533$, and $C = 0.3404$ cm⁻¹. The $K = 1$ and $K = 2$ separations from $K = 0$ are ~ 10 and ~ 40 cm⁻¹, respectively. Thus at very low temperatures only the $K = 0, 1$ levels are populated. According to the selection rules, only transitions with $\Delta K = \pm 1$ are observed.

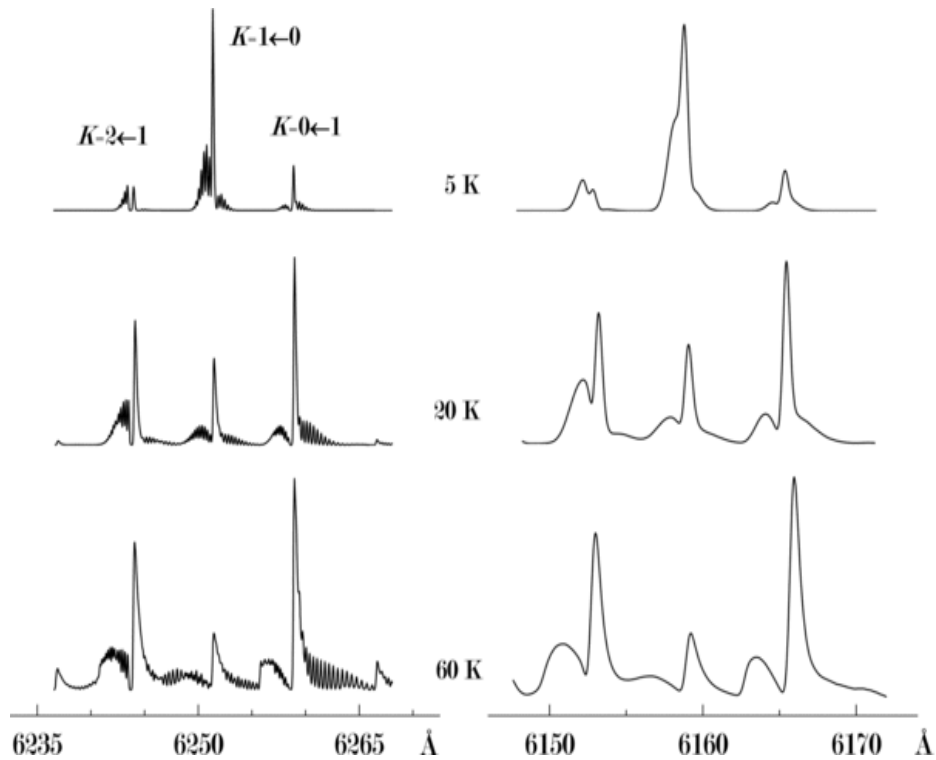


Figure 6.5: Simulated rotational profiles of the b (left) and c bands (right) of l -C₃H₂ which have been observed in the gas phase earlier. The structure is characteristic of an asymmetric top, showing the three K components 2-1, 1-0, and 0-1. The plot on the left uses 0.15 Å linewidth for the individual rotational transition, corresponding to 40,000 resolving power used in the astronomical observations. On the right 0.4 Å is used, compatible with the conditions of the astronomical observations as the pattern and broadening of the potassium atomic lines show.

In Figure 6.5 (left) are shown the simulations of the bands of l -C₃H₂ above 6000 Å, using the derived spectroscopic constants and a Lorentzian profile of width 0.15 Å, corresponding to the resolving power 40,000 used in astronomical measurements, for each individual line. The pattern is shown for temperatures of 5, 20, and 60 K. Three components, $K = 2-1$, $K = 1-0$, and $K = 0-1$ would be observed. At 5 K the population becomes concentrated in the $K = 0$ level of the X^1A_1 electronic ground state and thus the middle peak dominates. As the temperature rises the outer two peaks gain intensity because the population of the $K = 1$ level increases.

Though the resolving power in many astronomical measurements is around 40,000, observations such as those toward HD 206267 sample several clouds as the profiles of K and Ca lines show [50] and this leads to broadenings of 10-20 km s⁻¹, i.e., 0.2-0.4 Å in this wavelength region. Thus, the absorption pattern of l -C₃H₂ in such clouds would look like that shown in Figure 6.5 (right), where a 0.4 Å width (Lorentzian) is used in the simulation.

6.3.2.1.2. The 5450 Å Band

The 5450 and 4887 Å absorption bands of *l*-C₃H₂ are broad, without any rotational structure. This arises due to the short lifetime of the B^1B_1 electronic state as a result of the fast intramolecular relaxation process to the nearby lying A^1A_2 state. The profiles of the broad 5450 and 4887 Å bands can be predicted by simulating the 2_0^1 and 2_0^2 $B^1B_1 - X^1A_1$ transitions with the known rotational constants for the bands above 6000 Å [46]. Due to the broadness of the features, the precise value of the rotational constants has little influence on the overall contour. The bottom trace in Figure 6.6 shows the case with a 1 Å linewidth corresponding to 1 ps lifetime and a temperature of 10 K. Three components in the profile of this band would still be seen.

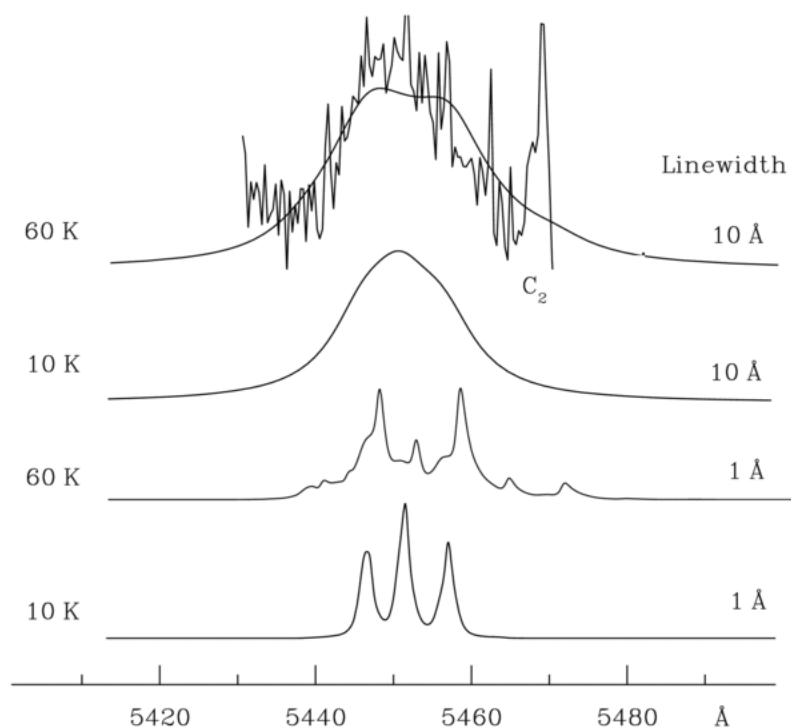


Figure 6.6: Simulation of the 5450 Å band profile of *l*-C₃H₂ $B^1B_1 - X^1A_1$ transition at 10 and 60 K taking 1 or 10 Å linewidth. The laboratory absorptions shown in Figure 6.4 were measured with a rotational temperature of around 60 K, determined by the rotational line intensity of the *l*-C₃H₂ bands above 6000 Å. The 10 Å linewidth corresponds to a lifetime of 100 fs for the excited electronic state.

The best fit to the observed 5450 Å profile was obtained with a 10 Å linewidth and 60 K temperature (top trace in Figure 6.6). The temperature of 60 K is chosen because the rotationally resolved bands of *l*-C₃H₂ measured above 6000 Å fit to 50-70 K. The linewidth of 10 Å corresponds to a 100 fs lifetime, which is often encountered in the

excited electronic states of polyatomic molecules subject to conical intersections. In fact in the case of $l\text{-C}_3\text{H}_2$, the next higher lying C^1A_1 electronic state, with onset near 2500 Å, has been shown experimentally to have a lifetime of 70 fs [51], so the inferred value of 100 fs is not unreasonable.

6.3.2.2. Astronomical Observations

6.3.2.2.1. Broad Bands

Broad absorptions are observed in the laboratory at 4887 and 5450 Å in the gas phase and one is predicted in the 5165-5185 Å range, but expected to be only one-half to one-third the strength of the 5450 Å absorption. The absorption spectrum in Figure 6.3 is a linear measurement and thus predicts that any corresponding DIBs should have comparable EWs and FWHM. There is a strong, broad DIB at 4881 Å with twice the FWHM (~ 25 Å), but similar central depth to the 5450 Å DIB. It is listed in many DIB compilations [26, 52, 53]. In early 2010, spectra were acquired in the regions of these DIBs at the Dominion Astrophysical Observatory with the 1.2 and 1.8 m telescopes at a resolution of $R = 18,000$ [4].

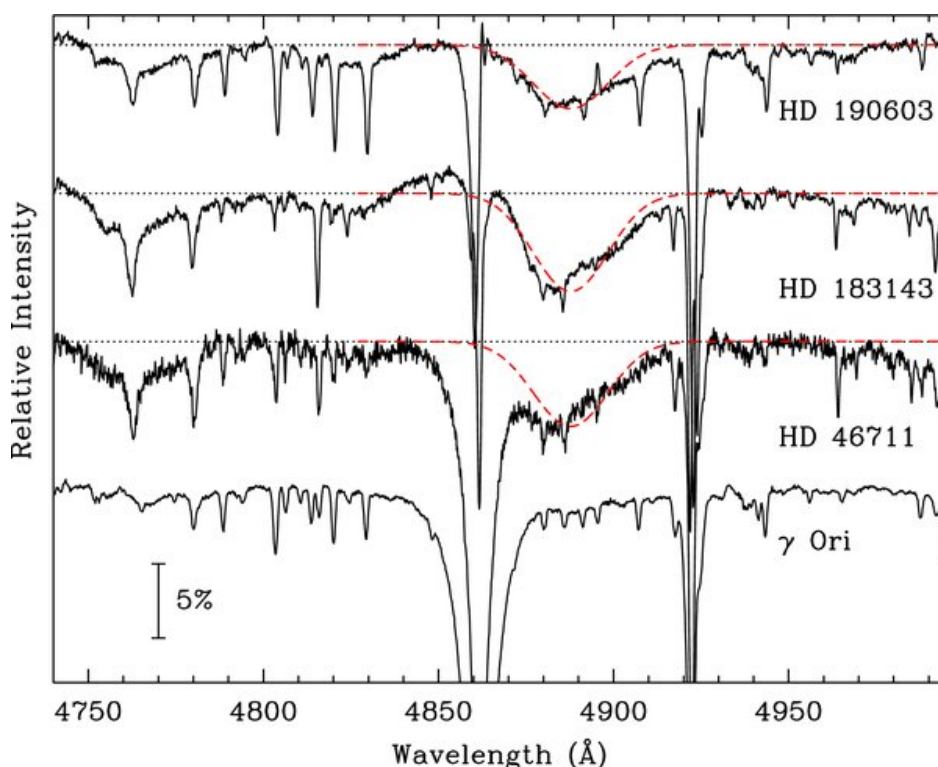


Figure 6.7: The 4881 Å DIB, already known from the literature, in spectra of HD 46711, 190603, 183143, and γ Ori, is compared to a Gaussian fit (FWHM 25 Å) to the laboratory absorption spectrum of $l\text{-C}_3\text{H}_2$ centered at 4887 Å (dashed red line). The short-wavelength side of the DIB profile is distorted to varying degrees by H_β at 4861 Å [4].

The coincidence of the laboratory and DIB profiles in the case of the 5450 Å band has already been discussed [40]. The Gaussian (25 Å FWHM) obtained from the CRD laboratory measurement of the 4887 Å absorption is superimposed on the DIB spectra in Figure 6.7. Astronomical spectra were newly recorded at 5450 Å and superposed with the laboratory recordings (Figure 6.8). The agreements in both cases are excellent. The wings of the strong stellar H_{β} line at 4861 Å make that part of the DIB hard to define for HD 46711. For the supergiant, HD 183143, there might also be a broad emission component.

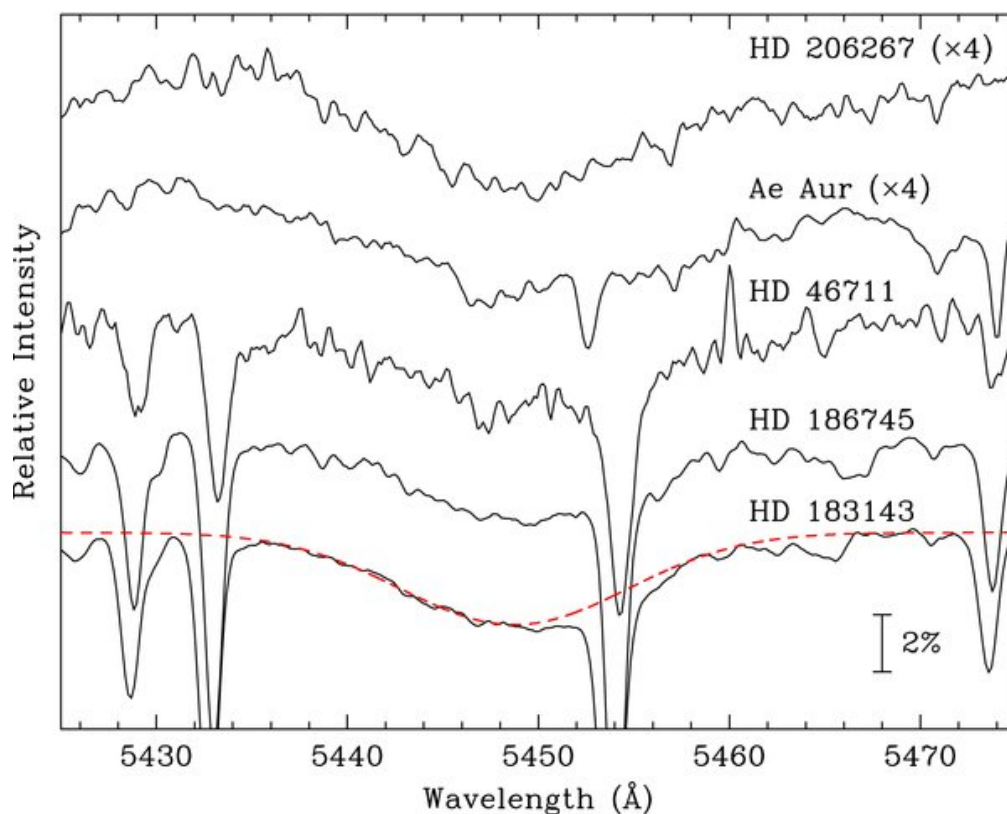


Figure 6.8: Spectra of HD 46711, 206267, 186745, 183143, and AE Aurigae showing the broad DIB at 5450 Å. The scales for the lightly reddened stars HD 206267 and AE Aurigae have been expanded by a factor 4. The gas-phase laboratory spectrum of $l\text{-C}_3\text{H}_2$ is shown by the dashed red curve superimposed on the HD 183143 spectrum. This confirms the agreement found earlier [40].

The case for a FWHM ~ 20 Å DIB in the 5165-5185 Å range is complicated by the presence of a previously known and well defined, broad DIB centered at 5160 Å. Unfortunately, the presence of strong stellar lines near 5173 Å in all the target stars make it impossible to say anything about an interstellar absorption feature in that

region. The intensities of the bands $< 4700 \text{ \AA}$ were below the detection limit of the CRD setup and hence not observed.

6.3.2.2.2. Narrow Triplets above 6000 \AA

The triplets offer quite a different challenge from the broad bands when it comes to unambiguous detection. An exact wavelength match was less critical for the broad bands.

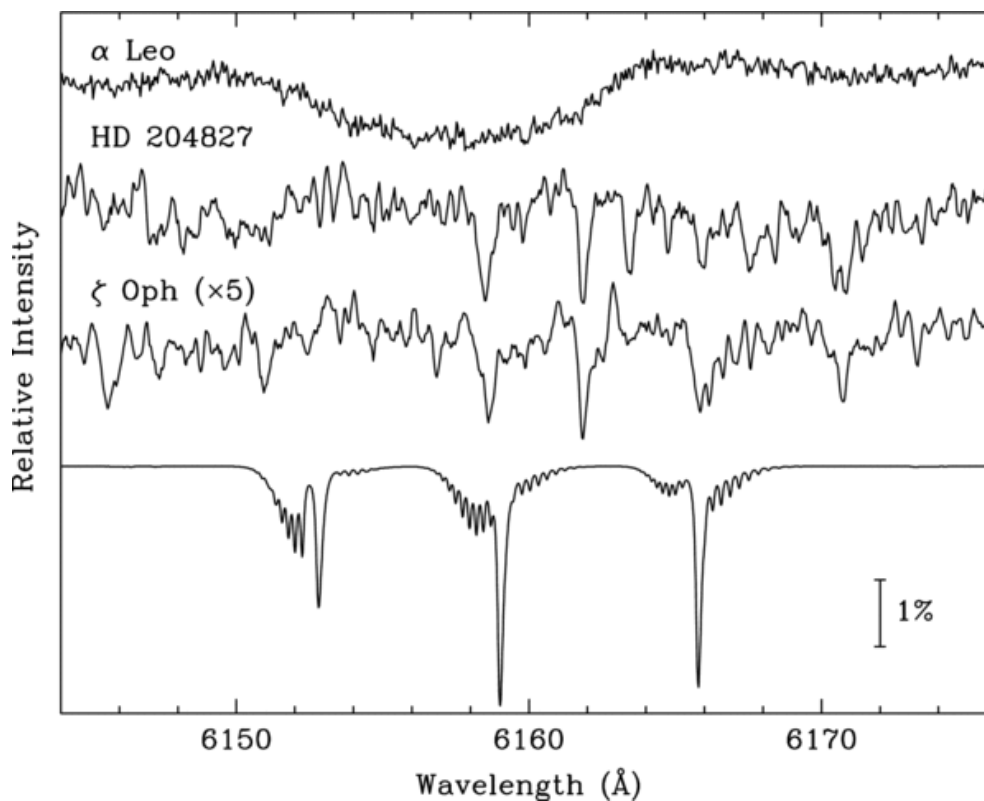


Figure 6.9: Spectra of HD 204827, ζ Oph, the unreddened standard, α Leo, and model line profiles for l -C₃H₂ at 10 K and 0.15 \AA FWHM. The spectrum for ζ Oph has been expanded by a factor of 5 relative to the others. The broad feature centered at 6159 \AA in α Leo is a rotationally broadened stellar line. Narrow DIBs lie within the 6159 and 6166 \AA model profiles for the two reddened stars [4].

There are many fewer broad DIBs known than sharp ones, making chance coincidence less likely. Also, the broad DIBs can be matched in width without significant distortion from spectral resolution and blurring by the velocity dispersion in the interstellar clouds. For the 4881 and 5450 \AA regions, there is little contamination by telluric lines and stellar lines are easily distinguished. By contrast, the spectra of the late-type B giants are full of stellar lines which are hard to distinguish from sharp DIBs. The highest density of sharp DIBs is in the 6000 \AA region, one every few \AA , which makes

the chance of coincidence likely. There are also many telluric lines. It should also be noted that the sharp DIBs of interest have central intensities of $<1\%$. As a result of these obstacles, the observations were restricted to reddened early B or O stars and spectra with a resolution $>40,000$ and signal-to-noise ratio (S/N) of several thousand per \AA [4].

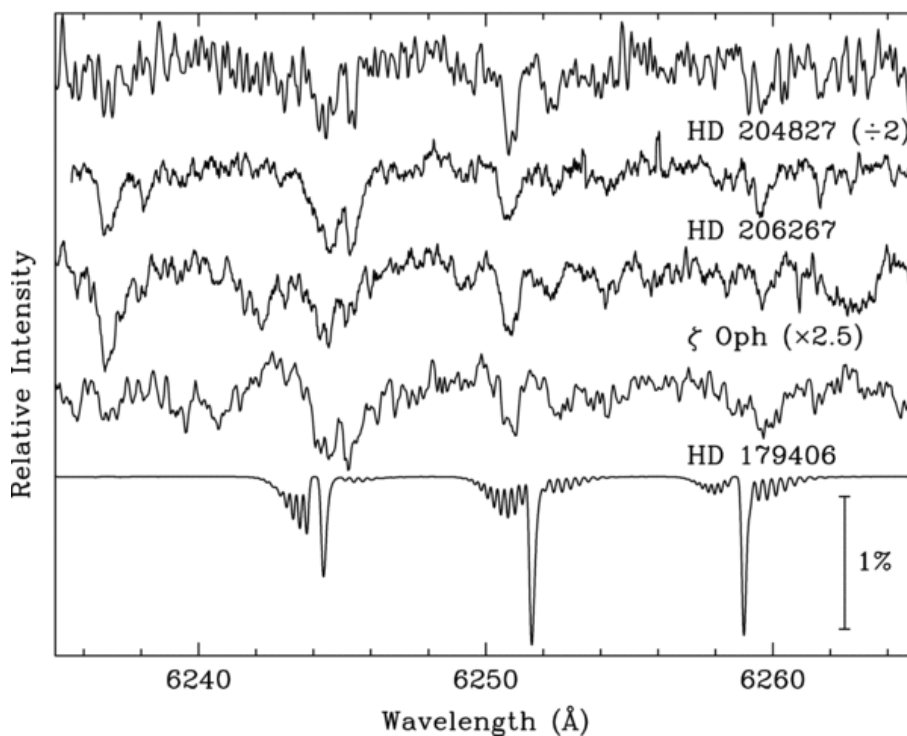


Figure 6.10: Spectra of HD 204827, HD 206267, ζ Oph, and HD 179406 together with model line profiles for l -C₃H₂ at 10 K and 0.15 \AA FWHM. The spectrum for ζ Oph has been expanded by a factor of 2.5 while that for HD 204827 has been halved. There are DIBs consistently within the limits of the model line profiles [4].

Figures 6.9 and 6.10 display the spectra of the reddened stars for two sets of the predicted l -C₃H₂ triplets together with model absorption profiles for 10 K and a 0.15 \AA FWHM, the latter to account for instrumental and interstellar broadening. There are clearly DIBs within the limits of the model profiles at 6159, 6166, 6244, 6251, and 6259 \AA . The line predicted at 6152 \AA was expected to be significantly weaker than those at 6159 and 6166 \AA , so the absence of a DIB at that wavelength is not necessarily a contradiction. The DIBs at 6244 and 6251 \AA appear to be doubles with the stronger component corresponding quite closely to the predicted absorption maximum.

For the triplets predicted near 6320 \AA , the region is heavily obscured by the telluric α -band of O₂ which, coupled with velocity corrections to the barycenter and

alignment to the interstellar K_1 velocities, makes it impossible to detect any DIB which might coincide with the predictions.

In none of the coincidences do the predicted profiles correspond well to those of the DIBs, suggesting that the intrinsic broadening is probably greater than the 0.15 Å assumed for the model. While the coincidences between DIBs and the model profiles are not unequivocal given the high density of sharp DIBs in this spectral region, their absence would have cast some doubt on the case for $l\text{-C}_3\text{H}_2$ as a DIB carrier.

6.3.3. Discussion

The choice of a rotational temperature for $l\text{-C}_3\text{H}_2$ in diffuse clouds has a consequence for the comparison with the laboratory data, as the simulations in Figure 6.5 and Figure 6.6 show. $l\text{-C}_3\text{H}_2$ has a large dipole moment (around 4 D) and may cool efficiently, in much the same way as do the diatomics CH, CH⁺, and CN, which attain 2.7 K in the diffuse medium. On the other hand, the temperatures inferred for other polar polyatomics detected in the diffuse medium are often higher, for example around 50 K for ammonia by millimeter-wave spectroscopy [54] and H_3^+ by IR measurements [55]. Due to the broadness of the 5450 Å DIB, the interstellar temperature of $l\text{-C}_3\text{H}_2$ cannot be clearly determined; anything in the range 10-60 K would fit as the two simulated profiles with 10 Å linewidth in Figure 6.6 show.

As a follow-up to the identification of $l\text{-C}_3\text{H}_2$ as a DIB carrier, one can make an estimate for the column density on the basis of the broad 5450 Å DIB. There are two calculations [56] of the overall oscillator strength, f , of the $B^1B_1 - X^1A_1$ electronic transition, 0.016 and 0.009. The former value was obtained with a higher level method and is used for the evaluation.

The f value for the 2_0^1 transition (5450 Å band) within this system is estimated from the calculation of the Franck–Condon factors [56]. This gives $f(2_0^1)/f_{\text{total}} (=0.016) = 0.2$.

Using the expression

$$N(\text{cm}^{-2}) = 1.13 \times 10^{20} \frac{EW(\text{Å})}{\lambda(\text{Å})^2 \times f}$$

yields for $\Lambda = 5450 \text{ \AA}$, $f(2_0^1) = 0.003$, $EW = 0.4 \text{ \AA}$ toward HD 183143: $N(l\text{-C}_3\text{H}_2) = 5 \times 10^{14} \text{ cm}^{-2}$.

Toward HD 183143, the column density of H_3^+ has been determined to be 10^{14} cm^{-2} [55] and $N(\text{C}_2) \approx 10^{14} \text{ cm}^{-2}$ [57]. Thus, the N value estimated for $l\text{-C}_3\text{H}_2$ is not unreasonable.

Thus the observations suggest that the broad, diffuse interstellar bands at 4881 and 5450 \AA are caused by the $B^1B_1 - X^1A_1$ transition of H_2CCC ($l\text{-C}_3\text{H}_2$). The large widths of the bands are due to the short lifetime of the B^1B_1 electronic state. The bands, predicted from absorption measurements in a neon matrix and observed by cavity ring-down in the gas phase, show exact matches to the profiles and wavelengths of the two broad DIBs. The strength of the 5450 \AA DIB leads to a $l\text{-C}_3\text{H}_2$ column density of $\sim 5 \times 10^{14} \text{ cm}^{-2}$ toward HD 183143 and $\sim 2 \times 10^{14} \text{ cm}^{-2}$ to HD 206267. Despite similar values of $E(B - V)$, the 4881 and 5450 \AA DIBs in HD 204827 are less than one-third their strength in HD 183143, while the column density of interstellar C_3 is unusually high for HD 204827 but undetectable for HD 183143. This can be understood if C_3 has been depleted by hydrogenation to species such as $l\text{-C}_3\text{H}_2$ toward HD 183143.

Bibliography

- [1] Nagarajan, R.; Maier, J. P. *Int. Rev. Phys. Chem.*, 29, 521, **2010**.
- [2] Belloche, A.; Garrod, R. T.; Mueller, H. S. P.; Menten, K. M.; Comito, C.; Schilke, P. *Astron. Astrophys.* 499, 215, **2009**.
- [3] Heger, M. L. *Lick. Obs. Bull.*, 10, 146, **1922**.
- [4] Maier, J. P.; Walker, G. A. H.; Bohlender, D. A.; Mazzotti, F. J.; Raghunandan, R.; Fulara, J.; Garkusha, I.; Nagy, A. *Astrophys. J.* 726, 41, **2011**.
- [5] <http://leonid.arc.nasa.gov/pjenniskens.html>
- [6] Merrill, P. W.; Wilson, O. C. *Astrophys. J.* 87, 9, **1938**.
- [7] Eyster, E. H. *Astrophys. J.* 86, 486, **1937**.
- [8] Swings, P. *MNRAS* 97, 212, **1937**.
- [9] Herbig, G. H. *Astrophys. J.* 137, 200, **1963**.
- [10] Duley, W. W. *Nature* 218, 153, **1968**.
- [11] Duley, W. W.; Graham, W. R. M. *Nature*, 224, 785, **1969**.
- [12] Adamson, A. J.; Whittet, D. C. B. *Astrophys. J.* 398, L69, **1992**.
- [13] Weinreb, S.; Barrett, A. H; Meeks, M. L.; Henry, J. C. *Nature* 200, 829, **1963**.
- [14] Smith, W. H.; Snow, T. P.; York, D. G. *Astrophys. J.* 218, 124, 1977.
- [15] Douglas, A. E. *Nature* 269, 130, **1977**.
- [16] Sarre, P. J.; Miles, J. R.; Kerr, T. H.; Hibbins, R. E.; Fossey, S. J. et al. *MNRAS* 277, L41, **1995**.
- [17] Sonnentrucker, P.; Cami, J.; Ehrenfreund, P.; Foing, B. H. *Astron. Astrophys.* 327, 1215, **1997**.
- [18] Thorburn, J. A.; Hobbs, L. M.; McCall, B. J.; Oka, T.; Welty, D. E. et al. *Astrophys. J.* 584, 339, **2003**.
- [19] Gillette, F. C.; Forest, W. J.; Merrill, K. M. *Astrophys. J.* 183, 87, **1973**.
- [20] Ruitkamp, R.; Cox, N. L. J.; Spaans, M.; Kaper, L.; Foing, B. H. et al. *Astron. Astrophys.* 432, 515, **2005**.
- [21] Maier J. P.; Walker, G. A. H.; Bohlender, D. A. *Astrophys. J.* 602, 286, **2004**.
- [22] Snow, T. P.; McCall, B. J. *Annu. Rev. Astron. Astrophys.* 44, 367, **2006**.
- [23] Maier, J. P.; Lakin, N. M.; Walker, G. A. H.; Bohlender, D. A. . *Astrophys. J.* 553, 267, **2001**.
- [24] Cox, P.; Güsten, R.; Henkel, C. *Astron. Astrophys.*, 206, 108, **1988**.

- [25] Liszt, R.; Lucas, R. *Astron. Astrophys.*, 358, 1069, **2000**.
- [26] Herbig, G. H. *Annu. Rev. Astron. Astrophys.* 33, 19, **1995**.
- [27] Motylewski, T. et al. *Astrophys. J.* 531, 312, **2000**.
- [28] Biennier, L.; Salama, F.; Allamandola, L. J.; Scherer, J. J.; *J. Chem. Phys.*, 118, 7863, **2003**.
- [29] Iglesias-Groth, S., Manchado, A., García-Hernández, D. A., González Hernández, J. I., & Lambert, D. L. *Astrophys. J.* 685, L55, **2008**.
- [30] Krełowski, J., Beletsky, Y., Galazutdinov, G. A., Kołos, R., Gronowski, M., & LoCurto, G. *Astrophys. J.* 714, L64, **2010**.
- [31] Maier, J. P.; Chakrabarty, S.; Mazzotti, F. J.; Rice, C. A.; Dietsche, R.; Walker, G. A. H.; Bohlender, D. A. *Astrophys. J. Lett.*, 729, L20, **2011**.
- [32] Searles, J. M.; Destree, J. D.; Snow, T. P.; Salama, F.; York, D. G.; Dahlstrom, J. *Astrophys. J.* 732, 50, **2011**.
- [33] Herbig, G. H. *Astrophys. J.* 271, 734, **1993**.
- [34] Beals, C. S.; Blanchet, G. H.; *Publ. Astr. Soc. Pac.* 49, 224, **1937**.
- [35] Cox, N. L. J.; Kaper, L.; Foing, B. H.; Ehrenfreund, P. *Astron. Astrophys.* 438, 187, **2005**.
- [36] Wallerstein, G.; Sandstrom, K.; Gredel, R. *Publ. Astr. Soc. Pac.* 119, 1268, **2007**.
- [37] Jenniskens, P.; Ehrenfreund, P.; Desert, F. X. *Astron. Astrophys.* 256, 1, **1992**.
- [38] Deeming, T. J.; Walker, G. A. H. , *ZsfAp*, 66, 175, **1967**.
- [39] Chlewicki, G.; van der Zwet, G. P.; van Ijzendoorn, L. J.; Greenberg, J. N. *Astrophys. J.* 305, 455, **1986**.
- [40] Linnartz, H.; Wehres, N.; Van Winckel, H.; Walker, G. A. H.; Bohlender, D. A.; Tielens, A. G. G. M.; Motylewski, T.; Maier, J. P. *Astron. Astrophys.*, 511, L3, **2010**.
- [41] Vrtilik, J. M.; Gottlieb, C. A.; Gottlieb, E. W.; Killian, T. C.; Thaddeus, P. A. *ApJ*, 364, L53, **1990**.
- [42] Cernicharo, J.; Gottlieb, C. A.; Guélin, M.; Killian, T. C.; Paubert, G.; Thaddeus, P.; Vrtilik, J. *ApJ*, 368, L39, **1991**.
- [43] Cernicharo, J.; Cox, P.; Fossé, D.; Güsten, R. *Astron. Astrophys.*, 351, 341, **1999**.
- [44] Madden, S. C.; Irvine, W. M.; Matthews, H. E.; Friberg, P.; Swade, D. A. *ApJ*, 97, 1403, **1989**.
- [45] Hodges, J. A.; McMahon, R. J.; Sattelmeyer, K. W.; Stanton, J. F. *ApJ*, 544, 838, **2000**.
- [46] Achkasova, E.; Araki, M.; Denisov, A.; Maier, J. P. *J. Mol. Spectrosc.*, 237, 70, **2006**.

- [47] Birza, P.; Chirokolava, A.; Araki, M.; Kolek, P.; Maier, J. P. *J. Mol. Spectrosc.*, 229, 276, **2005**.
- [48] Jacox, M. E. *J. Phys. Chem. Ref. Data*, 3, 1, **1994**.
- [49] Ding, H.; Pino, T.; Güthe, F.; Maier, J. P. *J. Chem. Phys.*, 115, 6913, **2001**.
- [50] Pan, K.; Federman, S. R.; Cunha, K.; Smith, V. V.; Welthy, D. E. *ApJ Supp.*, 151, 313, **2004**.
- [51] Noller, B.; Margraf, M.; Schröter, C.; Schultz, T.; Fischer, I. *Phys. Chem. Chem. Phys.*, 11, 5353, **2009**.
- [52] Jenniskens, P.; Désert, F.-X. *Astron. Astrophys. Supp.*, 106, 39, **1994**.
- [53] Hobbs, L. M.; York, D. G.; Snow, T. P.; Oka, T.; Thorburn, J. A.; Bishof, M.; Friedman, S. D.; McCall, B. J.; Rachford, B.; Sonnentrucker P.; Welty, D. E. *ApJ*, 680, 1256, **2008**.
- [54] Liszt, H. S.; Lucas, R.; Pety, J. *Astron. Astrophys.*, 448, 253, **2006**.
- [55] McCall, B. J.; Hinkle, K. H.; Geballe, T. R.; Moriarty-Schieven, G. H.; Evans II, N. J.; Kawaguchi, K.; Takano, S.; Smith, V. V.; Oka T. *ApJ*, 567, 391, **2002**.
- [56] Mebel, A. M.; Jackson, W. M.; Chang, A. H. H.; Lin, S. H. *J. Am. Chem. Soc.*, 120, 5751, **1998**.
- [57] Oka, T.; Thorburn, J. A.; McCall, B. J.; Friedman, S. D.; Hobbs, L. M.; Sonnentrucker, P.; Welty, D. E.; & York, D. G. *ApJ*, 582, 823, **2003**.

Chapter 7

Selective Determination of Radicals and Ions by Four-wave Mixing Technique

7.1. Introduction

This chapter demonstrates the potential of four-wave mixing (FWM) for the study of neutral and charged radicals generated in electrical discharges, both in terms of selectivity and sensitivity [1]. The technique is applied to the detection of both neutrals and ions like C_4H , HC_2S , HC_4H^+ and C_2^- in diluted plasmas. HC_4H^+ and C_2^- are the first ions to be detected by four-wave mixing spectroscopy.

Charged and neutral carbon radicals are of importance in various reactive environments, including planet atmospheres, combustion and interstellar media. However spectral measurements on these molecules are difficult because they are short-lived species, generated in small number densities. Also, a high spectral congestion due to the various species present in the expansion may hinder the sensitivity and selectivity of spectroscopic methods, resulting in overlapping spectra and sometimes higher background. This complicates the identification of these species.

The advantages of slit nozzles over circular nozzles in supersonic absorption spectroscopy have been discussed in chapter 4. The slit-jet expansion discharge has been recently coupled with resonantly enhanced four-wave mixing spectroscopy for the detection of HC_4S [2]. Initial studies showed that the sensitivity of degenerate four wave mixing (DFWM) using a slit nozzle can be significantly increased by several hundred times compared with the use of a circular pulsed discharge source, in agreement with an earlier report [3] and in accordance with the quadratic dependence exhibited by DFWM with the interaction path length. Estimates made on OH in a flame gave detection limits of $\sim 10^{11}$ molecules cm^{-3} per quantum state for DFWM [4]. After these first investigations, the technique remained yet to be coupled with the supersonic expansion discharge. The precision required in the alignment procedure, involving the spatial

positioning of three beams for which a high quality transverse profile plays a crucial role in the sensitivity and the artificial background created by scattering sources (*i.e.* windows) make this method relatively difficult to implement, in comparison with pulsed CRDS or LIF.

Current measurements show that DFWM can be almost as sensitive as the CRDS or LIF methods but with increased selectivity once combined with a short and timed discharge pulse. A background-free absorption signal with a high dynamic range makes DFWM more advantageous than CRDS. DFWM is also suited to study spectroscopic properties of non-fluorescing or predissociative molecules [5, 6], in contrast to LIF. Further improvements in species selectivity and sensitivity are achieved by the application of the double resonance variant of FWM, two-color resonant four-wave mixing spectroscopy (TC-RFWM) [7].

7.2. Experimental

The pulsed discharge slit nozzle has already been described in chapter 4. The slit used was $30 \times 1 \text{ mm}^2$. The high voltage applied was in the range of -400 to -1200 V, whereas the backing pressure was around 10 bar for the measured species. The average pressure in the vacuum chamber was kept to 0.05 mbar. The pulse valve was opened for 300 μs , and the discharge was on for 0.3-3 μs with the FWM technique. The pulse delay between the high voltage pulse and the laser was in the range of 4-10 μs , depending on the distance of the interaction region with the slit nozzle as well as the carrier being detected. The timing sequence was controlled by a delay pulse generator with a precision of 0.25 ns. Gas mixtures used for the efficient production of the HC_2S and C_4H radicals were $\text{CS}_2/\text{C}_2\text{H}_2/\text{Ar}$ (0.5/1/98.5%) and $\text{C}_2\text{H}_2/\text{Ar}$ (1/99%), respectively. For the production of the diacetylene cation, the precursor was C_2H_2 (or C_4H_2) diluted in argon.

Because the signal beam generated by the FWM process is coherent in nature, it is efficiently rejected against stray or scattered radiation by the use of spatial filters, irises, and a long path length from the interaction region to the detector. This enables the recording of background-free spectra, a high signal-to-noise (S/N) offering both high sensitivity and precise line positioning. The S/N achieved was on the order of $\sim 10^3$ for the strongest spectral lines of C_4H and HC_4H^+ and $\sim 10^4$ for HC_2S . The laser energy was kept in the 100 μJ per pulse adjusted by neutral density filters.

At low laser power, the DFWM signal is cubically dependent on laser intensity of the beams. For sufficiently large laser powers, the widths of the rotational lines can be severely broadened and may lead to line width splitting (saturation dip). In accordance with the DFWM theory, the line width of the rotational lines is dependent on the laser power. Under appropriate saturation conditions, the DFWM signal intensity is proportional to the square of the absorption cross section and number densities. Early experimental studies have also confirmed these theoretical predictions [8]. This saturation intensity is, of course, dependent on the selected species.

7.3. Species Selectivity in the Temporal Domain

The probing time of the DFWM technique is equal to the laser pulse duration (presently 7 ns). This is at least 3 orders of magnitude shorter than the time required for the operation of CRDS. In order to study transient species generated in the plasma, an optimal use of CRDS requires discharge pulse duration of several tens of μs . Current observations show that at such timings a large number of spectral carriers can be detected simultaneously, which results in congested spectra. The probing duration of DFWM offers the possibility to use short but intense high voltage pulses while maintaining appropriate generation conditions. Application of a pulse in the sub- μs range, however, has a drastic effect on the temporal distribution of the radicals in the molecular beam. Although a modeling of this process was not carried out, one can assume that the discharge pulse generates upstream, relatively to the slit, a reservoir of radicals with approximately the same kinetic energies. The design of the pulsed discharge nozzle is such that the residence time of the molecules in this active region is on the order of a few μs [9]. These subsequently expand towards the lower pressure regions with speeds in accordance to their masses. The current experimental conditions generate a highly dense and short (1 μs) molecular pulse. It was observed that molecules with different masses travel through the interaction region at varying times (within the range of several μs).

For neutrals, the lighter ones are measured at shorter laser-discharge delays. It is hence possible to discriminate the carriers by using short discharge pulses and appropriate time delays between the high voltage and laser firing. In such conditions, efficient radical selectivity is achieved which, in combination with a background-free

signal, results in a highly sensitive spectroscopic detection. When carrying out experiments with CRDS, its limitations impose the use of a 20 μs long high voltage pulse, generating a sufficiently long temporal distribution of the species for an efficient detection, but at a price in selectivity. The experimental illustration of this effect is shown in Figure 7.1. The spectra recorded with DFWM are readily assigned to either a hot band of the C_3 $A^1\Pi_u - X^1\Sigma_g^+$ or to the $B^2\Pi_i - X^2\Sigma^+$ (5_0^3) of C_4H [10], depending on the discharge delays, while the CRDS trace is rather congested. Notice that in the spectrum recorded with a longer laser-discharge delay (9 μs instead of 7 μs), the C_3 lines are completely absent.

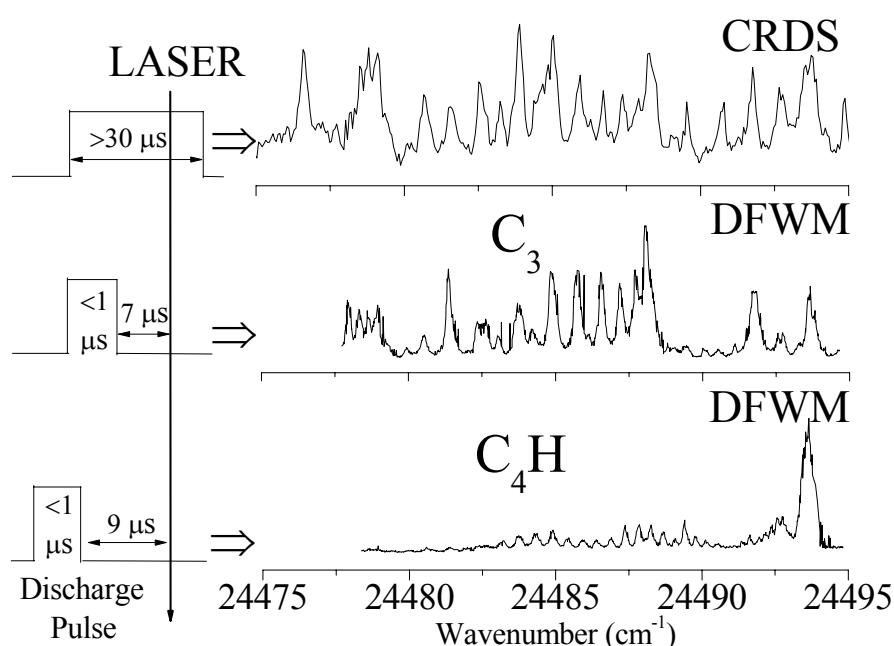


Figure 7.1: The selectivity offered by DFWM combined with a short and intense discharge high voltage pulse. Increasing the delay between the discharge and the laser by 2 μs enables disentanglement of the $B^2\Pi_i - X^2\Sigma^+$ (5_0^3) spectrum of C_4H which overlaps with a hot band of the $A^1\Pi_u - X^1\Sigma_g^+$ C_3 electronic transition. Top is a CRD scan which can only be combined with a discharge period of at least 20 μs , for which the C_3 and C_4H transitions overlap.

7.4. Species selectivity by Two-Color Resonant FWM

The two-color resonant four-wave mixing spectra were obtained by tuning the pump laser frequency to a molecular line while the probe laser was scanned. The recordings then show only the transitions which are resonant (*i.e.* involving a common state with the pump transition; either the upper state in stimulated emission pumping (SEP) or the lower state in the UP scheme), leading to simple and unambiguously assigned spectra,

even in the case of congested features. By taking advantage of this effect, it is possible to disentangle a transition of HC_2S which overlaps with the origin band of the C_3 $A^1\Pi_u - X^1\Sigma_g^+$ system (Figure 7.2).

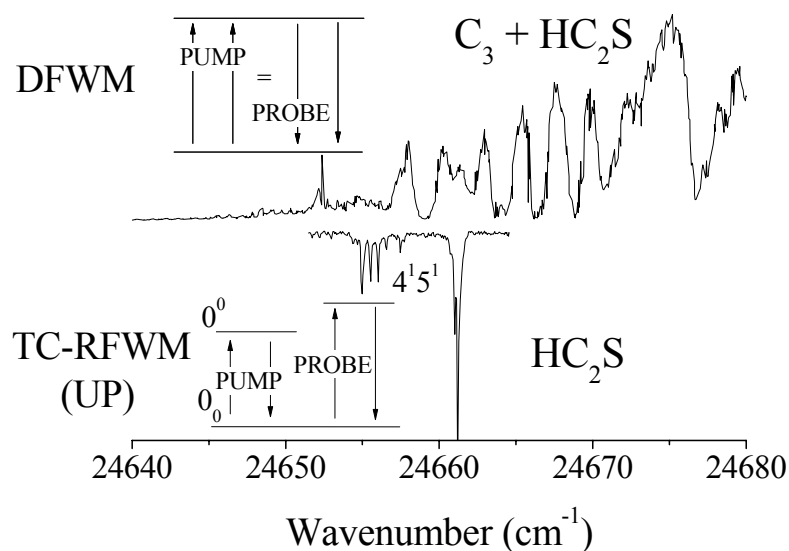


Figure 7.2: Scan showing the power of TCFWM for disentangling overlapping spectra. Upper trace is a DFWM spectrum recorded near the origin band of the C_3 cometary system. In the TC-RFWM case, where the pump wavelength is set to the origin band of HC_2S , scanning the probe frequency reveals rovibronic spectrum of this selected species (inverted trace). The origin band of C_3 is no longer resonant and is absent.

The DFWM scan of the region shows the intense C_3 origin band in the same spectral region where a vibronic feature of the $A^2\Pi_{3/2} - X^2\Pi_{3/2}$ electronic transition of HC_2S is blended and for which a rotational analysis cannot be readily carried out. By tuning the pump to the R branch of the origin of HC_2S and scanning the probe across the $4^1_0 5^1_0$ band, a rotationally resolved spectrum arising purely from HC_2S is obtained. In addition, the method offers the possibility to study the rotational structure in the ground state vibrational levels by carrying out optical-optical measurements based on a stimulated emission pumping scheme [11]. These recordings exemplify the main advantages of using TC-RFWM for the study of transient molecules, namely high sensitivity, species and spectral selectivity.

7.5. Detection of Ions by FWM

The detection of C_2 and C_3 with S/N of 10^6 - 10^8 and C_4H , HC_2S , HC_4S with S/N of 10^3 - 10^4 suggests that other radicals, including ions can be studied with this technique. The previously studied HC_4H^+ cation [12] was chosen in order to estimate the sensitivity of DFWM for the detection of charged molecules. Figure 7.3 shows the DFWM spectrum recorded near the band origin of the $A^2\Pi_u - X^2\Pi_g$ transition of HC_4H^+ by probing the ions close to the slit, near the region where the discharge is formed and where the density of the ions is the highest.

This is the first detection of a polyatomic cation by DFWM in a supersonic expansion discharge. The two bandheads are due to the two spin-orbit components. The doublets are inverted so that the $^2\Pi_{3/2}$ component is the most populated, corresponding to the strongest R_1 branch. The rotational temperature is estimated to be around 50 K.

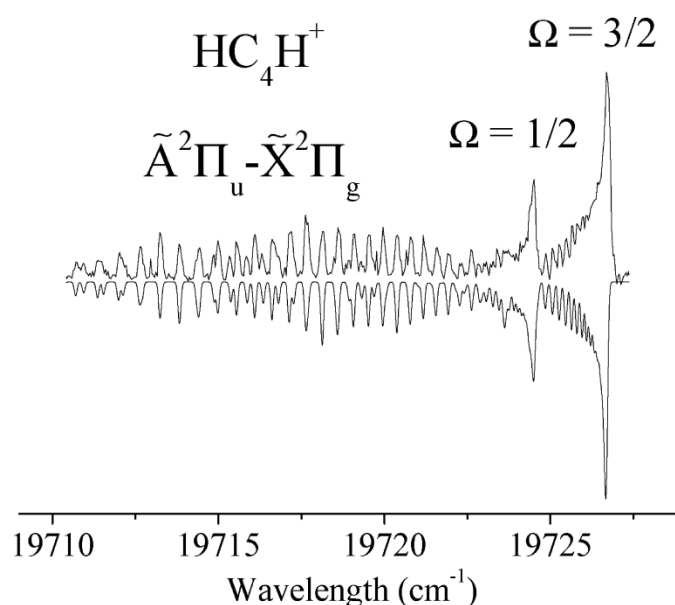


Figure 7.3: The top and bottom traces are the experimental DFWM and simulated spectra respectively, of the $A^2\Pi_u - X^2\Pi_g$ electronic transition of the diacetylene cation. The two spin-orbit components of HC_4H^+ overlap. The delay between the high voltage and the laser was set to 4-5 μ s. Notice the high S/N.

It can be noticed that changing the delay between the valve and the discharge from 600 μ s to 1.2 ms results in the $d^2\Pi_g - a^2\Pi_u$ electronic transition of the C_2 molecule being replaced by the $A^2\Pi_u - X^2\Pi_g$ transition of HC_4H^+ (Figure 7.4). While in the case

of the detection of neutrals, the delays between the laser and the discharge pulses are quite predictable and somewhat follow the kinetic rule (heavier species are slower than lighter ones), the detection of ions show some irregularities. For instance, to record the spectrum of HC_4H^+ , a laser-discharge delay of 4-5 μs was applied, whereas one would expect a similar delay as is used for the detection of C_4H (9 μs) which has almost an identical mass. Although this behaviour is not fully understood, it is partly due to the electrostatic effects caused by the high voltage DC electric field, oriented downstream parallel to the expansion and accelerating the positive ions [9].

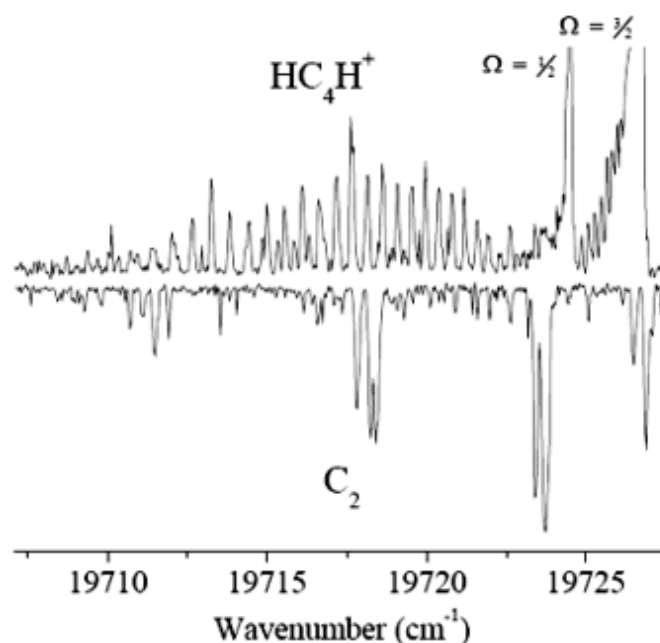


Figure 7.4: An illustration of the disentanglement of the C_2 (bottom trace) and HC_4H^+ (top trace) spectra using degenerate four-wave mixing. By changing the delay between the opening of the valve and the firing of the discharge (from 1.2 ms to 600 μs), it is possible to selectively obtain either the HC_4H^+ $A^2\Pi_u - X^2\Pi_g$ or the 3-3 hot band of the $d^2\Pi_g - a^2\Pi_u$ C_2 electronic transition.

A rather unique application of TC-RFWM is the selective disentanglement of overlapping transitions belonging to the same carrier, as demonstrated in Figure 7.5. TC-RFWM enables a study of rotational features belonging to either spin-orbit component of the origin band of the $A^2\Pi_u - X^2\Pi_g$ electronic system of HC_4H^+ . The pump laser was set near the bandhead of the $\Omega = 3/2$ component (at 19726.60 cm^{-1}). The resonant transitions consist of the $R_1(15.5)$ and $R_1(16.5)$ (corresponding to the degenerate case) and of four lines in the P_1 branch which are unambiguously assigned. The resonant lines in the Q_1 branch are too weak to be observed (by an order of

magnitude). The lines in the P_1 branch are 10-fold weaker than the in the R_1 branch due to the relatively high rotational temperature of the species (~ 50 K). However, because of the high S/N achieved, they are readily detected. This illustrates the ability of the technique to disentangle overlapping spectral features within the same spectroscopic system.

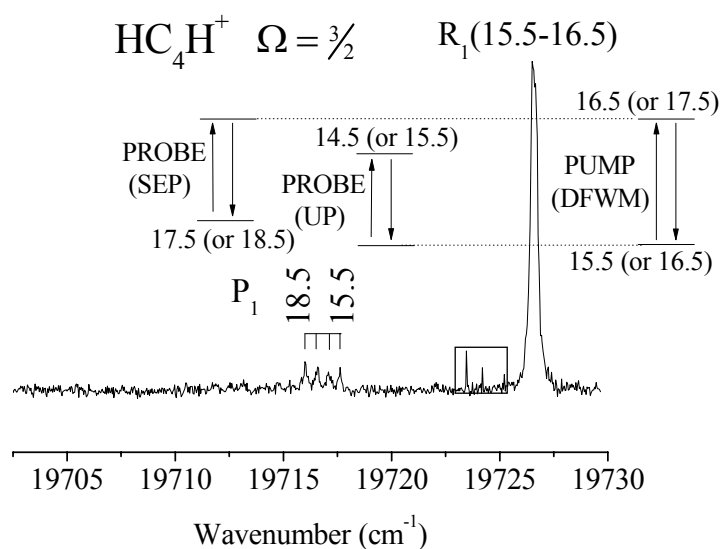


Figure 7.5: Two-color, resonant four-wave mixing scan of the $A^2\Pi_u - X^2\Pi_g$ electronic transition of HC_4H^+ obtained by setting the pump laser on the bandhead of the $\Omega = 3/2$ spin-orbit component (at 19726.60 cm^{-1}). Due to the double-resonance character of the technique, the $\Omega = 1/2$ component is absent from the trace, exemplifying the potential for disentangling overlapping features within the same spectroscopic system. Discharge fluctuations during the scan are indicated in the box.

DFWM can also be applied to the detection of negative ions. Figure 7.6 shows a DFWM trace made in the vicinity of the 1-0 $B^2\Sigma_u^+ - X^2\Sigma_g^+$ electronic transition of C_2^- . The plotted simulation used the spectroscopic constants determined previously [13]. Species selectivity by varying the discharge-probe laser delay was not as efficiently achieved as is the case of C_3 and C_4H . One of the reasons can be that the masses of C_2 and C_2^- are equal and separation due to kinetic effect is not effective in this case. Nevertheless, spectral selection can still be achieved by applying TC-RFWM. The spectrum in Figure 7.6 exhibits a relatively high S/N, greater than 10^2 for the strongest lines. This is the first detection of an anion using the technique. The observations suggest that four-wave mixing can be applied to the sensitive detection of negative and

positive ions and might serve as a general tool for the study of rotationally resolved transitions of ions in the future.

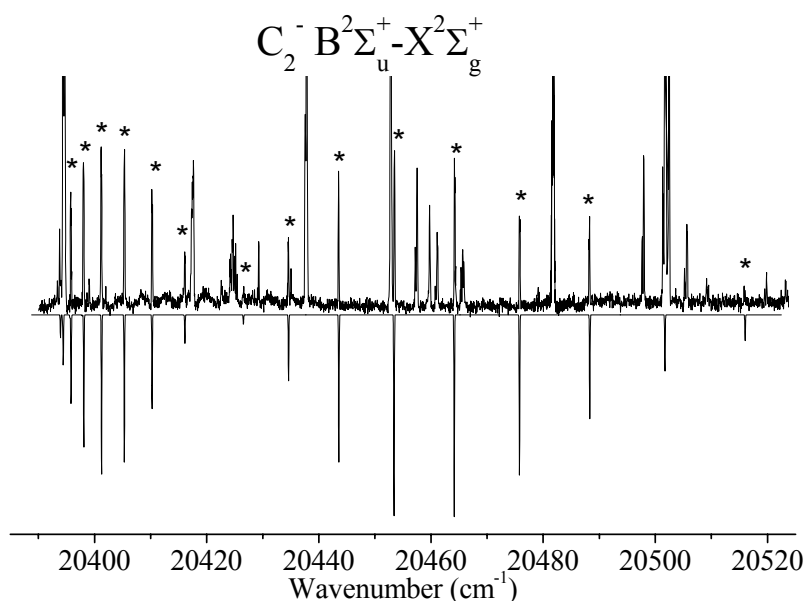


Figure 7.6: DFWM recording of the (1-0) $B^2\Sigma_u^+ - X^2\Sigma_g^+$ electronic transition of C_2^- (indicated with stars). The unmarked lines originate from hot bands of the $d^2\Pi_g - a^2\Pi_u$ system of C_2 . The inverted trace is the square of the simulated absorption spectrum at a rotational temperature of 300 K, a 0.1 cm^{-1} linewidth.

7.6. Sensitivity of DFWM

Although affected by a greater than linear dependence on number density, DFWM and TC-RFWM spectroscopies were proved to be sufficiently sensitive for the detection of less abundant radicals generated in discharges. In fact, the quadratic dependence of the DFWM signal on the interaction length leads to a significant enhancement in sensitivity once combined with the slit-jet source and offers selective probing of the species of interest when a short, intense discharge pulse is applied to the electrodes.

	C_2	HC_4S [11]	C_2^-	HC_4H^+
S/N	10^6	10^3	$>10^2$	10^3
DL (mol. cm^{-3})	10^9	3×10^9	$<5 \times 10^8$	$\sim 10^9$
Rotational Temp.(K)	140	30	250	65

Table 7.1: Detection limits achieved by DFWM for the studied radicals.

The density of the neutrals determined from parallel measurements carried out by the self-calibrated CRDS yields a detection limit (DL) around 10^9 molecules cm^{-3} for DFWM. Given the oscillator strength of the $A^2\Pi_u - X^2\Pi_g$ transition of HC_4H^+ (~ 0.04) [14] and an absorption coefficient measured by CRDS of $\sim 10^{-4}$ cm^{-1} , this yields a concentration of 3×10^{10} molecules cm^{-3} for the charged species. As the S/N by DFWM is around 10^3 , a DL of approximately 10^9 ions cm^{-3} was inferred. This is in accordance with earlier estimations made for selected radicals bearing similar intensities in the transition dipole moments (Table 7.1). The DL for C_2^- was estimated from the oscillator strength [15] and the Franck-Condon factor of the (1-0) transition [13] and scaled with respect to the C_2 DFWM signal intensity and density estimations obtained by CRDS.

Bibliography

- [1] Raghunandan, R.; Mazzotti, F. J.; Chauhan, C.; Tulej, M.; Maier, J. P. *J. Phys. Chem.* 113, 13402, **2009**.
- [2] Mazzotti, F. J.; Achkasova, E.; Chauhan, R.; Tulej, M.; Radi, P. P.; Maier, J. P. *Phys. Chem. Chem. Phys.* 10, 136, **2008**.
- [3] Mueller, T.; Vaccaro, P. H. *Chem. Phys. Lett.* 266, 575, **1997**.
- [4] Dreier, T.; Rakestraw, D. J. *Opt. Lett.* 15, 72, **1990**.
- [5] Butenhoff, T. J.; Rohlfing, E. A. *J. Chem. Phys.* 98, 5460, **1993**.
- [6] Dunlop, J. R.; Rohlfing, E. A. *J. Chem. Phys.* 100, 856, **1994**.
- [7] Ashfold, M. N. R.; Chandler, D. W.; Hayden, C. C.; McKay, R. I.; Heck, A. J. R. *Chem. Phys.* 201, 237, **1995**.
- [8] Farrow, R. L.; Rakestraw, D. J. *Science* 257, 1894, **1992**.
- [9] Remy, J.; Biennier, L.; Salama, F. *Plasma Sources Sci. Technol.* 12, 295, **2003**.
- [10] Hoshina, K.; Kohguchi, H.; Ohshima, Y.; Endo, Y. *J. Chem. Phys.* 108, 3465, **1998**.
- [11] Chauhan, R.; Mazzotti, F.J.; Raghunandan, R.; Tulej, M.; Maier, J.P.; Radi, P.P. *J. Phys. Chem.A.* 114, 3329, **2010**.
- [12] Kuhn, R.; Maier, J. P.; Ochsner, M. *Mol. Phys.* 59, 441, **1986**.
- [13] Jones, P. L.; Mead, R. D.; Kohler, B.E.; Rosner, S. D.; Lineberger, W. C. *J. Chem. Phys.* 73, 4419, **1980**.
- [14] Maier, J. P.; Thommen, F. *J. Chem. Phys.* 73, 5616, **1980**.
- [15] Leutwyler, S.; Maier, J. P.; Misev, L. *Chem. Phys. Lett.* 91, 206, **1982**.

Chapter 8

Non-Adiabatic Interactions - Renner Teller and Fermi Resonance Effects

8.1. Introduction

This chapter summarizes the Renner-Teller (R-T) vibronic analyses carried out on HC_4H^+ [1] and C_4H [2]. It also presents a theoretical overview of the non-adiabatic effects encountered in molecules. The sensitivity of two-color resonant four-wave mixing in the detection of weak vibronic levels is exemplified in the case of C_4H .

8.2. The Molecular Hamiltonian and the Born-Oppenheimer Approximation

The separation of electronic and nuclear motion forms the basis of the Born-Oppenheimer (BO) approximation, and molecular spectroscopy. The non-relativistic molecular Hamiltonian is given by [3, 4, 5, 6]

$$\hat{H} = \frac{-\hbar^2}{2} \sum_{\alpha} \frac{\nabla_{\alpha}^2}{M_{\alpha}} - \frac{\hbar^2}{2m_e} \sum_i \nabla_i^2 + \sum_{\alpha} \sum_{\beta > \alpha} \frac{Z_{\alpha} Z_{\beta} e^2}{4\pi \epsilon_0 r_{\alpha\beta}} - \sum_{\alpha} \sum_i \frac{Z_{\alpha} e^2}{4\pi \epsilon_0 r_{i\alpha}} + \sum_{i > j} \frac{e^2}{4\pi \epsilon_0 r_{ij}} \quad (8.1)$$

$$\text{or } \hat{H} = \hat{T}_N + \hat{T}_e + \hat{V}_{NN} + \hat{V}_{eN} + \hat{V}_{ee} \quad (8.2)$$

where α, β denote the nuclei in a molecule and i, j the electrons. $\hat{T}_N, \hat{T}_e, \hat{V}_{NN}, \hat{V}_{eN}, \hat{V}_{ee}$ indicate the nuclear kinetic energy, electronic kinetic energy, nuclear-nuclear repulsion energy, the electron-nuclear attraction energy and the electron-electron repulsion energy respectively. If spin-orbit effects are important, they can be added through a spin-orbit operator \hat{H}_{SO} .

The Schrödinger equation with this Hamiltonian $\hat{H}\psi_n = E\psi_n$ for an electronic state $|n\rangle$ is solved by invoking the Born-Oppenheimer approximation. The BO approximation rests on the fact that the nuclei are much more massive than the electrons, which allows us to say that the nuclei are nearly fixed with respect to electron motion.

The electronic structure is solved by clamping the nuclei at fixed positions and solving the purely electronic equation $\hat{H}_{el}\psi_{el} = E_{el}\psi_{el}$, in which

$$\hat{H}_{el} = \hat{T}_e + \hat{V}_{eN} + \hat{V}_{ee} . \quad (8.3)$$

For fixed nuclei, \hat{V}_{NN} can be added on to the electronic energy forming the total electronic energy

$$U = E_{el} + \hat{V}_{NN} . \quad (8.4)$$

The separation of the Schrödinger equation into electronic and nuclear parts allows approximating ψ as the product function

$$\psi \approx \psi_{el}\chi_N . \quad (8.5)$$

Then one needs to solve

$$(\hat{H}_{el} + \hat{V}_{NN}) \psi_{el}(r, R) = U(R)\psi_{el}(r, R) \quad (8.6)$$

$$[\hat{T}_N + U(R)]\chi_N(R) = E_N\chi_N(R) \quad (8.7)$$

Denoting $\hat{H}_0 = \hat{H}_{el} + \hat{V}_{NN}$ and $E^{(0)} = U(R)$, one obtains

$$\hat{H}_0 \psi_{el}(r, R) = E^{(0)}\psi_{el}(r, R) \quad (8.8)$$

$$[\hat{T}_N + E^{(0)}]\chi_N(R) = E_N\chi_N(R) \quad (8.9)$$

Thus the BO approximation separates the Schrödinger equation into two separate decoupled equations. In equation (8.6) the value of the total electronic energy depends parametrically on the particular nuclear positions, R . Clamping the nuclei at different positions will result in different numerical values for U and different functions for ψ_{el} . As the nuclei move, the electrons move so quickly that the $U(R)$ derived from (8.6) serves as the potential energy for the nuclear motion (8.7). The vibrational and rotational motions can also be approximately separated in equation (8.7). The terms neglected in the Born-Oppenheimer approximation can be examined by substituting the equation

$$\psi = \psi_{el}(r, R)\chi_N(R) \quad (8.10)$$

into the full Schrodinger equation.

On solving the resulting equation, it can be seen that by neglecting the first and second order derivatives of the electronic wavefunction with respect to the nuclear

coordinates $\nabla_{\mathbf{R}}\psi_{el}$ and $\nabla_{\mathbf{R}}^2\psi_{el}$ the remaining terms can still be separated to yield equations (8.6) and (8.7). These matrix elements which are neglected in the BO approximation can be grouped into diagonal terms and off-diagonal terms. The diagonal terms depend quadratically on changes in the electronic wavefunction ψ_{el} upon variations of nuclear coordinates. These terms are small due to the large nuclear mass.

One arrives at the *adiabatic approximation* by substituting the diagonal terms but neglecting the off-diagonal ones so that

$$[\hat{T}_N + U'(R)]\chi_N(R) = E_N\chi_N(R) \quad (8.11)$$

where $U'(R)$ contains the corrective term depending on the masses of the nuclei, meaning it is different for different isotopes. This leads to small shifts in the electronic energies for different molecular isotopomers. These shifts are small compared to isotopic shifts on vibrational and rotational energy levels.

Thus, it can be seen that there is a small delay depending on the kinetic energy of the nuclei as the electron cloud follows nuclear motion. At time t the nuclei in their configuration $R(t)$ experience a potential due to an electronic configuration which would belong to a slightly earlier nuclear configuration $R(t - \Delta t)$. However nuclear motion does not modify the electronic state $\psi_{el,m}$ in this approximation. i. e. it does not mix wavefunctions of different electronic states. The electronic wavefunctions follow the nuclear motion adiabatically and reversibly; the molecule remains on the same potential surface all the time.

However, if the off-diagonal elements are not negligible, the adiabatic approximation ceases to be valid, and the electronic and nuclear motions cannot be separated. In other words, the nuclear motion mixes different electronic BO states. The breakdown of the adiabatic approximation can be understood using a perturbation analysis. This means that we use the Hamiltonian

$$\hat{H} = \hat{H}_0 + \hat{H}' = \hat{H}_0 + \lambda W \quad , \quad (8.12)$$

where \hat{H}_0 is the unperturbed Hamiltonian and \hat{H}' encompasses the kinetic energy of the nuclei, which is embodied in the perturbation operator $\hat{H}' = \hat{T}_N \doteq \lambda W$. The parameter $\lambda < 1$ determines the size of the perturbation depending on the mass ratio m/M .

In this case, for an electronic state $|n\rangle$,

$$\chi_n = \chi_n^{(0)} + \lambda \chi_n^{(1)} + \lambda^2 \chi_n^{(2)} + \dots \quad (8.13)$$

giving the respective energy eigenvalues

$$E_n = E_n^{(0)} + \lambda E_n^{(1)} + \lambda^2 E_n^{(2)} + \dots \quad (8.14)$$

Solving for Schrödinger equation including perturbation gives

$$E_n = E_n^{(0)} + W_{nn} + \sum_{k \neq n} \frac{W_{nk} W_{kn}}{E_n^{(0)} - E_k^{(0)}} + O(\lambda^3) + \dots \quad (8.15)$$

Here, $W_{nk} = \langle \psi_{el,n}^{(0)} | \hat{H}' | \psi_{el,k}^{(0)} \rangle$ is the matrix element of the perturbation operator calculated with unperturbed solutions of (8.8) and W_{nn} is the adiabatic correction of the BO energy $E_n^{(0)}$. The third term in (8.15) describes the coupling between electronic states $|\psi_{el,n}^{(0)}\rangle$ and $|\psi_{el,k}^{(0)}\rangle$, and is small provided the energy difference $E_n^{(0)} - E_k^{(0)}$ of the unperturbed states $|\psi_{el,n}^{(0)}\rangle$ and $|\psi_{el,k}^{(0)}\rangle$ at a given nuclear configuration R is large compared to the matrix element W_{nk} .

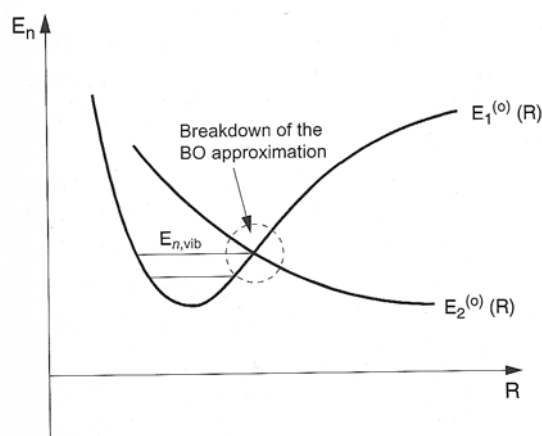


Figure 8.1: An illustration of the breakdown of BO approximation.

When potential energy surfaces cross, this energy difference becomes small consequently diverging the expression (8.15), in turn meaning that the BO approximation breaks down. This situation is frequently encountered in excited electronic states of a molecule, but rarely for ground states. In these cases the molecule cannot be described by the Born Oppenheimer approximation. Figure 8.1 shows an example for breakdown of the BO approximation.

8.3. Perturbations between Two Levels

A simple impression of how the analyses of the perturbations in HC_4H^+ and C_4H can be had by understanding perturbations between two levels. The energy matrix for the coupling states in the basis of the unperturbed wavefunctions $\psi_1^{(0)}$ and $\psi_2^{(0)}$ is

$$\begin{pmatrix} H_{11} & H_{12} \\ H_{21} & H_{22} \end{pmatrix} = \begin{pmatrix} E_1^0 & H_{12} \\ H_{21} & E_2^0 \end{pmatrix} \text{ with } H_{21} = H_{12} \quad (8.16)$$

where the diagonal elements describe the energies of the unperturbed levels and the off-diagonal elements the interaction energy. To get the perturbed energy levels, this matrix should be diagonalized i.e. equating the determinant to zero. This yields

$$E_{1,2} = \frac{E_1^0 + E_2^0}{2} \pm \sqrt{\left(\frac{E_1^0 - E_2^0}{2}\right)^2 + H_{12}^2} \quad (8.17)$$

for the energies of the experimentally observed energy levels (perturbed). The energy levels are shifted symmetrically, and their spacing increases with increasing coupling strength (Figure 8.2).

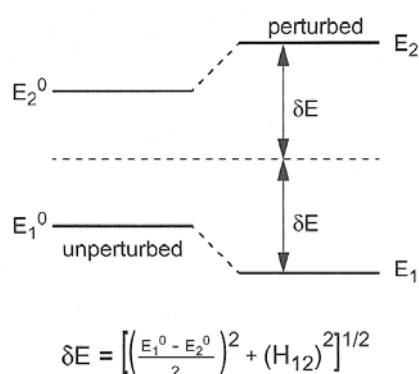


Figure 8.2: Schematic of the mutual repulsion of two interacting levels.

8.4. Types of Perturbations

The different possible couplings between molecular states are described by the corresponding perturbation operator \hat{H}' . The choice of the basis depends on the type of perturbation. For now, we discuss the perturbations which affect the molecules studied. The Hamiltonian H can be expressed as the sum of $H_{el,vib}$ and H_{rot} where $H_{el,vib}$ acts on the electronic and vibrational functions, and H_{rot} is the rotational part which depends on the total angular momentum.

8.4.1. Spin-Orbit Coupling

The Hamiltonian for the coupling between the spin s_i of the i th electron and its orbital angular momentum l_i for a molecule with respect to the nucleus k is given by

$$\hat{H}_{s,i} = \sum_i a_i l_i s_i . \quad (8.18)$$

In case of Hund's case (a), where L-S coupling dominates, the spin-orbit interaction within a state can be expressed as

$$\hat{H}_{s,L} = ALS \text{ with } L = \sum l_i \text{ and } S = \sum s_i . \quad (8.19)$$

Usually, the basis functions for Hund's coupling case (a) are chosen. Here, Λ and Σ are the good quantum numbers.

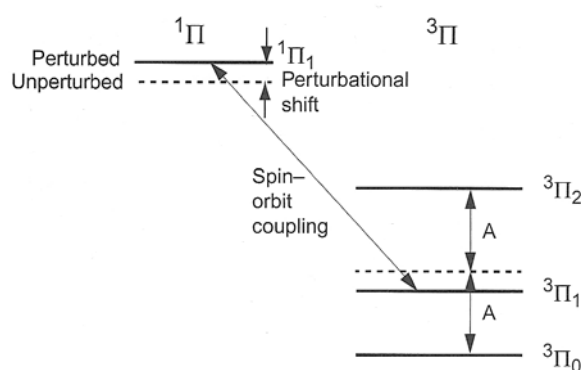


Figure 8.3: Spin-orbit coupling between electronic states.

The energies of the spin-orbit (s-o) components are given by the diagonal elements

$$\langle \Lambda, \Sigma, S, \Omega, v | \hat{H}_{s,L} | \Lambda, \Sigma, S, \Omega, v \rangle = A \Lambda \Sigma \quad (8.20)$$

The selection rules for the non-vanishing elements of the s-o coupling are

$$\Delta J = 0; \Delta S = 0, \pm 1; \Delta \Omega = 0; \text{ implying } \Delta \Lambda = \Delta \Sigma = 0 \text{ or } \Delta \Lambda = -\Delta \Sigma = \pm 1 \quad (8.21)$$

In case of linear polyatomic molecules, for strong s-o coupling Hund's coupling case (c) applies. Figure 8.3 shows the s-o coupling between a $^1\Pi$ and a $^3\Pi_1$ state.

8.4.2. Vibrational Coupling - Fermi Resonance

At low vibrational energies, vibrations of polyatomic molecules can be regarded as a superposition of normal vibrations. The different normal modes are linearly independent and the potential in which the vibration occurs is approximately harmonic.

Upon higher vibrational excitation, anharmonicities in the potential become noticeable resulting in couplings between the normal modes of vibration.

The termination of the infinite Taylor series of the real potential after the quadratic term is valid only for small vibrational amplitudes. For larger amplitudes as when a molecule undergoes high vibrational excitation, the eigenvalues can be calculated using perturbation calculations starting from the harmonic potential and including the higher terms of the Taylor expansion as the perturbation potential $V=W$. The result is to introduce anharmonic terms into the energy level equation. The energy eigenvalues E_i of the harmonic oscillator with vibrational quantum numbers (v_1, v_2, v_3) can then be expressed for non-degenerate vibrations as

$$E_i^{anh} = E_i^0(v_1, v_2, v_3) + \sum_k \frac{W_{ik}^2}{E_i^0 - E_k^0} \quad (8.22)$$

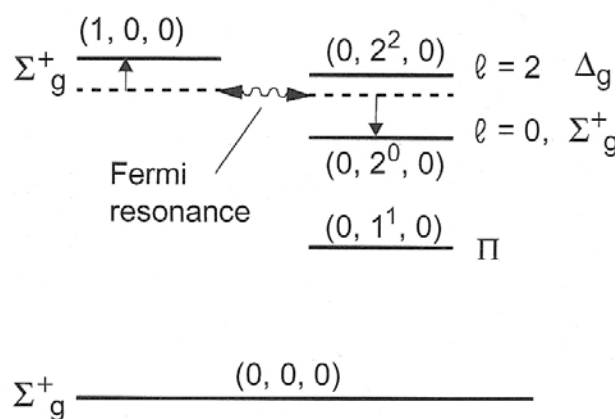


Figure 8.4: Fermi Resonance in CO₂. The dotted lines show unperturbed levels which repel each other.

If a near degeneracy occurs among k levels of the same symmetry, these terms cause a splitting [7, 8, 9], whose magnitude depends on the matrix element $W_{ik} = \int \psi_i^{0*} W \psi_k^0 d\tau$ of the perturbation; ψ_k^0 being the pure wavefunction for the vibrational level k . Often the fundamental transition of one normal vibration and an overtone transition of another vibration lead to excited levels of equal symmetries and almost equal energies. In such cases, the interaction between the levels is very strong and leads to large frequency shifts for both interacting levels. This phenomenon is called Fermi Resonance. The Fermi Resonance in CO₂ is shown in Figure 8.4. The total vibrational energy in case of these anharmonic potentials is given by introducing coupling coefficients x_{ij} as

$$G(v_1, v_2, \dots, v_{3N-6}) = \sum_i \omega_i \left(v_i + \frac{d_i}{2} \right) + \sum_i \sum_j x_{ij} \left(v_i + \frac{d_i}{2} \right) \left(v_j + \frac{d_j}{2} \right) + \dots \quad (8.23)$$

The effect of Fermi resonance on the vibronic energy levels of linear molecules in Π electronic states has been dealt with in detail [10]. The formulation describes two Fermi parameters W_1 and W_2 , unlike the case where a single term for a non-degenerate electronic state is considered. The present analysis for the $A^2\Pi_u$ state of HC_4H^+ involves the stretch vibration v_3 and the energetically close lying first overtone of the bending vibration v_7 . Therefore, a more accurate description requires the inclusion of Fermi resonance between these modes. The degenerate bending vibrations of C_4H and HC_4H^+ result in R-T interaction, splitting the vibronic states into several components.

8.4.3. Renner-Teller Coupling

If the electronic state is degenerate in the linear configuration, it is split into two potential curves $V^+(\varphi)$ and $V^-(\varphi)$ during a bending vibration, where φ is the bond angle (Figure 8.5). If the unperturbed potential is described by the quartic function

$$V^0(\varphi) = a\varphi^2 + b\varphi^4 \quad (8.24)$$

and the difference of the two R-T components by

$$V^+(\varphi) - V^-(\varphi) = \alpha\varphi^2 + \beta\varphi^4 \quad (8.25)$$

The lower potential curve possesses a maximum at $\varphi = 0$ and two minima at

$$\varphi_{\text{min}} = \pm \sqrt{\frac{1/2 - \alpha}{2b - \beta}}, \quad (8.26)$$

provided $\alpha > 2a$.

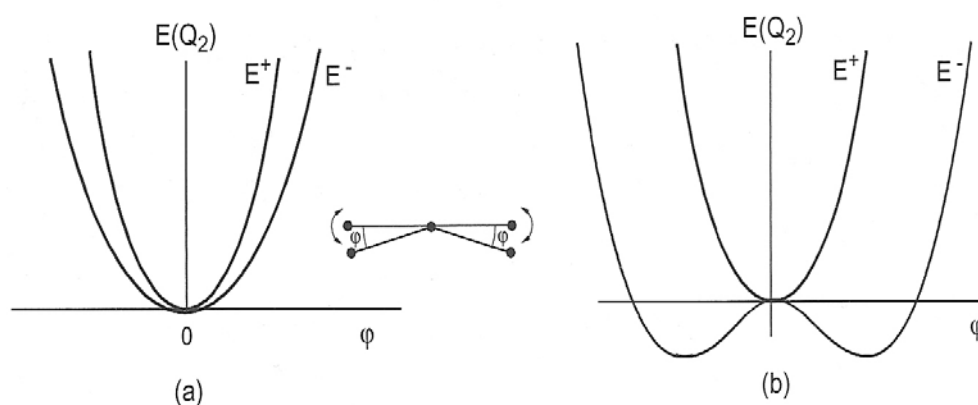


Figure 8.5: Potential curve splitting in the R-T effect (a) $\alpha < 2a$ (b) $\alpha > 2a$.

The coupling between the electronic orbital and nuclear motion shifts the vibronic levels in both PE curves, changing also the rotational constant. The resulting energy shifts depend on potential splitting given by the Renner parameter $\epsilon = \frac{\alpha}{2\alpha}$ and the vibrational angular momentum of the bending vibration.

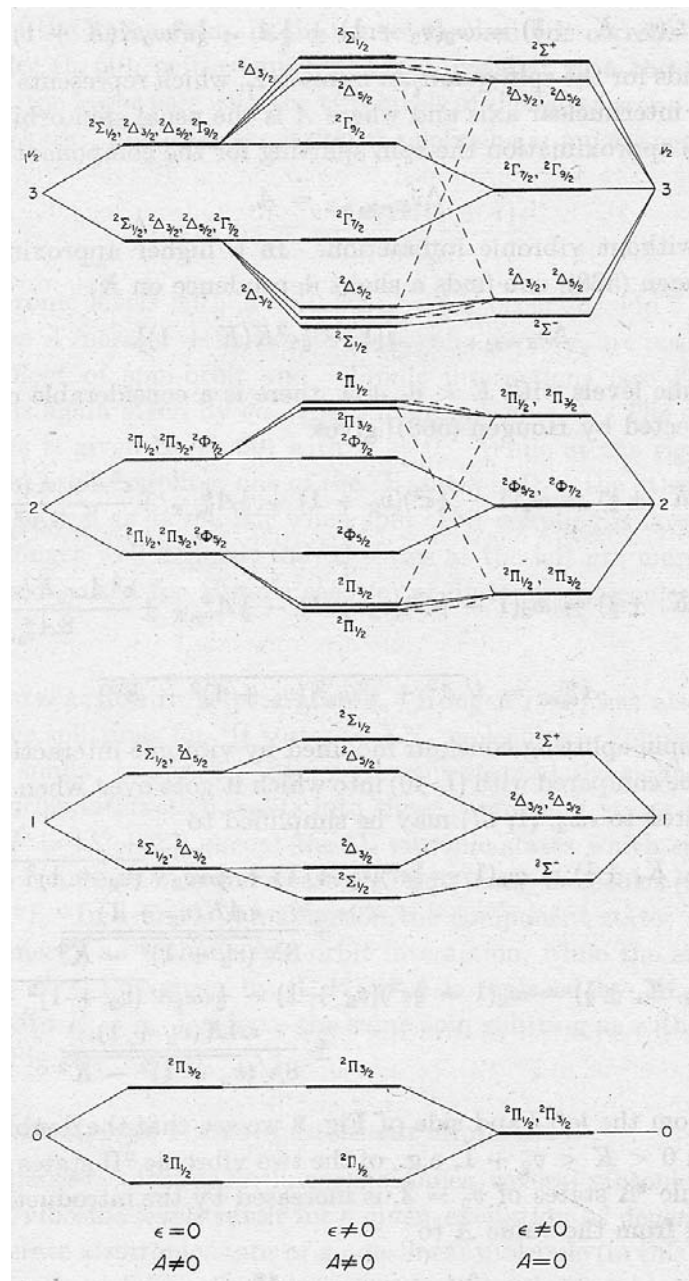


Figure 8.6: Vibronic interaction in ${}^2\Pi$ electronic state for a linear molecule [3].

The BO approximation collapses and vibronic levels originate with the coupling of the vibrational and electronic states. For a linear molecule in a Π state, the electronic orbital angular momentum is characterized by $\Delta = \pm 1$. The excitation of bending

vibration introduces an additional vibrational angular momentum with the projection quantum number l which takes values from $-v$ to $+v$ in increments of 2.

The resulting vibronic angular momentum is $K\hbar$ where

$$K = |\pm\Lambda \pm l|. \quad (8.27)$$

For $K = 0$, the vibrational term values for the case of Figure 8.5(a) are

$$G(v_2) = \omega_2 (1 \pm \epsilon)^{\frac{1}{2}} (v_2 + 1). \quad (8.28)$$

For $K \neq 0$ and $v_2 = K - 1$

$$G(v_2, K) = \omega_2 \left[v_2 + 1 - \frac{1}{8} \epsilon^2 K(K + 1) \right], \quad (8.29)$$

where ω_2 is the vibrational constant of the bending vibration. The splitting of an electronic Π state is shown in Figure 8.6.

8.5. HC₄H⁺

The astrophysical relevance of diacetylene cation has already been discussed. The ground and the first excited electronic states of HC₄H⁺ have the π electron configurations $(\pi_u)^4(\pi_g)^3$ and $(\pi_u)^3(\pi_g)^4$ respectively. The resulting electronic states ${}^2\Pi_g$ and ${}^2\Pi_u$ are inverted, with the $A^2\Pi_{u,3/2} - X^2\Pi_{g,3/2}$ transition lying $\sim 2 \text{ cm}^{-1}$ higher in energy relative to the $\Omega = 1/2$ component. The R-T analysis for the ν_6 mode in the linear ${}^2\Pi_g$ state of the diacetylene cation has been reported [11]. However, no interactions with other vibrations were considered.

In this work [1], a vibronic analysis of the $A^2\Pi_u - X^2\Pi_g$ electronic transition is made by using a restricted Hamiltonian which takes into account the s-o, the R-T and the Fermi interaction between the rotationally resolved $3\frac{1}{2}$ and $7\frac{3}{2}$ vibronic bands. The experimental observation of the perturbed energy levels is reproduced with good accuracy from the fit, which enables the evaluation of the R-T and Fermi constants. The change of the s-o constant ΔA upon electronic excitation for the origin band of the transition is 2.2 cm^{-1} ; however, the observed separation between the $\Delta\Omega = 0$ branches of the stretch and the degenerate bend at $T_{00} = 20520.828(4) \text{ cm}^{-1}$ and $T_{00} = 20573.659(4) \text{ cm}^{-1}$ are 15.4 cm^{-1} and 21.8 cm^{-1} , respectively. This indicates a relatively high s-o quenching upon vibrational excitation.

An effective Hamiltonian was set up with the diagonal elements forming the sum of H_{vib} and H_{SO} , while the off-diagonal terms of the matrix represent the Fermi and the R-T interactions. The eigenvalues for the perturbed energy levels and the corresponding wavefunctions are obtained from diagonalization of the matrix.

8.5.1. Experimental

Diacetylene cations were produced in the pulsed slit nozzle (30 x 1 mm²) incorporating a discharge in a high pressure expansion and probed using CRDS. The plasma was generated by applying a voltage of -700 V to 0.5 % diacetylene seeded in an argon-helium buffer gas mixture. The backing pressure was kept at 10 bar and the residual pressure inside the chamber was 0.07 mbar.

8.5.2. Renner-Teller and Fermi Resonance Analysis

A vibrational analysis of the observed vibronic levels was carried out by taking explicitly the R-T interaction of the ν_7 bending mode and the Fermi resonance interaction with the stretching vibration ν_3 . The matrix coefficients were calculated for levels of vibronic symmetry $K = | \pm \Lambda \pm l_7 |$ because the stretch is singly degenerate. The electron spin angular momentum has to be taken into consideration, hence the vibronic angular momentum becomes $P = | \pm \Lambda \pm l_7 \pm \Sigma |$. Electronic angular momentum Λ is restricted to ± 1 for the $^2\Pi$ state and the basis set is given by $| \Lambda; \Sigma; \nu_7; l_7; \nu_3 \rangle$. The matrix elements are non-vanishing only between those wavefunctions for which $\Delta\nu_7 = 0, \pm 2$ and $\Delta\nu_3 = \pm 1$, where ν_7 and ν_3 span 0, 1,, 7, 8. This gives rise to a 1620×1620 effective Hamiltonian matrix whose diagonal is formed by the vibrational and the s-o coupling terms, with the largest diagonalizable matrix of order 153×153. The off-diagonal elements make up the R-T and the Fermi resonance interaction. The coefficients of the matrix are then defined as:

$$H(\Delta\Lambda; \Delta\Sigma; \Delta\nu_7, \Delta l_7; \Delta\nu_3) = \langle \Lambda + \Delta\Lambda; \Sigma + \Delta\Sigma; \nu_7 + \Delta\nu_7, l_7 + \Delta l_7; \nu_3 + \Delta\nu_3 | H | \Lambda; \Sigma; \nu_7, l_7; \nu_3 \rangle$$

The diagonal and off-diagonal matrix elements for the R-T and the Fermi resonance [12] are given by the following formulae:

$$H_{ij, i=j} = \omega_7(\nu_7+1) + \omega_3(\nu_3+0.5) + A\Lambda\Sigma$$

R-T terms

$$H_{ij=ji} (\Delta\Lambda = 2; \Delta\Sigma = 0; \Delta v_7 = 2, \Delta l_7 = -2; \Delta v_3 = 0) = 0.25 \varepsilon_7 \omega_7 [(v_7-l_7+2)(v_7-l_7+4)]^{0.5}$$

$$H_{ij=ji} (\Delta\Lambda = 2; \Delta\Sigma = 0; \Delta v_7 = -2, \Delta l_7 = -2; \Delta v_3 = 0) = 0.25 \varepsilon_7 \omega_7 [(v_7+l_7)(v_7+l_7-2)]^{0.5}$$

$$H_{ij=ji} (\Delta\Lambda = 2; \Delta\Sigma = 0; \Delta v_7 = 0, \Delta l_7 = -2; \Delta v_3 = 0) = 0.5 \varepsilon_7 \omega_7 [(v_7+l_7)(v_7-l_7+2)]^{0.5}$$

Fermi terms

$$H_{ij=ji} (\Delta\Lambda = 0; \Delta\Sigma = 0; \Delta v_7 = 2, \Delta l_7 = 0; \Delta v_3 = \pm 1) = W_1 [((v_7+2)^2 - l_7^2)(v_3+0.5 \pm 0.5)]^{0.5}$$

$$H_{ij=ji} (\Delta\Lambda = 0; \Delta\Sigma = 0; \Delta v_7 = 0, \Delta l_7 = 0; \Delta v_3 = 1) = 2 W_1 (v_7+1)(v_3+1)^{0.5}$$

$$H_{ij=ji} (\Delta\Lambda = 2; \Delta\Sigma = 0; \Delta v_7 = 2, \Delta l_7 = -2; \Delta v_3 = \pm 1) = W_2 [((v_7-l_7+3)^2 - 1)(v_3+0.5 \pm 0.5)]^{0.5}$$

$$H_{ij=ji} (\Delta\Lambda = 2; \Delta\Sigma = 0; \Delta v_7 = -2, \Delta l_7 = -2; \Delta v_3 = \pm 1)$$

$$= W_2 [((v_7+l_7-1)^2 - 1)(v_3+0.5 \pm 0.5)]^{0.5}$$

$$H_{ij=ji} (\Delta\Lambda = 2; \Delta\Sigma = 0; \Delta v_7 = 0, \Delta l_7 = -2; \Delta v_3 = \pm 1)$$

$$= 2 W_2 [((v_7+1)^2 - (l_7-1)^2)(v_3+0.5 \pm 0.5)]^{0.5}$$

$A^2\Pi_u$						
Energy		K	v_7	v_3	P	Vib. Sym.
Fit	Expt.					
	31.1	0	0	0	0.5	Π
804.93	804.81	1	0	1	1.5	Π
822.16	822.76	1	0	1	0.5	Π
861.84	860.84	1	2	0	1.5	Π
871.51	872.39	1	2	0	0.5	Π
$X^2\Pi_g$						
	33.3	0	0	0	0.5	Π
971.62	971.50	1	0	1	1.5	Π
998.59	998.65	1	0	1	0.5	Π
860.40	860.64	1	2	0	1.5	Π
895.44	895.61	1	2	0	0.5	Π

Table 8.1: Renner-Teller levels (cm^{-1}) obtained from analysis of the v_3 stretch and the v_7 bend vibrations in the $A^2\Pi_u$ and $X^2\Pi_g$ electronic state of HC_4H^+ matched with the respective experimental energy levels.

The eigenvalues of this matrix give the perturbed energy levels and the eigenvectors the wavefunctions of the modes involved. The vibronic assignment is made by taking the vector coefficient with the maximum absolute value, and attributing the

corresponding quantum numbers to the level. A least-squares fit is then performed to obtain the spectroscopic parameters which give the best match between the observed and calculated energy levels. In the lowest order approximation where the s-o interaction constant A_{SO}' is unvaried, the optimized molecular constants are determined as $\omega_3'=811.8 \text{ cm}^{-1}$, $\omega_7'=403.2 \text{ cm}^{-1}$, $\varepsilon_7'=0.065$, $W_1'=10.3 \text{ cm}^{-1}$ and $W_2'=5.1 \text{ cm}^{-1}$. The fit gave an accuracy of 0.6 cm^{-1} and 1 cm^{-1} residual error per energy level for the bend and the stretch vibrations respectively, with a global mean square error of 2.15 cm^{-1} . The fitted vibronic energy levels and the experimental levels with their assignments are shown in Table 8.1. The two s-o components of the first overtone of the bend vibration are found to lie at 872 cm^{-1} and 862 cm^{-1} , giving a splitting of -10 cm^{-1} . This value is in reasonable agreement with experimentally observed -11.55 cm^{-1} . Similarly, the s-o components of the stretching mode lie at 822 cm^{-1} and 805 cm^{-1} ; the -17 cm^{-1} splitting matches the measured value of -17.95 cm^{-1} . The energy level analysis indicates that the $P=1.5$ components of these modes are separated by 57 cm^{-1} , which agrees with the experimental separation of 56 cm^{-1} between the $R_1(15.5-19.5)$ and $R_1(14.5-18.5)$ bandheads of the $3\frac{1}{2}$ and the $7\frac{1}{2} A^2\Pi_u-X^2\Pi_g$ vibronic systems, respectively.

	$A^2\Pi_u$	$X^2\Pi_g$
ω_3	811.8	956.2
ω_7	403.2	435.4
ε_7	0.065	0.028
A_{SO}	-31.1(fixed)	-33.3(fixed)
W_1	10.3	7.2
W_2	5.1	10.9

Table 8.2: Molecular constants (cm^{-1}) for the ground and excited electronic states of HC_4H^+ for the $\nu_3 (\sigma_g^+)$ and $\nu_7 (\pi_g)$ modes. ε_7 is unitless.

The electronic ground state vibrational energy levels for the $3\frac{1}{2}$ and the $7\frac{1}{2}$ transitions were used to calculate the vibronic interactions for the $X^2\Pi_g$ state. High-resolution emission spectra involving these modes have been recorded previously [13] and unambiguously assigned using double resonance labeling by a stimulated emission pumping technique [14, 15]. The molecular constants for $X^2\Pi_g$ and $A^2\Pi_u$ electronic states are listed in Table 8.2. As the number of parameters is equal to the number of observations, the uncertainties are not estimated. The W_1'' Fermi resonance interaction coefficient obtained in the $X^2\Pi_g$ state is 7.2 cm^{-1} and $W_2''=10.9 \text{ cm}^{-1}$. An ambiguity in the sign of the R-T ε_7 and the W_1 and W_2 parameters still exists which cannot be determined

by the fit. The magnitudes of W_1 and W_2 are reversed in the two electronic states. The R-T parameter $\varepsilon_7''=0.028$ is reduced by a factor of two relative to that in the $A^2\Pi_u$ state. The relation $|\omega_7''\varepsilon_7''| \ll A_{SO}''$ with $\omega_7''=435.4 \text{ cm}^{-1}$ and $A_{SO}''=-33.3 \text{ cm}^{-1}$ (fixed) is satisfied by the mode, suggesting a weak R-T interaction. The values of A' obtained for the bending and the stretching vibrations as a result of the perturbed energy eigenvalues are -35 cm^{-1} and -27 cm^{-1} respectively. The previously measured [14] effective s-o coupling constant $A'=-27 \text{ cm}^{-1}$ for the stretching mode in the $X^2\Pi_g$ state confirms this value. The vibrational frequency ω_3'' is determined as 956.2 cm^{-1} . The energy levels detected at 18866.07 cm^{-1} and 18862.19 cm^{-1} are the $\Omega=3/2$ and $\Omega=1/2$ components of the ν_3 transition [13, 14] in the $X^2\Pi_g$ state. These have been used for the fit, giving a residual error of 0.2 cm^{-1} for the bending mode, and 0.1 cm^{-1} per level for the stretch global MSE of 0.10 cm^{-1} (Table 8.1). This results in the same trend in the $X^2\Pi_g$ and $A^2\Pi_u$ electronic states, with the ν_3 stretch harmonic frequency at higher energies than the $\nu_7 = 2$ bend overtone.

The present analysis did not include the other degenerate bending modes ν_8 and ν_9 whose overtone and combination bands lie in the same wavelength region as ν_3 . Based on the emission spectrum, the interactions of $\nu_8+\nu_9$ or $4\nu_9$ with ν_3 are inferred to be weak [13]. Apart from the $\nu_3 = 1$ and $\nu_7 = 2$ modes, the spectrum shows only weak features, therefore the other modes do not appear to borrow intensity from the ν_3 mode through Fermi resonance. Within the present Hamiltonian approach, the match between the experimentally observed levels and the calculated ones shows good agreement. As the number of observations is limited to five, it would be unreasonable to increase the number of variable parameters. Within the limited R-T model used, which is basically equivalent to a linear triatomic R-T taking into consideration only one bending vibration, the experimental levels are reproduced with sufficient accuracy. Knowledge of additional levels would enable introduction of additional terms in the Hamiltonian, as well as additional vibrations.

Qualitative support of the magnitude of the ν_6 [11] and the ν_7 R-T parameters in the $X^2\Pi_g$ state comes from a prediction (neglecting Fermi resonance and anharmonicity) using the harmonic frequencies given by theoretical calculations [16]. The R-T constants are obtained using the formula $\varepsilon'' = |\omega_i''^2 - \omega_j''^2| / (\omega_i''^2 + \omega_j''^2)$ where ω_i'' and ω_j''

are the non-degenerate frequencies [16, 17]. The obtained constants $\varepsilon_7'' = 0.04$ ($\omega_7=500, 477 \text{ cm}^{-1}$), $\varepsilon_6'' = 0.15$ ($\omega_6=772, 660 \text{ cm}^{-1}$) are in agreement with the analysis of the experimental data.

8.6. C₄H

The linear butadiynyl C₄H was identified in the carbon rich star IRC+10216 in 1978 [18, 19] as well as in dense clouds [20]. Five years after its detection, the laboratory spectrum was reported by microwave spectroscopy [21] confirming its existence in the interstellar medium [22, 23]. C₄D was later observed by radio astronomy [24]. Since then, the electronic structure of the C₄H radical has been of interest from a spectroscopic point of view. A study of the $B^2\Pi - X^2\Sigma^+$ electronic transition by laser induced fluorescence yielded the origin at around 24033 cm^{-1} and provided a tentative assignment of the two lowest bending modes in the excited state [25]. The photoelectron spectrum of the C₄H⁻ anion located the $A^2\Pi$ state about 213 cm^{-1} above the $X^2\Sigma^+$ ground state [26]. The spectroscopy of the radical is challenging because of the close lying $X^2\Sigma^+$ and $A^2\Pi$ states. The order of the electronic states is reversed for the higher members of the C_{2n}H species. Figure 8.7 gives a qualitative idea about the order of the electronic states in C₄H.

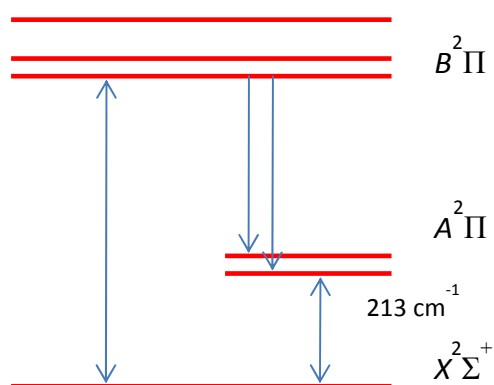


Figure 8.7: The order of electronic states in C₄H. Notice the $A^2\Pi$ state which lies 213 cm^{-1} above the ground state.

The R-T effective Hamiltonian relevant to a linear triatomic molecule in a $^2\Pi$ electronic state with a single degenerate bending vibration is known [27]. The formalism for a tetra-atomic with two bending modes has been quantified in the case of

HC₂S recorded by microwave spectroscopy [28], and a model for polyatomic linear molecules sketched [29].

In the present study, the experimental determination of the energy above the ground state of the vibronic levels is possible with the double-resonance four-wave mixing technique, without the ambiguity of hot bands. The assignment is aided by a theoretical treatment of the R-T and spin-orbit interactions derived previously for a tetra-atomic molecule [28].

8.6.1. Experimental

A 3×0.3 mm slit was used for the supersonic expansion and a pulse of 1100-1800 kV was applied to 1% acetylene in argon (7-10 bar) for production of the C₄H radical. The high-voltage pulse duration was 0.3-1.0 μs for the degenerate four-wave mixing (DFWM) measurements but 0.3-3 μs for the two-color resonant four-wave mixing (TC-RFWM), because of increased selectivity. A longer discharge pulse in DFWM resulted in a spectrum with predominant features originating from the C₃ $A^1\Pi_u - X^1\Sigma_g^+$ electronic system [30]. The delay between the valve and the discharge trigger was 1200-2100 μs and 5-7 μs between the laser and the discharge, depending on the distance of the laser beam to the slit.

Pulses of 7 ns duration were generated by dye lasers pumped by the 355 nm output of Nd:YAG lasers with linewidths of 0.06 cm⁻¹ (double grating) and 0.15 cm⁻¹ (or 0.05 cm⁻¹ with an intracavity etalon). A wavemeter provided the calibration. The degenerate scan allowed selection and detection of specific transitions of C₄H for the pump laser. Double resonance scans were made at higher or lower energy relative to the pump frequency and gave access to the allowed transitions resonant with the pump photons. By increasing the intensity of the probe or the pump lasers, it is possible to access weak vibronic transitions.

The experimental setup was modified compared to the previous arrangement to permit fast switching between the degenerate and double-resonance configuration. This was achieved by using a 50% beamsplitter so that the two probes travelled through the same path. The difference in alignment induced by the wavelength difference between pump and probe as well as index of refraction variation with frequency of the

beamsplitter was negligible and no realignment was necessary throughout the whole range of the dyes used.

The C_4H radical was probed close to the slit. In this region, the observed rotational temperature of approximately 100 K combined with non-linear four-wave mixing effects produces an intensity enhancement of the R bandhead which gives rise to the observation of even the weakest vibronic bands. Observation of transitions originating from the ground electronic state in vibrationally excited levels shows that the vibrational temperature is a few hundreds K.

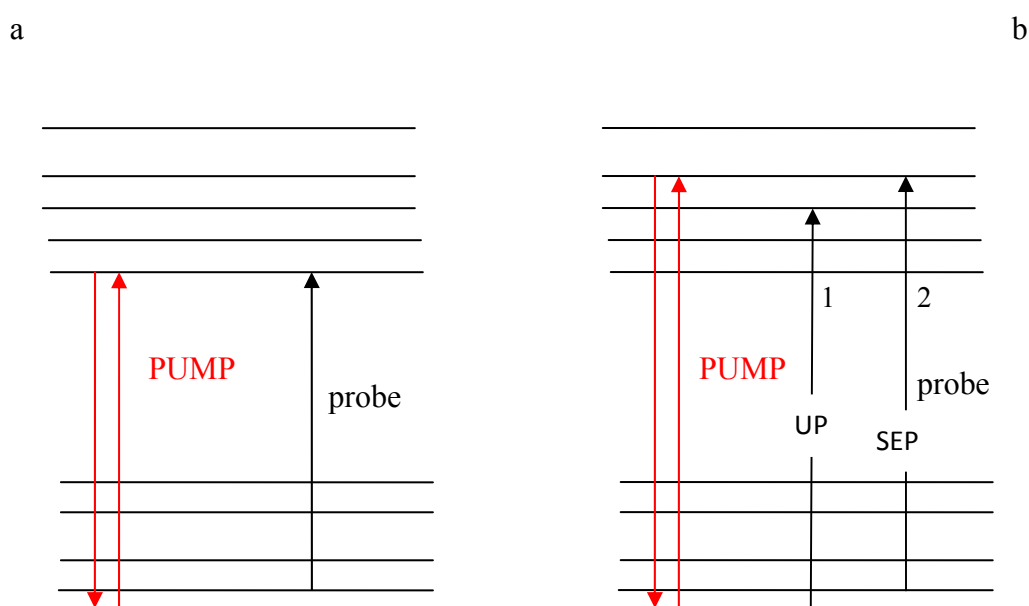


Figure 8.8: Two-color resonant four-wave mixing with pump frequency tuned either to the origin (a) or to an excited state (b) of an electronic transition. A probe lower in frequency is considered. The levels detected map out the ground state manifold in case (a) while levels in the excited (1) and the ground state (2) are resonant in case (b).

The stimulated emission pumping (SEP) scheme (transitions resonant with a common upper state) leads to unambiguous determination of the vibrational/electronic energy levels above the ground state provided that the pump laser is tuned to an origin band of a given electronic transition. A scan of the probe to the lower energy range will reveal the ground state levels as shown in Figure 8.8(a). However, if the pump is tuned to an excited vibronic state, an ambiguity arises (Figure 8.8(b)) even if the probe

frequency is less than the one of the pump. In this case, the resonant transition can connect to a common state in the upper or the lower manifold.

In case the origin of an electronic system is not readily assigned and hot bands are present, it is possible to scan first in a degenerate fashion to obtain the transitions (including hot bands or excited states) and secondly to map the ground and excited state levels with a series of double-resonance spectra by sitting on each and every transition without realigning the optics. This scheme of operation is similar to two-color laser induced fluorescence.

8.6.2. Results

8.6.2.1. Single Color

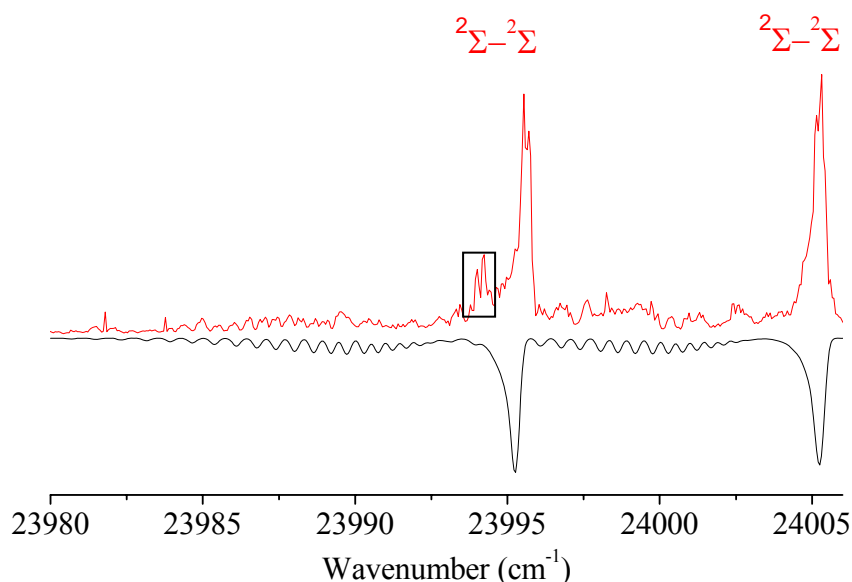


Figure 8.9: Degenerate four-wave mixing scan of the newly detected ${}^2\Sigma^+ - {}^2\Sigma^+$ bands of C_4H . The experimental spectrum (top) is matched against the simulation (inverted trace) at a temperature of 40 K. The feature in the box could not be reproduced in the simulation.

Most of the bands observed previously using LIF [25] were also detected with DFWM, some of them being concealed by the presence of strong C_3 $A^1\Pi_u - X^1\Sigma_g^+$ hot bands. Among these, the $B^2\Pi - X^2\Sigma^+$ origin band of C_4H [25] was not measured by DFWM because of spectral congestion and weak signals. However, two relatively intense transitions were recorded with R bandheads at 23995 and 24005 cm^{-1} (Figure 8. 9). The latter was used as a pump transition, in addition to the ${}^2\Sigma^+ - X^2\Sigma^+$ band at

24493 cm^{-1} (labeled J in reference [25]) and the origin of the $B^2\Pi_{3/2} - X^2\Sigma^+$ transition at 24023 cm^{-1} . The symmetries of the levels involved are of $^2\Sigma$ character.

8.6.2.2. Double Resonance

The double resonance method has increased selectivity compared to the degenerate case. The previously detected [25] $B^2\Pi - X^2\Sigma^+$ transition overlapping with a hot band of the $A^1\Pi_u - X^1\Sigma_g^+$ electronic transition of C_3 is readily observed in the two-color configuration when pumping on the J feature [25] at 24493 cm^{-1} , which originates from the $X^2\Sigma^+$ ground state and accedes to a vibration located 470 cm^{-1} above and within the $B^2\Pi$ state. Consequently, the spectral region can be scanned by pumping on the $B^2\Pi - X^2\Sigma^+$ origin band: levels lying above the ground state will be detected with lower probe frequency and the excited states with higher one.

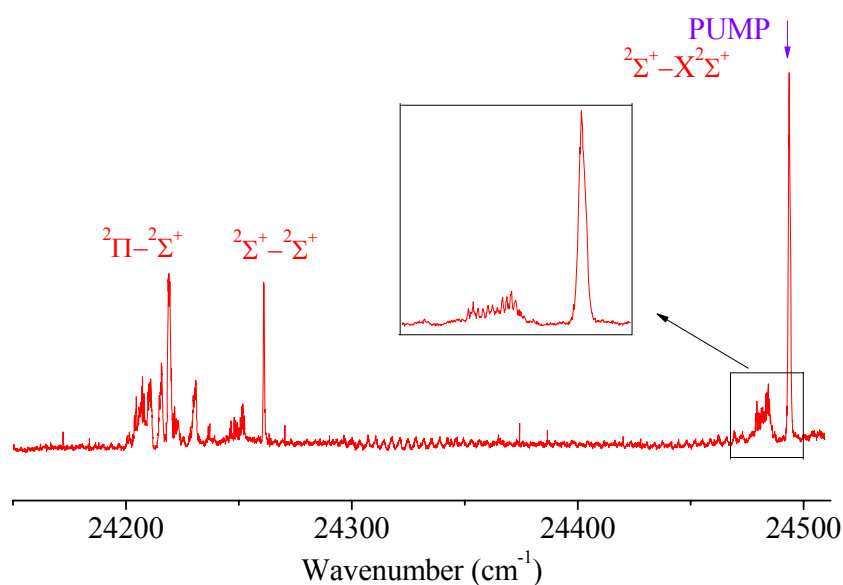


Figure 8.10: Rotationally resolved two-color four-wave mixing spectrum of C_4H with the pump frequency resonant with the “J” $B^2\Sigma - X^2\Sigma^+$ transition [25] at 24493 cm^{-1} . Three bands are visible: two $B^2\Sigma^+ - X^2\Sigma^+$ and one $B^2\Pi - X^2\Sigma^+$. The oscillations around 24300 cm^{-1} are due to minute spatial drift of the probe beam while scanning the wavelength.

The technique provides rotationally resolved spectra (Figure 8.10). The recording was made by setting the pump frequency at 24493 cm^{-1} (J feature) and are interpreted as follows. Two $^2\Sigma - ^2\Sigma$ transitions are visible, one is the pump transition

and the other is detected 234 cm^{-1} red-shifted; more interestingly a third is identified as ${}^2\Pi - {}^2\Sigma$ lying 262 cm^{-1} towards lower energy. The resolved P lines and R branches of the latter transition allow an estimate of the spin-orbit splitting in the upper state, inferred from the separation between the bandheads.

The ${}^2\Pi - {}^2\Sigma$ transition shown in Figure 8.11 was recorded by setting the pump wavelength on the R head of the “J” band and scanning in the vicinity of 24200 cm^{-1} . Due to the higher rotational temperature achieved in the discharge, the trace displays a succession of band heads as well as the simulations. The spectroscopic constants involved in the pump transition were taken from reference [25]. The rotational lines were calculated with the PGOPHER program [31] and a homemade software simulated the double-resonance traces shown as middle trace in Figure 8.11. The small mismatch in the line positions is due to the fact that the rotational constant in the excited state could not be perfectly fitted.

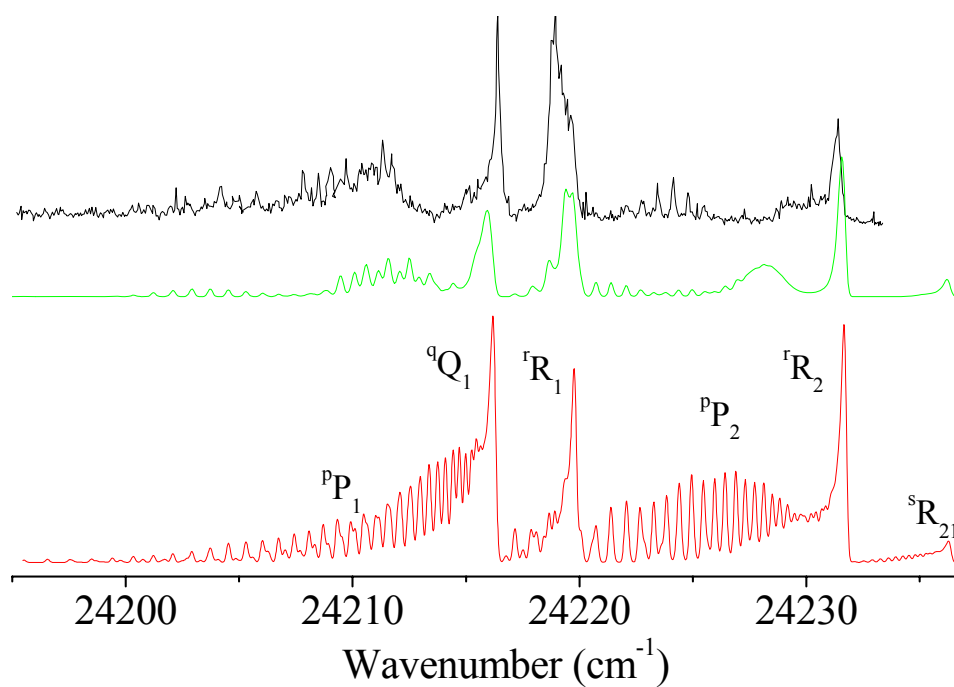


Figure 8.11: Double resonance spectrum of the $B\ {}^2\Pi - X\ {}^2\Sigma^+$ transition of C_4H with pump frequency set on the $B\ {}^2\Sigma - X\ {}^2\Sigma^+$ band at 24493 cm^{-1} (on the R band head). The bottom trace is the simulation of the absorption squared. The experimental spectrum shows a selected subset of J lines in each of the P, Q, R bands and is reproduced in the middle trace by a two-color simulation. The mismatch between the spectra is due to the use of approximate (non-fitted) spectroscopic constants in the upper state.

8.6.2.3. $A^2\Pi$ State Spin-Orbit Splitting

Figure 8.12 shows a two-color scan of the C_4H $B^2\Pi - X^2\Sigma$ system with pump on the $B^2\Pi_{3/2} - X^2\Sigma^+$ transition [25]. The frequency was precisely measured by setting the pump on the “J” band and scanning the probe towards lower frequencies, thus confirming the previous spectroscopic data [25]. The intense peak corresponds to the $A^2\Pi_{3/2}$ level while the weaker one to $A^2\Pi_{1/2}$. A photoelectron spectroscopic experiment located the $A^2\Pi$ state at 213 cm^{-1} [26] above the X state, close to the one detected by double resonance spectroscopy (222 cm^{-1}). No rotational lines were resolved for this state while scanning the probe laser, because of the relatively large laser power required for the detection of the R bandheads causing saturated four-wave-mixing signals.

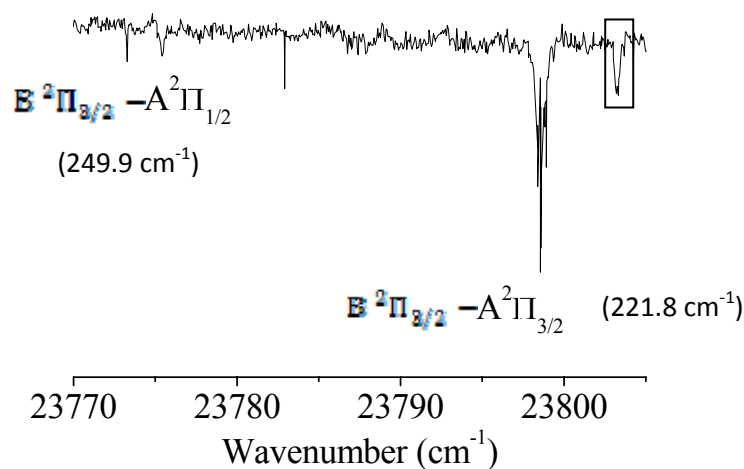


Figure 8.12: Two-color four-wave mixing spectrum of the C_4H $B^2\Pi - X^2\Sigma^+$ transition with pump laser set on the $B^2\Pi_{3/2} - X^2\Sigma^+$ origin band. The two peaks labeled on the plot correspond to the two spin-orbit components of the $A^2\Pi$ state located 213 cm^{-1} above the $X^2\Sigma^+$ as also observed by photoelectron spectroscopy [26]. Feature in box unknown. Energies of the spin orbit components with respect to the ground state are indicated.

At 250 cm^{-1} , a second level is detected and identified as belonging to the $\Omega = 1/2$ manifold, resulting in a separation of -28 cm^{-1} between the spin-orbit (s-o) components. It is interesting to observe that even the weak $B^2\Pi_{3/2} - A^2\Pi_{1/2}$ transition is detected.

In the present case, the probe frequency is set on the less intense $B^2\Pi_{3/2} - A^2\Pi_{1/2}$ transition and the pump one on the strong $B^2\Pi_{3/2} - ^2\Sigma^+$ are in a SEP fashion. The measured s-o splitting in the $A^2\Pi$ state is consistent with an empirical value based on the following observations. The $B^2\Pi$ of C_4H and $X^2\Pi$ states of C_6H arise from the singly unoccupied orbital configurations $1\pi^3$ and $2\pi^3$, respectively. These two electronic states have a similar s-o constant, ~ -16 cm^{-1} [25, 32]. Similarly, the C_4H $A^2\Pi$ and C_6H $A^2\Pi$ states should have comparable splitting, ≈ -25 cm^{-1} , because they arise from $2\pi^3$ and $3\pi^3$ open shell configurations. This alternating behavior is similar to that described in the theoretical calculations of the s-o splitting of the HC_nS series [33]. The A_{so} parameter was determined via the R-T analysis.

8.6.3. Renner-Teller Analysis: Effective Hamiltonian

The R-T analysis was carried out as in reference [34], using an effective Hamiltonian diagonalization. The matrix coefficients were calculated according to previously determined formulae [12] for any level of vibronic symmetry $K = |l_7 \pm l_6 \pm \Lambda|$ (l_7 and l_6 are the vibronic angular momenta associated with the two degenerate vibrations and Λ the electronic angular momentum). l_7 was varied from $-v_7$ to v_7 while Σ and Λ took all possible combinations of $\pm 1/2$ and ± 1 values, respectively. The off-diagonal terms related to ϵ_6 and ϵ_7 are non-zero within block matrices obeying $\Delta v_7 = 0, \pm 2$ according to the formulas given in reference [12]. The R-T interaction related to the cross-interaction R-T parameter, ϵ_{67} has non-vanishing terms in the Hamiltonian for $\Delta v_7 = \pm 1, \Delta l_7 = -1, \Delta v_6 = \pm 1, \Delta l_6 = -1, \Delta \Lambda = -2$ and complex conjugate. The s-o and the R-T interaction for the two lowest bending vibrations were taken into consideration. The analysis did not involve the vibronic interactions between the $X^2\Sigma^+$ and $A^2\Pi$ states. Terms were taken up to $v = 4$ and $|P| \leq 2.5$ resulting in a block-diagonal square matrix of size 568×568 (largest block size is 105×105) expressed in a $|v_7, v_6, l_7, l_6, \Lambda, \Sigma\rangle$ basis set. The assignment was made by choosing the $|v_7, v_6, l_7, l_6, \Lambda, \Sigma\rangle$ element which had the highest coefficient (reported in Appendix F) of the eigenvector basis expansion. This formalism, in principle only valid for a tetra-atomic molecule, is used for C_4H as previously done for the excited state [25]. The quartic terms of the potential energy

curve relatively to a bending angle are contained in the anharmonic terms of the model which were not considered.

The parameters ϵ_6 , ϵ_7 , ϵ_{67} , ω_6 , ω_7 and A_{60} were fitted and a vibrational energy level assignment could be inferred from the experimental data (Appendix F and Figure 8.13). The R-T parameters were initially set equal to the ones given in reference [25] based on the assumption that the skeletal cis and trans C-C-C-C bending of C₄H in the $B^2\Pi$ and $A^2\Pi$ states have similar characteristics. However, the experimental line list was not reproduced satisfactorily. A higher $|\epsilon_6|$ value is required in order to reproduce all the observed levels, as explained below. A least-squares fit was performed by matching the calculated levels with the experimental findings (12 levels included), one of them being a R-T component lying 122 cm⁻¹ below the $A^2\Pi$ state. This procedure led to a satisfactory fit of the levels of higher energy. An average residual error of around 3.6 cm⁻¹ (per level) was achieved. The results of the R-T fit are summarized in Table 8.3.

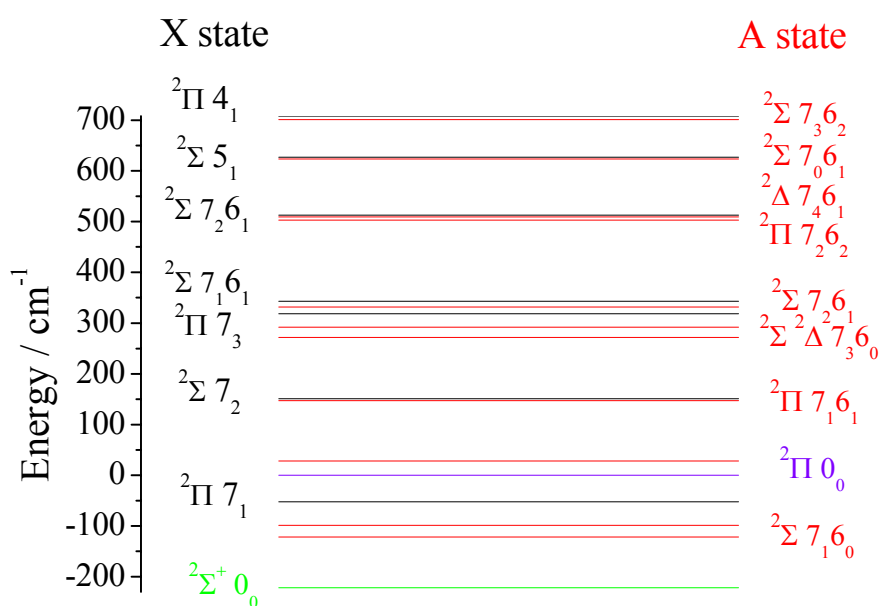


Figure 8.13: Energy level diagram for C₄H showing the vibronic levels detected by two-color stimulated emission pumping resonant four-wave mixing along with their assignments (Appendix F). Not all levels given in Appendix F are shown.

The signs of the R-T parameters are ambiguous and were inferred from the previous analysis of the $B^2\Pi$ excited electronic state [25]. The number of parameters included in the fit was purposely kept small (5) in view of the limited experimental

levels available. Possible inclusion of Sears resonance [12], as well as anharmonicities was thus not taken into account and the simple model of reference [25] was preferred instead, as the lowest vibronic levels were to be reproduced. On the basis of the experimental linelist, several of the energy levels are assigned to vibrations in the electronic $X^2\Sigma^+$ ground state.

A_{90}	-45.5 (fixed)
ω_6	401.4 ± 4.0
ω_7	190.8 ± 1.0
ϵ_6	-0.99 ± 0.01
ϵ_7	-0.061 ± 0.03
ϵ_{67}	-0.105 ± 0.01

Table 8.3: Spectroscopic constants inferred for C_4H in the $A^2\Pi$ state (in cm^{-1} , ϵ is dimensionless).

The R-T parameters differ somewhat from those given for the $B^2\Pi$ excited state of C_4H in reference [25]. The large $\epsilon_6 = -0.99(1)$ indicates that the potential surface has an energy minimum in a non-linear geometry. A CASSCF calculation carried out by constraining a linear geometry for C_4H leads to a large splitting for the ν_6 mode [36] and might confirm this; furthermore the molecule is quasi-linear for this bending vibration in the excited state [25]. The calculations indicate that the linear configuration is a local energy minimum [35]. More precisely, the vibrational harmonic *ab initio* calculations show a large splitting ($441 - 2007\text{ cm}^{-1}$) [35] for the two R-T components associated with the ν_6 bending vibration. This results in $|\epsilon_6| \approx 0.90$, which is close to the value given in Table 8.3. As shown in Appendix F, there is a vibrationally excited mode resulting from the diagonalization which lies below the $A^2\Pi$ state, at approximately -122 cm^{-1} with a $^2\Sigma$ character. This corresponds to the observations made by anion photoelectron spectroscopy for which a level at approximately $\sim -125\text{ cm}^{-1}$ is detected [26]. The analysis indicates that it is a combination of the 7_1 vibrational state mixed with 7_{162} , 7_{164} and more weakly with 7_{360} , 7_{362} and 7_{364} because of the relatively high R-T parameter ϵ_6 .

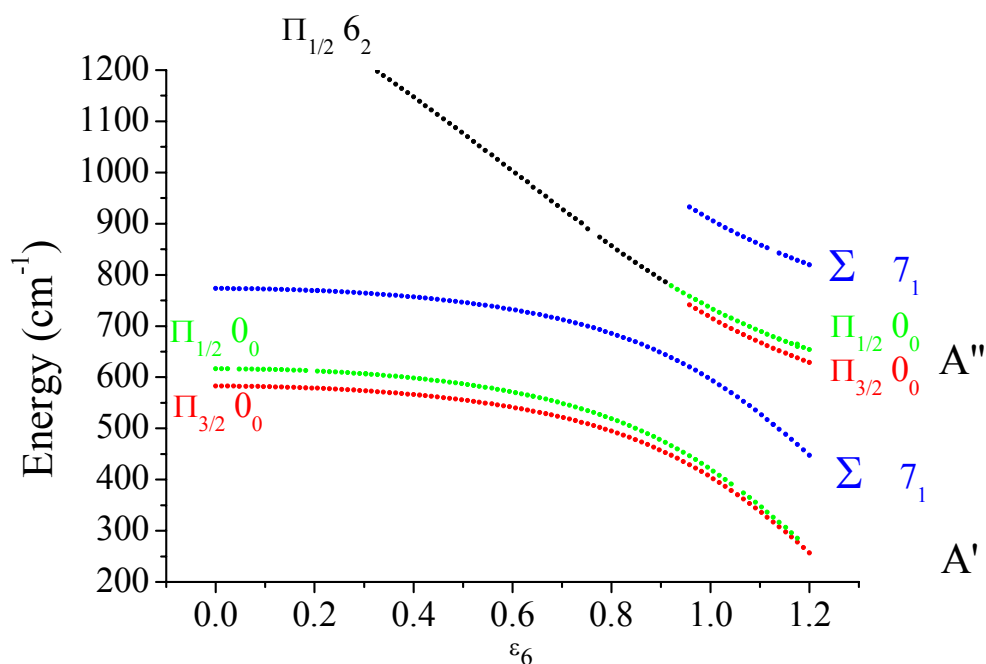


Figure 8.14: Energy level dependence on ϵ_6 with $\epsilon_7 = -0.1$, $\epsilon_{47} = 0$. The $A' \Pi v = 0$ level starts to split for $|\epsilon_6| \approx 0.95$. The higher energy component is significantly mixed with the 6_2 state. Symmetries in the C_s point group are indicated on the right.

This effect is depicted by the energy level diagram shown in Figure 8.14 for a small to large R-T coupling parameter ϵ_6 . The variation of the energy levels with large ϵ_6 shows that the $v = 0$ level splits into a second component (at $\epsilon_6 \approx -0.95$) 314 cm^{-1} higher in energy. At $\epsilon_6 \approx -0.99$ both components comprise 50% of the $v = 0$ basis vector with a slightly higher value for the lower level. When the R-T parameter $|\epsilon|$ is larger than 0.5, the lower potential curve has a negative curvature at the linear geometry versus the bending angle. For some value of the bending angle in a trans-bent configuration of the chain one of the two potentials shows a minimum. The height of the barrier suggested from the fit is around 300 cm^{-1} . The ${}^2\Pi_x$ and ${}^2\Pi_y$ orbitals split in two components on bending of the molecule and gives the potential functions shown in Herzberg [2] for mode ω_6 . One of the curvatures in the quadratic term is positive while the other is negative. In such a case, the molecule is qualified as quasi-linear relative to the ω_6 vibration. This does not occur for mode ω_7 for which both curvatures are positive.

For $|\epsilon_\delta| < 0.92$ the highest component in energy of the “split” ${}^2\Pi_{1/2} v = 0$ level starts to be assigned as ${}^2\Pi_{1/2} v_\delta = 2$. This behavior results from a linear-bent geometry and corresponding symmetries in the C_s point group are indicated on Figure 8.13. The feature detected at $-117 \pm 25 \text{ cm}^{-1}$ by photoelectron spectroscopy [26] relative to the ground state, which was attributed to a hot band, matches with the first level listed in Appendix F, the lower $v = 0$ component, although this was not included in the fitted data.

The lowest modes in energy (lying below the $A {}^2\Pi$ state) did not vary by more than $20\text{-}30 \text{ cm}^{-1}$ if the basis set size was increased. This indicates that the basis is complete within the relatively low values of vibrational excitation in the levels recorded experimentally. However, complete convergence of the Hamiltonian matrix could not be achieved because for such a high R-T parameter $\epsilon_\delta = -0.99$, the basis set needs to be large (with a single bending mode, it was tested that v_{\max} had to be greater than $60\text{-}80$). Because of hardware memory limitations, convergence of the Hamiltonian could not be reached. A restricted basis set was thus used ($v_{\max} = 4$), the main focus of this work being to reproduce the lowest vibrational levels of the $A {}^2\Pi$ and $X {}^2\Sigma^+$ electronic states of C_4H . Furthermore, in the current theoretical treatment, the potential energy curve is expanded to a quadratic term only (no anharmonicity is included). The present analysis is thus not completely satisfactory; it however serves the purpose of reproducing the experimental vibrational progression for the two lowest bending modes in the $A {}^2\Pi$ state, with a small number of variable parameters. Such an unusually large R-T parameter has already been calculated for the BF_2 linear molecule in the excited state (the ground state having a bent geometry), $\epsilon \approx 0.93$ for the degenerate vibrational mode [36].

Although neither the higher energy ω_2 vibration (C-H bend) nor the “symmetric” stretch ω_4 were taken into consideration, the energy levels could be reproduced quite satisfactorily. The calculated levels match the experimental values because the measured levels lie below such vibrations and do not appear to have strong interactions with the modes taken into consideration.

Bibliography

- [1] Raghunandan, R.; Mazzotti, F. J.; Esmail, A. M.; Maier, J. P. *J. Phys. Chem. A*, 115, 9365, **2011**.
- [2] Mazzotti, F. J.; Raghunandan, R.; Esmail, A. M.; Maier, J. P. *J. Chem. Phys.* 134, 164303, **2011**.
- [3] Herzberg, G. H. "Electronic Spectra and Electronic Structure of Polyatomic Molecules," in *Molecular Spectra and Molecular Structure, Vol. 3: Van Nostrand Reinhold Inc., New York: 1966*.
- [4] Demtröder, W. *Molecular Physics: Wiley VCH: Weinheim: 2005*.
- [5] Perić, M.; Peyerimhoff, S. *The Role of Degenerate States in Chemistry: Advances in Chemical Physics, Vol.124: Ed. Baer, M.; Due Billing, G.: John Wiley and Sons, Inc.: 2002*.
- [6] Bunker, P.; Jensen, P. *Molecular Symmetry and Spectroscopy: NRC Research Press: Ottawa: 2006*.
- [7] Dixon, R. N. *J. Chem. Phys.* 31, 258, **1959**.
- [8] Low, W. *Phys. Rev.* 97, 1664, **1955**.
- [9] Nielson, H. H.; Amat, G.; Goldsmith, M. *J. Chem. Phys.* 26, 1060, **1957**.
- [10] Hougen, J. T. *J. Chem. Phys.* 37, 403, **1962**.
- [11] Ramos, C.; Winter, P. R.; Zwier, T. S.; Pratt, S. T. *J. Chem. Phys.* 116, 4011, **2002**.
- [12] He, S.; Clouthier, D. J. *J. Chem. Phys.* 123, 014316/1-, **2005**.
- [13] Callomon, J. H. *Can. J. Phys.* 34, 1046, **1956**.
- [14] Celii, F. G.; Maier, J. P.; Ochsner, M. *J. Chem. Phys.* 85, 6230, **1986**.
- [15] Celii, F. G.; Maier, J. P. *J. Opt. Soc. Am. B.* 7, 1944, **1990**.
- [16] Szczepanski, J.; Wang, H.; Jones, B.; Arrington, C. A.; Vala, M. T. *Phys. Chem. Chem. Phys.* 7, 738, **2005**.
- [17] Sunahori, F. X.; Wei, J.; Clouthier, D. J. *J. Chem. Phys.* 128, 244311/1, **2008**.
- [18] Guelin, M.; Green, S.; Thaddeus, P. *Astrophys. J.* 224, L27, **1978**.
- [19] Cernicharo, J.; Guelin, M.; *Astron. Astrophys.* 309, L27, **1996**.
- [20] Guelin, M.; Cernicharo, J.; Travers, M. J.; McCarthy, M. C.; Gottlieb, C. A.; Thaddeus, P.; Ohishi, M.; Saito, S.; Yamamoto, S. *Astron. Astrophys.* 317, L1 **1997**.
- [21] Gottlieb, C. A.; Gottlieb, E. W.; Thaddeus, P.; Kawamura, H. *Astrophys. J.* 275, 916, **1983**.

- [22] Guelin, M.; Cernicharo, J.; Navarro, S.; Gottlieb, C. A.; Thaddeus, P. *Astron. Astrophys.* 182, L37, **1987**.
- [23] Yamamoto, S.; Saito, S.; Guelin, M.; Cernicharo, J.; Suzuki, H.; Ohishi, M. *Astrophys. J.* 323, L149, **1987**.
- [24] Woodward, D. R.; Pearson, J. C.; Gottlieb, C. A.; Thaddeus, P. *Astrophys. J.* 333, L29, **1988**.
- [25] Hoshina, K.; Kohguchi, H.; Ohshima, Y.; Endo, Y. *J. Chem. Phys.* 108, 9, **1998**.
- [26] Zhou, J.; Garand, E.; Neumark, D. M. *J. Chem. Phys.* 127, 154320, **2007**.
- [27] Aarts, J. F. M. *Mol. Phys.* 35, 1785, **1978**.
- [28] Tang, J.; Saito, S. *J. Chem. Phys.* 105, 18, **1996**.
- [29] Peric, M. *Mol. Phys.* 105, 59, **2007**.
- [30] Raghunandan, R.; Mazzotti, F. J.; Chauhan, R.; Tulej, M.; Maier, J. P. *J. Phys. Chem. A.* 113, 13402, 2009.
- [31] Western, C. M. *PGOPHER, a Program for Simulating Rotational Structure*, <http://pgopher.chm.bris.ac.uk>.
- [32] Linnartz, H.; Motylewski, T.; Vaizert, O.; Maier, J. P.; Apponi, A. J.; McCarthy, M. C.; Gottlieb, C. A.; Thaddeus, P. *J. Mol. Spectrosc.* 197, 1, **1999**.
- [33] Mitrushchenkov, A.; Linguerri, R.; Rosmus, P.; Maier, J. P. *Mol. Phys.* 107, 1549 **2009**.
- [34] Hoshina, K.; Endo, Y. *J. Chem. Phys.* 127, 184304, **2007**.
- [35] Graf, S.; Geiss, J.; Leutwyler, S. *J. Chem. Phys.* 114, 4542, **2001**.
- [36] Tarroni, R.; Clouthier, D. J. *J. Chem. Phys.* 133, 064304, **2010**.

Chapter 9

Concluding Remarks

This thesis describes the experimental measurements and spectral analysis of transient hydrocarbon species. The electronic spectra of these species have been recorded by both linear and non-linear spectroscopic techniques, viz. cavity ring-down (CRDS) and four wave mixing (FWM) spectroscopy. The molecules were produced using pulsed slit jet discharge or laser ablation coupled with supersonic expansion. CRDS offers high sensitivity because of the large absorption pathlengths achieved inside the cavity and its immunity towards shot-to-shot laser fluctuations. Four-wave mixing achieves where CRDS fails, in terms of selectivity of the species studied. This is achieved by applying very short discharge pulse lengths, in the nanosecond time scale. As a consequence, the molecules are separated out in the plasma discharge based on their masses.

The ${}^3\Pi - {}^3\Pi$ electronic transition of C_6H^+ has been measured using CRDS; this is the first gas phase detection of the cation. Partially resolved P lines and observation of band heads permitted a rotational contour fit. Spectroscopic constants in the ground and excited-state were determined. Broadening of the spectral lines indicates the excited-state lifetime to be around 100 ps. The electronic transition of $C_6H_3^+$ at 26402 cm^{-1} assumed to be ${}^1A_1 - X{}^1A_1$ in C_{2v} symmetry could not be rotationally resolved. Thus, it is concluded that the excited electronic state is short-lived as a result of lifetime broadening by intramolecular processes.

The identification and characterization of specific radicals and ions demands techniques exhibiting a substantial selectivity in order to disentangle the spectral features, especially in harsh environments where these features overlap. The potential of degenerate and two-color FWM applied to selectivity of transient species has been studied extensively in this work. In particular, it is shown that FWM can be used to select out various molecular systems like C_3/C_4H , C_3/HC_2S and C_2/HC_4H^+ only by varying the timings between the experimental components (laser/valve/discharge) while applying extremely short ($<1\mu s$) discharge pulses. The two color variant is

exceptionally powerful in disentangling overlapping features even within the same spectroscopic system. This is demonstrated in the case of HC_4H^+ where P lines of the $\Omega=3/2$ spin orbit component are effectively separated out from the overlapping $\Omega=1/2$ component in the $A^2\Pi_u - X^2\Pi_g$ electronic transition.

The first ever detections of ions (both polyatomic cations and anions- HC_4H^+ , C_2^-) by FWM are presented. Generally, it is difficult to generate anions in sufficient abundance for spectroscopic studies. Negative ions are far less abundant in most of the experimental environments than neutrals or cations. Often, anions are generated in plasma where numerous species coexist whose spectra may overlap. Therefore, highly sensitive methods are required that are suitable for low-density environments. The results suggest convincingly that nonlinear four-wave mixing spectroscopy is applicable to study numerous neutral, cationic and anionic radicals that are produced in plasma environments by applying a discharged free-jet expansion.

However, from an experimental point of view, FWM in its BOXCAR configuration poses challenges with regard to the alignment of the setup. This can be overcome if one succeeds to implement the phase conjugate geometry, which would allow a Doppler free response in addition. Recently, motorised mirror mounts were proposed in order to achieve better signal optimization. Other kinds of laser induced grating spectroscopy (LIGS), like Self-LIGS could be implemented where one detects the first order diffraction signal due to the spatial overlap of two incident beams.

Both CRDS and FWM have been employed as tools for spectroscopic investigation of non-adiabatic effects in linear polyatomic molecules. The excitation of the $v_3 = 1$ ($\sigma_g^+ \text{C}-\text{C}$ stretch) and the $v_7 = 2$ ($\pi_g^2 \text{C}\equiv\text{C}-\text{C}$ bend) levels in the $A^2\Pi_u$ electronic state of diacetylene cations results in Renner-Teller (R-T) and Fermi interactions. The 3_0^1 and 7_0^2 vibronic bands in the $A^2\Pi_u - X^2\Pi_g$ transition of HC_4H^+ have been measured with rotational resolution using cavity ring-down spectroscopy in a supersonic slit jet discharge. A vibronic analysis has been carried out taking into consideration the R-T, spin-orbit, and Fermi resonance interactions between the v_3 and v_7 modes. The spectroscopic constants for the excited electronic state are compared with the ground state.

The double resonance four-wave mixing approach was used to unambiguously identify the vibronic R-T manifold in the $A^2\Pi$ state up to 700 cm^{-1} above $v = 0$ of C_4H by pumping on the origin $B^2\Pi - X^2\Sigma^+$ electronic transition. On the basis of the experimental linelist, several of the energy levels are assigned to vibrations in the electronic $X^2\Sigma^+$ ground state. An assignment of the levels was carried out by a R-T analysis, leading to a relatively large ϵ_g in the ground state for the second lowest bending mode as previously found in the upper state. This study results in the detection of levels located below the $A^2\Pi$ state because of high R-T interaction, as is found for example for C_4D .

CRDS has also been employed to detect broad absorption features of the $B^1B_1 - X^1A_1$ transition of H_2CCC ($l\text{-}C_3H_2$). The observations provide evidence that the broad, diffuse interstellar bands (DIBs) at 4881 and 5450 \AA are caused by the $B^1B_1 - X^1A_1$ transition of H_2CCC ($l\text{-}C_3H_2$). The large widths of the bands are due to the short lifetime of the B^1B_1 electronic state. The conclusion that these absorptions belong to C_3H_2 has been drawn through a number of measurements and observations (isotope shifts, gas-matrix shifts, precursor tests etc.). The bands in the gas phase show exact matches to the profiles and wavelengths of the two broad DIBs. This makes $l\text{-}C_3H_2$ a carrier of the DIBs, which have remained a long standing mystery in astronomy.

An interesting inference concerns the anti-correlation with C_3 abundance in diffuse clouds. From the measurements of the 4881 and 5450 \AA DIBs in four stars covering a large range in reddening and supplemented by previous measurements of HD 204827 [1] by Hobbs et al., it is found that these two DIBs correlate much more closely with each other than with $E(B - V)$. This implies a common carrier. HD 204827 was specifically observed previously because of its exceptionally high column density of interstellar C_3 . On the contrary, no C_3 could be detected toward HD 183143. By contrast, from the spectra, the 4881 and 5450 \AA DIBs in HD 204827 are less than one-third their strength in HD 183143. There is a similar, negative trend between the line-of-sight abundance of interstellar C_3 [2] and the strengths of the 4881 and 5450 \AA DIBs for the stars in the present work. The inference seems clear: hydrogenation of C_3 to species such as $l\text{-}C_3H_2$ leads to depletion of C_3 with a consequent enhancement of the 4881 and 5450 \AA DIBs.

An obvious question is the role of *c*-C₃H₂. Radio astronomy has established that this cyclic isomer is ubiquitous in dense and diffuse interstellar media, but *c*-C₃H₂ does not have an allowed electronic transition in the DIB region. Apart from *l*-C₃H₂, also *l*-C₃H has many absorption bands in the DIB region [3]. Some of these peaks are actually observed in the CRD spectra measured nearby to the broad bands of *l*-C₃H₂. However, as has already been concluded, due to the small oscillator strength of such individual transitions, the DIB absorptions would have EWs of mÅ or less. Nevertheless, chemically the presence of *l*-C₃H in addition to the here proven *l*-C₃H₂ could be investigated with high S/N DIB measurements because the gas-phase data are available. Another related aspect concerns the possible presence of *l*-C₃H₂⁺ in the diffuse medium [4]. It was pointed out that *l*-C₃H₂⁺ formation could be significant via associate electron attachment to *l*-C₃H₂. Also, with better sensitivity, measurements can be undertaken to measure the weak $2^1_0-4^1_0$ B¹B₁-X¹A₁ transition of H₂CCC (*l*-C₃H₂) which could not be detected by the present set-up. Mass selection with CRDS would be an added advantage.

The present work provides an insight to understanding not only the fundamental spectroscopic properties of these transient species but also their astrophysical significance. Moreover, it also demonstrates the highly sensitive and selective capabilities of the employed experimental techniques, which could be of use in other fields like combustion, trace gas analysis, to name a few.

Bibliography

- [1] Hobbs, L. M. et al. *Astrophys. J.* 680, 1256, **2008**.
- [2] Oka, T.; Thorburn, J. A.; McCall, B. J.; Friedman, S. D.; Hobbs, L. M.; Sonnentrucker, P.; Welty, D. E.; York, D. G. *Astrophys. J.*, 582, 823, **2003**.
- [3] Ding, H.; Pino, T.; Güthe, F.; Maier, J. P.; *J. Chem. Phys.*, 115, 6913, **2001**.
- [4] Güthe, F.; Tulej, M.; Pachkov, M. V.; Maier, J. P. *Astrophys. J.* 555, 466, **2001**.

Appendix A

Dispersion Effects in CRDS

Consider a cavity formed by two mirrors with radius of curvature r , separated by a distance $L < 2r$ and the round trip time $t_r = 2L/n_0c$. Here n_0 is the index of refraction in the medium between the mirrors. The intensity reflectivity and transmittivity are denoted as R and T respectively. Assume the input field is mode matched to the TEM_{00} transverse mode of the cavity. The output of the RDC subjected to arbitrary excitation can be written in the form of a Green's function [Ref. 21, Chapter 2] as

$$E_0(t) = \int G(t - t') E_i(t') dt' , \quad (A.1)$$

where $E_i(t')$ and $E_0(t)$ are the electric fields of the input and output radiations respectively. Physically, $G(t - t')$ gives the output of the cell following a delta function input at time t' . Under appropriate conditions, $G(t)$ takes the form

$$G(t) = \frac{1}{\sqrt{2\pi}} \sum_q A(\omega_q) \exp\left(-\frac{t - \frac{t_r}{2}}{t_{\alpha}(\omega_q)}\right) \exp\left[i\omega\left(t - \frac{t_r}{2}\right)\right] \Theta\left(t - \frac{t_r}{2}\right) , \quad (A.2)$$

where ω_q and $A(\omega_q)$ are the angular frequency and excitation amplitude of the q th resonance mode; $t_{\alpha}(\omega_q)$ is the ring down time of the q th mode; $\Theta(t)$ is the unit step function that equals zero for $t < 0$ and one for $t \geq 0$. They are given as

$$A(\omega_q) = \sqrt{2\pi} \frac{T^{\frac{1}{2}} e^{-\alpha(\omega)L/2}}{t_r R_{eff}(\omega)} \quad (A.3)$$

$$R_{eff}(\omega) = R(\omega) e^{-\alpha(\omega)L} \quad (A.4)$$

$$t_{\alpha}(\omega_q) = \frac{t_r R_{eff}(\omega)}{2[1 - R_{eff}(\omega)]} \quad (A.5)$$

The resonance condition for the q th mode is given by

$$k(\omega_q)L = \pi q + \theta \quad (A.6)$$

with $k(\omega) = n(\omega)\omega/c$ the wavenumber of the radiation and $\theta = \arg(-R)$ the phase shift per reflection from the mirrors.

Consider the cavity is filled with a sample with a resonant susceptibility $\chi(\omega) = \chi' - i\chi''$, where the macroscopic polarization is defined by $P(\omega) = \chi(\omega)E(\omega)$. The resulting index of refraction for small $|\chi|$ can be written as

$$n(\omega) = n_0 \left[1 + \frac{\chi'(\omega)}{2n_0^2} \right] - i \frac{\chi''(\omega)}{2n_0} . \quad (\text{A.7})$$

The absorption coefficient is then given as

$$\alpha(\omega) = \frac{\omega \chi''(\omega)}{c n_0} . \quad (\text{A.8})$$

The cavity resonance frequencies in the presence of molecular resonance are calculated by substituting (A.6) in (A.7). When χ' is small,

$$\omega_q = \omega_q^0 \left[1 - \frac{\chi'(\omega_q)}{2n_0^2} \right], \quad (\text{A.9})$$

where

$$\omega_q^0 = \frac{2}{\tau_r} (\pi q + \theta) = \frac{2}{n_0 L} (\pi q + \theta) \quad (\text{A.10})$$

is the cavity mode condition without sample dispersion.

The small dispersion contributions cause the periodicity between the beating of different cavity modes with period τ_r to be lost, and this affects the shape of the pulses leaving the cavity.

Appendix B

Electronic Spectra of Linear C_{2n+1} Chains

The sensitivity of a pulsed valve coupled with laser vaporization was tested by measuring the origin and vibronic bands of ${}^2\Pi_u \leftarrow X{}^2\Sigma_g^+$ transition of C_5 using CRDS. C_5 molecules are generated by focusing a 7 ns, 30 mJ, 355 nm Nd:YAG laser beam onto a graphite rod that is mounted in the throat of a 12 mm long slit. The rod undergoes both translation and rotation to continuously expose a fresh surface to the ablation laser pulse, and the plasma is probed at a distance of 4 mm from the slit.

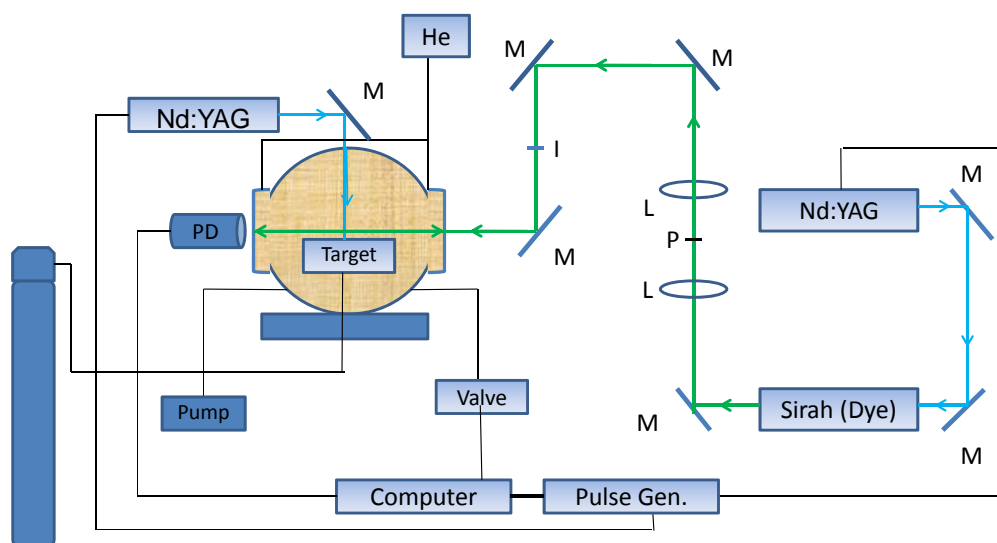


Figure B.1: Experimental Configuration. M: Mirror, I: Iris, P: Pinhole, L: Lens.

The ablation laser is set to coincide with the buffer flow (11 bar He) over the target area. Inside the chamber, the pressure was kept constant at 0.045 mbar. The probe is generated by a 0.06 cm^{-1} , 7 ns, 20 Hz dye laser pumped by the 355 nm output of

the Nd:YAG laser. The absorption spectrum of C_5 is compared to what has been obtained using previous setups and with the pulsed slit nozzle discharge source. The alignment is optimized on the $(0, 0)$ $d^3\Pi_g \leftarrow a^3\Pi_u$ transition of C_2 . The timings between the ablation and probe lasers, and the gas pulse are critical for cluster production and detection.

B.1 C_5

B.1.1. Comparison to previous CRD-laser ablation setups

The electronic spectra of 0_0^0 band of the $A^1\Pi_u-X^1\Sigma_g^+$ electronic transition of C_5 detected using the described unit and two separate laser ablation setups are shown in Figure B.3 [1, 2]. The weaker $2_0^1, 7_0^2$ vibronic transitions had not been detected at the time of measurement, possibly owing to the lack of good signal to noise. The experimental spectrum is shown plotted against the simulation at 30 K rotational temperature, 0.1 cm^{-1} linewidth with spectroscopic constants $B''=0.0853133$ cm^{-1} , $B'=0.0855$ cm^{-1} , $T_{00}=19566.56$ cm^{-1} (Figure B.2). Unlike Figure B.3 ((b), (c)), the rotational contour of the newly recorded spectrum shows a strong Q branch, and weak P and R branches, as expected for a $A^1\Pi_u-X^1\Sigma_g^+$ transition. The averaged spectrum of the origin band is also shown. The sensitivity obtained using the current laser ablation source was observed to be increased by a factor of 2.

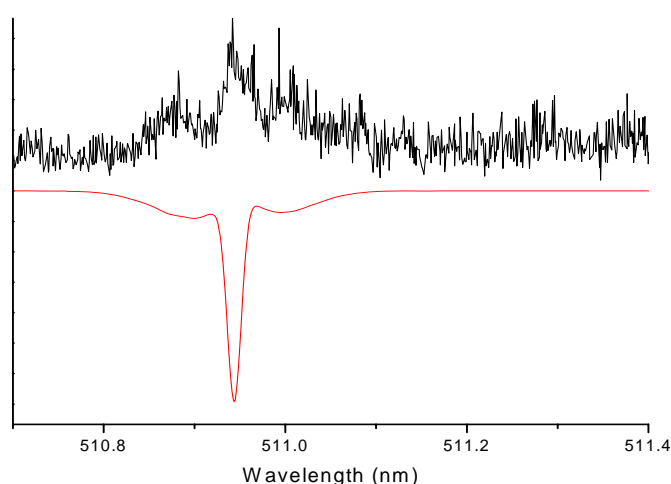


Figure B.2: The experimental spectrum of 0_0^0 band of the $A^1\Pi_u-X^1\Sigma_g^+$ electronic transition of C_5 shown plotted against simulation.

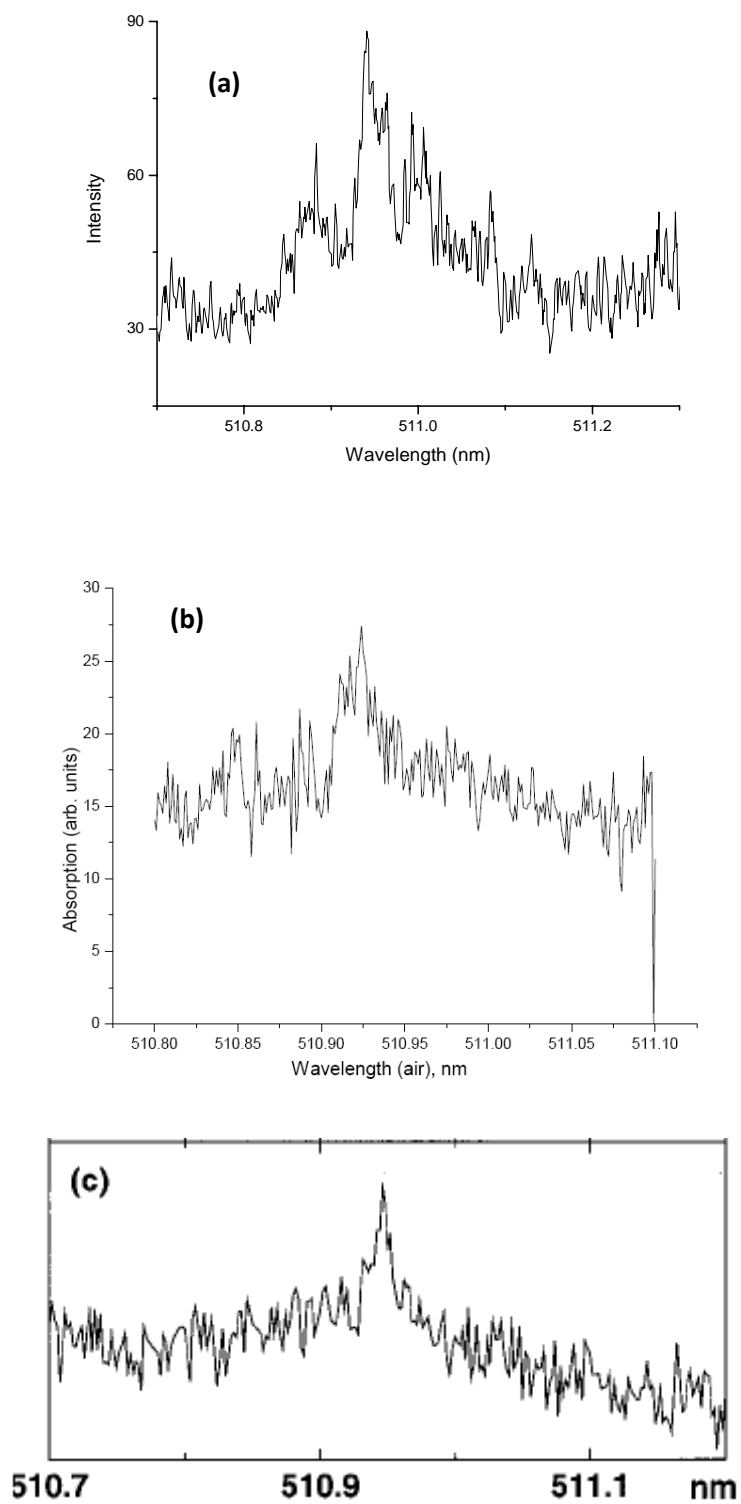


Figure B.3: Comparison of origin band of the $A^1\Pi_u-X^1\Sigma_g^+$ transition of C_5 for (a) the current setup (b) Ref. [1] (c) Ref. [2].

B.1.2. Comparison with high voltage discharge spectra

The sharp peaks in the discharge spectrum are due to rotational transitions in the 0-0 and 1-1 vibrational bands of the $d^3\Pi_g \leftarrow a^3\Pi_u$ electronic transition of C_2 . Because of the lower rotational temperatures obtained in laser vaporization, the C_2 overlap can be completely removed which makes the rotational profile more predominant (Figure B.4).

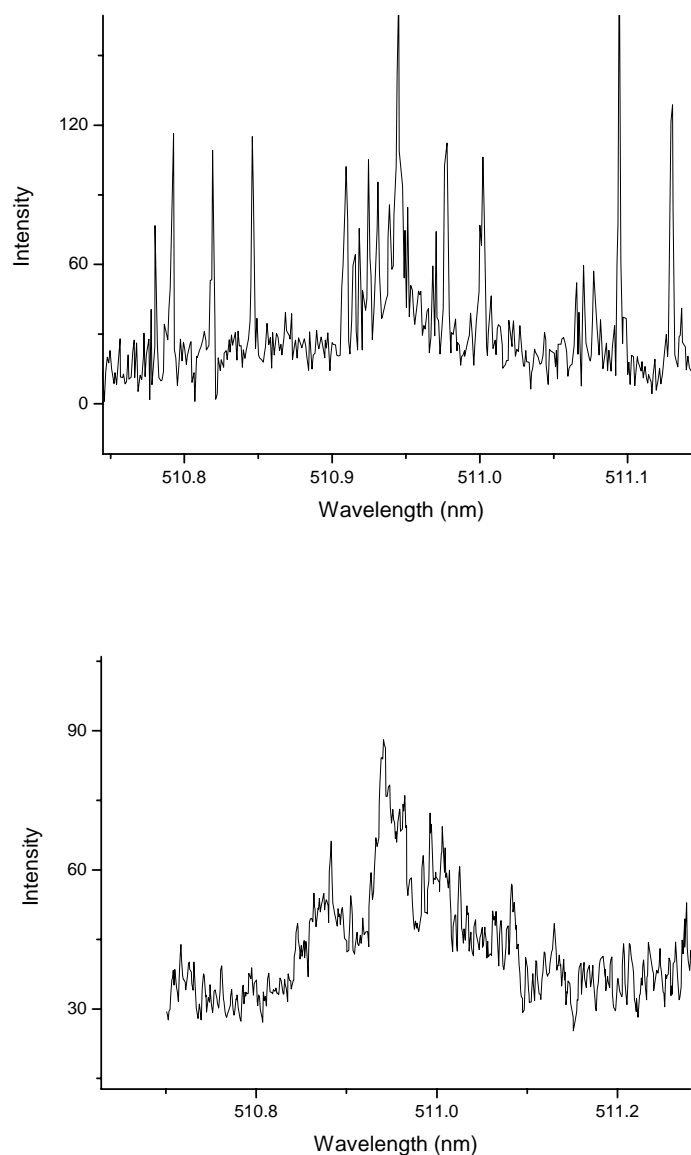


Figure B.4: Electronic spectra of C_5 obtained using the discharge source (top) and the laser vaporization source (bottom).

B.1.3. Detection of vibronic transitions in $A^1\Pi_u$ electronic state

Besides the $A^1\Pi_u-X^1\Sigma_g^+$ origin band of C_5 , the transitions 7_0^2 ($\lambda_{\text{air}}=503.81$ nm) and 2_0^1 ($\lambda_{\text{air}}=497.48$ nm), to vibrationally excited levels in the upper $^1\Pi_u$ state, were also detected (Figure B.5).

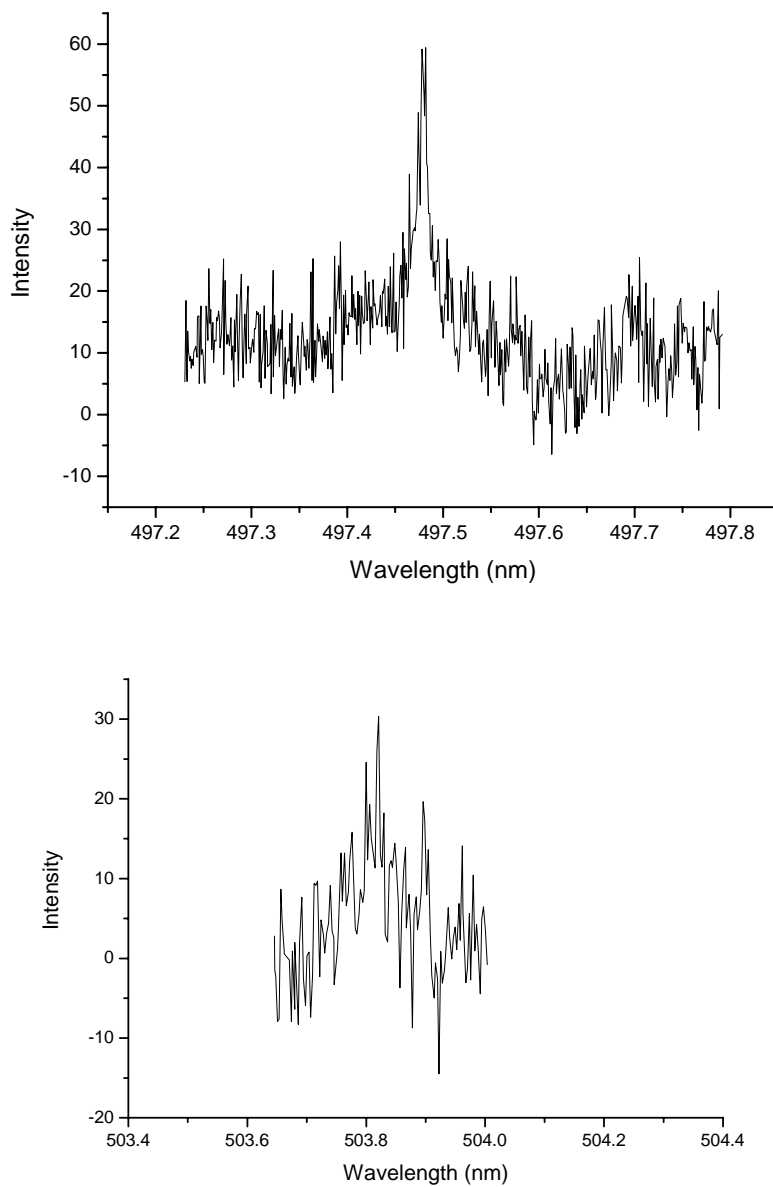


Figure B.5: The 2_0^1 (top) and 7_0^2 (bottom) vibronic bands of $A^1\Pi_u-X^1\Sigma_g^+$ transition of C_5 .

B.2. Detection feasibility for Linear C_{2n+1} Chains

Long carbon chains with odd numbered atoms are considered good candidates as diffuse interstellar band carriers [3]. As such, attempts were undertaken to detect the ${}^1\Sigma_u^+ - X{}^1\Sigma_g^+$ transition of C₁₅ at 419.6 nm and the ${}^1\Pi_u - X{}^1\Sigma_g^+$ transition of C₇ at 542.3 nm as recorded in Ne matrices[4]. These were however unsuccessful. Therefore, an estimation of detection limits for these transitions was carried out with the experimentally measured C₅ transition and the theoretically predicted oscillator strengths for the higher carbon chains [5-9]. The absorption cross section of C₅ measured by CRDS is determined to be 1.7×10^{-14} cm²/molecule. Given the oscillator strength of the $A{}^1\Pi_u - X{}^1\Sigma_g^+$ transition of C₅ (~ 0.015) and an absorption coefficient measured by CRDS of $\sim 3.8 \times 10^{-5}$ cm⁻¹, this yields a concentration of 2.13×10^9 molecules cm⁻² for the neutral C₅ species.

Species	Concentration, N (molecules/cm ⁻²)	$f {}^1\Pi_u$	$f {}^1\Pi_u \times N$ (molecules/cm ⁻²)	$f {}^1\Sigma_u^+$	$f {}^1\Sigma_u^+ \times N$ (molecules/cm ⁻²)
C ₃	0.5×10^9	0.059	5×10^8	1.1	9.3×10^8
C ₅	2.13×10^9	0.015	34×10^7	2.2	4.6×10^9
C ₇	5.3×10^8	0.006	31×10^6	3.24	1.7×10^9
C ₉	1.3×10^8	0.0062	8×10^5	4.86	6.3×10^8
C ₁₁	3.2×10^7	0.005	1×10^5	5.64	1.8×10^8
C ₁₃	8×10^6	0.0035	28×10^4	6.922	5.5×10^7
C ₁₅	2×10^6	0.0030	6×10^3	8.092	1.6×10^7

Table B.1: Detection feasibility estimation for the long carbon chains which can be achieved by laser ablation-CRDS.

The abundance of C₇ was found to be 3-5 less than C₅ according to the infrared studies which were carried out using a similar vaporization setup [10]. Assuming that the particle density decreases by a factor of 4 for every addition of 2 carbon atoms, the concentrations of higher carbon chains can be calculated. From the obtained signal to noise, a detection limit of approximately 10^7 molecules cm⁻² was inferred for the Π - Σ transitions and 10^9 molecules cm⁻² for the Σ - Σ transitions. This implies that the C₁₅ and C₇ transitions of interest would fall below the estimated detection limits. Table B.1 shows the molecule number densities calculated for the long carbon chains. Another

reason for the non-detection of C₁₅ could be attributed to the possibility of monocyclic ring character in long carbon chains with more than 10 carbon atoms [11]. For example, the cyclic isomer for C₁₃ has been observed to be vastly more stable than the linear structure in the IR using similar experimental conditions [12]. In case of C₁₁, calculations predict the cyclic isomer to be energetically more stable than the linear by 1.44 - 2.46 eV [9]. However, these calculations predict very low oscillator strengths for the electronic transitions of cyclic isomers [9] which would render the detection of these monocyclic carbon rings difficult. As an alternative, a reasonable candidate for detection of longer carbon chains is the ${}^1\Sigma_u^+ - X\,{}^1\Sigma_g^+$ transition of C₇ at 250 nm, provided high reflectivity mirrors for CRDS are available in this wavelength region. In case one estimates a 3 times decrease in concentration for these chains, the ${}^1\Sigma_u^+ - X\,{}^1\Sigma_g^+$ transition of C₉ would also fall just within the detection limits.

Bibliography

- [1] PhD thesis, Chauhan, R. *University of Basel*, **2010**.
- [2] Motylewski, T.; Vaizert, O.; Giesen, T. F.; Linnartz, H.; Maier, J. P. *J. Chem. Phys.* 111, 6161, **1999**.
- [3] Maier, J. P.; ; Walker, G. A. H.; Bohlender, D. A. *Astrophys. J.* 602, 286, **2004**.
- [4] Forney, D.; Freivogel, P.; Grutter, M.; Maier, J. P. *J. Chem. Phys.* 104, 4954, **1996**.
- [5] Kolbuszewski, M. *J. Chem. Phys.* 102, 3679, **1995**.
- [6] Hanrath, M.; Peyerimhoff, S. D. *Chem. Phys. Lett.* 337, 368, **2001**.
- [7] Giuffreda, M. G.; Deleuze, M. S.; François, J.-P.; Trofimov, A. B. *Int. J. Quantum Chem.* 85, 475, **2001**.
- [8] Mühlhäuser, M.; Froudakis, G. E.; Peyerimhoff, S. D. *Chem. Phys. Lett.* 336, 171, **2001**.
- [9] Mühlhäuser, M.; Froudakis, G. E.; Peyerimhoff, S. D. *Phys. Chem. Chem. Phys.* 3, 3913, **2001**.
- [10] Heath, J. R.; Sheeks, R. A.; Cooksy, A. L.; Saykally, R. J. *Science* 249, 895, **1990**.
- [11] Van Orden, A.; Saykally, R. J. *Chem. Rev.* 98, 2313, **1998**.
- [12] Giesen, T. F.; Van Orden, A.; Hwang, H. J.; Fellers, R. S.; Provençal, R. A.; Saykally, R. J. *Science* 265, 756, **1994**.

Appendix C

Rotational Assignment for the 3_0^1 and 7_0^2 $A^2\Pi_u-X^2\Pi_g$ transitions of HC_4H^+

The table below lists the observed and calculated rotational lines (cm^{-1}) for the 3_0^1 $A^2\Pi_u-X^2\Pi_g$ and 7_0^2 $A^2\Pi_u-X^2\Pi_g$ transition of HC_4H^+ .

$3_0^1 A^2\Pi_u-X^2\Pi_g$				$7_0^2 A^2\Pi_u-X^2\Pi_g$			
Assignment	Observed (o)	Calculated (c)	o - c	Assignment	Observed (o)	Calculated(c)	o - c
$P_2(25.5)$	20501.793	20501.744	0.050	$P_2(21.5)$	20553.817	20553.868	-0.051
$P_2(23.5)$	20502.964	20502.938	0.026	$P_2(19.5)$	20554.902	20554.931	-0.029
$P_2(20.5)$	20504.629	20504.630	-0.001	$P_2(17.5)$	20555.936	20555.944	-0.008
$P_2(19.5)$	20505.167	20505.167	0.000	$P_2(16.5)$	20556.417	20556.432	-0.015
$P_2(18.5)$	20505.694	20505.692	0.002	$P_2(15.5)$	20556.887	20556.908	-0.021
$P_2(17.5)$	20506.210	20506.203	0.007	$P_2(14.5)$	20557.368	20557.371	-0.003
$P_2(16.5)$	20506.711	20506.702	0.009	$P_2(13.5)$	20557.806	20557.823	-0.017
$P_2(15.5)$	20507.178	20507.188	-0.010	$P_2(12.5)$	20558.253	20558.262	-0.009
$P_2(11.5)$	20508.988	20509.005	-0.017	$P_2(11.5)$	20558.711	20558.690	0.021
$P_2(8.5)$	20510.261	20510.237	0.024	$P_2(10.5)$	20559.133	20559.106	0.027
$P_1(34.5)$	20510.261	20510.259	0.002	$P_2(9.5)$	20559.498	20559.510	-0.012
$P_2(5.5)$	20511.307	20511.359	-0.052	$P_2(8.5)$	20559.94	20559.903	0.038
$P_1(26.5)$	20516.031	20516.033	-0.002	$P_2(5.5)$	20561.047	20561.011	0.036
$R_2(13.5)$	20516.031	20516.047	-0.016	$P_2(4.5)$	20561.381	20561.357	0.024
$R_2(30.5)$	20516.031	20516.052	-0.021	$R_2(2.5)$	20563.725	20563.718	0.007
$P_1(24.5)$	20517.309	20517.326	-0.017	$R_2(4.5)$	20564.189	20564.193	-0.004
$P_1(23.5)$	20517.929	20517.951	-0.022	$R_2(7.5)$	20564.827	20564.819	0.008
$P_1(22.5)$	20518.533	20518.560	-0.027	$R_2(8.5)$	20565.014	20565.005	0.010
$P_1(21.5)$	20519.160	20519.155	0.005	$R_2(9.5)$	20565.175	20565.178	-0.003
$P_1(20.5)$	20519.711	20519.736	-0.025	$R_2(10.5)$	20565.33	20565.339	-0.009
$P_1(19.5)$	20520.305	20520.302	0.003	$P_1(26.5)$	20571.674	20571.619	0.055
$P_1(18.5)$	20520.855	20520.854	0.001	$P_1(24.5)$	20573.007	20572.964	0.043
$P_1(17.5)$	20521.376	20521.392	-0.016	$P_1(23.5)$	20573.642	20573.615	0.028
$P_1(16.5)$	20521.911	20521.915	-0.004	$P_1(22.5)$	20574.251	20574.250	0.001
$P_1(15.5)$	20522.411	20522.424	-0.013	$P_1(21.5)$	20574.893	20574.870	0.023
$P_1(14.5)$	20522.924	20522.919	0.005	$P_1(20.5)$	20575.508	20575.475	0.033
$P_1(13.5)$	20523.386	20523.399	-0.013	$P_1(18.5)$	20576.67	20576.641	0.029
$P_1(12.5)$	20523.853	20523.866	-0.013	$P_1(17.5)$	20577.218	20577.201	0.017
$P_1(11.5)$	20524.304	20524.319	-0.015	$P_1(16.5)$	20577.741	20577.746	-0.005
$P_1(10.5)$	20524.746	20524.757	-0.011	$P_1(14.5)$	20578.792	20578.791	0.001

$P_1(6.5)$	20526.385	20526.371	0.014
$P_1(5.5)$	20526.734	20526.740	-0.006
$P_1(4.5)$	20527.116	20527.095	0.021
$P_1(3.5)$	20527.449	20527.436	0.013
$P_1(2.5)$	20527.792	20527.763	0.029
$R_1(41.5)$	20527.792	20527.826	-0.034
$R_1(38.5)$	20528.808	20528.764	0.045
$R_1(2.5)$	20529.434	20529.436	-0.002
$R_1(3.5)$	20529.684	20529.666	0.018
$R_1(4.5)$	20529.895	20529.883	0.012
$R_1(5.5)$	20530.095	20530.086	0.009
$R_1(6.5)$	20530.281	20530.275	0.007
$R_1(7.5)$	20530.460	20530.449	0.011
$R_1(8.5)$	20530.630	20530.611	0.020
$R_1(9.5)$	20530.745	20530.758	-0.013
$R_1(28.5)$	20530.884	20530.859	0.025
$R_1(10.5)$	20530.884	20530.891	-0.007

- The average residual error for the fit is **0.01**

$P_1(13.5)$	20579.276	20579.291	-0.015
$P_1(12.5)$	20579.771	20579.775	-0.004
$P_1(11.5)$	20580.239	20580.245	-0.006
$P_1(10.5)$	20580.694	20580.699	-0.005
$P_1(9.5)$	20581.129	20581.138	-0.009
$P_1(7.5)$	20581.967	20581.969	-0.002
$P_1(6.5)$	20582.356	20582.362	-0.006
$R_1(32.5)$	20585.433	20585.430	0.003
$R_1(2.5)$	20585.433	20585.442	-0.009
$R_1(31.5)$	20585.64	20585.653	-0.013
$R_1(3.5)$	20585.64	20585.665	-0.025
$R_1(4.5)$	20585.867	20585.872	-0.005
$R_1(30.5)$	20585.867	20585.861	0.006
$R_1(5.5)$	20586.048	20586.064	-0.016
$R_1(29.5)$	20586.048	20586.054	-0.006
$R_1(6.5)$	20586.235	20586.240	-0.005
$R_1(28.5)$	20586.235	20586.231	0.004
$R_1(7.5)$	20586.412	20586.401	0.011
$R_1(27.5)$	20586.412	20586.393	0.020
$R_1(8.5)$	20586.534	20586.547	-0.013
$R_1(26.5)$	20586.534	20586.539	-0.005
$R_1(9.5)$	20586.669	20586.677	-0.008
$R_1(25.5)$	20586.669	20586.669	0.000
$R_1(24.5)$	20586.796	20586.785	0.011
$R_1(10.5)$	20586.796	20586.791	0.005
$R_1(23.5)$	20586.877	20586.885	-0.008
$R_1(11.5)$	20586.877	20586.891	-0.014

- The average residual error for the fit is **0.02**

Appendix D

Precursor Tests: $l\text{-C}_3\text{H}_2$

The 5450 Å vibronic band of $l\text{-C}_3\text{H}_2$ overlaps with a broad absorption centered at 5476 Å. Refer chapter 6 for details. These absorptions have been deconvoluted using the two Gaussians shown (Figure D.1). That they belong to different molecules was established using a precursor test, with allene and acetylene as precursors. As expected, the intensity of the signal dropped with the even-numbered carbon precursor. However, the relative intensities of these bands varied with the precursor proving that they originate from different species.

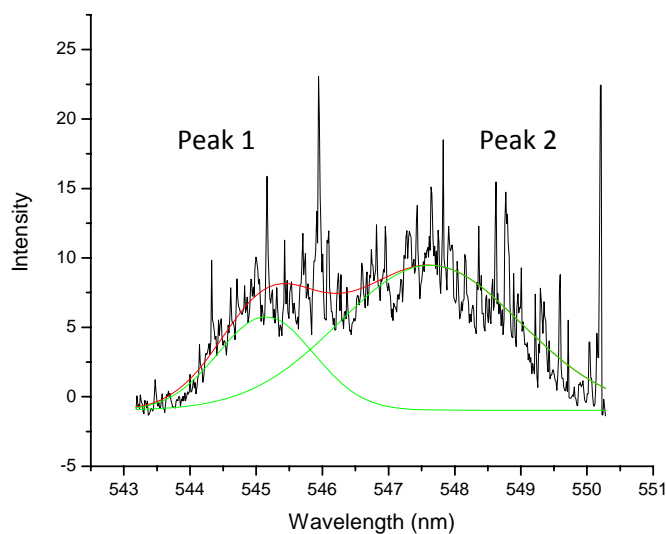


Figure D.1: The absorption spectrum shown deconvoluted using two Gaussians.

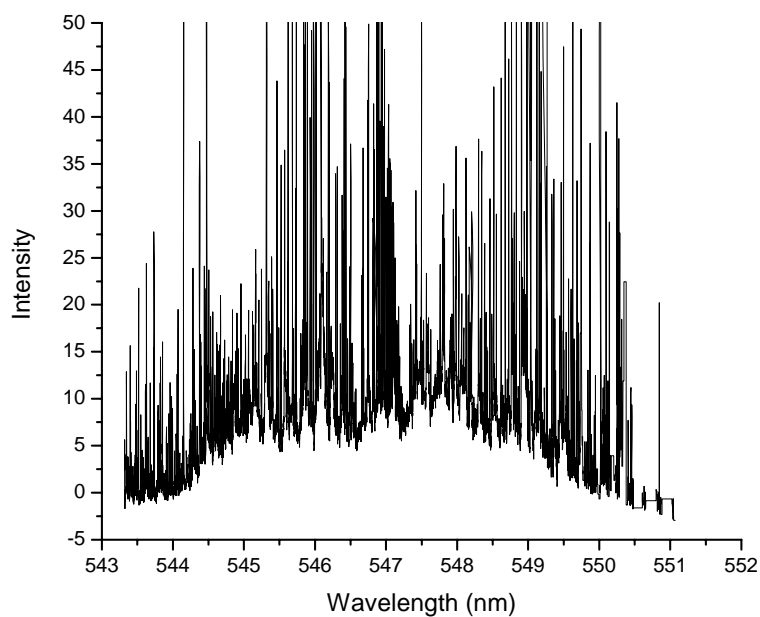


Figure D.2: Absorption spectrum observed using 0.5% allene in Ar as precursor.

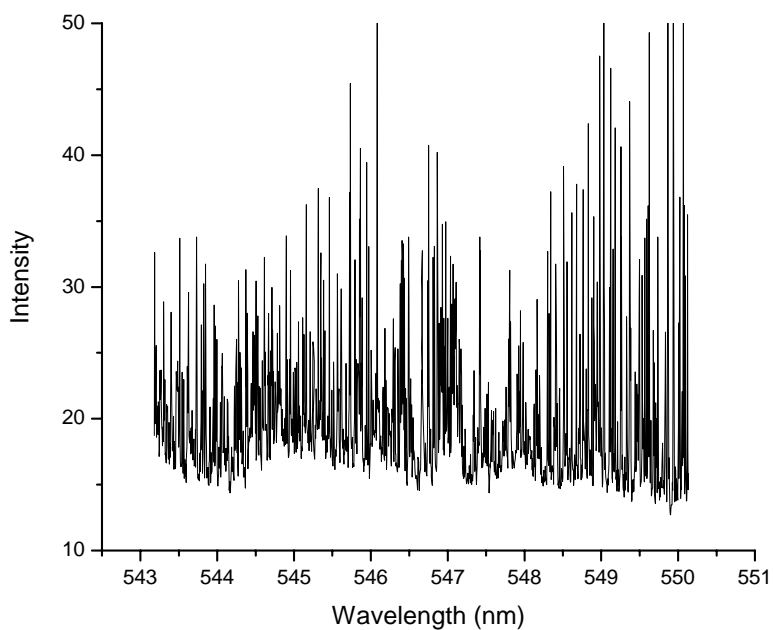
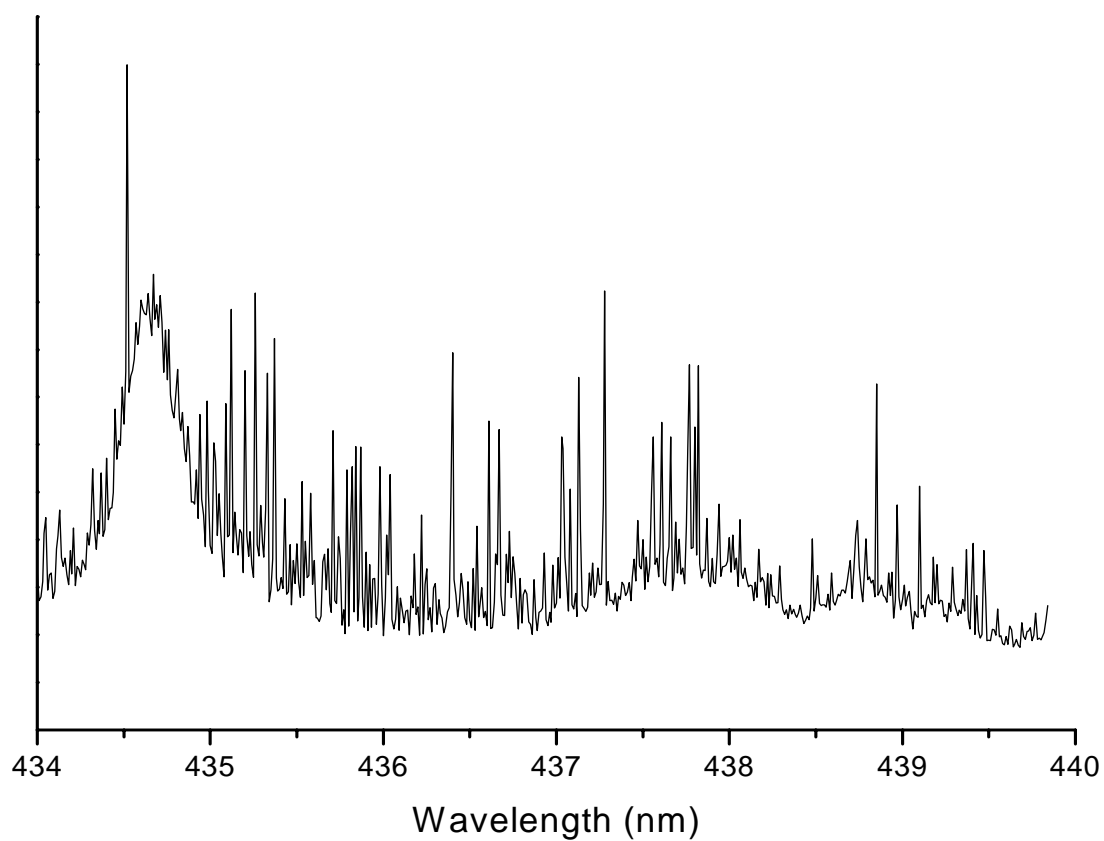


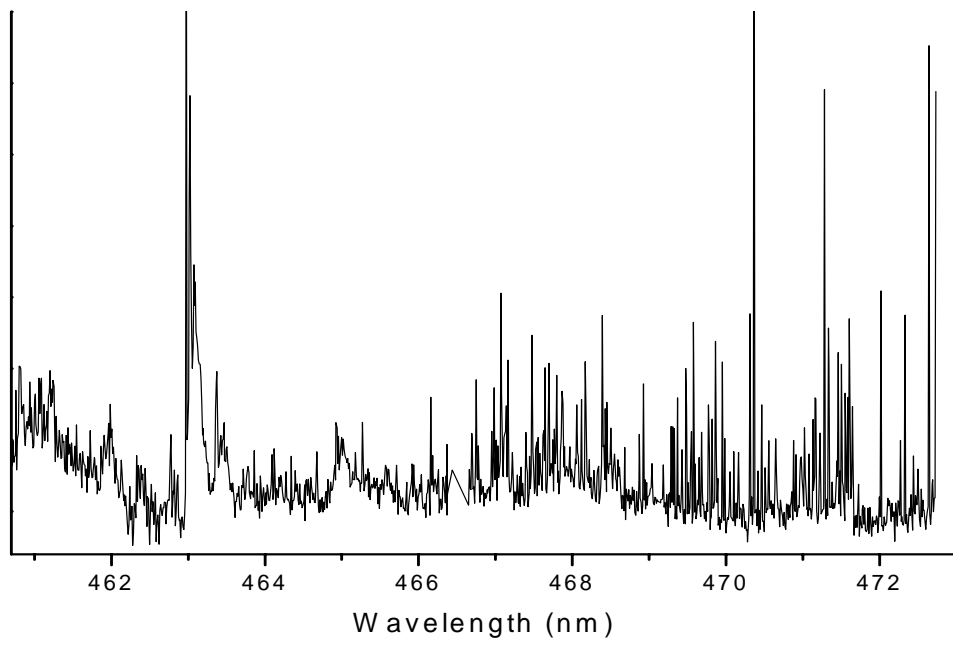
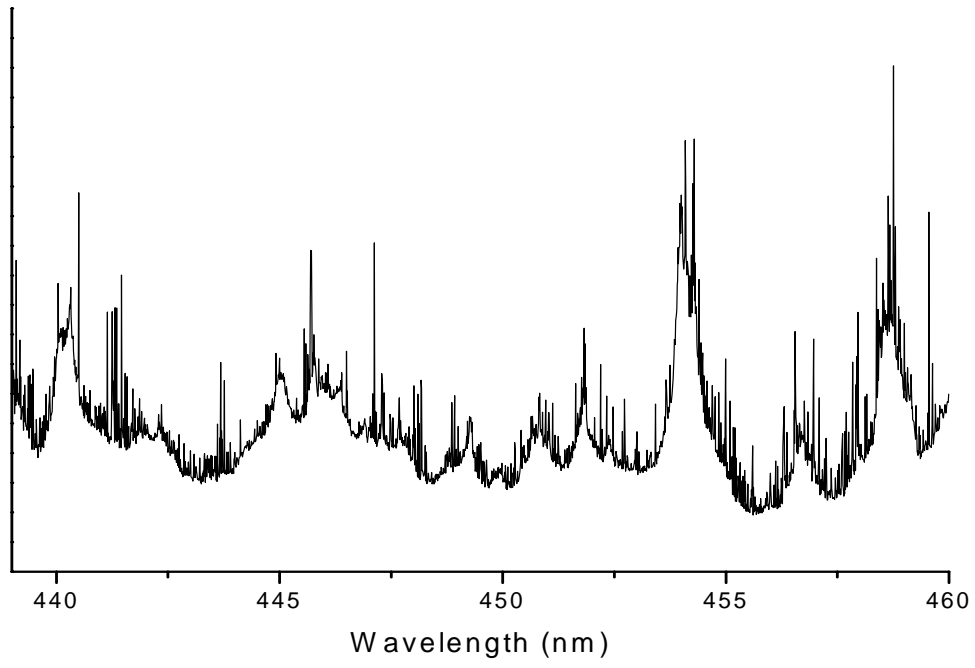
Figure D.3: Absorption spectrum observed using 0.5% acetylene in Ar as precursor. Note how Peak 2 shows varied response in the rate of decrease of signal with a precursor of even-numbered carbon atoms.

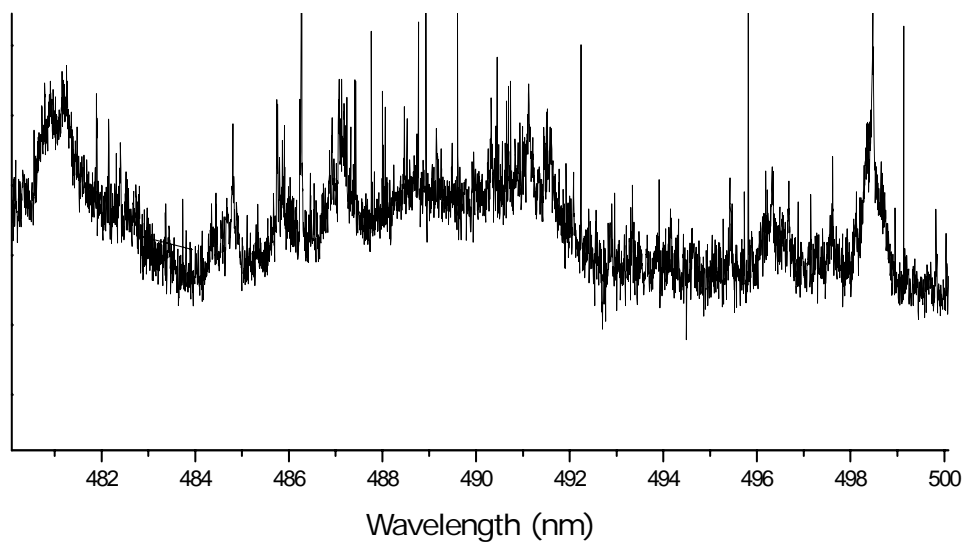
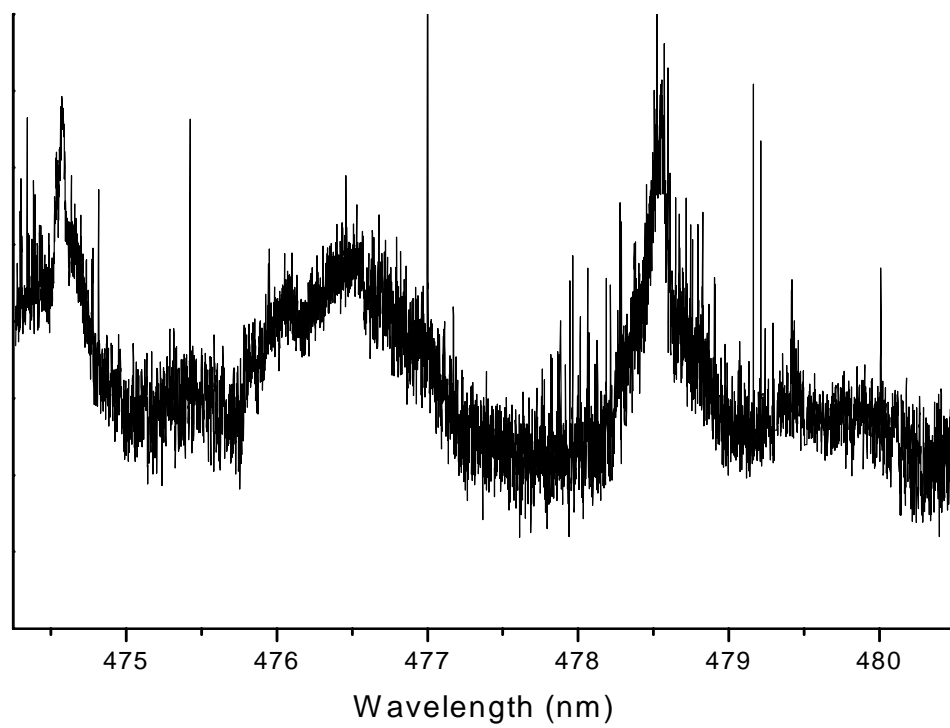
Appendix E

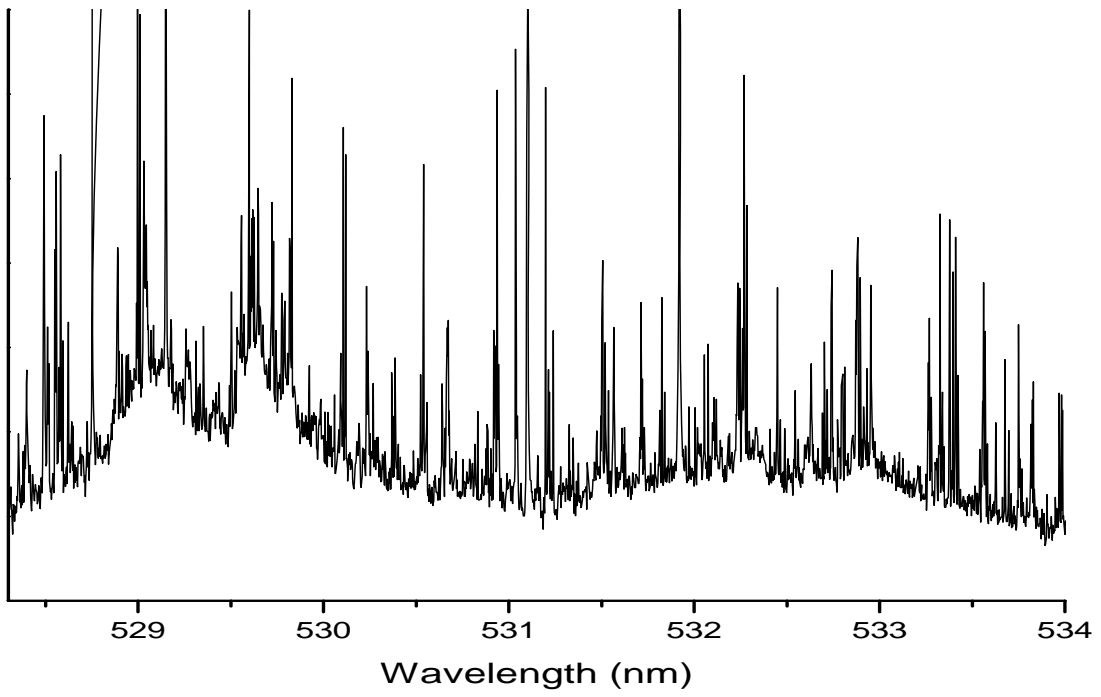
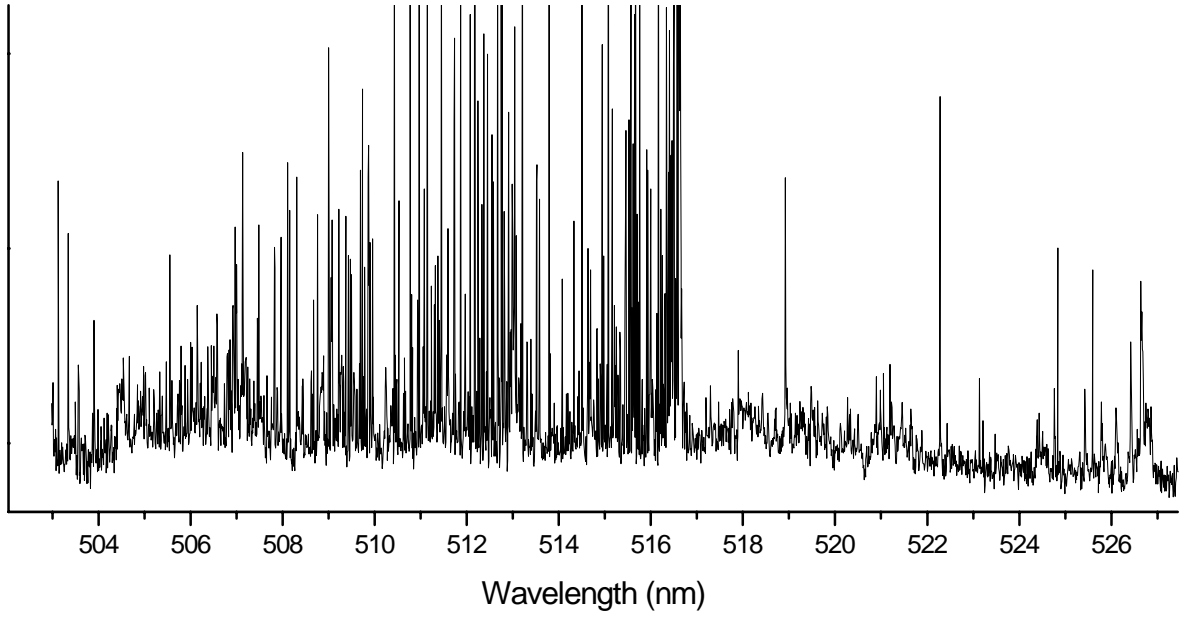
Unidentified Broad Bands Recorded by CRDS

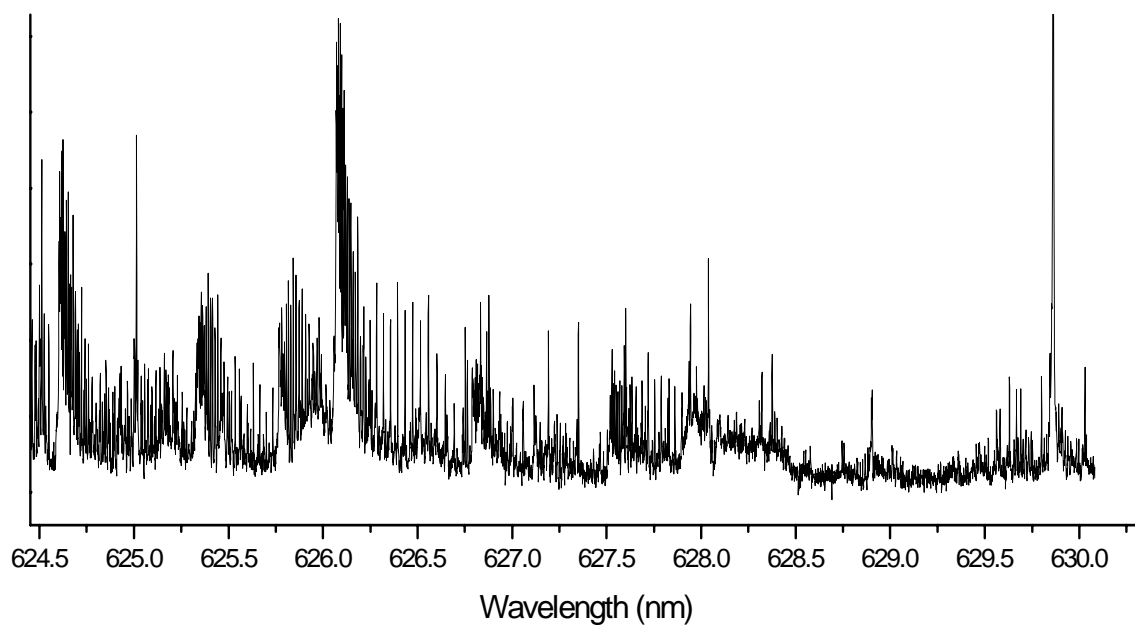
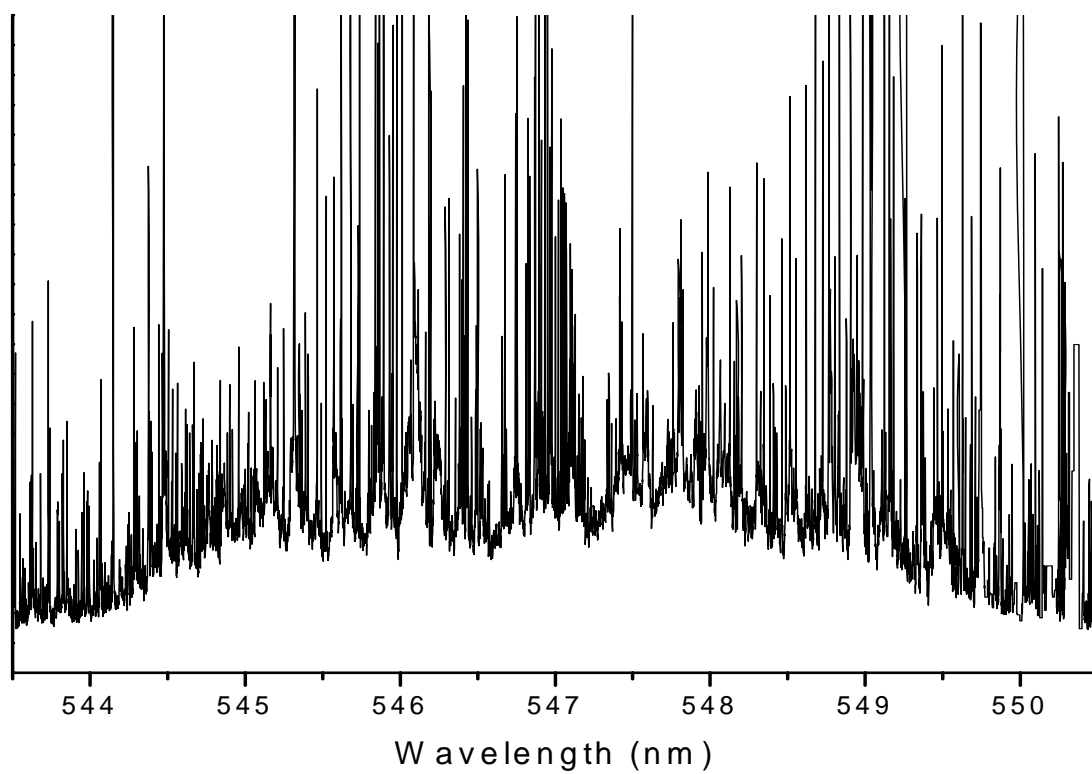
Scans recorded in the range 434 - 630 nm with 0.5% allene/argon discharge are listed below for future reference.











Appendix F

Perturbed energy levels - C₄H

Table showing the experimental and theoretical data obtained from the vibronic analysis (Refer chapter 8) given in cm⁻¹. The assignment $|v_7, v_6, l_7, l_6, \Delta, \Sigma\rangle$ is made using the largest coefficient η obtained in the $|v_7, v_6, l_7, l_6, \Delta, \Sigma\rangle$ basis expansion.

K	E(cm ⁻¹) ^a	v ₆	v ₇	P	η^b	Calculated ^c	Observed ^d	Residuals ^e	Calculated ^f	Observed ^g	Assignment ^h
1.00	394.80	0	0	1.50	-0.75	-314.6			-92.8		
1.00	414.77	0	0	0.50	0.71	-294.6			-72.8		
0.00	439.96	1	0	0.50	0.62	-269.4			-47.6		
							-221.8			0	X ² E ⁺
							-212.5			9.3	
							-202.1			19.7	
							-195.2			26.6	
							-135.1			86.7	
							-126.6			95.2	
							-123.9			97.9	
0.00	587.62	0	1	0.50	0.71	-121.8	-121.8	0.0	100.0	100	A 7 ₁ 6 ₀
2.00	592.23	0	1	1.50	0.65	-117.2			104.6		
							-109.1			112.7	
							-104.3			117.5	
0.00	609.90	0	1	0.50	-0.68	-99.5	-98.8	0.7	122.3	123	A 7 ₁ 6 ₀
							-89.5			132.3	
1.00	626.08	1	1	1.50	0.6	-83.3	-85.8		138.5	136	
1.00	627.13	1	1	0.50	-0.59	-82.3			139.5		
							-77.3			144.5	
							-70.7			151.1	
							-65.4			156.4	
2.00	655.90	1	0	2.50	0.75	-53.5	-51.9	1.6	168.3	169.9	X 7 ₁
2.00	676.59	1	0	1.50	-0.73	-32.8			189.0		
1.00	709.40	0	0	1.50	0.6	0.0	0.0	0.0	221.8	221.8	A ² Π _{3/2}
							4.9			226.7	
1.00	733.21	0	0	0.50	-0.65	23.8	28.1	4.3	245.6	249.9	A ² Π _{1/2}
1.00	767.38	0	2	1.50	-0.66	58.0			279.8		

3.00	769.20	0	2	2.50	-0.59	59.8			281.6		
1.00	778.08	0	2	0.50	-0.53	68.7			290.5		
1.00	791.70	0	2	0.50	0.49	82.3			304.1		
1.00	803.22	0	2	1.50	0.67	93.8			315.6		
0.00	811.79	1	2	0.50	0.56	102.4			324.2		
2.00	812.85	1	2	2.50	0.58	103.5			325.3		
2.00	814.86	1	2	1.50	-0.56	105.5			327.3		
3.00	842.73	2	0	2.50	0.57	133.3			355.1		
1.00	848.15	1	1	1.50	-0.74	138.8	147.4	8.6	360.6	369.2	A 6 ₁₇ ₁
							150.9			372.7	X 7 ₂
							156.0			377.8	
1.00	868.57	1	1	0.50	-0.71	159.2			381.0		
3.00	889.32	1	1	2.50	0.59	179.9			401.7		
0.00	892.22	0	1	0.50	0.56	182.8			404.6		
2.00	900.09	0	1	2.50	0.58	190.7			412.5		
0.00	921.74	0	1	0.50	0.62	212.3			434.1		
2.00	922.76	0	1	1.50	-0.63	213.4			435.2		
2.00	948.32	0	3	2.50	0.61	238.9			460.7		
0.00	962.03	0	3	0.50	-0.62	252.6			474.4		
2.00	963.36	0	3	1.50	0.55	254.0			475.8		
2.00	980.62	0	3	1.50	-0.67	271.2	269.3			491.1	
0.00	984.54	0	3	0.50	0.59	275.1	271.8	-3.3	496.9	493.6	A 6 ₀₇ ₃
							281.3			503.1	
2.00	996.59	0	3	2.50	-0.65	287.2	291.9	4.7	509.0	513.7	A 6 ₀₇ ₃
1.00	1000.65	1	3	1.50	-0.55	291.3			513.1		
1.00	1001.59	1	3	0.50	0.54	292.2			514.0		
3.00	1006.22	1	3	2.50	0.55	296.8			518.6		
2.00	1017.96	2	1	2.50	-0.56	308.6			530.4		
							318.6			540.4	X 7 ₃
							323.0			544.8	
2.00	1034.46	2	1	1.50	0.57	325.1			546.9		
0.00	1039.58	1	2	0.50	-0.72	330.2	331.7	1.5	552.0	553.5	A 6 ₁₇ ₂
0.00	1060.51	1	2	0.50	0.7	351.1	343.0		572.9	564.8	X 7 ₁₆ ₁
2.00	1060.51	1	2	2.50	-0.58	351.1			572.9		
1.00	1076.93	0	2	0.50	-0.54	367.5			589.3		
1.00	1080.04	0	2	1.50	0.5	370.6			592.4		
2.00	1080.09	1	2	1.50	0.59	370.7			592.5		
1.00	1110.67	0	2	1.50	0.59	401.3			623.1		
3.00	1112.08	0	2	2.50	-0.61	402.7			624.5		
1.00	1112.89	0	2	0.50	0.6	403.5			625.3		
0.00	1147.86	3	0	0.50	0.64	438.5			660.3		

1.00	1155.83	0	4	1.50	-0.6	446.4			668.2		
3.00	1158.19	0	4	2.50	0.51	448.8			670.6		
1.00	1167.49	0	4	0.50	-0.6	458.1			679.9		
1.00	1175.37	0	4	0.50	-0.49	466.0			687.8		
3.00	1180.39	0	4	2.50	0.71	471.0			692.8		
1.00	1187.57	0	4	1.50	-0.62	478.2			700.0		
1.00	1209.85	2	2	1.50	0.56	500.5	502.9	2.4	722.3	724.7	A 6 ₂ 7 ₂
0.00	1216.03	1	4	0.50	-0.55	506.6	509.6	3.0	728.4	731.4	A 6 ₁ 7 ₄
							512.5			734.3	X 7 ₂ 6 ₁
2.00	1216.31	1	4	2.50	0.57	506.9			728.7		
2.00	1218.41	1	4	1.50	-0.56	509.0			730.8		
3.00	1223.25	2	2	2.50	0.55	513.9			735.7		
1.00	1225.59	2	2	0.50	-0.52	516.2			738.0		
1.00	1233.32	1	3	0.50	-0.64	523.9			745.7		
1.00	1248.75	1	3	1.50	0.47	539.4			761.2		
1.00	1254.84	1	3	1.50	-0.5	545.4			767.2		
2.00	1266.34	0	3	1.50	-0.51	556.9			778.7		
0.00	1268.32	0	3	0.50	0.44	558.9			780.7		
2.00	1271.17	2	3	2.50	-0.41	561.8			783.6		
1.00	1272.31	1	3	0.50	0.59	562.9			784.7		
3.00	1281.35	1	3	2.50	-0.59	572.0			793.8		
2.00	1302.73	0	3	2.50	-0.56	593.3			815.1		
0.00	1306.45	0	3	0.50	-0.58	597.1			818.9		
2.00	1307.44	0	3	1.50	0.59	598.0			819.8		
0.00	1330.53	1	0	0.50	0.72	621.1	623.5	2.4	842.9	845.3	A 6 ₁ 7 ₀
							626.8			848.6	A 5 ₁
							629.3			851.1	
1.00	1340.03	3	1	0.50	-0.64	630.6			852.4		
1.00	1340.55	3	1	1.50	-0.63	631.2			853.0		
2.00	1345.12	3	0	2.50	0.7	635.7			857.5		
2.00	1372.81	3	0	1.50	-0.67	663.4			885.2		
2.00	1382.46	2	3	2.50	-0.55	673.1			894.9		
0.00	1394.15	2	3	0.50	-0.57	684.8			906.6		
2.00	1398.24	2	3	1.50	0.55	688.8			910.6		
0.00	1410.32	2	3	0.50	0.57	700.9	700.8	-0.1	922.7	922.6	A 6 ₂ 7 ₃
							708.2			930	X 4 ₁

^a The energy is the total vibronic energy.

^b Largest coefficient in the basis expansion.

^c Calculated energy relative to A²Π_{3/2}.

- ^d Observed energy relative to $A^2\Pi_{3/2}$. These levels calculated by taking the energy difference between the R-bandheads of the pump and the probe. The estimated uncertainty on the energy levels is around 2 cm^{-1} .
- ^e Residuals = obs-calc.
- ^f Calculated energy relative to $X^2\Sigma^+$.
- ^g Observed energy relative to $X^2\Sigma^+$.
- ^h Tentative assignment for the levels belonging to the $X^2\Sigma^+$ and $A^2\Pi$ states which were not included in the model.

Rotationally Resolved Ground State Vibrational Levels of HC₂S Studied by Two-Color Resonant Four-Wave Mixing[†]

Richa Chauhan,[‡] Fabio J. Mazzotti,[‡] Ranjini Raghunandan,[‡] Marek Tulej,^{§,‡} Peter P. Radi,^{||} and John P. Maier^{*,‡}

Department of Chemistry, University of Basel, Klingelbergstrasse 80, CH-4056 Basel, Switzerland, and General Energy Research, Paul Scherrer Institute, CH-5232 Villigen, Switzerland

Received: October 11, 2009; Revised Manuscript Received: November 13, 2009

A high-resolution study of the $\tilde{X}^2\Pi_{3/2}$ ground state rovibronic energy levels of jet-cooled HC₂S radical using the double-resonance two-color four-wave mixing technique (TC-RFWM) is reported. The rotational structure of the bands is observed by excitation of selected R-branch lines in the origin band of the $\tilde{A}^2\Pi_{3/2}-\tilde{X}^2\Pi_{3/2}$ electronic system. The second laser frequency is scanned to transfer the population from the rotational level(s) of the upper state to selected vibronic levels of the ground state. Fourteen rotationally resolved vibrational bands have been recorded for energies up to 1800 cm⁻¹ above the $v'' = 0$ $\tilde{X}^2\Pi_{3/2}$ electronic ground state. Effective rotational constants and origins are determined for levels that involve fundamental and overtone combinations of the ν_3 (CS stretch), ν_4 (CCH bend), and ν_5 (CCS bend) vibrations. This illustrates the power and advantages of the TC-RFWM approach for the study of the ground state manifold of reactive intermediates produced in low concentrations with high resolution, good signal-to-noise and wide dynamic range.

I. Introduction

The resonant four-wave mixing (RFWM) technique has been recently applied to spectroscopic investigations of charged and neutral species generated in a supersonic discharge.^{1–3} The detection limit of $\sim 10^8$ molecules cm⁻³ or lower determined in these studies is comparable to that achieved for laser induced fluorescence (LIF) or cavity ring-down spectroscopy (CRDS) rendering the RFWM technique highly competitive.^{1,2,4} Compared to linear methods, the application of RFWM can be advantageous due to complementary capabilities.^{2,5} The high signal-to-noise ratio stems from the fully resonant processes involved and from an essentially background-free signal. Furthermore, because the method is based on molecular absorption, it is not dependent on the lifetime of the upper level and is consequently applicable to the detection of predissociative or short-lived excited states.^{6–8} The nonlinear character of the coherent method introduces the quadratic scaling of the signal intensity with species number density.⁹ This is considered as a limitation of its sensitivity but leads also to a high dynamic range of the RFWM response. RFWM has been exploited in a variety of environments including flames, low-pressure gases and to a lesser extent in supersonic free-jet expansions.^{10–12}

The paper presents the spectroscopic study of the ground state energy levels of HC₂S radical. It shows that the RFWM can be a superior method for studying the molecular structure in the ground state. From the analysis of the rotationally resolved spectra new structural parameters are determined for a number of vibrational energy levels. The unambiguous spectroscopic assignment can be prepared in a straightforward manner using intermediate level labeling. We show that the approach is applicable to the species present in low concentrations and the

spectra can be measured with a high signal-to-noise ratio due to a fully resonant process. The method is background free in contrast to absorption techniques where a weak signal need to be extracted from a large, fluctuating one. The laser-like signal is detected due to coherent character of the four-wave mixing process and the signal beam can be probed remotely without significant loss, reducing background due to stray light. This approach shows the potential of providing a detailed insight to the spectroscopic pattern in the ground state manifold. An access to high lying energy levels in the ground state can also be useful in studies of the reactive properties of transient species such as unimolecular dissociation.

The investigations discussed here utilize a two-color variant of resonant four-wave mixing (TC-RFWM) resulting in a stimulated emission pumping (SEP) type experiment. Classically, the SEP method is based on optical–optical double-resonance involving two laser beams.^{13,14} The first beam (PUMP) transfers population from an initial ground state to a specific level in the electronic excited state while a second beam (DUMP) is used to bring the population back to the ground state manifold. The common SEP detection relies on the competition between spontaneous and stimulated emission by the DUMP laser and results in a small decrease in fluorescence (fluorescence-dip) signal. Only fluorescing molecules can be studied using this technique. In contrast, TC-RFWM does not rely on fluorescing molecules and provides often superior signal-to-noise ratios. The signal is generated by a nonlinear process coupling three input laser beams (2 PUMP and 1 DUMP) that are (i) resonant with two molecular transitions, (ii) share a common (upper) level, and (iii) satisfy the phase matching condition. The double-resonance feature offers a high selectivity for species detection. In addition, intermediate level labeling simplifies complex and congested one-color spectra, allowing precise measurements of line positions and, in most cases, a straightforward assignment of the observed transitions. However, the technique is sensitive to alignment and requires a high quality laser spatial profile as well as good control of beam

[†] Part of the “Benoît Soep Festschrift”.

* Corresponding author. E-mail: j.p.maier@unibas.ch.

[‡] University of Basel.

[§] Present address: Institute of Physics, Planetology and Space Research, University of Bern, Sidlerstr. 5, CH-3012 Bern, Switzerland.

^{||} Paul Scherrer Institute.

intensities to avoid broadening of the molecular transitions due to saturation effects. A variety of theoretical investigations of TC-RFWM can be found in the literature including discussion of the polarization-based schemes and saturation effects.^{15–18} The derivation of the signal intensities based on diagrammatic perturbation theory was particularly well tested experimentally.^{15,19,39}

The interest in HC₂S stems from its importance in interstellar chemistry. A number of sulfur containing carbon chains have been detected by millimeter-wave techniques in star forming regions and in circumstellar envelopes²⁰ and their importance in understanding physical conditions in these regions was discussed.²¹ Although HC₂S has not been yet detected in space, it is expected to be an important intermediate for the formation of large sulfur-containing molecules.²² Two bimolecular reactions are proposed to contribute to the synthesis of HC₂S under interstellar conditions: the sulfur cation with acetylene and the carbon dimer with H₂S.^{22,23}

HC₂S has been extensively studied by spectroscopy. Since its first detection via the $\tilde{A}^2\Pi-\tilde{X}^2\Pi$ electronic transition in flash photolysis of thiophene,^{24,25} HC₂S has attracted considerable attention by experiment and theory. It is an example of a tetraatomic molecule that exhibits a complex coupling of the spin-orbit and Renner-Teller effects. In this context, a number of experimental and theoretical approaches were applied to study the vibrational and rotational structure of this molecule in both the ground and excited state. The ground state structural parameters determined initially from the emission spectra studied in the range 390–450 nm²⁶ have been improved by millimeter-wave spectroscopy for several vibrational bands including the ν_4 and ν_5 bending modes frequencies.^{27,28} The extensive studies by dispersed fluorescence have provided the spin-orbit splitting of 259 cm⁻¹ in the ground state and the vibrational energy levels up to 1700 cm⁻¹.²⁹ The excited state of HC₂S was investigated by LIF yielding complex rovibrational structure.^{30,31} In parallel, theoretical studies attempted to combine spin-orbit with Renner-Teller interactions to explain the experimental findings.^{32,33} Effective Hamiltonian calculations were carried out to shed light on the complex ground state vibrational structure of this radical.^{34,35} In model calculations accompanying the LIF studies it has been shown that the large Renner-Teller effect observed in the excited state and the different HCCS and DCCS excited state zero-point spin-orbit splitting can be explained with the assumption of a quasilinear excited state geometry.³¹ In spite of considerable advances made in the understanding of the spectral complexity of HC₂S, the theoretical approaches developed so far do not offer an unambiguous explanation of all features observed.³³

In this paper, the structure of the $\tilde{X}^2\Pi_{3/2}$ ground state of the HC₂S radical is further characterized by measuring rotationally resolved spectra of vibrational levels by TC-RFWM. Due to the high sensitivity of the method 14 excited vibrational states could be observed in the ground state manifold, 650–1800 cm⁻¹ above the $\nu'' = 0$ $\tilde{X}^2\Pi_{3/2}$ level. The selectivity of the optical-optical double-resonance method permits an unambiguous assignment based on intermediate level labeling and yields effective rotational constants and band origins.

II. Experimental Setup

The HC₂S radical was produced by a slit-jet discharge.³⁶ The slit length was 30 mm × 1 mm and -1000 V was applied to the electrodes, which were separated by 2 mm. The discharge pulse length was 3–10 μ s, resulting in a short but intense pulse of radicals. During the operation of the assembly at 10 Hz, a pressure in the source chamber of approximately 0.05 mbar was

maintained by the vacuum system for a backing pressure of 5–10 bar. The timing between the two lasers, the triggering of the valve and the discharge voltage were controlled by a fast electronic delay generator. These timings are critical for the efficient production of HC₂S which was generated by using a C₂H₂/CS₂ (1%/0.5%) mixture in argon as precursor. The optical configuration used has also been described.³ Two separate Nd:YAG pumped dye lasers were used, one with an intracavity etalon and the other with a double grating. The spectral bandwidth of the two laser sources was around 0.05 cm⁻¹. Frequency calibration was achieved by a wavemeter with an accuracy of 0.002 cm⁻¹. For degenerate four-wave mixing, one of the lasers was split into three components of equal intensities by broadband beam splitters and sent into the vacuum chamber in a BOXCARS configuration.³⁷ The output energy of the lasers used was attenuated with neutral density filters. In case of TC-RFWM measurements, the third beam was replaced by the output of the second laser (probe or DUMP) and scanned in frequency as the PUMP laser remained at a fixed wavelength. The signal beam, which is coherent and collimated in nature, was separated from the stray radiation by a 6 m detection arm consisting of several irises and spatial filters to obtain nearly background-free spectra. The signal was detected with a photomultiplier. Special masks were used to position the three beam crossing angles ($\sim 1.4^\circ$) to satisfy the phase-matching condition $k_1 + k_3 = k_2 + k_4$, where the wave vectors k_1 , k_2 (PUMP), and k_3 (probe) generate the signal beam wave vector k_4 .⁹ The PUMP beams were positioned such that the optically induced fringes were directed along the flow of molecules in the supersonic expansion.⁷ The polarizations of the three beams were vertical in the laboratory frame. The signal was digitized by a fast oscilloscope and averaged for 2–3 s for every scan step of the spectrum.

III. Results and Discussion

Initial experiments were performed by applying DFWM spectroscopy on the origin band of the $\tilde{A}^2\Pi_{3/2}-\tilde{X}^2\Pi_{3/2}$ transition of HC₂S. The spectrum is reproduced in Figure 1 and shows a well resolved P-branch and a heavily congested R-branch. A least-squares fit to the resolved line positions by means of the PGOPHER program³⁸ was carried out by constraining the rotational and centrifugal distortion constants

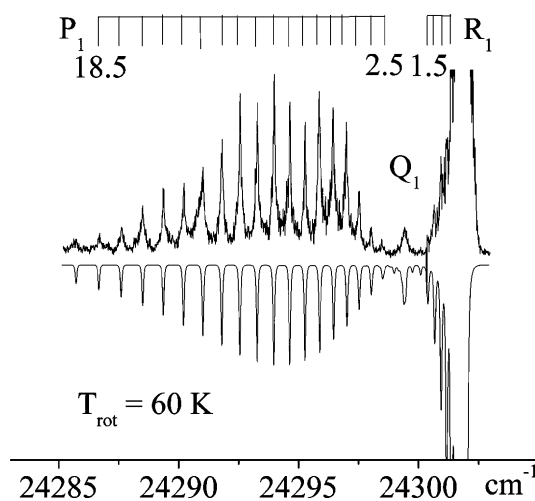


Figure 1. Rotationally resolved DFWM spectrum of the origin band of the HC₂S $\tilde{A}^2\Pi_{3/2}-\tilde{X}^2\Pi_{3/2}$ electronic system. The inverted trace is the square of the PGOPHER simulation, assuming a Lorentzian line shape (0.1 cm⁻¹ fwhm) and a rotational temperature of 60 K.

of the $\tilde{A}^2\Pi_{3/2}$ state to the values given in ref 26. The spectroscopic constants found in the previous measurement,²¹ such as the rotational constant of the lower state, $B_0'' = 0.195\,693(11)\text{ cm}^{-1}$ and the origin at $T_{00} = 24\,299.4430(20)\text{ cm}^{-1}$ were confirmed. The low J -numbers observed for the jet-cooled radicals prevent an accurate determination of the quartic centrifugal distortion constant, which therefore was fixed at $2.4 \times 10^{-8}\text{ cm}^{-1}$. A simulated DFWM spectrum at a rotational temperature of approximately 60 K is shown inverted in Figure 1. The excellent agreement with the published values validates the procedure for the evaluation of rotational constants and band origins and will be applied in the following for the rotational analysis of higher lying vibrational levels measured by TC-RFWM.

Rotationally resolved double-resonance spectra were obtained by applying the TC-RFWM technique. The pump beams were tuned to known rotational transitions in the 0_0^0 band of the $\tilde{A}^2\Pi_{3/2}-\tilde{X}^2\Pi_{3/2}$ electronic system, exciting well-defined rotational states of the upper level (intermediate level labeling). Subsequently, with the pump laser frequency fixed, the dump (or probe) beam was scanned in the range of selected vibronic bands in the ground state that share a common upper level with the pumped $v' = 0$ state. Note that the phase matching conditions⁹ are met exactly only for one combination of the pump and dump frequencies. Scanning the latter causes a phase mismatch, which reduces the signal intensity. However, in practice, the effect can be neglected and a range of $\sim 900\text{ cm}^{-1}$ is achievable without major realignment.⁷ The observed TC-RFWM spectra display excellent signal-to-noise ratios up to $\sim 10^4$ for the stronger transitions and allow an accurate determination of line positions. Furthermore, the expected simplification by the double-resonance selection rules reduces ambiguities for the assignment that occur in the one-color spectrum where overlapping transitions are frequently present.

Figure 2 exemplifies the method and the assignment procedure for rotational transitions. The frequency of the pump laser at $24\,295.21\text{ cm}^{-1}$ corresponds to the $P_1(8.5)$ transition of HC₂S in the origin band of the $\tilde{A}^2\Pi_{3/2}-\tilde{X}^2\Pi_{3/2}$ electronic transition. By scanning the probe laser over the same band, we obtain a nearly degenerate two-color four-wave mixing spectrum (upper trace). Alternatively, the probe laser is scanned around 23520 cm^{-1} , addressing the vibrational level of the ground state exhibiting one quantum excitation in ν_3 (lower trace). The resonant lines consist of the $P_1(8.5)$, $R_1(6.5)$, and $R_1(8.5)$ transitions according to the insets in the figure. A minor contribution of a neighboring transition of the pumped $P_1(8.5)$ in the origin band is observed in the lower trace. In fact, $P_1(9.5)$ is simultaneously excited due to saturation broadening and yields the "satellite" transitions $P_1(9.5)$ and $R_1(7.5)$ in the 3_1^0 band. TC-RFWM is thus able to characterize the high lying vibrational levels in the $\tilde{X}^2\Pi_{3/2}$ state of the supersonically cooled radical by SEP type approach.

As was demonstrated previously,³ a convenient way of using TC-RFWM is to tune the pump laser to the band head where numerous rotational levels are excited concomitantly due to overlapping transitions. A scan of the probe laser yields then several resonant transitions to the ground rotational level(s) in a single spectrum. Figure 3 displays an example of TC-RFWM spectra obtained by pumping the band head of the origin transition at $24\,301.9\text{ cm}^{-1}$. For these experiments it is advantageous to remove the intracavity etalon of the laser to broaden the bandwidth to approximately 0.15 cm^{-1} and to excite, therefore, a broad range of P-branch transitions simultaneously

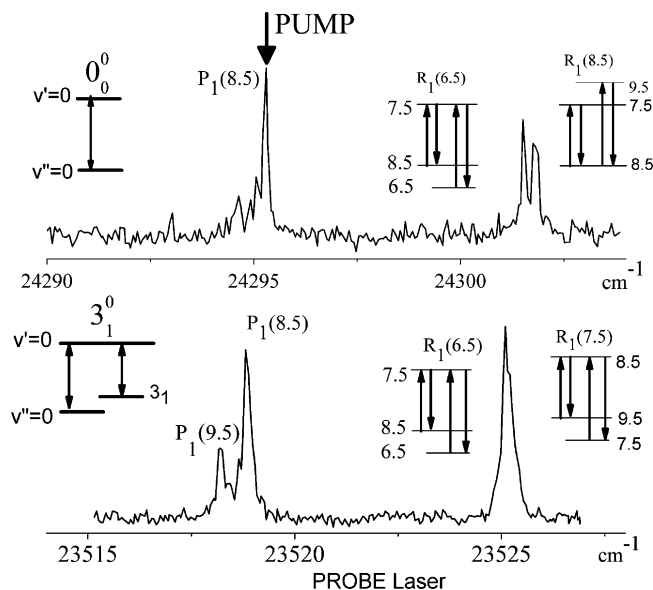


Figure 2. TC-RFWM spectrum. The pump frequency was fixed on the $P_1(8.5)$ transition of the origin band of the $\tilde{A}^2\Pi_{3/2}-\tilde{X}^2\Pi_{3/2}$ transition (PUMP). The probe was scanned through the origin (upper trace) and 3_1^0 (lower trace) bands. The nearly degenerate TC-RFWM (upper trace) displays three transitions: the degenerate TC-RFWM at $P_1(8.5)$ and two R_1 transitions sharing the upper and lower level ($R_1(6.5)$ and $R_1(8.5)$, respectively). The SEP spectrum connecting the $v' = 0$ $\tilde{A}^2\Pi_{3/2}$ state to the $3_1 \tilde{X}^2\Pi_{3/2}$ level only exhibits two resonant lines that share the common upper level with $J = 7.5$ and $v' = 0$. The $P_1(9.5)$ transition, and $R_1(7.5)$ which contributes to the 23535 cm^{-1} peak, are present due to saturation effects (see text).

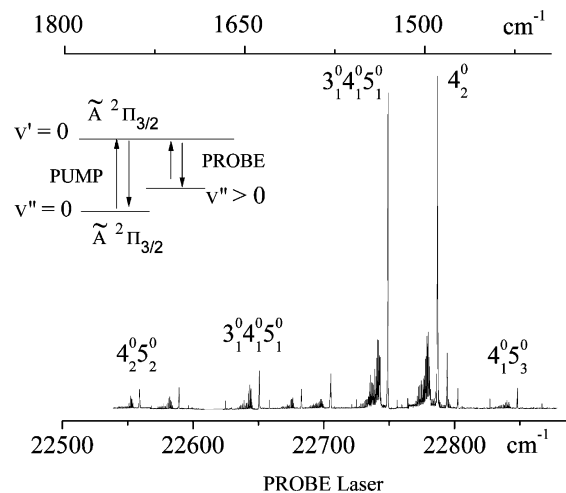


Figure 3. Rotationally resolved stimulated emission spectrum of vibrationally excited ground state levels of the $\tilde{A}^2\Pi_{3/2}-\tilde{X}^2\Pi_{3/2}$ electronic transition of HC₂S. The pump laser was set on the band-head of the $\tilde{A}^2\Pi_{3/2}-\tilde{X}^2\Pi_{3/2}$ origin and excites numerous rotational levels simultaneously. The horizontal scale (cm^{-1}) at the top shows the energy above the $v'' = 0$ $\tilde{X}^2\Pi_{3/2}$. The inset is the scheme of the double resonance approach.

($J = 9.5-21.5$). The subsequent scan of the probe laser in the vicinity of the 5_2^0 band gives rise to a large number of rotationally resolved transitions that are in resonance with the labeled states of the upper level. To avoid power broadening, the measurements have been performed at input intensities below saturation of the molecular transitions. An overview of the TC-RFWM spectrum in the range between $22\,500$ and $22\,900\text{ cm}^{-1}$ is shown in Figure 3.

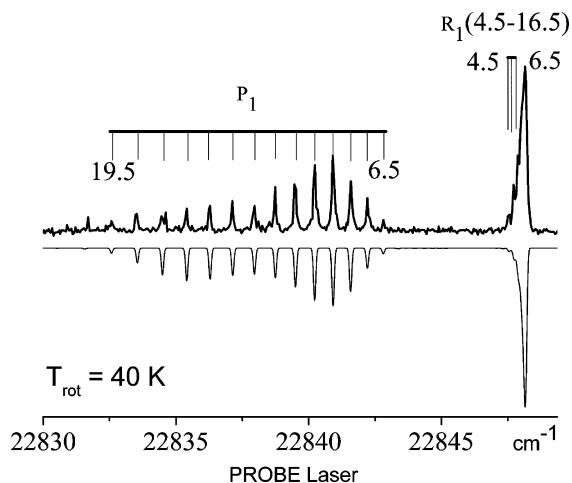


Figure 4. Vibronic structure of the transition detected by TC-RFWM. The pump was set on the bandhead of the origin band in the $\tilde{A}^2\Pi_{3/2}-\tilde{X}^2\Pi_{3/2}$ transition of HC_2S . A least-squares fit to the line positions yields the rotational constant and the vibronic origin of the band. A synthetic spectrum with the optimized molecular constants and assuming a Boltzmann distribution for a rotational population at 40 K is shown inverted (see text for details). Intensities are computed by taking into account partial saturation of the transitions.³⁹

The $4_1^0 5_3^0$ band around $22\,840\text{ cm}^{-1}$ is shown in more detail in Figure 4. The rotationally resolved band structure resembles a $^2\Pi-^2\Pi$ system with a weak Q branch. The assignment of these transitions is straightforward. Intermediate level labeling from the $\tilde{X}^2\Pi_{3/2}$ state by the pump laser yields only transitions to levels in the ground state with the same spin component $\Omega = 3/2$. If ambiguities are encountered for the assignment of specific J -levels, the method described above using a narrow bandwidth laser is applied and yields unambiguous results. The substantial signal-to-noise ratio provides accurate line positions suitable for the determination of effective rotational parameters.

A least-squares fit to the observed frequencies has been carried out using the PGOPHER program³⁸ and constraining the molecular constants in the $\tilde{A}^2\Pi_{3/2}$ state to the values of ref 26. For each recorded band, two parameters are obtained, B_{eff}'' and the band origin. Around 14 lines were used for the fit of each band. The resulting vibronic origins are determined with a 10% higher precision compared to the previous work by dispersed fluorescence.²⁹ Furthermore, rotational constants of

the ground state vibrations are determined for 14 vibrational levels of which 12 are reported for the first time. The results are summarized in Table 1. The vibrational assignment and the labeling of the bands (first column) follow the work of ref 29. As can be seen in Table 1, among the five normal modes of the linear molecule, ν_3 (CS stretch), ν_4 (CCH bend), and ν_5 (CCS bend) are obtained from the detected overtones and combination bands. The rotational constants inferred in ref 26 for the two commonly detected ground state vibrational levels (5 and 16) are in agreement with our results to within one standard deviation. However, their tentative assignment of band 16 is in disagreement with the present study. A direct linear trend in the variation of the rotational constant versus the vibrational excitation quantum number is not apparent. The finding is rationalized by considering that Renner–Teller interaction and perturbations may induce a nontrivial potential energy surface along the internal coordinates of the molecule. There are two vibronic bands (4 and 16) for which the rotational constant decrease with respect to the $v'' = 0$ state (Table 1). The energetically lowest level of them has been assigned as 3_1 and the other as the $3_1 4_1 5_1$ combination.

IV. Conclusion

Double-resonance spectroscopy by TC-RFWM offers a way to access specific vibronic levels of the ground state and to simplify the complex rotational band structure by intermediate level labeling. In the present work, TC-RFWM spectra were recorded and analyzed for the $\tilde{A}^2\Pi_{3/2}-\tilde{X}^2\Pi_{3/2}$ electronic transition of HC_2S . These are background-free, show a high dynamic range ($\sim 10^4$) and high signal-to-noise ratio for the weakest ro-vibrational bands (~ 150), enabling their accurate rotational analysis to be made. Rotational constants for selected ground state vibrations with $\tilde{X}^2\Pi_{3/2}$ symmetry were determined by taking advantage of the unambiguous assignment capability of the method. The work reports rotational constants for 14 vibronic bands. With the exception of the constants for the bands 5 and 16 in Table 1, these values are determined for the first time. An uncertainty of 0.005 cm^{-1} improves the values by a factor of 10. The present work combined with the previous results on HC_2S should be an incentive for ab initio calculations and a better understanding of the complex and overlapping ground state vibrational structure of this interesting Renner–Teller molecule.

TABLE 1: Spectroscopic Constants Determined for the Vibrationally Excited Levels in the $\tilde{X}^2\Pi_{3/2}$ Ground Electronic State of HC_2S^a

label	T_{0v}	B_{eff}''	B_{eff}'' (ref 26)	residuals ($\times 10^{-2}$)	level	$B_{\text{eff}}'' - B_0''$ ($\times 10^{-3}$)
24	1742.527(13)	0.196140(85)		2.8	$4_2 5_2$	0.45(9)
23	1712.2348(28)	0.197288(22)		0.6	$3_1 4_2$	1.59(2)
20	1650.9168(64)	0.196803(31)		1.6	$3_1 4_1 5_1$	1.11(3)
19	1618.7326(34)	0.196677(16)		0.8	$4_3 5_1$	0.98(2)
18	1596.388(11)	0.195786(53)		2.7	3_2	0.09(5)
16	1552.786(11)	0.195553(52)	0.19558(12)	2.7	$3_1 4_1 5_1$	-0.14(5)
14	1514.7266(77)	0.196683(37)		1.9	4_2	0.99(4)
13	1507.3883(81)	0.196570(55)		1.3	$3_1 5_2$	0.88(6)
12	1499.1669(78)	0.196791(43)		0.9	$4_2 5_2$	1.10(4)
11	1453.5528(37)	0.197119(22)		0.8	$4_1 5_3$	1.43(2)
6	870.334(11)	0.196899(76)		2.5	4_2	1.21(8)
5	822.228(10)	0.195820(45)	0.19595(16)	2.6	$4_1 5_1$	0.13(5)
4	776.4297(66)	0.195537(30)		1.9	3_1	-0.16(3)
2	675.9444(62)	0.19610(40)		1.2	5_2	0.41(4)

^a The labels and assignments are based on ref 13. All term values and spectroscopic constants are in cm^{-1} . Values in parentheses are one standard deviation.

Acknowledgment. This work has been supported by the Swiss National Science Foundation (Project 200020-124349/1 and 200020-115958) and the Swiss Department of Energy (BFE, Contract 100708).

References and Notes

- (1) Raghunandan, R.; Mazzotti, F. J.; Chauhan, R.; Tulej, M.; Maier, J. P. *J. Phys. Chem. A* **2009**, *113*, 13402.
- (2) Tulej, M.; Meisinger, M.; Knopp, G.; Walser, A. M.; Gerber, T.; Radi, P. P. *J. Raman Spectrosc.* **2007**, *38*, 1022.
- (3) Mazzotti, F. J.; Achkasova, E.; Chauhan, R.; Tulej, M.; Radi, P. P.; Maier, J. P. *Phys. Chem. Chem. Phys.* **2008**, *10*, 36.
- (4) Tulej, M.; Meisinger, M.; Knopp, G.; Walser, A. M.; Beaud, P.; Gerber, T.; Radi, P. P. *J. Raman Spectrosc.* **2006**, *37*, 680.
- (5) Tulej, M.; Knopp, G.; Beaud, P.; Gerber, T.; Radi, P. P. *J. Raman Spectrosc.* **2005**, *36*, 109.
- (6) Tulej, M.; Meisinger, M.; Knopp, G.; Walser, A. M.; Beaud, P.; Gerber, T.; Radi, P. P. *J. Raman Spectrosc.* **2006**, *37*, 376.
- (7) Butenhoff, T. J.; Rohlfing, E. A. *J. Chem. Phys.* **1993**, *98*, 5460.
- (8) Liu, C.-P.; Reid, S. A.; Lee, Y.-P. *J. Chem. Phys.* **2005**, *122*, 124313.
- (9) Vaccaro, P. H. In *Nonlinear Spectroscopy for Molecular Structure Determination*; Hirota, E., Field, R. W., Maier, J. P., Tsuchiya, S., Eds.; Blackwell Scientific: Oxford, U.K., 1998; p 75.
- (10) Farrow, R. L.; Rakestraw, D. J. *Science* **1992**, *257*, 1894.
- (11) Butenhoff, T. J.; Rohlfing, E. A. *J. Chem. Phys.* **1992**, *97*, 1595.
- (12) Radi, P. P.; Tulej, M.; Knopp, G.; Beaud, P.; Gerber, T. *J. Raman Spectrosc.* **2003**, *34*, 1037.
- (13) Dai, H.-L., Field, R. W., Eds. *Molecular Dynamics and Spectroscopy by Stimulated Emission Pumping*; World Scientific: Singapore, 1995.
- (14) Buntine, M. A.; Chandler, D. W.; Hayden, C. C. *J. Chem. Phys.* **1992**, *97*, 707.
- (15) Williams, S.; Tobiasson, J. D.; Dunlop, J. R.; Rohlfing, E. A. *J. Chem. Phys.* **1995**, *102*, 8342.
- (16) Williams, S.; Rohlfing, E. A.; Rahn, L. A.; Zare, R. N. *J. Chem. Phys.* **1995**, *102*, 8342.
- (17) Bracamonte, A. E.; Vaccaro, P. H. *J. Chem. Phys.* **2003**, *119*, 887.
- (18) Costen, M. L.; McKendrick, K. G. *J. Chem. Phys.* **2005**, *112*, 164309.
- (19) Hung, W.-C.; Huang, M.-L.; Lee, Y.-C.; Lee, Y.-P. *J. Chem. Phys.* **1995**, *103*, 9941.
- (20) Gordon, V. P.; McCarthy, M. C.; Apponi, A. J.; Thaddeus, P. *Astrophys. J. Suppl.* **2002**, *138*, 297, and references therein.
- (21) Minh, Y. C.; van Dishoeck, E. F. *From Molecular Clouds to Planetary Systems* **2000**, 197.
- (22) Yamada, M.; Osamura, Y.; Kaiser, R. I. *Astron. Astrophys.* **2002**, *395*, 1031.
- (23) Smith, D.; Adams, N. G.; Giles, K.; Herbst, E. *Astron. Astrophys.* **1988**, *200*, 191.
- (24) Krishnamachari, S. L. N. C.; Venkitachalam, T. V. *Chem. Phys. Lett.* **1978**, *55*, 116.
- (25) Krishnamachari, S. L. N. G.; Ramsay, D. A. *Faraday Discuss. Chem. Soc.* **1981**, *71*, 205.
- (26) Coquart, B. *Can. J. Phys.* **1985**, *63*, 1362.
- (27) Tang, J.; Saito, S. *J. Chem. Phys.* **1996**, *105*, 8020.
- (28) McCarthy, M. C.; Vrtilik, J. M.; Gottlieb, E. W.; Tao, F.-M.; Gottlieb, C. A.; Thaddeus, P. *Astrophys. J.* **1994**, *431*, L127.
- (29) He, S.-G.; Clouthier, D. J. *J. Chem. Phys.* **2005**, *123*, 014317.
- (30) Kohguchi, H.; Ohshima, Y.; Endo, Y. *Chem. Phys. Lett.* **1996**, *254*, 397.
- (31) He, S.-G.; Clouthier, D. J. *J. Chem. Phys.* **2004**, *120*, 8544.
- (32) Perić, M.; Stevanović, L.; Jerosimić, S. *J. Chem. Phys.* **2002**, *117*, 4233.
- (33) Perić, M.; Marian, C. M.; Peyerimhoff, S. D. *J. Chem. Phys.* **2001**, *114*, 6086.
- (34) He, S.-G.; Clouthier, D. J. *J. Chem. Phys.* **2005**, *123*, 014317.
- (35) He, S.-G.; Clouthier, D. J. *J. Chem. Phys.* **2005**, *123*, 014316.
- (36) Motylewski, T.; Linnartz, H. *Rev. Sci. Instrum.* **1999**, *70*, 1305.
- (37) Prior, Y. *Appl. Opt.* **1980**, *19*, 1741.
- (38) PGOPHER, a Program for Simulating Rotational Structure. Western, C.M., University of Bristol <http://pgopher.chm.bris.ac.uk>.
- (39) Bultitude, K.; Bratfalean, R.; Ewart, P. *J. Raman Spectrosc.* **2003**, *34*, 1030.

JP909738N

Curriculum Vitae

Ranjini Raghunandan

Institute of Physical Chemistry
University of Basel
Klingelbergstrasse 80
Basel - 4056
Switzerland

Email: r.raghunandan@unibas.ch
Born on January 21, 1985
Female
Single
Indian citizen

Education

University of Basel, Switzerland

Doctor of Philosophy in Physical Chemistry

(Oct. 2007 - Aug. 2011)

Summa cum laude

Thesis Title: Linear and Nonlinear Spectroscopic Techniques applied to Study of Transient Molecular Species
Supervisor: Prof. Dr. J. P. Maier, F.R.S.

Cochin University of Science and Technology, India

Master of Sciences (5 year integrated) in Photonics

(Oct. 2002 - Jul. 2007)

Gold Medalist

Thesis Title: Imaging and Interferometric Analysis of Protein Crystal Growth
Supervisor: Prof. Dr. K. Muralidhar (Indian Institute of Technology, Kanpur)

Teaching Experience

University of Basel, Switzerland

Laboratory courses in physical chemistry for undergraduate students

(Feb. 2008 to Jul. 2011)

Conference Presentations

- Oral Presentation: Symposium on Astrochemistry - IAU Symposium 280, Toledo, Spain, 2011.
- Poster: Frontiers in Spectroscopy - Faraday Discussion 150, Basel, Switzerland, 2011.
- Poster: 21st International Conference on High Resolution Molecular Spectroscopy, Poznan, Poland, 2010.
- Poster: S³C - Symposium on Size Selected Clusters, Brand, Austria, 2009.
- Poster: SPIE Photonics Europe, Strasbourg, France, 2008.

Peer Reviewed Publications

- **Renner-Teller and Fermi Resonance interactions for the $v_3 = 1$ and $v_7 = 2$ vibronic levels in the $A^2\Pi_u$ and $X^2\Pi_g$ electronic states of HC_4H^+** , [Raghunandan, R.](#); Mazzotti, F. J.; Esmail, A. M.; Maier, J. P. *J. Phys. Chem. A*, 115, 9365, 2011.
- **Characterization of C_4H in the $A^2\Pi$ and $X^2\Sigma^+$ states by double resonance four-wave mixing**, Mazzotti, F. J.; [Raghunandan, R.](#); Esmail, A. M.; Maier, J. P. *J. Chem. Phys.* 134, 164303, 2011.
- **Identification of H_2CCC as a diffuse interstellar band carrier**, Maier, J. P.; Walker, G. A. H; Bohlender, D. A.; Mazzotti, F. J.; [Raghunandan, R.](#); Fulara, J.; Garkusha, I.; Nagy, A. *Astrophys. J.* 726, 41, 2011.
- **Electronic Spectra of C_6H^+ and $C_6H_3^+$ in the Gas Phase**, [Raghunandan, R.](#); Mazzotti, F. J.; Maier, J. P. *J. Am. Soc. Mass Spectrom.* 21, 694, 2010.
- **Rotationally Resolved Ground State Vibrational Levels of HC_2S Studied by Two-Color Resonant Four-wave Mixing**, Chauhan, R.; Mazzotti, F.J.; [Raghunandan, R.](#); Tulej, M.; Maier, J.P.; Radi, P.P. *J. Phys. Chem. A*. 114, 3329, 2010.
- **Selective Detection of Radicals and Ions in a Slit-Jet Discharge by Degenerate and Two-Color Four-wave Mixing**, [Raghunandan, R.](#); Mazzotti, F. J.; Chauhan, R.; Tulej, M.; Maier, J. P. *J. Phys. Chem. A*. 113, 13402, 2009.
- **Imaging and interferometric analysis of protein crystal growth**, [Raghunandan, R.](#); Gupta, A. S.; Muralidhar, K. *Proc. SPIE* 6991, 69912H, 2008.

